MEMS-BASED NOZZLES AND TEMPLATES FOR THE FABRICATION OF ENGINEERED TISSUE CONSTRUCTS

A Dissertation
Presented to
The Academic Faculty

by

Nisarga Naik

In Partial Fulfillment
of the Requirements for the Degree
of Doctor of Philosophy in the
School of Electrical and Computer Engineering

Georgia Institute of Technology
December 2010

MEMS-BASED NOZZLES AND TEMPLATES FOR THE FABRICATION OF ENGINEERED TISSUE CONSTRUCTS

Approved by:

Dr. Mark Allen , Advisor
School of Electrical and Computer Engineering
Georgia Institute of Technology

Dr. Pamela Bhatti
School of Electrical and Computer Engineering
Georgia Institute of Technology

Dr. Oliver Brand
School of Electrical and Computer Engineering
Georgia Institute of Technology

Dr. Jeff Shamma
School of Electrical and Computer Engineering
Georgia Institute of Technology

Dr. Elliot Chaikof
Department of Surgery
Beth Israel Deaconess Medical Center
Harvard Medical School

Date Approved: October 14, 2010

ACKNOWLEDGEMENTS

First of all, I would like to express my deepest thanks to my advisor, Dr. Mark Allen, for his invaluable guidance, support, and understanding all through my time in graduate school. My Ph.D. experience would not have been the same without the direction of such a wonderful teacher. I would like to thank Dr. Elliot Chaikof for his advice, support, and constant encouragement which helped me develop a passion for biology. I am grateful for the support of my committee members Dr. Pamela Bhatti, Dr. Oliver Brand, and Dr. Jeff Shamma. I greatly appreciate their guidance and feedback on my research.

I wish to extend my thanks to the past and present members of Microsensors and Microactuators group. Their help, advice, and moral support helped me tackle innumerable processing puzzles. I would especially like to thank Wenjun Xu, Zhan Liu, Avishek Aiyar, Dr. Florian Herrault, Preston Galle, Dr. Yong-Kyu Yoon, and Dr. Christophe Courcimault. I am very grateful to Richard Shafer for his technical assistance and advice with the setup of numerous experimental apparatus and Purnima Sharma for her help with administrative work.

I want to acknowledge the members of Chaikof lab for generously providing me with biomaterials and cells. I would particularly like to thank Vivek Kumar and Dr. Jeff Caves for their efforts and assistance during this research and for various troubleshooting suggestions. I want to thank Dr. Ari Glezer and his group for their help with fluid mechanical characterization. I really appreciate the Nanotechnology Research Center cleanroom staff members for their enthusiastic support of the cleanroom facilities.

A special thanks to all my friends for being a very important part of making my time in graduate school fun and exciting.

Finally, I would like to express my utmost gratitude to my family. I would not have been able to accomplish this milestone without their presence in my life. I want to thank my parents: my father for being my biggest source of inspiration and for always encouraging me to follow my passion, and my mother for her deepest love and care that has always made everything seem so easy. I want to thank my sister, Nikhila, for being my best friend and confidant, and my strongest support system, and my brother-in-law, Krishna, for always generously providing me with direction and motivation. Lastly, I want to thank my husband, Minal, for his patience, understanding, daily dose of pep-talks, and most importantly, his everlasting love and support.

TABLE OF CONTENTS

LIST OF TABLES

LIST OF FIGURES

SUMMARY

This dissertation presents the application of MEMS-based approaches for the construction of engineered tissue substitutes. MEMS technology can offer the physical scale, resolution, and organization necessary for mimicking native tissue architecture. Micromachined nozzles and templates were explored for the fabrication of acellular, biomimetic collagenous fibrous scaffolds, microvascular tissue structures, and the combination of these structures with cell-based therapeutics. The influence of the microstructure of the tissue constructs on their macro-scale characteristics was investigated.

Proteic components of the native fibrous connective tissues in human anatomy, collagen and elastin, were utilized for the fabrication of acellular fibrous tissue scaffolds. MEMS-based approaches offered control over the dimensions, geometries, and distribution of the fibers. Collagen fibers were first produced by a conventionally employed wet-spinning process, but utilizing micromachined nozzles. Two distinct fabrication strategies were developed for high-strength silicon and glass-metal micro/nanonozzles designed to sustain the high pressures (> 10 MPa) necessary to generate micro/nanofluidic viscous jet flows. This research was initiated with the characterization of the micromachined nozzles with test fluids, liquid butane and propane, for demonstrating the feasibility of pressure-driven nanofluidic jets. A micromachined nozzle-based wet-spinning apparatus for collagen fibers was developed. The nozzle dimensions and hydrodynamic focusing effects were investigated for modulating the fiber dimensions and geometries. A 10 μm inner diameter nozzle yielded

the smallest fiber with a dimension of 2 μm × 400 nm. Hydrodynamic focusing was applied by varying the flow rates of coaxial laminar flows of collagen and coagulant buffer solutions for exercising control over the dimensions of the resultant fibers, and also for producing *in situ* crimped fibers. This approach delivered fibers with a minimum dimension of 30 μm × 5 μm.

For more precise control over the fiber network spatial layouts, a template-based approach was developed for the fabrication of collagen micro/nanofiber networks and collagen-elastin fiber reinforced composites (FRCs). Appropriate silicon templates allowed for the construction of hollow and solid fiber networks with straight fibers, in-plane and out-of-plane crimped fibers, and porous fibers. Collagen FRCs were fabricated by embedding the fiber networks in an elastin matrix. Fiber network layouts and volume fractions were adjusted to introduce anisotropic elastic behavior in the composite materials. Increasing Young's moduli with fiber volume fraction for straight FRCs, and a strain-dependent stiffness for crimped FRCs, were demonstrated.

Finally, MEMS strategies were adopted for the development of cellularized collagen and polydimethylsiloxane (PDMS) microvascular scaffolds. First, a microvascular insulin bioreactor device was constructed to house locally immobilized pancreatic islet cells with an ultimate goal of development of a bioartificial pancreas (BP). A glucose stimulation test and insulin secretion assay demonstrated that the bioreactor device responded to a stimulatory glucose concentration (300mg/dl) by secreting 8-fold more insulin as compared to basal glucose concentration (60mg/dl). Next, a deformable reentrant PDMS microvascular network was developed for improved

endothelial cell seeding of high length-to-width aspect ratio microchannels. A feasibility experiment was successfully performed demonstrating the cell seeding approach.

CHAPTER 1

INTRODUCTION

1.1 Objectives

The objective of this dissertation was to employ micromachining strategies and static microelectromechanical systems (MEMS) constructs, such as nozzles and templates, for the fabrication and engineering of synthetic tissue constructs. The two types of tissue constructs targeted were acellular biomimetic fibrous tissue scaffolds comprising of proteins, collagen and elastin; and microvascular networks optionally supporting cell-based therapeutics. Three specific aims were outlined.

Specific aim 1: The first objective of this research was to develop and utilize micromachined micro/nanonozzles for the fabrication and dimensional control of collagenous fibers for tissue scaffolds. This work was divided into three phases: 1) the development of microfabrication strategies for high-pressure-withstanding micro/nanonozzles necessary for the generation of viscous micro/nanofluidic jets; 2) the empirical investigation of liquid micro/nanojets emanating from micromachined nozzles integrated with a high-pressure generation fluidic apparatus; and 3) the development of a micromachined-nozzle-based wet-spinning system for collagen micro/nanofibers. This study is discussed in Chapter 2.

Specific aim 2: The second objective of this research was to develop a microtransfer-molding-based approach for the fabrication of spatially-designed collagen micro/nanofiber networks as well as collagen-fiber reinforced elastin composite tissue scaffolds based on these networks. It was postulated that by constructing fiber reinforced

composite (FRC) tissue scaffolds with a defined fiber orientation, distribution, and dimension, the mechanical behavior of the resultant material can be controlled. This study is discussed in Chapter 3.

Specific aim 3: The third objective of this research involved the incorporation of cell-based therapeutics in micromachined vascular networks for mimicking specific tissue or organ functionalities. We endeavored to apply the established MEMS processing technology of micromolding for the fabrication of microvascular networks as well as islet cells and endothelial cells within these networks for imparting distinct therapeutic characteristics to the constructs. This study is discussed in Chapter 4.

1.2 Background

1.2.1 Tissue engineering

The official U.S. government website for organ and tissue donation and transplantation [1] reports that as of July 2010, over 108,000 people are on the waiting list for transplant surgeries in the U.S. alone. While this number has continued to rise over the years, a severe shortage of donor organs and tissues has been a significant handicap for meeting these demands. Only 14,631 donors and 28,464 transplant surgeries were reported in the year 2009 (Figure 1.1). This has motivated a great deal of interest in tissue engineering. The term ‘tissue engineering’ was first established by Y. C. Fung in 1988 and later defined as “the application of principles of engineering and life sciences towards the development of biological substitutes to restore, maintain or improve tissue functions” [2]. Synthetic tissues and organs are being considered as attractive alternatives

for autologous (tissue obtained from the same patient) and allogenic (tissue obtained from the same species) transplants.

The past few decades have seen the utilization of various methods and materials, both natural and synthetic, for the development of constructs emulating body tissue and organ functions. The human body is a complex system of cells and extracellular components, grouped into a large number of tissues and organs, and substituting these parts requires generating successful interactions between the living and the non-living components. Efforts have been directed towards the development of both cell-based constructs performing various biochemical functions and constituting the 'living' component of the human anatomy, and polymeric scaffolds for supporting, nourishing, and facilitating cell growth and function, constituting the 'non-living' component of the human anatomy.

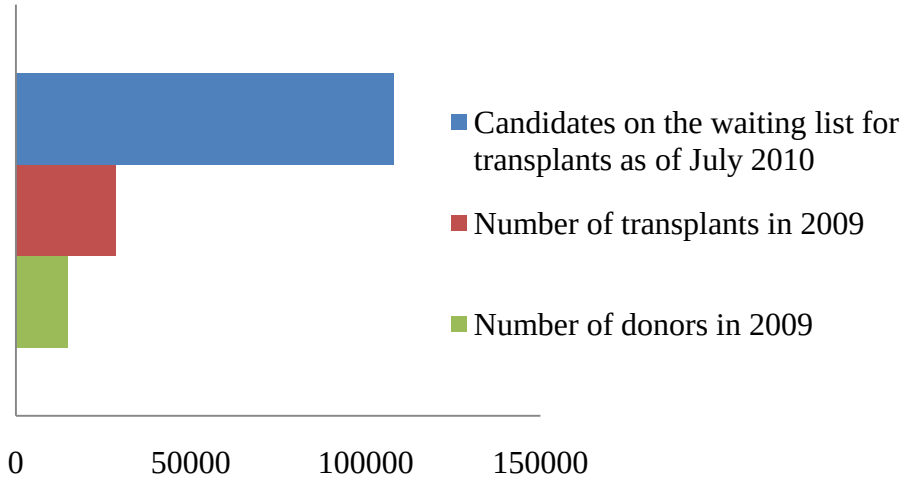

Figure 1.1. Information from the U.S. government official website for organ and tissue donation and transplantation [1].

1.2.1.1 Tissue scaffolds: mimicking the acellular component of the human anatomy

Native fibrous connective tissue composition

The extracellular component of connective tissues, such as tendons, ligaments, cartilage, blood vessels, and bones, is composed of proteic fibers. These extracellular components support and create an environment for the cells to function appropriately, as well as bear and transmit loads encountered by the tissues. These structural proteins primarily comprise collagen and elastin.

- *Collagen*

Collagen is the most abundant protein in the human anatomy contributing to more than 25 % of the total body protein content. It is responsible for providing strength, structure, and mechanical integrity to the tissues and organs. Fibrous collagenous tissues also act as strata for cellular interactions, proliferation, differentiation, and signal transduction, and provide cues for the development of cell phenotypes. The structures, dimensions, organization, and concentration of the collagen fibers in a tissue, therefore, influence the biomechanical characteristics of the tissue as well as the associated cell behavior.

Amino acids ($H_2NCHRCOOH$) are the building blocks of all proteins. Amino acids are organic compounds comprising a carbon atom bonded with an amine functional group ($-NH_2$), a carboxylic acid functional group (-COOH), a hydrogen atom (-H), and a variable side chain (-R), and are distinguished according to their variable side chain. There are 20 different types of amino acids that compose subunits of proteins. Proteins are formed by linear chains of amino acids, the sequence of amino acids connected by covalent peptide bonds being unique to each protein (Figure 1.2) [3].

Amino acid

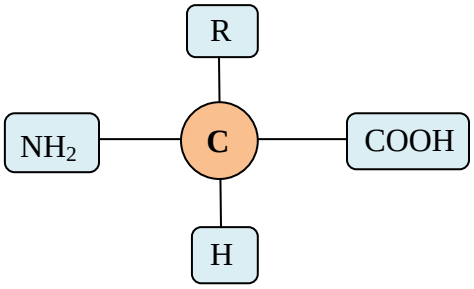

Examples of amino acids	Chemical formula
Lysine (Lys)	$C_6H_{14}N_2O_2$
Histidine (His)	$C_6H_9N_3O_2$
Leucine (Leu)	$C_6H_{13}NO_2$
Threonine (Thr)	$C_4H_9NO_3$

Primary structure of a protein

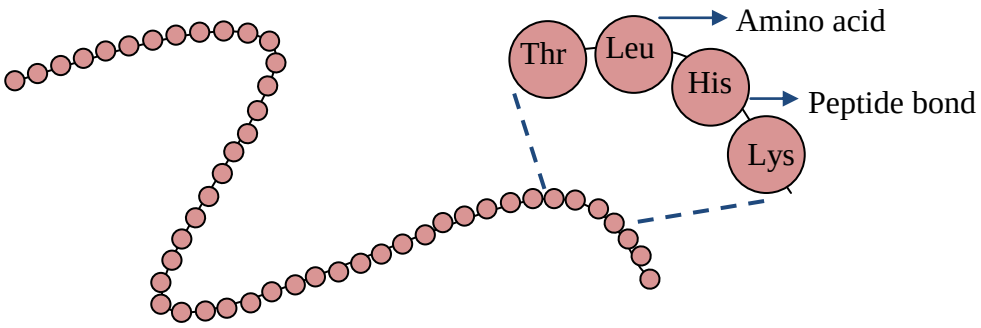

Figure 1.2. Primary structure of a protein.

Over 20 types of fibrillar and non-fibrillar collagen have been identified and reported, distinguished based on the variations in the patterns of amino acids in their polymeric chains. Collagen type I, exhibiting a fibrillar structure, is the most abundant

class of collagen and easy to isolate, hence used most commonly in medical research. Each collagen molecule is made up of a triple helical structure of linear chains of amino acids also known as polypeptide strands, and is 300 nm in length and 1.5 nm in diameter [4]. Each of these three chains has a repeating sequence of amino acids, Glycine (Gly), Proline (Pro), and Hydroxyproline (Hyp), typically in the pattern Gly-Pro-X or Gly-X-Hyp, where X is any other amino acid. The tight arrangement of the peptide chains and the covalent crosslinks between the molecules impart strength and rigidity to collagen. Native collagen displays a hierarchical structure, with collagen molecules self-assembling into aggregates to form fibrils which further associate to form fibers, as shown in Figure 1.3. The collagen fibril and fiber dimensions and arrangements depend on the tissue from which they originate. The fibril dimensions typically range from 10-500 nm, and can assemble into fibers with diameters of up to tens of microns.

As the collagen molecules self-assemble, they are observed to be displaced from each other by 67 nm. Due to this displacement, the axially packed collagen molecules display overlap and gap regions (Figure 1.4). This displacement structure gives collagen fibrils a characteristic striated appearance. This property can be observed using electron microscopy (EM) [7] or atomic force microscopy (AFM) (Figure 1.5) [8]. Each striated subunit is known as a D-period, and this unique characteristic of native fibrillar collagen is called D-periodicity. This D-periodicity imparts not only characteristic structural properties to the fibrils, but also is associated with guiding cell motility [9].

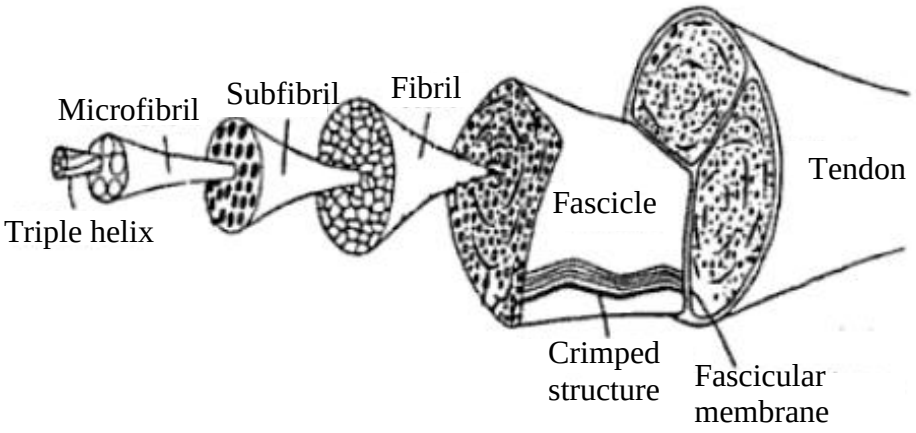

Figure 1.3. Hierarchical structure of fibrillar collagen [5].

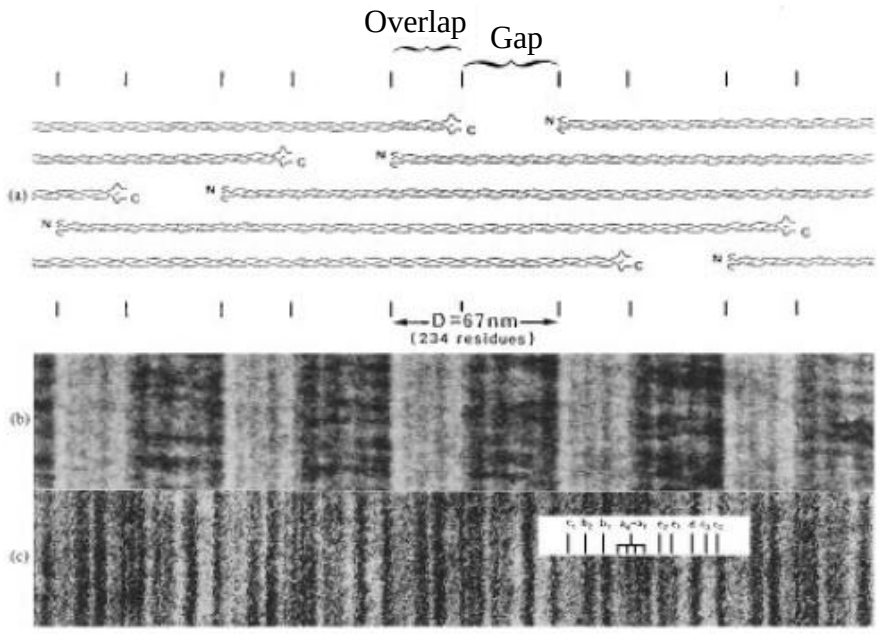

Figure 1.4. The arrangement of collagen molecules resulting in D-periodic banding [6].

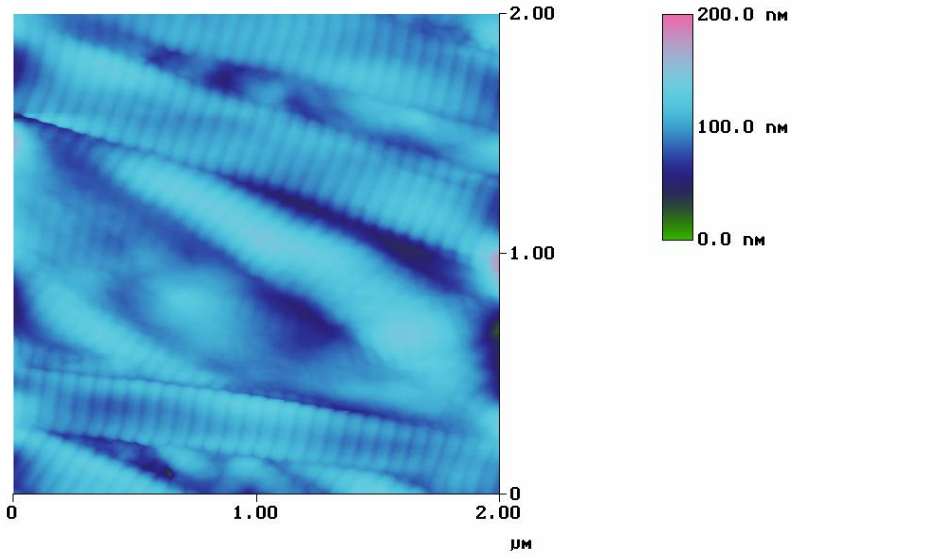

Figure 1.5. Characteristic D-periodic banding observed in a native collagen fibril represented by an AFM image of a rat tail tendon.

- *Elastin*

Elastin is a spring-like elastic protein responsible for resilient deformation of many tissues. It plays a predominant role in distensible tissues such as the blood vessels, skin, and lung. It is also found in small percentages in other connective tissues such as tendons, ligaments, and cartilages. The precursor to elastin, known as tropoelastin, is mainly composed of the amino acids valine (Val), glycine (Gly), proline (Pro), and alanine (Ala) with repeating peptide units such as Gly-Val-Gly-Val-Pro, Gly-Val-Pro-Gly-Val, and Gly-Val-Gly-Val-Ala-Pro [10]. These amino acids are organized in an irregular 'coiled' fashion and confer upon the protein its elastic properties [11].

Synthetic tissue scaffolds

The function of synthetic tissue scaffolds is to serve as three-dimensional architectural support for transplanted or host cells. They provide the cells with a biomimetic environment for facilitating their attachment, proliferation, and proper

functioning necessary for tissue regeneration. Various polymeric materials in the form of foams [12-15], hydrogels [16], and fibrous networks [17-18] have been investigated as synthetic tissue scaffolds. In particular, polymeric fibrous meshes have emerged as important constructs for tissue engineering as they display a high surface-to-volume ratio and possess good mechanical properties, and also most appropriately represent the structure and morphology of the extracellular matrix (ECM).

- *Materials used for synthetic tissue scaffolds*

The key metrics determining the quality and effectiveness of a synthetic tissue scaffold are its biocompatibility, bioresorbability, non-immunogenicity, and mechanical and structural properties. Given these considerations, a multitude of natural and synthetic polymeric micro/nanofibers have been explored as candidate materials. The most popular synthetic polymers examined for engineered tissue analogs include poly(glycolic acid) (PGA), poly(L-lactic) acid (PLLA), poly(caprolactone) PCL, and poly(ethylene glycol) PEG. Similarly, popular naturally derived polymers for this application include collagen, chitosan, alginate, silk, hyaluronic acid (HA), and gelatin [19].

Synthetic tissue constructs have been realized from both synthetic and natural polymers. In particular, collagen has proved to be a very attractive choice for synthetic tissue constructs and has a long history of application in medicine. Collagen, naturally existing as the primary structural component of mammalian tissues, possesses excellent biocompatibility, bioresorbability, and biomechanical properties as shown in several *in vitro* and *in vivo* studies [20-22]. Also, being the native tissue substrates for maintaining cellular functionalities, collagen tissues have demonstrated success in their interactions with different types of cells *in vitro*. The role of collagen structure in providing guidance

cues for the development of cell phenotype and maintaining cell functionalities has been a subject of study for many years. Regenerated collagen constructs have been shown to be compatible with various cells and supportive of adhesion and proliferation of cells including fibroblasts [23-25], endothelial cells [26-27], stem cells [28-29], chondocytes [30], and osteoblasts [31].

- *Methods used for the fabrication of fibrous tissue scaffolds*

Various top-down approaches have been investigated for the fabrication of polymeric micro/nanofibers for tissue engineered scaffolds, and the most commonly used methods include electrospinning and wet-spinning.

Electrospinning is an approach for drawing very fine polymer fibers using an electrically charged jet of a polymer solution. A typical electrospinning setup consists of a needle connected to a high-voltage (10 to 50 kV) power supply, a syringe pump, and a grounded collector plate, as shown in Figure 1.6. The syringe pump is used to extrude the polymer solution at a constant rate. When a voltage is applied to the needle, the flowing liquid is stretched into a Taylor cone. If the tension of the polymer is high enough, a charged liquid jet is formed. This charged jet is continuously deposited on the grounded electrode as micro/nanofibers. The charge on the jet leads to bending instability, causing the diameter of the polymer filament to be reduced to the micro/nanoscale [32]. The polymer solution properties such as surface tension, viscosity, conductivity, and dielectric constant of the solvent dictate the dimension and morphology of the spun fibers.

Electrospun nanofibrous scaffolds have been extensively researched for tissue scaffold applications (Figure 1.7). Materials including PGA, PLLA, Polyethylene

terephthalate (PET), PCL, HA, collagen, and elastin have been investigated for the manufacture of vascular [33], cartilage [34], bone [35] and nerve [36] tissue scaffolds, with the produced fibers ranging from 50 nm to 2 μm in diameter.

Extrusion-based fiber spinning is one of the oldest techniques for manufacturing polymer fibers, and is based on the natural silk-spinning method. Silkworms produce silk fibers by forcing liquid silk through openings in their heads, known as spinnerets. The silk jets, on coming in contact with air, precipitate as silk fibers. Similarly, wet spinning, one of the forms of synthetic fiber-spinning, involves extrusion of a polymer solution through spinnerets/nozzles into a precipitating liquid (Figure 1.8). Filaments of the polymer solution driven through the nozzles come in contact with the coagulant solution and precipitate as fibers [37].

Substantial research has been directed towards wet-spinning of polymer microfibers for biological applications. Drug-loaded hollow microfibers of copolymers of poly(lactic acid) (PLA) and PCL (diameter > 100 μm) [38], and of PLLA (diameter 80-100 μm) [39] have been investigated using wet- and dry-spinning approaches. Wet-spinning of chitosan, followed by *in situ* chemical polymerization of aniline has been utilized for an electroactuating biopolymer hydrogel/polyaniline microfiber (diameter > 50 μm) for application in artificial muscles [40]. Wet-spun collagen fiber meshes have been applied in various tissue scaffold applications (Figure 1.9) [41-44].

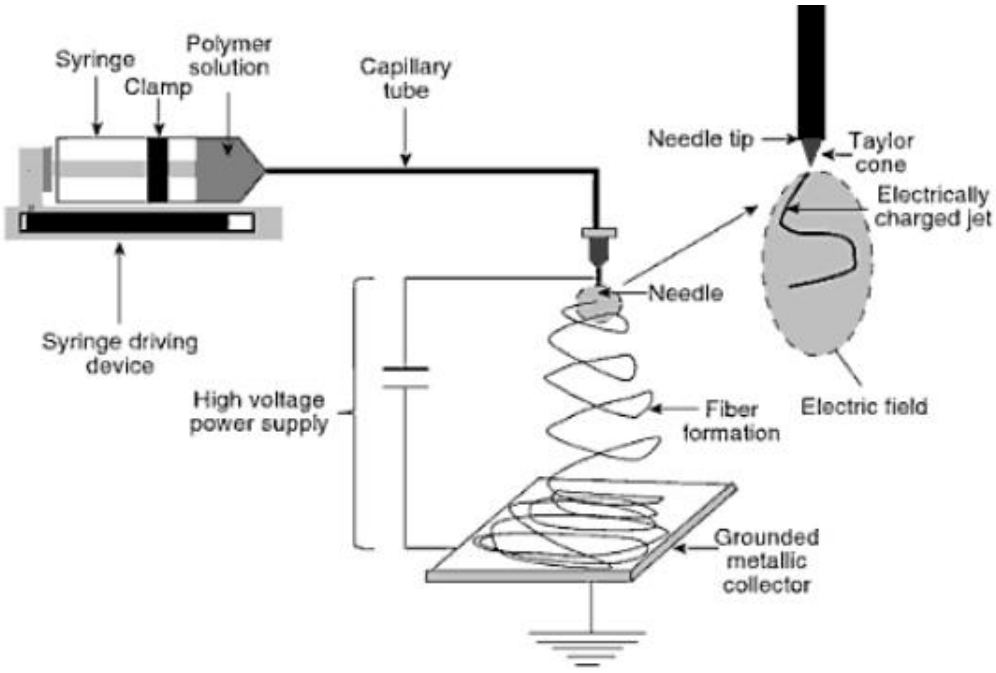

Figure 1.6. A fiber electrospinning apparatus [32].

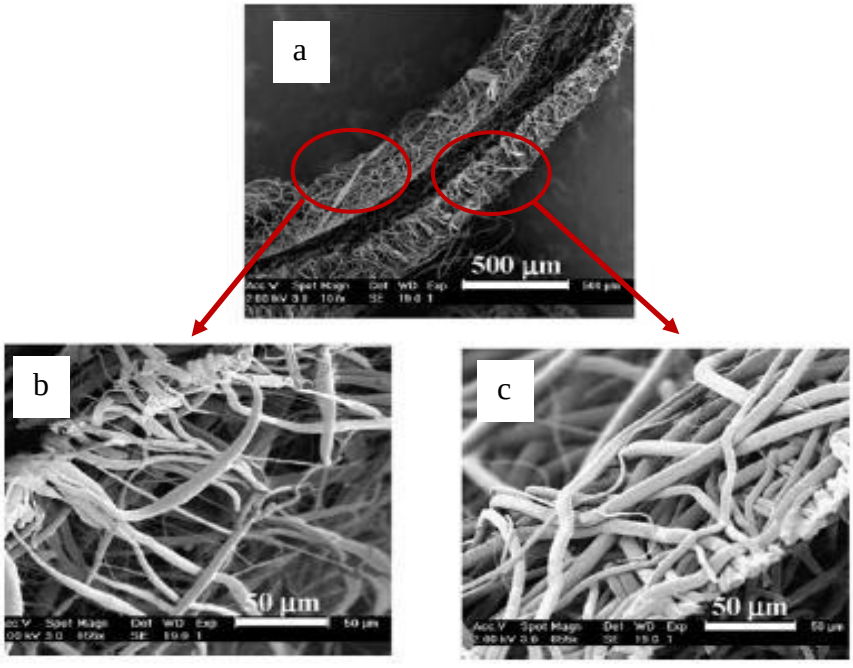

Figure 1.7. a) A bilayer electrospun fibrous mat for blood vessel tissue engineering, close-up images of b) PCL fibers, and c) PLA fibers [33].

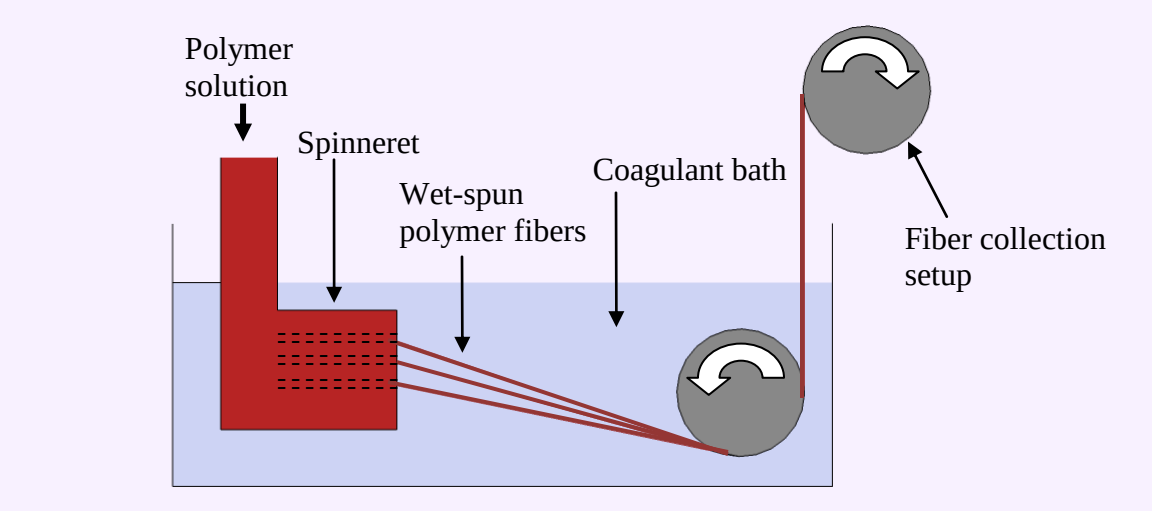

Figure 1.8. A fiber wet-spinning apparatus.

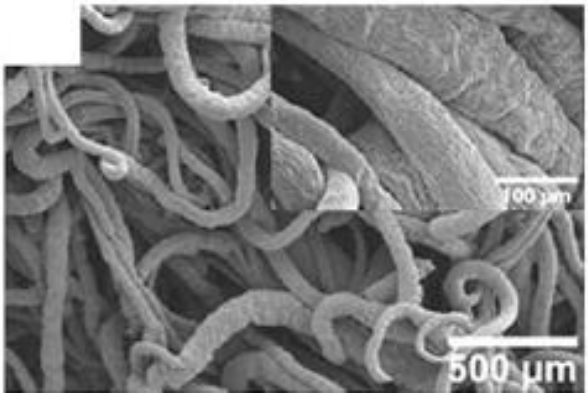

Figure 1.9. A wet-spun PCL/chitosan fibrous scaffold [39].

Biomaterials used in the current research

- *Regenerated collagen type I*

Collagen, obtained as naturally derived material from murine, porcine, and bovine models and regenerated *in vitro*, is extensively used in tissue-engineering-based studies. Typically, collagen-rich tissues such as tendon and skin are used as the source for extraction. The cross-links in the native proteins are disrupted either using dilute acids or

proteolytic enzymes such as pepsin. Collagen is perceived as a particularly suitable material for tissue engineering because after the extraction and processing, the resultant monomeric collagen material can be subjected to physiological conditions to trigger self-assembly of the collagen molecules into a fibrillar material with the characteristic native tissue structure.

Regenerated collagen type I, isolated from Sprague-Dawley rat tail tendons was utilized in this thesis. The extraction process is described in detail previously [45]. To initiate the extraction process, the tendons from rat tails (Pel-Freez Biologicals, Rogers, AK) were recovered and solubilized in 10 mM HCl (pH= 2) at room temperature. Centrifugation and filtration at 4°C were followed to separate the soluble collagen. Collagen was precipitated by addition of NaCl in 10 mM HCl and centrifugation. The collagen was finally re-solubilized in 10 mM HCl and dialyzed against 20 mM phosphase buffer solution. This resulted in a monomeric collagen type I solution in 10 mM HCl. Self-assembly of this monomeric collagen solution into fibrillar collagen could be activated by bringing the solution to physiological conditions of neutral pH (pH ~ 7) and 37 °C temperature. Glutaraldehyde (0.5 wt% glutaric acid dialdehyde in 1× phosphate buffered saline (PBS)) was used as the crosslinking agent for the self-assembled collagen.

- *Elastin-mimetic protein polymer*

As described earlier, tropoelastin, the precursor for elastin, is primarily composed of amino acids valine (Val), glycine (Gly), proline (Pro), and alanine (Ala) with repeating peptide units such as Gly-Val-Gly-Val-Pro, Gly-Val-Pro-Gly-Val, and Gly-Val-Gly-Val-Ala-Pro. Genetic engineering of bacteria, such as Escherichia coli (E. coli), has enabled scientists to synthesize elastin-mimetic protein polymers mimicking these pentapeptide

sequence units. Several biological, mechanical, and chemical characteristics can be introduced in these elastin-mimetic polymers by modifying the repeat sequence of the peptides. Elastin pentapeptide units are soluble in water at lower temperatures but collapse and aggregate at a distinct transition temperature determined by the peptide organization.

Elastin-mimetic protein LysB10 obtained from E. coli culture was utilized in this thesis. The synthesis process for this material involved genetically engineered bacterial culture, protein expression, cell lysis, and purification, described in detail elsewhere [10]. This elastic protein exhibited a distinct property of temperature dependent solubility. It solubilized in water at low temperatures (4 °C) and underwent gelation at 37 °C

1.2.1.2 Tissue constructs with cell-based therapeutics

Cells, typically considered the smallest units of life, work in concert with the acellular components in the body to form functional systems. Therefore, cell-based therapeutics for tissue and organ regeneration or restoration constitute the second integral component of tissue engineering. This involves the use of independent isolated cells or the combination of tissue scaffolds with autologous, allogenic or xenogenic cells for tissue regeneration or emulation of specific tissue or organ functions.

Cells of different origins are utilized depending on the intended application. For example, lung cells, stem cells, fibroblasts, and chondrocytes have been employed for the regeneration of tissues, such as the lung [46], bone [47], skin [48], and cartilage [49]. Organ-specific cells such as islet cells, hepatocytes, and para-thyroid cells encapsulated in biodelivery constructs have been applied for the development of bioartificial organs

mimicking the functions of the pancreas [50], liver [51], and thyroid [52-53], respectively.

Bioartificial organs are cell-based tissue engineered constructs, comprising organ-specific cells encapsulated in an implantable capsule or device. When implanted in the body they produce therapeutic products to restore or improve an organ function. Bioartificial organs have been investigated as potential remedies for diseases such as diabetes mellitus, hypoparathyroidism, and hepatic failure [55]. Cell-based bioartificial organs are categorized as extravascular or intravascular constructs.

Extravascular constructs (Figure 1.7) are installed outside the vascular system in sites such as the peritoneal cavity or subcutaneous tissue. The organ-specific cells are encapsulated in materials such as alginate [56], agarose [57], and PEG [58] to either form spherical microcapsules containing a single or a few cells, or fibrous or plate macrocapsules housing a large number of cells, as shown in Figure 1.10. The encapsulation materials protect the cells from being attacked by the body's immune system. The biggest disadvantage of these devices is their lack of contact with the blood stream, resulting in an inadequate supply of nutrient and oxygen and limited long term cell viability. Additionally, cell aggregation further aggravates the mass transport issues in plate and fibrous microcapsules, and these constructs tend to fracture under the physiological stress.

Intravascular bioartificial organ constructs typically consist of a blood flow through a conduit or a bundle of hollow capillaries separated from a chamber containing the organ-specific cells by a semipermeable membrane. They are implanted surgically into the body as an arteriovenous shunt. An example of an intravascular bioartificial

pancreas is illustrated in Figure 1.11 [55]. These devices permit nutrients, oxygen, and stimulants (such as glucose) to diffuse through the semipermeable membrane to the cells, and metabolites and hormones (such as insulin) produced by the cells to diffuse into the blood flow. The semipermeable membrane mainly acts as a deterrent for immunocytes and antibodies in the blood, hence protecting the implanted cells from being attacked by the host's immune system. Although these devices have shown immense promise, they can suffer from cell aggregation, limiting mass transport of nutrients and oxygen to the cells. For a single flow of blood supplying nutrients to several layers of packed cells, the efficiency of the cells furthest from the flow suffers. Also, these devices tend to be bulkier than their microscale bioreactor counterparts.

a) Macroencapsulation

b) Microencapsulation

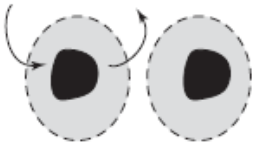

Figure 1.10. Representative extravascular cell-based bioartificial organs [54].

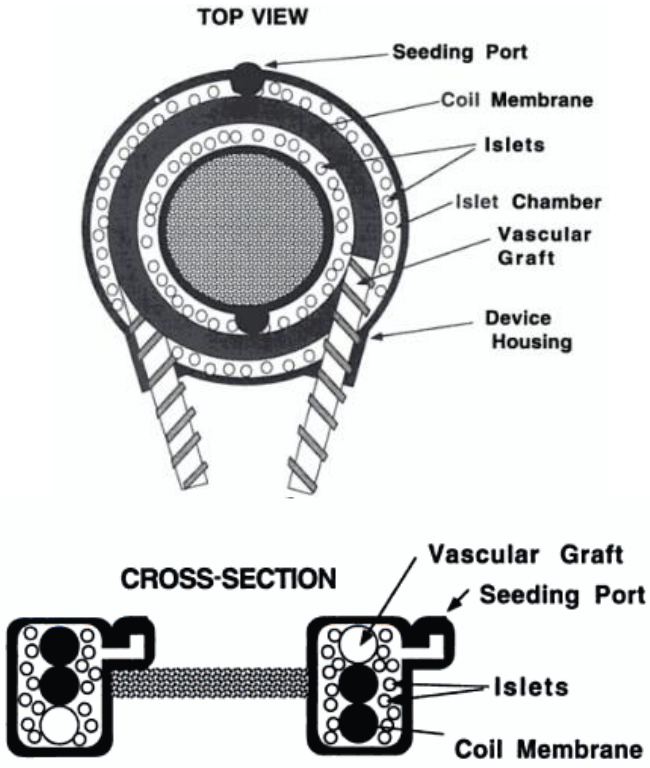

Figure 1.11. A representative intravascular cell-based bioartificial organ [55].

Cell-based studies are often conducted with the aid of bioreactors. A bioreactor is a device that supports a biologically active environment and hosts a biological reaction, usually in the form of biochemical activities involving living organisms. Bioreactors are employed to create an *in vitro* cell culture to simulate the environment and stimuli that the cells may experience *in vivo*. Of much relevance to the current study are microchannel bioreactors. Microchannel bioreactors comprise of miniaturized channels with cultured cells, sometimes contained in grooves or wells (Figure 1.12) [59] inside the microchannels, observed under a perfusion flow configuration. Various types of cells including fibroblasts, stem cells, and hepatocytes have been investigated in such an environment for the optimization and study of operational parameters such as flow rates and pressure drops across the channels [60-62].

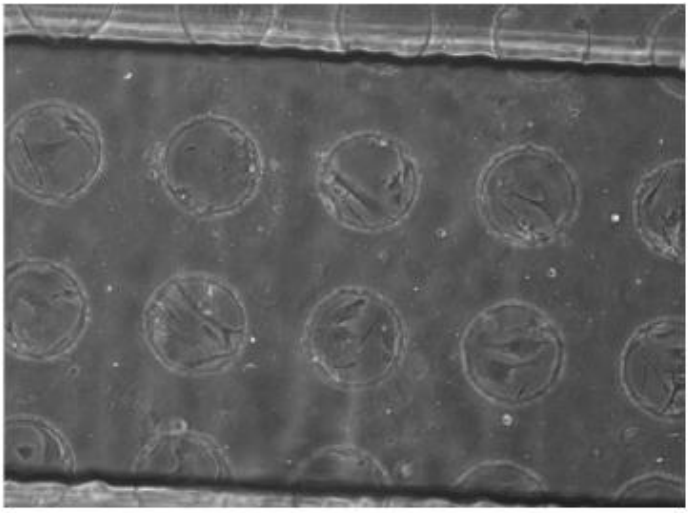

Figure 1.12. A microchannel bioreactor with cells cultured in microwells (diameter = 100 μm) [59].

1.2.2 Role of MEMS in tissue engineering

The native tissue architectures defined by nature consist of submicron to micron scale structures arranged into an intricate, interconnected system. The microstructure of native tissues largely determine their macro-scale behavior. Tissue engineering often focuses on creating constructs with biomimetic structures harnessing nature's designs. MEMS processing technology offers the size scale and resolution necessary to mimic the native tissues and also the ability to create organized 2-dimensional (2D) and 3-dimensional (3D) structures. This has led to its utilization in acellular and cellular tissue engineering applications and relevant studies.

Micropatterning approaches have been utilized for controlling the spatial organization and surface topology of tissue scaffolds. Micromolding is the most extensively used microscale technology for manipulating tissue scaffold material. It has been utilized for fabricating microvascular networks [63], patterning nano-features on scaffolds for providing guidance for cellular alignment (Figure 1.13b) [64], and

microencapsulation of hepatocytes in patterned microwell alginate tissue scaffolds, (Figure 1.14a) [65] among many tissue engineering applications. While micromolding offers the most gentle processing approach for naturally derived materials, many synthetic scaffolds have been developed using MEMS patterning approaches, such as microsterolithography (Figure 1.13a) [66], optical lithography [67], laser micromachining [68], and x-ray lithography [64].

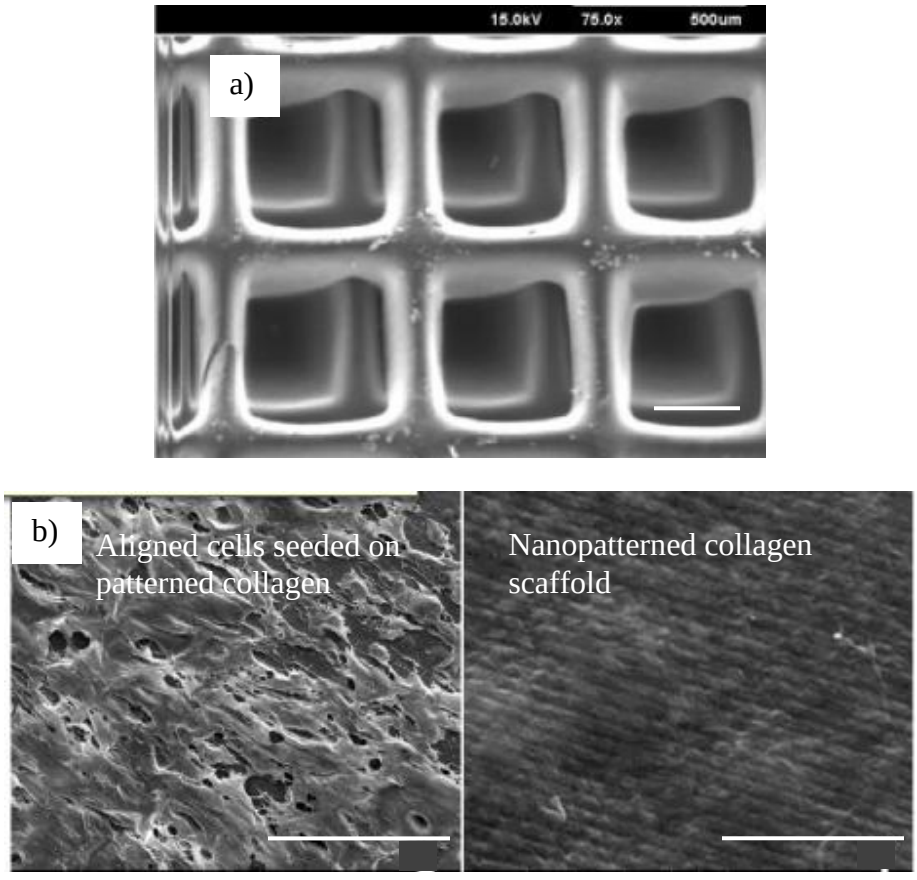

Figure 1.13. MEMS for tissue scaffolds: a) a PEG scaffold fabricated using microstereolithography (scale bar = 200 μm) [66], and b) a cellularized collagen scaffold nanopatterned using templates fabricated by x-ray lithography (scale bar = 200 μm and 10 μm) [64].

MEMS strategies have been applied to cell-based tissue constructs and relevant studies. MEMS-based microfluidic bioreactors and microtissue cultures have been developed for analyzing cell behavior in simulated physiological environments (Figure 1.14b), as well as for testing artificial organ functionality *in vitro* using organ-specific cells [69-70]. Lithography [71], microcontact printing [72], and ink-jet printing [73] have been adopted for patterning proteins capable of promoting cellular adhesion for controlling cellular attachment and patterning. Ink-jet printing has also shown the possibility of laying down cells directly into configurations mimicking biological patterns [74].

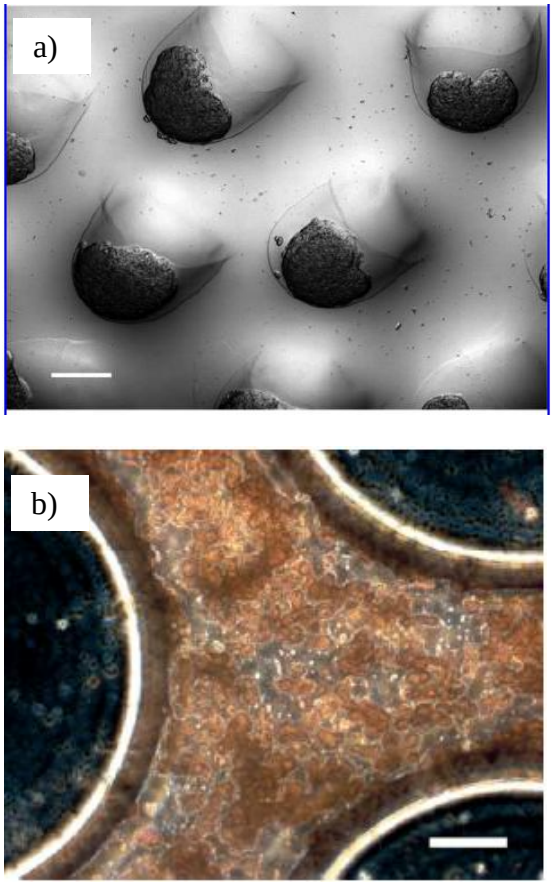

Figure 1.14. MEMS for cell-based tissue engineering: a) an alginate tissue microarray with encapsulated hepatocytes (scale bar = 300 µm) [65], and b) hepatocytes cultured in a microfluidic PGS scaffold (scale bar = 50 µm) [67].

This dissertation was an effort to further explore the features offered by MEMS processing technology and demonstrate its potential towards the development of engineered tissue constructs. These constructs included acellular fibrous tissue scaffolds, and microvascular constructs with cellular incorporation. It was endeavored to establish the characteristics imparted by the microstructure of the tissue constructs on their macro-scale behavior.

1.3 References

1. http://organdonor.gov/, U.S. government official website for information on organ and tissue donation and transplantation, accessed on July 30, 2010

2. Kai-Uwe Lewandrowski, Donald L. Wise, Michael J. Yaszemski, Joseph D. Gresser, Debra J. Trantolo, David E. Altobelli, "Tissue Engineering And Biodegradable Equivalents, Scientific And Clinical Applications," 1st edition, CRC Press, 2002

3. David E. Sadava, H. Craig Heller, Gordon H. Orians, "Life, the science of biology," 8th edition,W. H. Freeman, 2006

4. Peter Fratzl, "Collagen: Structure and Mechanics," 1st edition, Springer, 2008

5. Knut Schmidt-Nielsen, "Animal physiology: adaptation and environment," Cambridge University Press, 1997

6. K E Kadler, D F Holmes, J A Trotter, and J A Chapman, "Collagen fibril formation," Biochemical Journal, 1996, 316(1), p 1–11

7. Holmes DF, Graham HK, Trotter JA, "STEM/TEM studies of collagen fibril assembly," Micron, 2001, 32(3), p 273-285

8. Gutsmann, T. Fantner, G.E.; Venturoni, M.; Ekani-Nkodo, A.; Thompson, J.B.; Kindt, J.H.; Morse, D.E.; Fygenson, D.K.; Hansma, P.K., "Evidence that collagen fibrils in tendons are inhomogeneously structured in a tubelike manner," Biophysical Journal, 2003, 84(4), p 2593-8

9. Poole K, Khairy K, Friedrichs J, et al., "Molecular-scale topographic cues induce the orientation and directional movement of fibroblasts on two-dimensional collagen surfaces," Journal of molecular biology, June 2005, 349(2), p 380-386

10. Sallach, R., "Recombinant Elastin-Mimetic Protein Polymers as Design Elements for an Arterial Substitute," in Wallace H. Coulter Department of Biomedical Engineering. 2008, Georgia Institute of Technology: Atlanta

11. Anthony L. Andrady, "Science and Technology of Polymer Nanofibers," Wiley-Interscience, August 25, 2008

12. Day RM, Boccaccin AR, Maquet V, et al., "*In vivo* characterisation of a novel bioresorbable poly(lactide-co-glycolide) tubular foam scaffold for tissue engineering applications," Journal of materials science-materials in medicine., 2004, 15(6), p729-734

13. AG Mikos, JS Temenoff , "Formation of highly porous biodegradable scaffolds for tissue engineering," Electronic journal of biotechnology, 2000, 3, p 23

14. Tessa Hadlock, Cathryn Sundback, Daniel Hunter, Mack Cheney, Joseph P. Vacanti, "A polymer foam conduit seeded with Schwann cells promotes guided peripheral nerve regeneration," Tissue Engineering. 2000, 6(2), p 119-127

15. Carina Danielsson, Sylvie Ruault, Marc Simonet, Peter Neuenschwander and Peter Frey, "Polyesterurethane foam scaffold for smooth muscle cell tissue engineering," Biomaterials, 2006, 27(8), p 1410

16. Drury JL, Mooney DJ , "Hydrogels for tissue engineering: scaffold design variables and applications," Biomaterials, 2003, 24(24), p 4337-4351

17. Smith LA, Ma PX , "Nano-fibrous scaffolds for tissue engineering," Colloids and surfaces B-Biointerfaces, 2004, 39(3), p 125-131

18. Scaffolds for tissue fabrication, Peter X. Man, materials today, Volume 7, Issue 5, May 2004, Pages 30-40

19. Joseph D. Bronzino, "Tissue Engineering and artificial organs-The Biomedical Engineering Handbook," 3rd edition, CRC Press, 2006

20. Jeyanthi R, Rao KP, "*In vivo* biocompatibility of collagen-poly(hydroxyethyl methacrylate) hydrogels," Biomaterials, 1990, 11(4), p238-43

21. Gagnieu CH, Forest PO, " *In vivo* biodegradability and biocompatibility of porcine type I atelocollagen newly crosslinked by oxidized glycogen,", Biomedical materials and engineering, 2007, 17 (1), p 9-18

22. Caves, Jeffrey M. (Department of Surgery, Emory University, Atlanta, GA 30332, United States); Kumar, Vivek A.; Wen, Jing; Cui, Wanxing; Martinez, Adam; Apkarian, Robert; Coats, Julie E.; Berland, Keith; Chaikof, Elliot L., "Fibrillogenesis in continuously spun synthetic collagen fiber," Journal of Biomedical Materials Research - Part B Applied Biomaterials, 2010, 93(1), p 24-38

23. Croce, Maria Antonietta, Silvestri, Chiara; Guerra, Deanna; Carnevali, Elena; Boraldi, Federica; Tiozzo, Roberta; Parma, Bruna , "Adhesion and Proliferation of Human Dermal Fibroblasts on Collagen Matrix", Journal of Biomaterials Applications, 2004, 18(3), p 209-222

24. Venugopal JR, Zhang YZ, Ramakrishna S , "*In vitro* culture of human dermal fibroblasts on electrospun polycaprolactone collagen nanofibrous membrane," Artificial organs, 2006, 30(6), p 440-446

25. Jarman-Smith ML, Bodamyali T, Stevens C, et al., "Porcine collagen crosslinking, degradation and its capability for fibroblast adhesion and proliferation," Journal of

materials science-materials in medicine, 2004, 15(8), p 925-932

26. Bayless KJ, Kwak HI, Su SC, "Investigating endothelial invasion and sprouting behavior in three-dimensional collagen matrices," Nature protocols, 2009, 4(12), p 1888-1898

27. Titorencu I, Albu MG, Giurginca M, et al., "*In vitro* Biocompatibility of Human Endothelial Cells with Collagen-Doxycycline Matrices," Molecular crystals and liquid crystals, 2010, 523, p 82-96

28. Tsai KS, Kao SY, Wang CY, et al., "Type I collagen promotes proliferation and osteogenesis of human mesenchymal stem cells via activation of ERK and Akt pathways," Journal of biomedical materials research part A, 2010, 94A(3), p 673-682

29. Kobayashi K, Suzuki T, Nomoto Y, et al., "A tissue-engineered trachea derived from a framed collagen scaffold, gingival fibroblasts and adipose-derived stem cells," Biomaterials, 2010, 31(18), p4855-4863

30. Yen HJ, Tseng CS, Hsu SH, et al., "Evaluation of chondrocyte growth in the highly porous scaffolds made by fused deposition manufacturing (FDM) filled with type II collagen," Biomedical microdevices, 2009, 11 (3), p615-624

31. Lynch MP, Stein JL, Stein GS, et al. " The influence of type I collagen on the development and maintenance of the osteoblast phenotype in primary and passaged rat calvarial osteoblasts: modification of expression of genes supporting cell growth, adhesion, and extracellular matrix mineralization" Experimental cell research, 1995, 216(1), p 35-45

32. Challa S. S. R. Kumar, "Nanocomposites," Wiley-VCH, 2010

33. Vaz, C.M.; van Tuijl, S.; Bouten, C.V.C.; Baaijens, F.P.T.; "Design of scaffolds for blood vessel tissue engineering using a multi-layering electrospinning technique"; Acta Biomaterialia, 2005, 1(5), p 575-82

34. Li WJ, Chiang H, Kuo TF, et al, "Evaluation of articular cartilage repair using biodegradable nanofibrous scaffolds in a swine model: a pilot study," Journal of tissue engineering and regenerative medicine, 2009, 3(1), p 1-10

35. Yoshimoto H, Shin YM, Terai H, et al., "A biodegradable nanofiber scaffold by electrospinning and its potential for bone tissue engineering," Biomaterials, 2003, 24(12), p 2077-2082

36. Bini TB, Gao SJ, Tan TC, et al., " Electrospun poly(L-lactide-co-glycolide) biodegradable polymer nanofibre tubes for peripheral nerve regeneration," Nanotechnology, 2004,15(11), p 1459-1464

37. Fred W. Billmeyer Jr., "Textbook of Polymer Science," 3rd edition, John Wiley & Sons, 1984

38. Polacco, Giovanni; Cascone, Maria Grazia; Lazzeri, Luigi; Ferrara, Stefania; Giusti, Paolo, "Biodegradable hollow fibres containing drug-loaded nanoparticles as controlled release systems"; Polymer International, 2002, 51(12), p 1464-1472

39. Lazzeri, Luigi; Cascone, Maria Grazia; Quiriconi, Simone; Morabito, Letterio; Giusti, Paolo; "Biodegradable hollow microfibres to produce bioactive scaffolds," Polymer International, 2005, 54(1), p 101-107

40. Ismail, Yahya A.; Shin, Su Ryon; Shin, Kwang Min; Yoon, Seong Gil; Shon, Kiwon; Kim, Sun I.; Kim, Seon Jeong; "Electrochemical actuation in chitosan/polyaniline microfibers for artificial muscles fabricated using an *in situ* polymerization," Sensors and Actuators, B: Chemical, 2008, 129(2), p 834-840

41. Spinks, Geoffrey M.; Shin, Su Ryon; Wallace, Gordon G.; Whitten, Philip G.; Kim, Sun I.; Kim, Seon Jeong; "Mechanical properties of chitosan/CNT microfibers obtained with improved dispersion," Sensors and Actuators, B: Chemical, 2006, 115 (2), p 678-684

42. Razal JM, Kita M, Quigley AF, et al., "Wet-Spun Biodegradable Fibers on Conducting Platforms: Novel Architectures for Muscle Regeneration," Advanced functional materials, 2009, 19(21), p 3381-3388

43. Malheiro VN, Caridade SG, Alves NM, et al., "New poly(epsilon-caprolactone)/chitosan blend fibers for tissue engineering applications," Acta biomaterialalia, 2010, 6(2), p418-428

44. Yang CY, Chiu CT, Chang YP, et al., "Fabrication of Porous Gelatin Microfibers Using an Aqueous Wet Spinning Process," Artificial cells, blood substitutes, and biotechnology, 2009, 37(4), p 173-176

45. Caves, J., "Architecturally defined scaffolds from synthetic collagen and elastin analogues for the fabrication of bioengineered tissues," Wallace H. Coulter Department of Biomedical Engineering. 2008, Georgia Institute of Technology: Atlanta

46. Andrade CF, Wong AP, Waddell TK, et al., "Cell-based tissue engineering for lung regeneration," American journal of physiology-lung cellular and molecular physiology, 2007, 292(2), p L510-L518

47. Bueno EM, Glowacki J, "Cell-free and cell-based approaches for bone regeneration," Nature reviews rheumatology, 2009, 5(12), p 685-697

48. Golinski PA, Zoller N, Kippenberger S, et al., "Development of an Engraftable Skin Equivalent based on Matriderm (R) with Human Keratinocytes and Fibroblasts," Handchirurgie mikrochirurgie plastische chirurgie, 2009, 41(6), p 327-332

49. Wakitani S, Goto T, Pineda SJ, et al., "Mesenchymal cell-based repair of large, full-thickness defects of articular-cartilage," Journal of bone and joint surgery-American volume, 1994, 76A(4), p 579-592

50. Seda Kizilel, Marc Garfinkel, Emmanuel Opara, "Diabetes Technology & Therapeutics" The Bioartificial Pancreas: Progress and Challenges, December 2005, 7(6), p 968-985

51. Allen Jared W. ; Hassanein Tarek, Bhatia Sangeeta N.," Advances in bioartificial liver devices," Hepatology, 2001, 34(3), pp. 447-455

52. Chen, Guxiang; Peng, Yan; Lou, Peiling; Liu, Jinping "Bioartificial thyroid. The *in vitro* culture of microencapsulated rabbit thyroid tissue," ASAIO Transactions, 1991, 37(3), p439-440

53. Toni R, Casa CD, Spaletta G, Marchetti G, Mazzoni P, Bodria M, Ravera S, Dallatana D, Castorina S, Riccioli V, Castorina EG, Antoci S, Campanile E, Raise G, Rossi R, Ugolotti G, Martorella A, Roti E, Sgallari F, Pinchera A., "The bioartificial thyroid: a biotechnological perspective in endocrine organ engineering for transplantation replacement," Acta Biomed. 2007, 78(2), p 152

54. Kizilel S, Garfinkel M, Opara E, "The bioartificial pancreas: progress and challenges," Diabetes Technol Ther, 2005, 7(6), p 968-85

55. Willem M. Kühtreiber, Robert Paul Lanza, "Cell Encapsulation Technology and Therapeutics," 1st edition, Birkhäuser Boston, 1999

56. Halle, J.-P., Orive, G.; Tam, S.K.; Pedraz, J.L., "Biocompatibility of alginate-poly-l-lysine microcapsules for cell therapy," Biomaterials, 2006, 27(20), p 3691-700

57. Shoichet MS, Li RH, White ML, et al., " Stability of hydrogels used in cell encapsulation: An *in vitro* comparison of alginate and agarose ," Biotechnology and bioengineering, 1996, 50(4), p 374-381

58. Weber LM, He J, Bradley B, et al., "PEG-based hydrogels as an *in vitro* encapsulation platform for testing controlled beta-cell microenvironments," Acta biomaterialia,2006, 2(1), p 1-8

59. Korin, Natanel, Bransky, Avishay; Khoury, Maria; Dinnar, Uri; Levenberg, Shulamit, "Design of well and groove microChannel bioreactors for cell culture," Biotechnology and Bioengineering, 2009, 102(4), p 1222-1230

60. Korin, N., Bransky, A.; Dinnar, U.; Levenberg, S., ”A parametric study of human fibroblasts culture in a microchannel bioreactor,” Lab on a Chip, 2007, 7(5), p 611-17

61. Korin, N., Bransky, A.; Dinnar, U.; Levenberg, S., “The culture of human embryonic stem cells in microchannel perfusion bioreactors,” Proceedings of the SPIE - The International Society for Optical Engineering, 2006, v 6416, p 8

62. Park, Jaesung, Toner, Mehmet; Yarmush, Martin L.; Tilles, Arno W., ”Microchannel bioreactors for bioartificial liver support,” Microfluidics and Nanofluidics, 2006, 2(6), p 525-535

63. Shin, Michael, Matsuda, Kant; Ishii, Osamu; Terai, Hidetomi; Kaazempur-Mofrad, Mohammed; Borenstein, Jeffrey; Detmar, Michael; Vacanti, Joseph P., “Endothelialized networks with a vascular geometry in microfabricated poly(dimethyl siloxane),” Biomedical Microdevices, 2004, 6(4), p 269-278

64. Zorlutuna, P.; Elsheikh, A.; Hasirci, V., “Nanopatterning of collagen scaffolds improve the mechanical properties of tissue engineered vascular grafts,” 2009, Biomacromolecules, 10(4), p 814-821

65. Rago AP, Chai PR, Morgan JR., “Encapsulated arrays of self-assembled microtissues: an alternative to spherical microcapsules,” Tissue Eng Part A., 2009,15(2), p 387-95

66. Lu, Yi; Mapili, Gazell; Suhali, Gerry; Chen, Shaochen; Roy, Krishnendu, “A digital micro-mirror device-based system for the microfabrication of complex, spatially patterned tissue engineering scaffolds,” Journal of Biomedical Materials Research - Part A, May 2006, 77(2), p 396-405

67. Liu VA, Bhatia SN , “Three-dimensional photopatterning of hydrogels containing living cells,” Biomedical microdevices, Dec 2002, 4(4), p 257-266

68. Mapili G, Lu Y, Chen SC, et al., “ Laser-layered microfabrication of spatially patterned functionalized tissue-engineering scaffolds,” Journal of biomedical materials research part B-Applied biomaterials , Nov 2005, 75B(2), p 414-424

69. Leclerc E, Sakai Y, Fujii T, “Microfluidic PDMS (polydimethylsiloxane) bioreactor for large-scale culture of hepatocytes,” Biotechnology progress, May-Jun 2004, 20(3), p 750-755

70. Ostrovidov S, Jiang JL, Sakai Y, et al., “Membrane-based PDMS microbioreactor for perfused 3D primary rat hepatocyte cultures,” Biomedical microdevices, 2004, 6(4), p 279-287

71. Carrico IS, Maskarinec SA, Heilshorn SC, et al., " Lithographic patterning of photoreactive cell-adhesive proteins ," Journal of the American chemical society, Apr 2007, 129(16), p 4874

72. Kane RS, Takayama S, Ostuni E, et al., " Patterning proteins and cells using soft lithography," Biomaterials, Dec 1999, 20 (23-24), p 2363-2376

73. Roth EA, Xu T, Das M, et al., "Inkjet printing for high-throughput cell patterning," Biomaterials, Aug 2004, 25(17), p 3707-3715

74. Nakamura M, Kobayashi A, Takagi F, Watanabe A, Hiruma Y, Ohuchi K, Iwasaki Y, Horie M, Morita I, Takatani S., "Biocompatible inkjet printing technique for designed seeding of individual living cells.," Tissue Engineering, Nov-Dec 2005, 11(11-12), p 1658-66.

CHAPTER 2

MICROMACHINED NOZZLES FOR THE WET-SPINNING OF COLLAGEN MICRO/NANOFIBERS

2.1 Introduction

Collagen micro/nanofibers have emerged as important materials for tissue engineering, and their manufacture and manipulation has been a subject of extensive study. Native fibrous collagen is an integral structural component of various tissues. It also acts as a substrate for maintaining cellular activities, and the characteristic 67 nm D-periodicity observed in the native collagen fibrils is believed to be associated with providing important guidance cues necessary for cellular motility [1]. Extracted collagen material is considered an attractive choice for implantable tissue structures as it can be processed to regenerate the unique D-periodic chemical structure of the native tissues *in vitro*. Also, the distribution and concentration of fibers of this material in a tissue can be adjusted to achieve a specific biomechanical property. Similar to other polymeric micro/nanoscale fibers, electrospinning and wet-spinning are the two conventional approaches adopted for the fabrication of collagen fibers.

Electrospinning is a popular choice for the production of synthetic and natural polymer fibers for extracellular matrix (ECM), since the resultant fibers are in the same range of dimensions as observed in the native tissues. Matthews et al. reported the first demonstration of collagen electrospinning in 2002 [2]. Collagen was dissolved in the solvent 1,1,1,3,3,3-hexafluoro-2-propanol (HFP) to produce electrospun fibers (100-730 nm in diameter). This protocol was adopted by various groups for further investigation of

this approach for engineered tissue scaffolds [3-6]. Although some of these reports have documented the appearance of native D-periodic banding evidencing the presence of native morphology in electrospun collagen nanofibers, strongly conflicting reports have demonstrated the absence of the native striated morphology in fibers produced in this fashion, indicating the degradation of collagen [7]. The use of corrosive and toxic fluoroalcohols such as HFP as solvents has been identified as one of the main contributors to the degradation of the resultant collagen fibers. The fibers produced by electrospinning usually form a non-woven porous mesh of fibers. A partial alignment of fibers has been achieved using a rotating collection mandrel placed between the extrusion nozzle and the grounded electrode, as shown in Figure 2.1 [3].

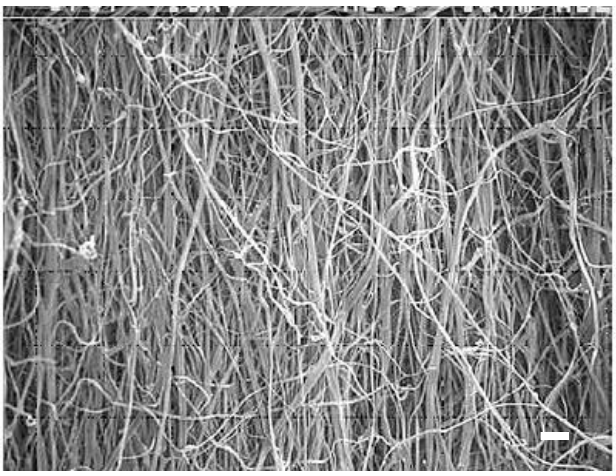

Figure 2.1. An electrospun collagen fiber mesh collected on a rotating mandrel to obtain aligned fibers (scale bar = 10 μm). [3]

Wet-spinning is one of the oldest extrusion techniques for producing polymer fibers. It has been used on an industrial scale for the manufacture of commercial fibers such as acrylic, rayon, aramid, and modacrylic since the early 19th century. Schimpf et al. were the first to present the wet-spinning of fibers from acid-soluble collagen in 1977 [8].

An 890 µm die was used to extrude acid-soluble collagen into an alkaline coagulant solution, and crosslinked using glutaraldehyde. Several research groups have since employed a wet-spinning approach for the production of collagen-based fabric for use as prosthetic tissues. Different aspects of the fiber spinning process, such as operating conditions, fibril self assembly and alignment, crosslinking conditions, and mechanical manipulation for the enhancement of the biological and mechanical performance of the resultant tissues have been investigated [9-13]. This approach has demonstrated *in vitro* regeneration of the native collagen morphology [14]. Also, aligned fiber meshes have been constructed by manual arrangement of fibers or by using a motorized rotating fiber collection setup (Figure 2.2). Although substantial progress has been made in the production of collagen fibers using this approach, the obtained fiber diameters (25-200 µm) are observed to be relatively large compared to the native tissue size scales. Also, the arrangement and packing densities of the fibers obtained in fashion are limited by the fiber collection approach.

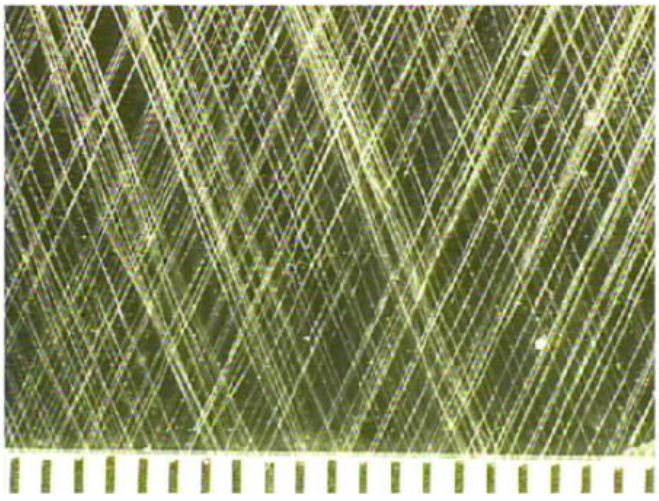

Figure 2.2. Wet-spun collagen fibers collected using a motorized collection setup (fiber spacing = 150-230 µm) [14].

The first documentation on wet-spinning of collagen fibers using regenerated collagen reported by Schimpf et al. [8] suggested that the smallest attainable fiber dimension is restricted by the pressure-withstanding capability of the wet-spinning fluidic apparatus and nozzle, as the pressure drops necessary to drive fluids through nozzles increase with the decreasing nozzle diameters. Considering this constraint, the goal of this research was to develop a high-pressure-withstanding micro/nanonozzle-based wet-spinning system for the extrusion of collagen micro/nanofibers.

Overcoming viscous and frictional forces exerted by the walls of a pipe on a fluid flowing through it causes a pressure loss in the fluid across the pipe. Such a pressure drop across a pipe with a laminar, incompressible fluid flow is represented by the Hagen Poiseuille equation (Equation 2.1) (Figure 2.3) [15].

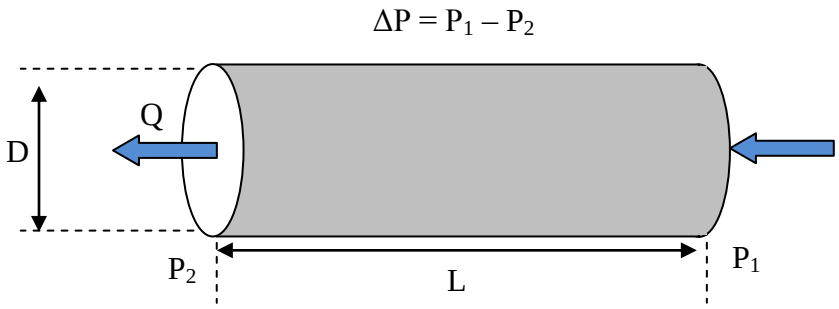

Figure 2.3. Schematic representation of the Hagen-Poiseuille flow through a pipe.

$$\Delta P = \frac{128\,\mu L Q}{\pi D^4} \tag{2.1}$$

Where,

ΔP = pressure drop across the pipe

μ = dynamic viscosity of the fluid

L = length of the pipe

Q = flow rate of the fluid

D = diameter of the pipe

Laminarity of a flow through a pipe is determined by a dimensionless quantity known as the Reynolds number [15]. Reynolds number indicates the ratio of the inertial forces to viscous forces, as shown in Equation 2.2. A flow with Reynolds number less than approximately 2600 is considered to be laminar.

$$Re = \frac{\rho v D}{\mu} \tag{2.2}$$

Where,

Re = Reynolds number

ρ = density of the fluid

v = mean velocity of the flow

D = diameter of the pipe

μ = dynamic viscosity of the fluid

Table 2.1 presents the upper and lower limits of Reynolds numbers for the range of flow parameters for collagen wet-spinning considered in the current research. The Reynolds numbers are observed to be far less than 2600, justifying the applicability of Hagen Poisuille's equation to this flow regime.

Table 2.1. Reynolds numbers for collagen flow through micronozzles.

	D, μm	Q, ml/min	Viscosity, Pa.s	Density, kg/m^3	Re
Lower limit	1	3×10^{-14}	1	1000	3.75×10^{-05}
Upper limit	50	0.08	1	1000	0.03

It can be deduced from Equation 2.1 that for a given fluid and a flow rate, the pressure drop is inversely proportional to the fourth power of the diameter of a pipe. This indicates the need for very high driving pressures for fluid flow through pipes with diameters scaled down to the nanoscale. Therefore, the scope of this work entailed three tasks. The first task was to develop microfabrication strategies for high-pressure-withstanding micro/nanonozzles capable of generating pressure-driven micro/nanofluidic jets. The study of pressure-driven sub-10 μm liquid jets has mostly been limited to computational analysis. Therefore, the second objective was to test the feasibility of pressure-driven micro/nanojet generation and carry out an empirical investigation of the flow behavior of liquid jets on these scales. The final objective was to utilize the developed high-pressure-driven micro/nanojet generation system for the production of collagen micro/nanofibers and control over their dimensions and geometries.

2.2 Fabrication and characterization of silicon and glass-metal composite micro/nanonozzles

In the past several decades, applications of micro/nanofluidic jets have expanded to a variety of areas including microelectronic cooling, drug delivery, ink jet printing, and microsurgery [16-19]. Even so, very limited experimental investigation has been reported on sub-10 μm jets, and fluidic jet studies on this scale have mostly been confined to fluid

dynamic simulations [20-21]. Therefore, the first milestone of the current research was to develop fabrication approaches for micromachined micro/nanonozzles, and generate and characterize liquid micro/nanojets driven through them.

Since the current research demanded extrusion of nanofluidic jets, there were three considerations to be made while choosing the appropriate material and fabrication approach for the nozzles, as described below:

1. A fabrication approach capable of constructing nozzles with inner dimensions on the nanoscale was required.
2. The micromachined nozzles needed to exhibit a high-pressure withstanding capacity in order to sustain the high pressure drops necessary to obtain substantial micro/nanofluidic jet flows.
3. Packaging demanded a long (> 5 mm) nozzle shaft for the ease of assembly with a high-pressure generation and jet imaging apparatus.

The literature reports several approaches and materials employed for the fabrication of micro/nanonozzles. Materials explored include silicon [22], silica [23], silicon nitride [24], metals such as nickel [25] and palladium [26], and polymers such as PMMA [27] and SU8 [28]. Tensile strength of a material is one of the primary determinants of the burst pressure of a tube. Based on a comparison of the tensile strengths of the different materials utilized for the construction of micro/nanonozzles, silicon- and metal-based nozzles appeared better suited for high-pressure applications as compared to the polymeric nozzles (Table 2.2).

Table 2.2. Ultimate tensile strengths (UTS) of candidate materials for the fabrication of micro/nanonozzles.

Material	Tensile strength, MPa
Silicon	6000 [29]
Silicon dioxide	670-940 [30]
Silicon nitride	4150-4600 [30]
Nickel	562 [31]
PMMA	50-70 [32]
SU8	50-80 [33]

The reported silicon-based fabrication methods primarily focused on out-of-plane nozzles. Wang et al. fabricated silica nozzles on a silicon substrate using a three-mask process involving inductively coupled plasma (ICP) etching for electrospraying applications. The nozzles were fabricated to have a depth greater than 200 μm and a diameter of 10 μm [23]. Efforts have been directed towards fabrication approaches for submicron nozzles based on silicon substrates. Farooqui et al. fabricated the first free-standing out-of-plane silicon nitride nanonozzle (diameter 585 nm) in 1992 (Figure 2.4a) [24]. Voigt et al. demonstrated silicon nanonozzle fabrication using anisotropic backside etching and focused ion beam (FIB) milling for drilling the nanoscale orifice. An aperture size of 100 nm was obtained by FIB milling (Figure 2.4b) [22]. Although the silicon-based out-of-plane nozzles demonstrated the potential to scale down the orifice dimensions to the submicron range, their dimensions in the flow length were limited by the width of the substrate rather than by design, also presenting a potential packaging

concern. The reported in-plane metal nozzles were not suitable for proceeding towards nanoscale dimensions [26].

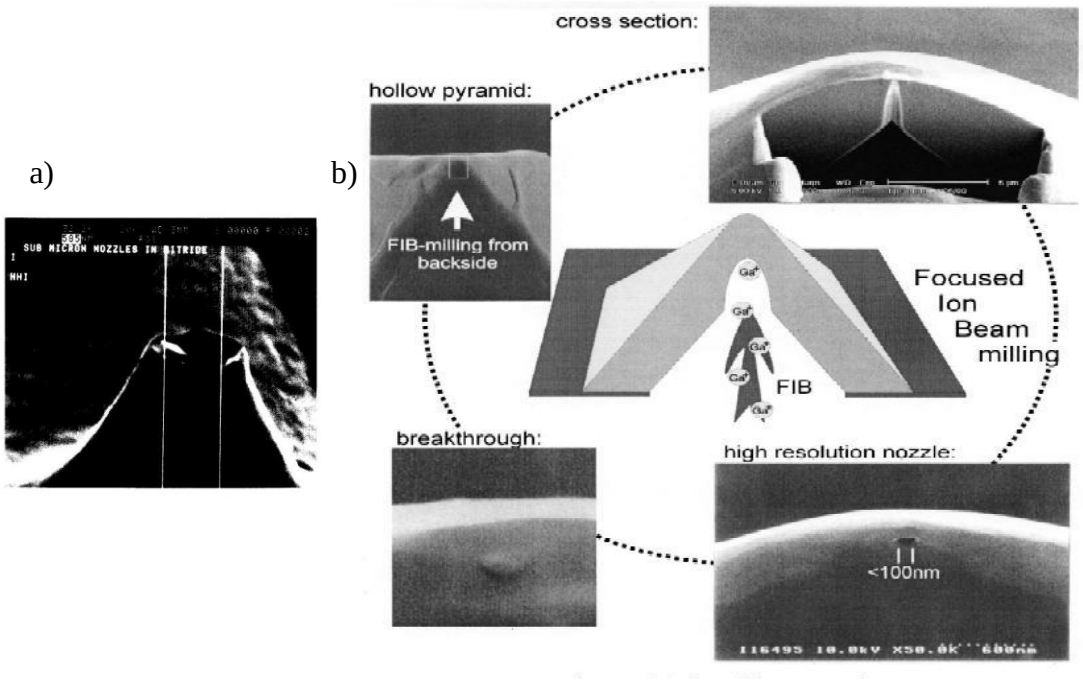

Figure 2.4. Out-of-plane nanonozzles: a) silicon nitride [24], and b) silicon [22].

In this research, two distinct manufacturing approaches were adopted to achieve a robust microfabricated nozzle with a nanoscale orifice, as discussed in the following sections. These nozzles were designed to exhibit the capacity to withstand high differential pressures (>1000 psi) necessary to generate high speed or viscous liquid flows through small orifices.

2.2.1 In-plane silicon micro/nanonozzles

This section presents a fabrication approach for in-plane silicon micro/nanonozzles with dimensions ranging from 500 nm to 12 μm and the examination of liquid jets ejected through them. Unlike out-of-plane silicon nozzles, the dimensions of

the nozzles in the current approach were not limited by fabrication constraints. Important three-dimensional features of the nozzle, namely, the channel and the fluidic reservoir could be defined by design, thereby meeting important fluid-mechanical criteria such as a fully developed flow.

2.2.1.1 Fabrication development

Figure 2.5 illustrates the fabrication process sequence for the in-plane silicon nozzles. A double-side polished, 450-μm thick, (100) silicon wafer was chosen as the substrate material. A 1-μm thick silicon dioxide (SiO_2) layer was thermally grown on the silicon wafer using wet-oxidation (2.5 hours, 1100 ºC). Positive photoresist SC 1827 (Shipley Co., Marlboro, MA) was spin coated on the wafer and patterned using photolithography to delineate the nozzle structure. The photoresist pattern was transferred to the SiO_2 layer using inductively coupled plasma (ICP) etching. After removing the photoresist layer using acetone and oxygen plasma reactive ion etching (RIE), the nozzle channels and reservoirs were etched into the silicon substrate using anisotropic potassium hydroxide (KOH) etching (concentration of KOH = 40% at 70˚C, etch rate 0.6 μm/min). Patterns to facilitate subsequent chip individualization were aligned with the etched nozzle patterns and marked lithographically on the backside of the wafer using the backside alignment feature offered by a Karl Suss MA6 mask aligner (Suss MicroTec Inc., Waterbury Center, VT). These alignment marks were etched using ICP. The SiO_2 layer was etched away using hydrofluoric (HF) acid, and the wafer was cleaned with piranha etch (3:1 mixture of concentrated sulfuric acid (H_2SO_4) with hydrogen peroxide (H_2O_2)) in preparation for silicon fusion bonding. The patterned wafer was fusion bonded with a (100)-oriented silicon wafer to form enclosed in-plane nozzles.

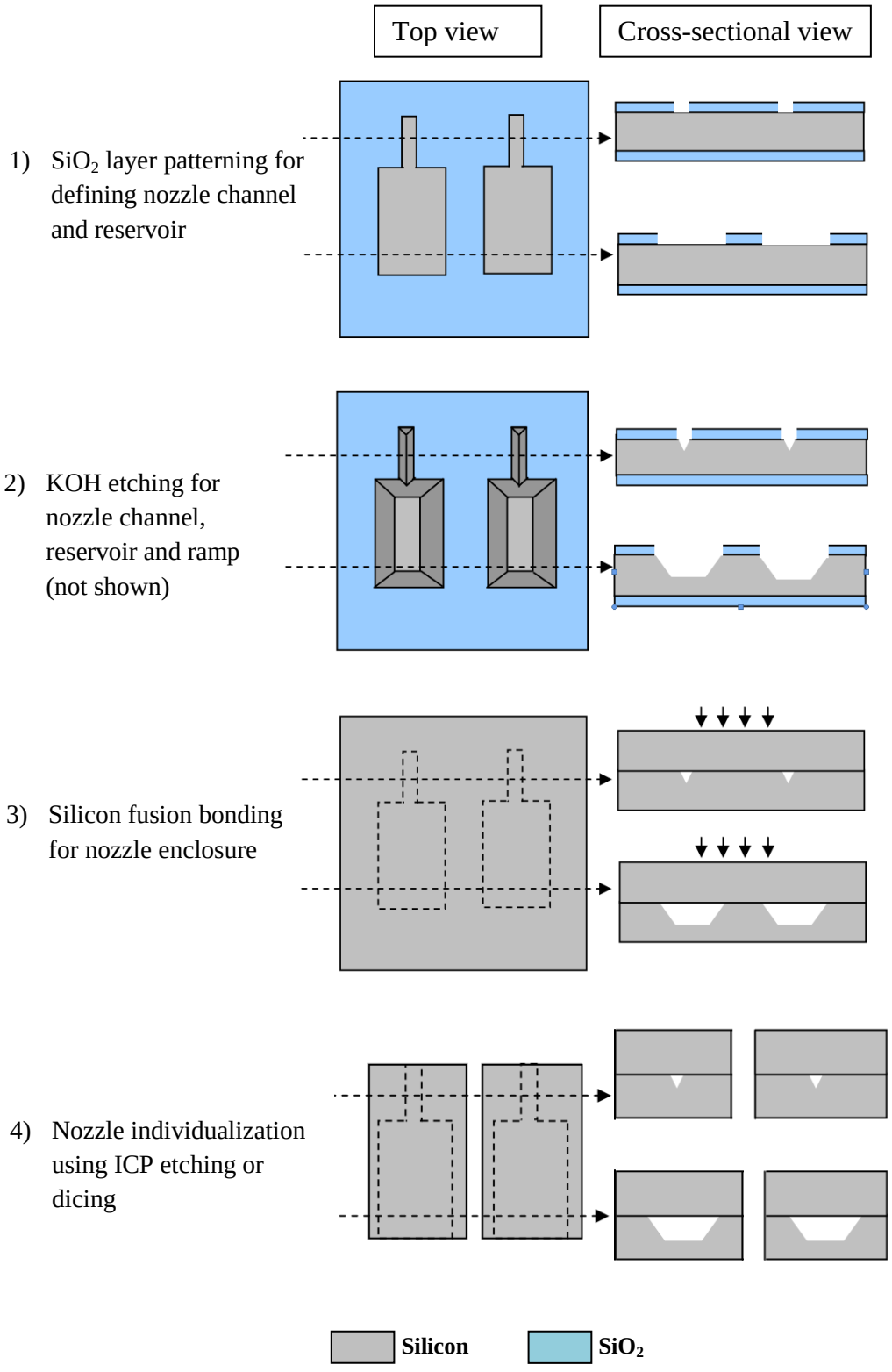

Figure 2.5. Fabrication process sequence for in-plane silicon nozzles.

The fused wafers were annealed at 1100 ˚C for 4 hours to strengthen the bond between the two wafers. The nozzles were then individualized using a through-wafer ICP etch utilizing the Bosch process, or alternatively using dicing by following the alignment patterns on the back of the wafer. The surface containing the nozzle exit orifice was polished using chemical mechanical polishing (CMP) with the aid of a polishing cloth and alumina abrasive slurry (particle size: 1, 0.3, 0.05 μm). This removed any fabrication imperfection on the exit plane (Figure 2.6). Finally, thermal wet-oxidation was optionally utilized to reduce the inner dimensions of the nozzles to construct submicron nozzles. This process was termed as 'oxidative sealing'. The nozzles were cleaned ultrasonically and with piranha etch prior to fluidic testing.

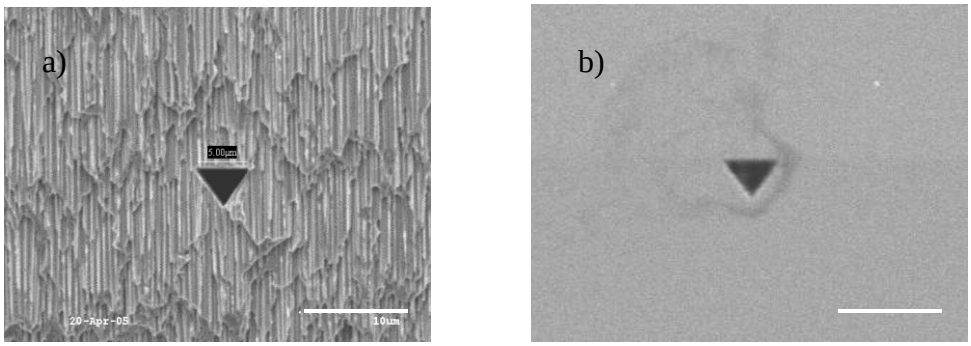

Figure 2.6. The orifice exit: a) before CMP, b) after CMP (scale bars = 10 μm).

Nozzle structure

The fabricated nozzles comprised a trapezoidal cross-section reservoir (width: 150 μm, 500 μm, depth: 40 μm, length: 7 mm), a triangular cross-section channel (width: 500 nm - 12 μm), and a ramp connecting the reservoir and the channel, as shown in Figure 2.7.

As a fluid enters the channel section of a nozzle from the reservoir, it requires some length to develop its velocity profile, or in other words to achieve a fully developed flow [34]. A fully developed flow in a channel is dependent on its length-to-diameter ratio. In the current study, the channel length was designed to be 10 times the channel width.

Anisotropic KOH etching

KOH etching has a characteristic silicon-orientation-dependent etch rate. The etch rates are in an ascending order for silicon crystal planes (111), (100), and (110). A single step KOH etching was able to construct the three features of the nozzle: the reservoir, the channel, and the ramp, on account of its orientation-dependent nature (Figure 2.7). The reservoir was etched to its required depth using a timed etch. Since the channel width was up to 500-fold smaller than the reservoir width, the depth of the channel was dictated by anisotropic etch stop resulting from the intersection of the slowest etching (111) planes [29]. The ramp was fabricated by the undercut of the convex corners in the nozzle structure offering a gradual transition for the fluid from the reservoir to the channel. This feature avoided the excess pressure drop resulting in a laminar flow through a sudden contraction in a nozzle [35]. For KOH concentration of 40% at 70 ºC, the undercut of the convex corners (in x and y directions) was observed to be 2.5 times the etch rate along the depth of the nozzle (z direction).

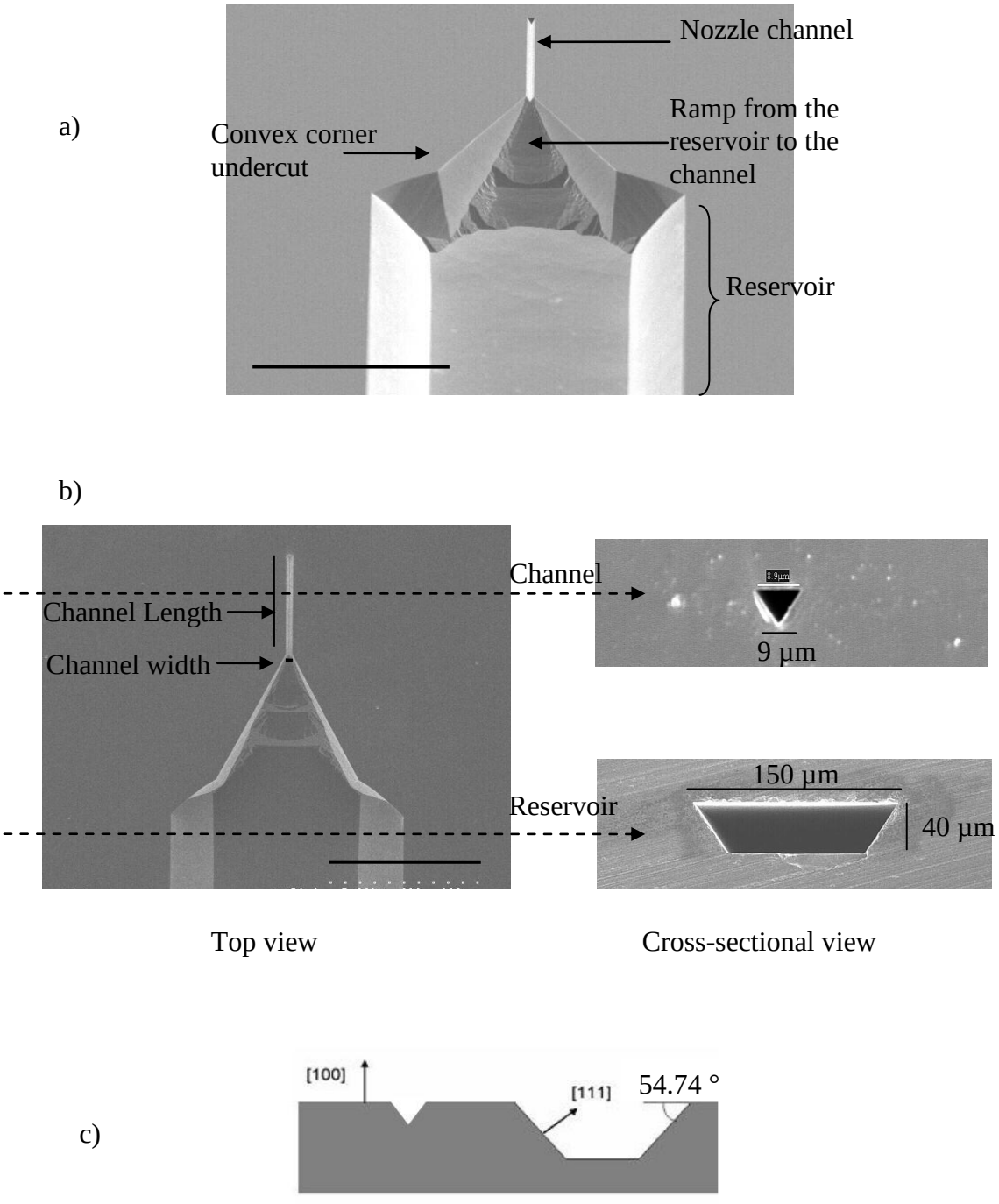

Figure 2.7. A KOH etched nozzle: a) tilted view illustrating different parts of the nozzle-channel, reservoir, and ramp, b) top and cross-sectional views, and c) a schematic of the KOH etch profile (scale bars = 100 µm).

Oxidative sealing of the nozzles

The individualized nozzles were thermally oxidized to scale down the orifice sizes from the micron to submicron range. Thermal oxidation is a process for growing thin films of SiO_2 on a silicon substrate and is achieved by placing the substrate in very high temperatures in the presence of oxidants such as molecular oxygen or oxygen in the presence of water vapor. In this process, as the oxidation progresses, the oxidizing agent diffuses through the grown SiO_2 film to react with the silicon layer to further form SiO_2. Consequently, 46% of the SiO_2 film is formed below the original silicon surface while 54 % is formed above, as shown in Figure 2.8. The rate of growth of a thermally grown oxide is mathematically expressed by the Deal-Grove model [36].

The silicon nozzles had two faces defined by (111) planes and one face defined by a (100) plane. The thickness of the SiO_2 layer grown above the original surfaces determined the contraction of nozzle orifice dimensions. The opening size after oxidative sealing could be estimated by a trigonometric analysis of the geometry of the triangular nozzle (Figure 2.9), as expressed in Equation 2.3.

$$w = W - 1.4t_1 - 2.4t_2 \tag{2.3}$$

Where,

w = Final width of the sealed nozzle

W = Original width of the sealed nozzle

t_1 = Oxide thickness above the original silicon surface for a (100) plane

t_2 = Oxide thickness above the original silicon surface for a (111) plane

Figure 2.8a illustrates a 500-nm wide nozzle obtained after a 16 hour long wet oxidation at 1100 °C of a 3-μm wide triangular nozzle. Using this approach, nanoscale orifices could be obtained without resorting to serial processing nanofabrication

techniques. Owing to compressive stresses at the concave corners, the oxide thickness in the vicinity of the corners of the triangles was smaller as compared to the rest of each edge leading to a nonuniform oxide profile along the edge. A near-circular cross-section channel could be obtained by oxidizing the triangular channel, and etching the grown SiO_2 with HF (Figure 2.8b). Figure 2.9 compares the measured widths of the sealed nozzles with the estimated widths obtained using (Equation 2.3).

Design variations

Using this fabrication approach, variants of the above design could be obtained by an additional photolithography step to obtain various nozzle profiles suitable for fluid flow applications. To achieve this, the channel was etched using ICP while the reservoir was fabricated by KOH etching to obtain the ramp (Figure 2.10).

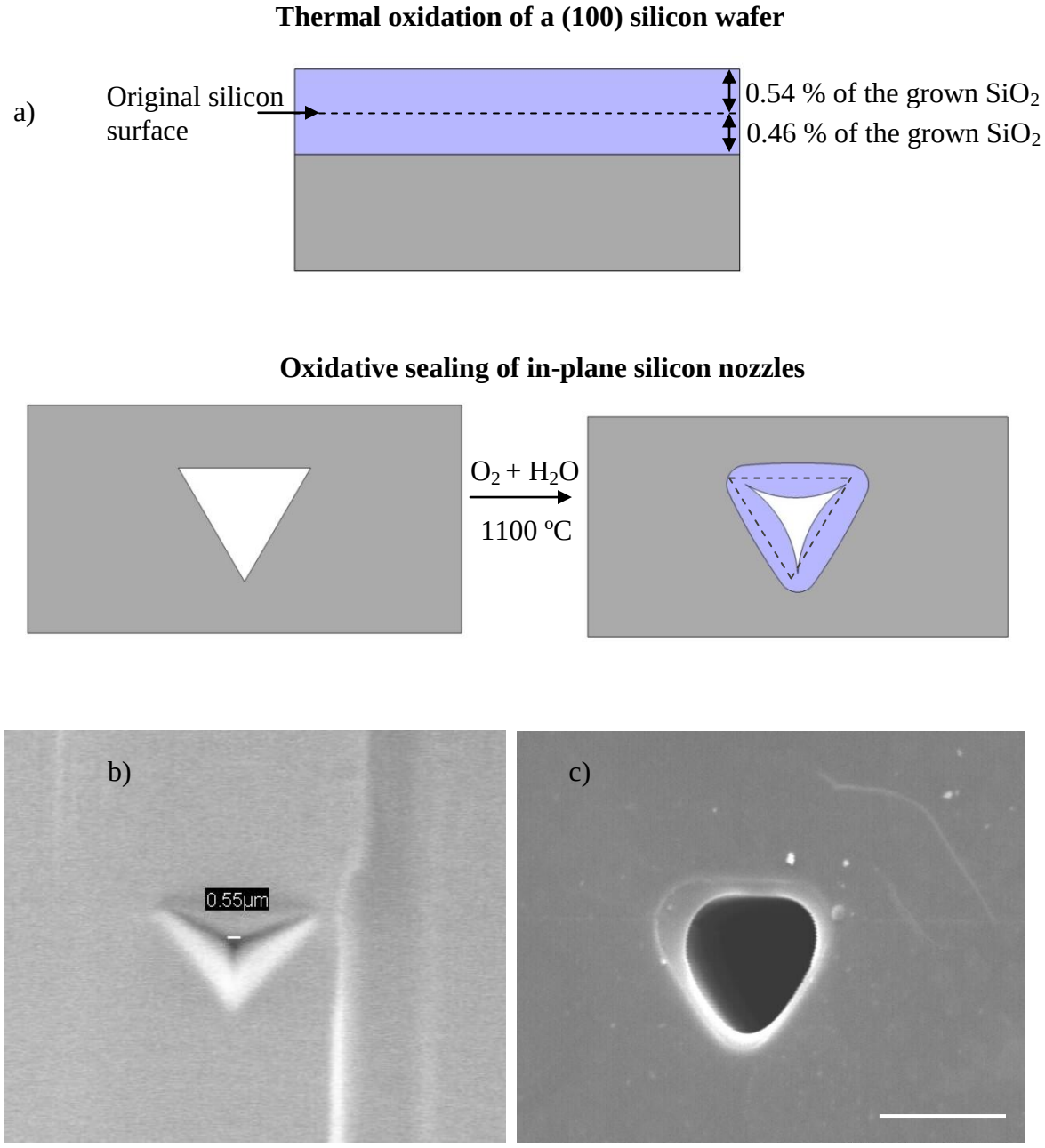

Figure 2.8. Oxidative sealing of in-plane silicon nozzles: a) a schematic representation, b) a 500-nm wide orifice obtained by thermal oxidation of a 3-µm wide silicon orifice, and c) a 9-µm wide rounded triangular cross-section orifice obtained after oxidation of a 7-µm wide orifice and etching away the SiO_2 layer (scale bar = 10 µm).

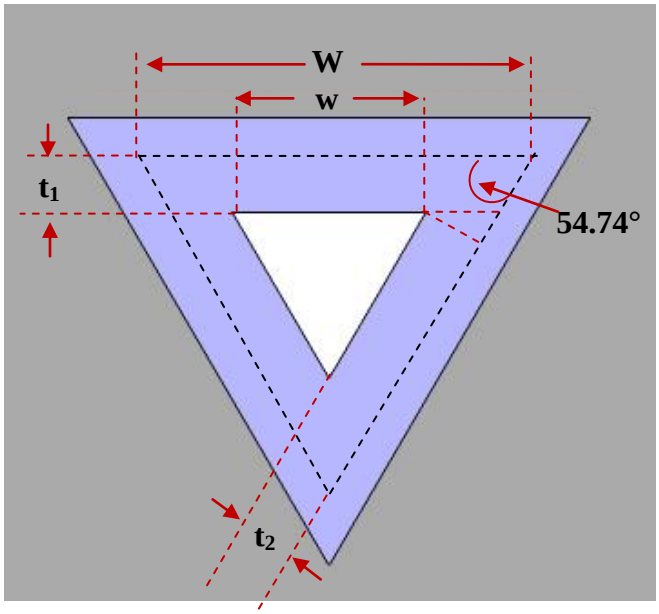

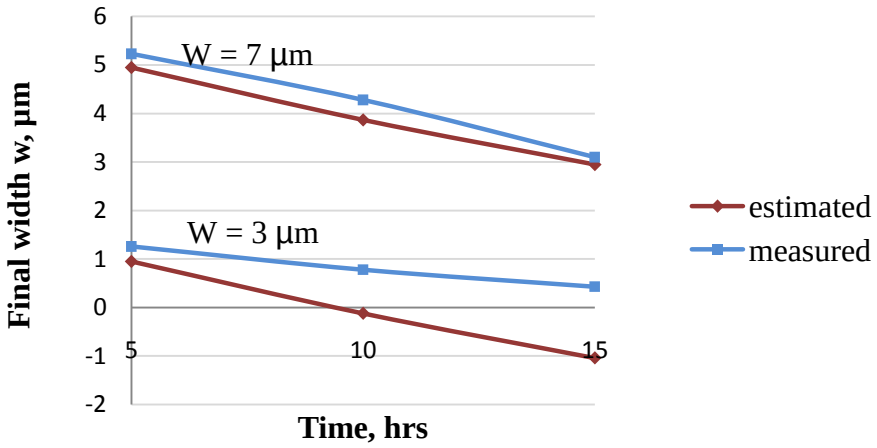

Figure 2.9. Estimation of the oxidatively sealed nozzle dimension (not taking into consideration the oxide thinning effect at the concave corners).

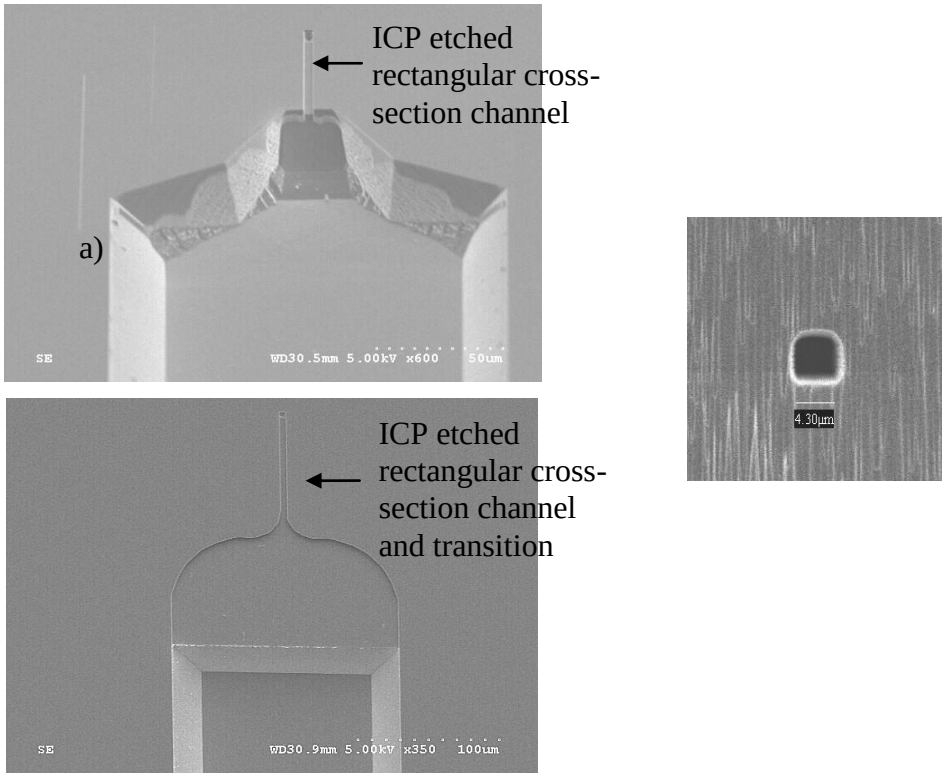

Figure 2.10. Nozzle channels etched using ICP to obatin a 4 µm × 4 µm rectangular cross-sectional nozzle.

2.2.1.2 Testing and characterization of the silicon micro/nanonozzles

The formation of macro- and micro-scale liquid jets, and mechanisms of their decay into droplets has been a subject of investigation for centuries [37]. Optical microscopy and x-ray spectroscopy have been used as visualization and characterization methods for microscale liquid jets [37-38]. The current work focused on developing a microfluidic system suitable for the generation and visual characterization of liquid jets down to the nanoscale.

Burst pressure

The burst pressure for the fabricated nozzles was approximately estimated using the Barlow formula expressed by Equation 2.4 [39]. This formula relates the internal pressure that a circular pipe can withstand to its dimensions and material strength.

$$P = \frac{2 \times S \times T}{D} \tag{2.4}$$

Where,

P = Burst pressure of a tubular pipe

S = Ultimate tensile strength of the material

T = Wall thickness of the pipe

D = Outer diameter of the pipe

For the purpose of estimating the burst pressure of the in-plane silicon nozzles, the dimensions in the direction of the substrate width were assumed. For a 1-μm wide nozzle channel, a burst pressure of 800000 psi was estimated. During the liquid jet generation tests, the fused silicon nozzles were observed to withstand pressures upto the maximum pressure generation capacity of the fluidic apparatus (2200 psi), sparing a few occasional instances of nozzle burst observed for pressures above 1500 psi. These bursts were believed to result from the propagation of silicon fusion bonding imperfections (Figure 2.11).

Micro/nanojet generation and visualization apparatus

The microfabricated nozzles were integrated with a high-pressure fluidic apparatus for jet generation using a machined stainless steel frame acting as a micro-to-macro interface. The nozzles were packaged with the frame using epoxy E-120HP (Loctite Corp.) to form a leak proof interface (Figure 2.12). The epoxy was chosen based

on its excellent mechanical properties and a capacity to withstand exposures to a wide range of solvents. Liquid propane (surface tension: 0.0075 N/m, vapor pressure: 124 psi) and butane (surface tension: 0.0123N/m, vapor pressure: 32 psi) were used as the working fluids following molecular dynamic simulations by Moseler and Landman [20].

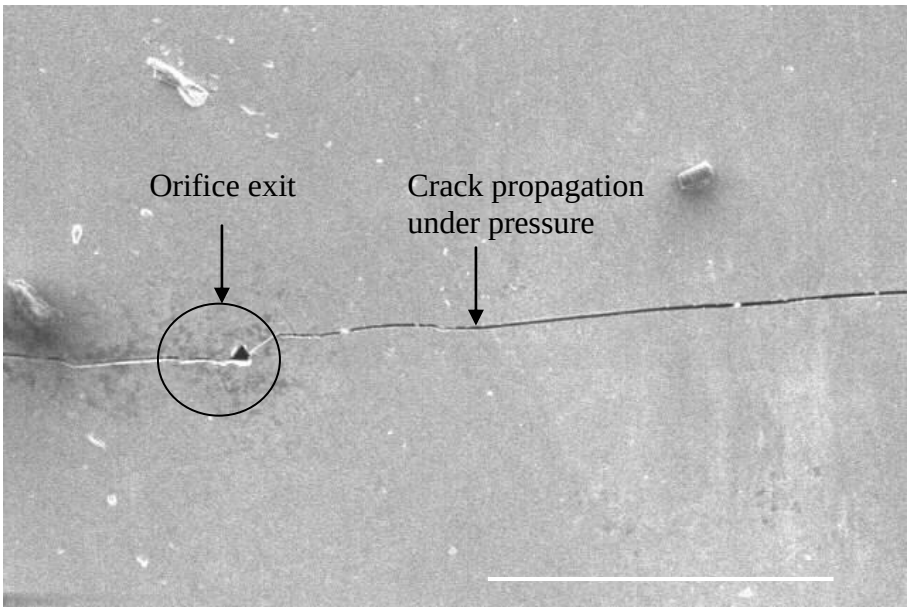

Figure 2.11. Silicon nozzle burst initiated by bonding imperfections (scale bar = 200 μm).

A schematic of the high-pressure fluidic apparatus used for generating micro/nanojets through the micromachined nozzles is illustrated in Figure 2.12a. In this system, nitrogen was used for pressurizing [up to 2200 psi (15 MPa)]. Before the system was filled with the working fluid, it was first pressurized slightly above its vapor pressure using nitrogen, and then the liquid (propane or butane) was pumped into the reservoir to the desired level. The system was then pressurized using nitrogen (above the liquid level) to the desired working pressure.

Figure 2.13 shows a schematic of the jet visualization and imaging setup. The microjets were visualized using a laser shadowgraph imaging approach, which involves shining a collimated beam of light on the object while capturing its shadow from the other side. The flow field was illuminated using Nd:YAG laser (532 nm). Instantaneous images of the flow were captured using a charge coupled device (CCD) camera.

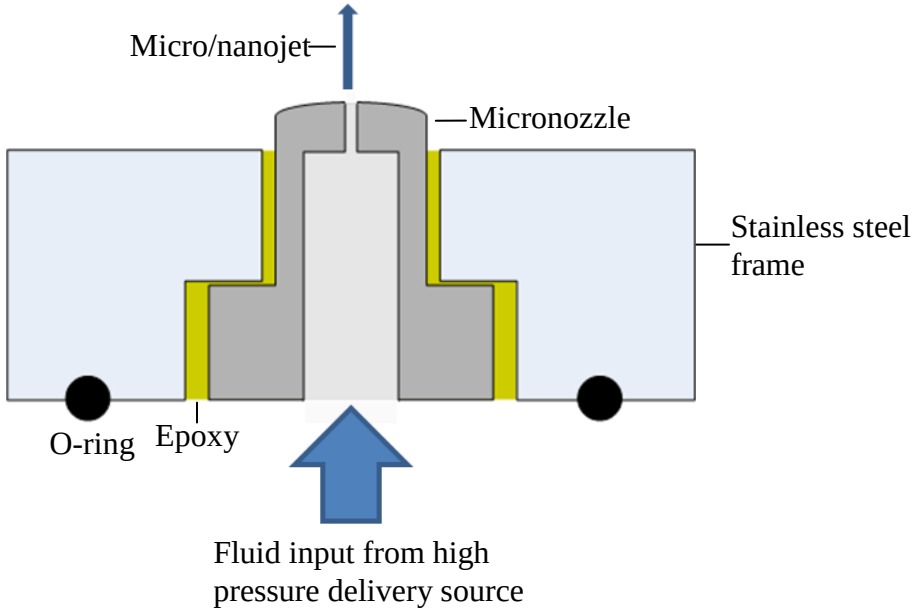

Figure 2.12. A stainless steel frame as a macro-to-micro interface for the in-plane silicon nozzles.

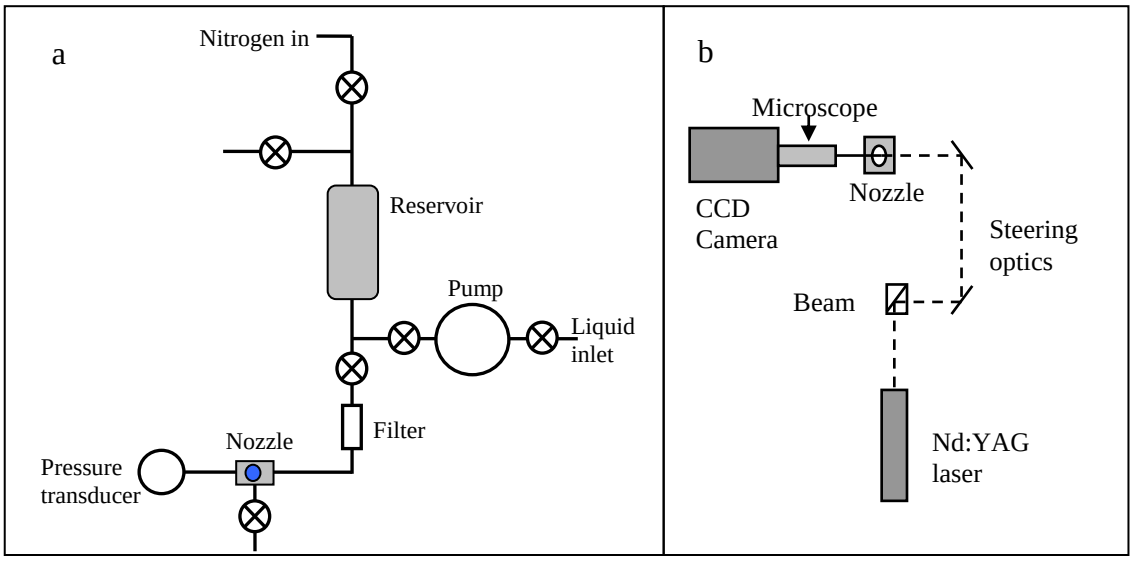

Figure 2.13. a) A high-pressure fluidic apparatus, and b) a micro/nanojet imaging shadowgraph system.

Liquid micro/nano jet generation

Fluidic micro/nanojets were generated by applying pressures ranging from 50 psi (0.3 MPa) to 2200 psi (15 MPa) to nozzles with dimensions varying from 500 nm to 12 μm.

- *Formation and breakup of jets*

A typical laminar liquid jet issued from a nozzle consists of an initial columnar section that 'pinches off' into atomized droplets at a certain distance downstream. Jet breakup is influenced by surface tension properties of the liquid, inertial and viscous forces in the liquid, and instabilities and disturbances originating from the fluid and the ambient [40]. The evaporative micro/nanojets extruded from the micromachined nozzles displayed a similar behavior (Figure 2.14). The jet breakup into droplets occurred at a certain distance from the exit plane. The breakup distances of the jets, measured from the exit plane of the orifice to the initiation point of droplet formation, were observed to vary

with the applied driving pressures. Increasing driving pressures indicate increasing jet velocities in the laminar flow regime, and generally, the jet breakup distance increases linearly with the jet velocities in this regime [40]. Figure 2.15 illustrates representative shadowgraph images for 12 μm and 1 μm butane jets respectively, illustrating the variation of jet breakup distance with driving pressures. For both the nozzles, the breakups occurred further downstream with increasing driving pressures. Aberrant behavior displayed by the 12 μm jets above 500 psi was intermittently observed. This characteristic may be attributed to the presence of contamination or bubbles at the exit orifice as discussed later.

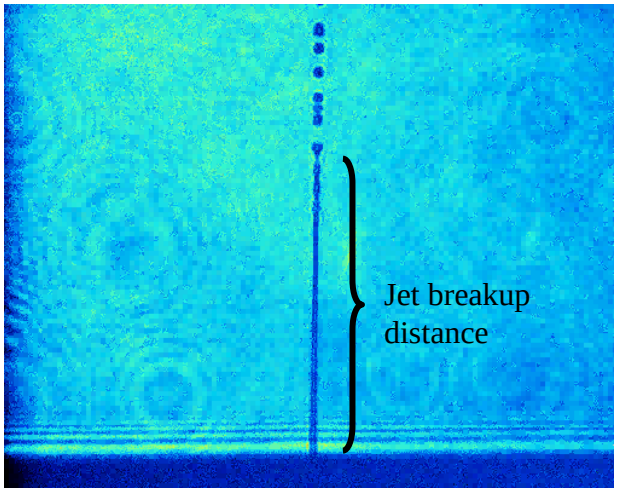

Figure 2.14. A shadowgraph image of a 10 μm butane microjet.

a)

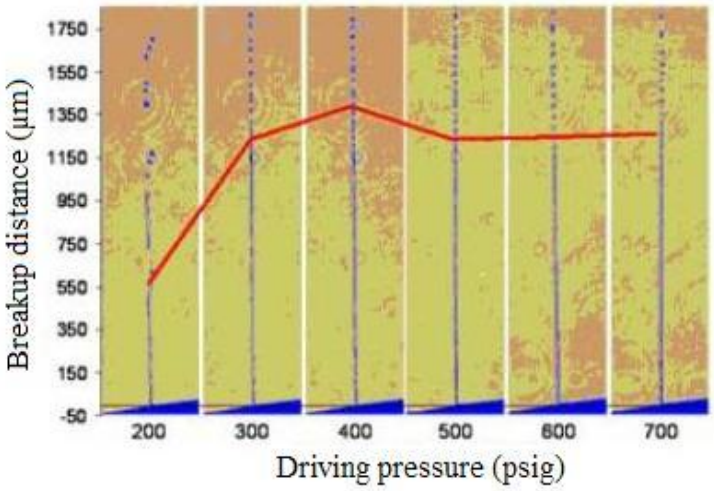

b)

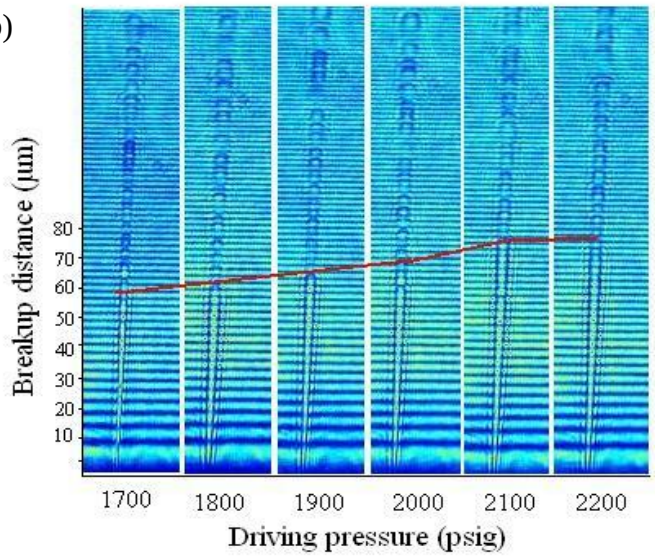

Figure 2.15. Shadowgraph images illustrating the variation of the breakup distance with the driving pressure for, a) 12 µm butane jets, and b) 1 µm butane jets.

- *Velocity of jet streams*

The velocity of the atomized droplets could be estimated over a range of driving pressures by the cross-correlation of identifiable droplet images in successive frames that were taken at a given time delay (Figure 2.16). This method was applied for estimating the jet velocities issued from 6, 2.5, and 1 µm wide nozzles. According to the Hagen Poisueille law (Equation 2.1), the fluid flow velocity in a tube increases linearly with the

pressure drop across the tube for a given fluid. This trend was observed for the investigated jet flows, as shown in Figure 2.17.

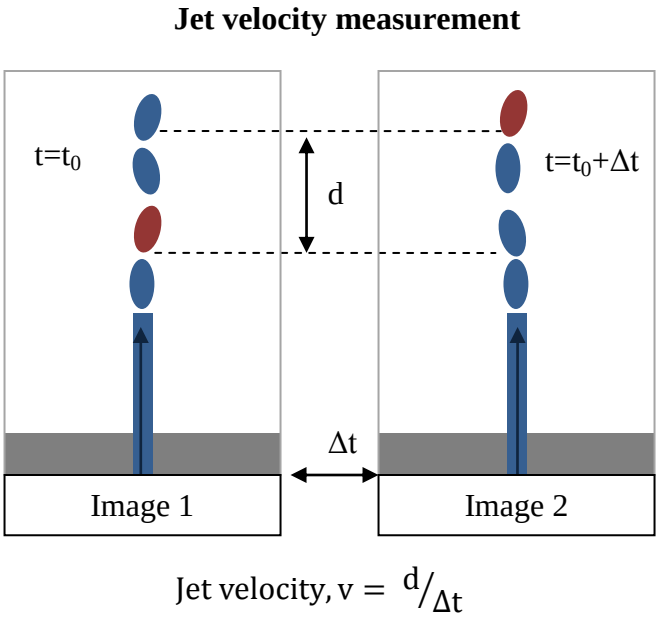

Figure 2.16. The scheme for jet velocity measurement using shadowgraph imaging.

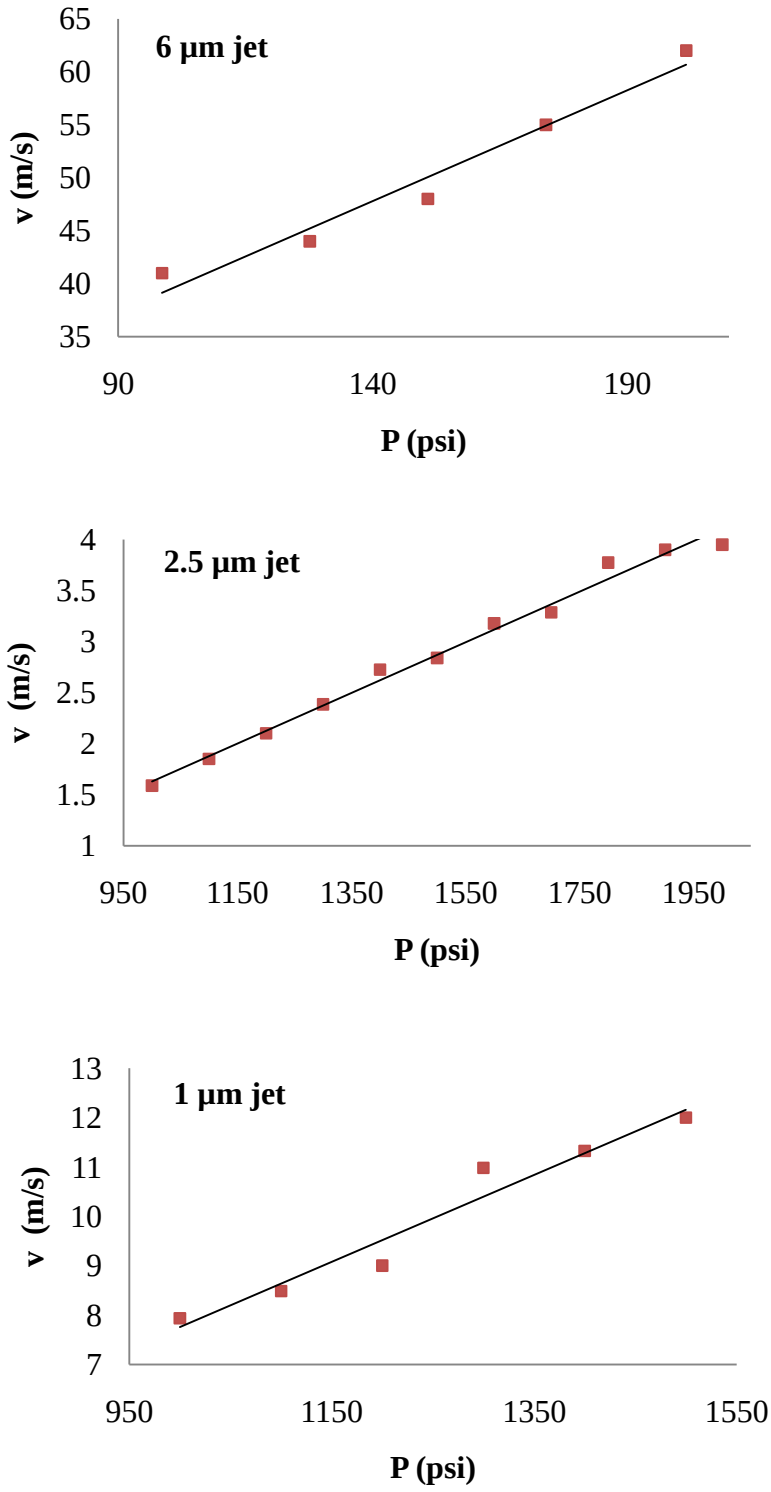

Figure 2.17. Velocity measurement of micro/nanojets using shadowgraph imaging for: a) 6 µm, b) 2.5 µm, and c) 1 µm nozzles.

2.2.1.3 Discussion of the encountered problems

Though sub-10 μm laminar fluidic flows could be generated using the developed apparatus, and the jet characteristics could be recorded for each jet, repeatability was rare. A significant inconsistency was noted between different nozzles and different experiments for the same nozzle in terms of driving pressures, jet breakup distances, and jet velocities. Figure 2.18a illustrates the variation the of jet driving pressures for 6 μm nozzles from the same batch, and Figure 2.18b shows the variation of breakup distances for 4 μm nozzles at a driving pressure of 1700 psi (11.5 MPa). Several instances of jet instabilities such as pooling, spraying, and splitting were also observed (Figure 2.19). As a result of this, correlations between nozzle dimensions, driving pressures, jet breakup distances, and jet velocities could not be drawn.

Upon inspection of the nozzle orifices after fluidic testing, it was concluded that the noted inconsistency was an outcome of partial or complete obstruction of flow caused by clogging of the nozzles. Figure 2.20 illustrates the SEM images of a nozzle prior to the fluidic testing and the clog appearing after the jet flow. Potential sources for the nozzle contamination were the condensation of moisture and dust at the orifice opening resulting from the Joule-Thompson and latent heat induced freezing of compressed butane and propane jets, residue from the working fluids, the apparatus, or the micronozzles themselves. To eliminate any impurities being introduced from the nozzle and its fabrication approach, the silicon-based micro/nanonozzles machining method was analyzed once again. Alumina particles introduced during CMP of the nozzles were a possible source for particulate incorporation in the nozzle channels. The silicon nozzles also lacked axis-symmetry, a feature often seen in fluid mechanical studies. Also, the

oxidized submicron nozzles often failed to extrude jets, challenging the patency and the uncertain three-dimensional profile of the SiO_2 channel. Considering these factors, and to eliminate the introduction of any instabilities introduced as a result of the manufacturing approach, the second generation of nozzles was fabricated using mechanical reinforcement of conventional pulled micropipettes.

a)

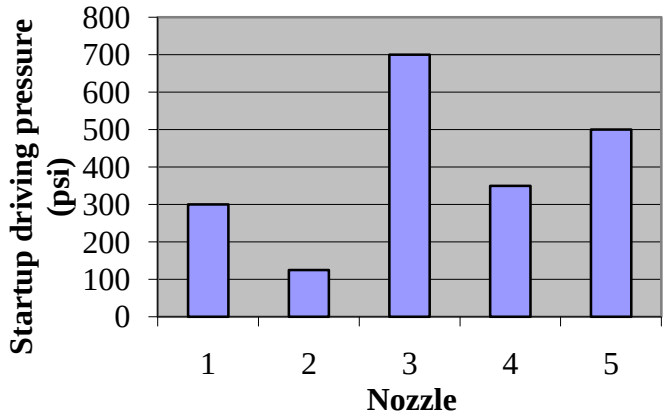

b)

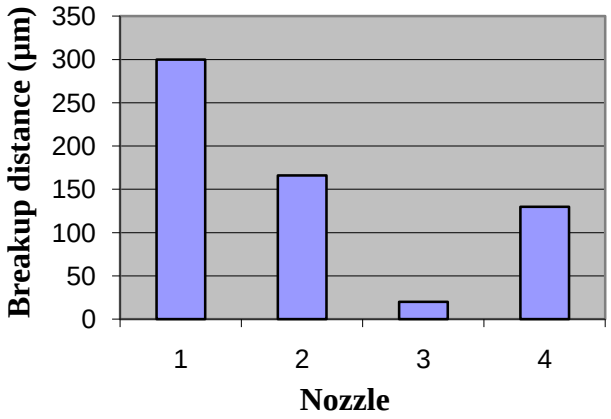

Figure 2.18. Variability in jet characteristics: a) variation of the jet startup driving pressures for 6 µm nozzles from the same batch, and b) variation of the jet breakup distances for 4 µm nozzles from the same batch driven at 1700 psi.

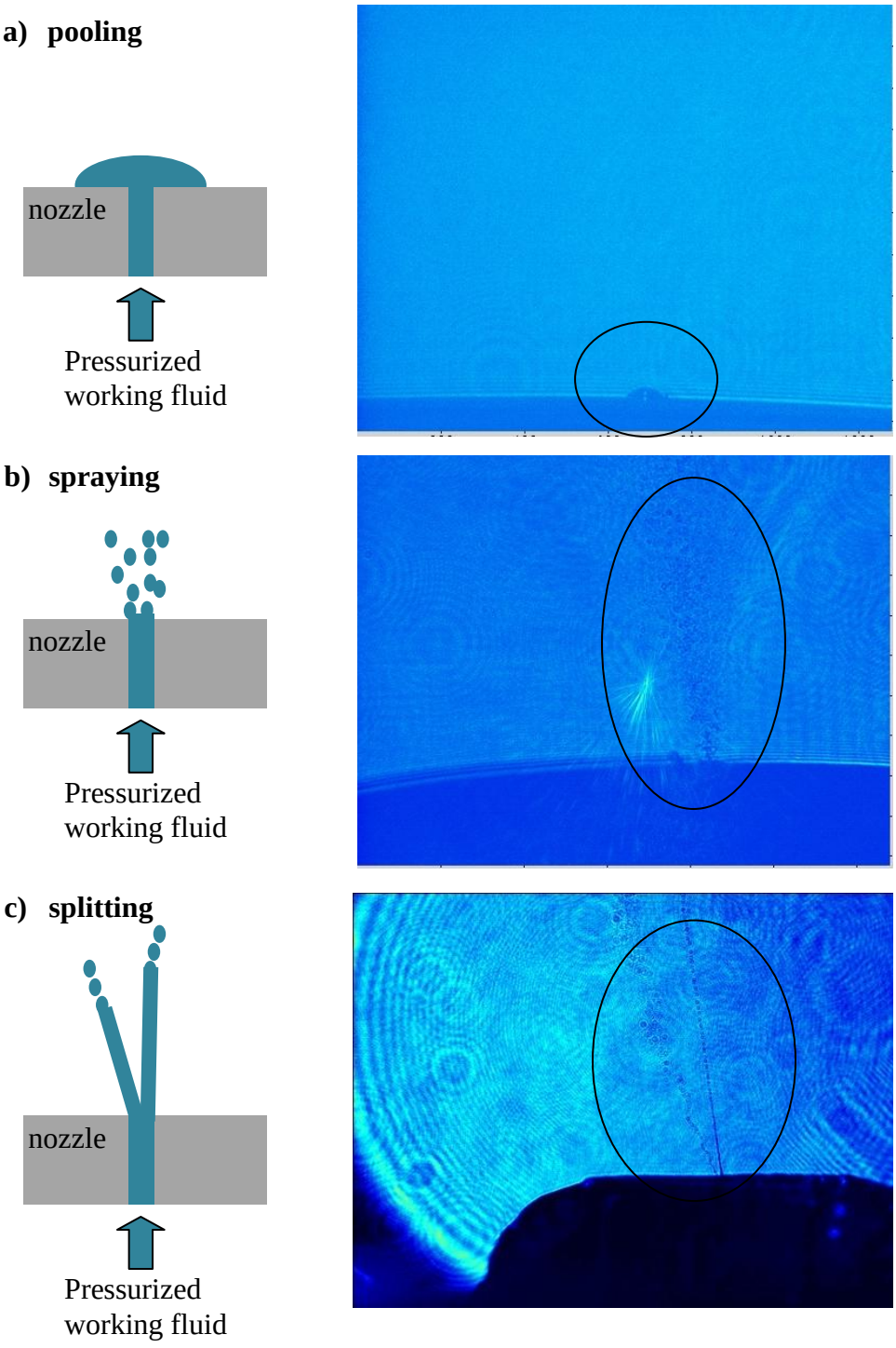

Figure 2.19. Shadowgraph images illustrating jet-instabilities: a) pooling, b) spraying, and c) splitting.

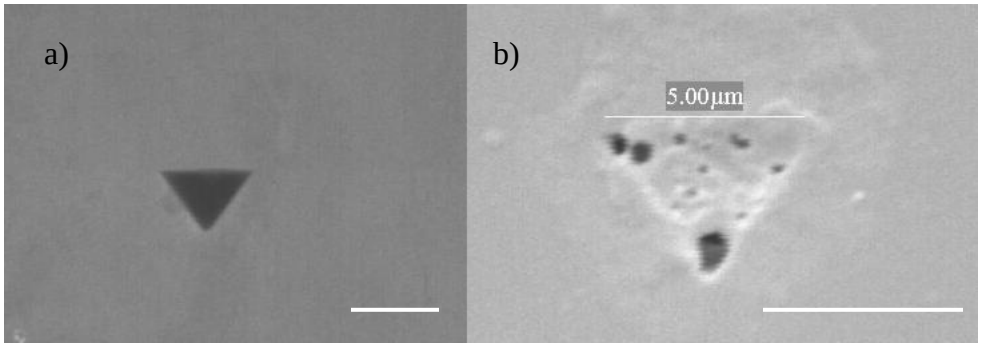

Figure 2.20. A 5-µm wide nozzle, a) before fluidic testing, b) after fluidic testing, illustrating nozzle clogging (scale bars = 5 µm).

2.2.2 Glass-metal composite micro/nanonozzles

A non-lithographic fabrication approach was developed for high-strength glass-metal composite micro/nanonozzles with orifice diameters ranging from 430 nm to 100 µm. Conventional borosilicate micropipettes were used as a foundation, and nickel was used as a strengthening layer to construct the high-pressure-withstanding micro/nanonozzles. The nozzles were fabricated to have an axis-symmetric geometry without any sudden boundary changes offering an ideal environment for the fluid to flow. In addition to the simplicity of the fabrication process, this approach also offered the ability to incorporate a wireless temperature control system for the nozzles to assist in circumventing the ice formation at the tip of the nozzle.

2.2.2.1 Fabrication development

The fabrication sequence for glass-metal composite nozzles is illustrated in Figure 2.21. Borosilicate glass capillaries were pulled into micro/nanopipettes using a P-97 micropipette puller manufactured by Sutter Instrument Company. The micropipette puller

consisted of a heating coil, an airjet cooling system, and clamps to secure the glass capillaries such that the center of the tube to be pulled was positioned in the heating coil. To initiate the micropipette pulling process, the glass tube was fastened to the machine and heated locally by the heating coil. A constant tensile force was simultaneously applied to the ends of the tube. The glass tube was locally melted and drawn into a micropipette. At a specified time, a hard pull was applied to the ends of the tube to break it into two individual micropipettes. By varying the machine parameters such as the heat, velocity of glass carriage under constant load at which the hard pull was applied, force of the hard pull, and air cooling time, the tip diameter and the taper length of the micropipette could be controlled.

The glass micropipette was sputter coated with a titanium/copper (Ti/Cu) seed layer. A 20-50-μm thick layer of nickel was electroplated to mechanically reinforce the micropipettes. This step concealed the entire glass pipette including the micro/nano orifice tips. To uncover the concealed orifice, focused ion beam (FIB) milling was employed to precisely mill out the top layer of nickel from the nozzle tip.

Using this technique, nozzles with tip diameters ranging from 430 nm to 100 μm were fabricated (Figure 2.22). A pure nickel nozzle could be fabricated by etching away the glass support using HF acid (Figure 2.22e). This technique could also be applied for the fabrication of metal multibarrel micropipettes (Figure 2.22f). This fabrication approach was believed to be non-invasive, such that the nozzle interiors did not come in contact with any contamination during the manufacturing process.

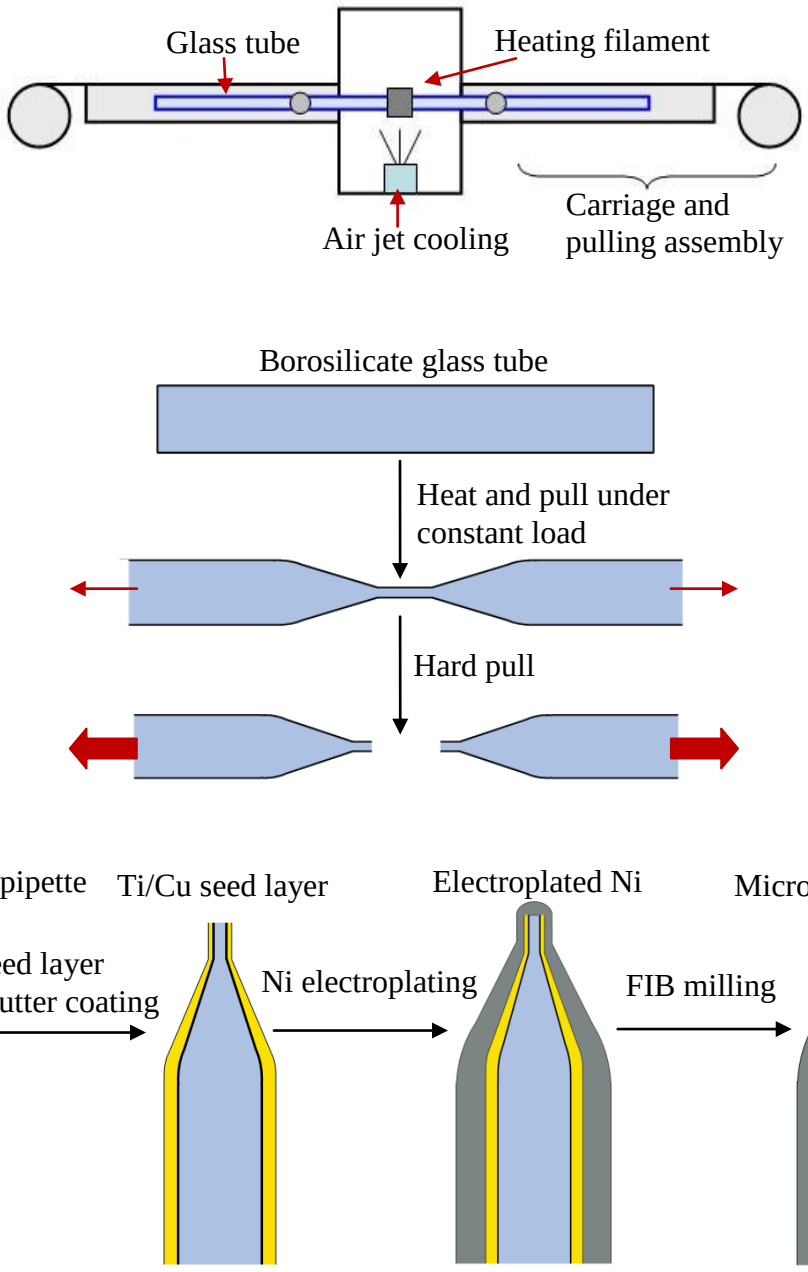

Figure 2.21. Fabrication process flow for glass-metal composite micro/nanonozzles.

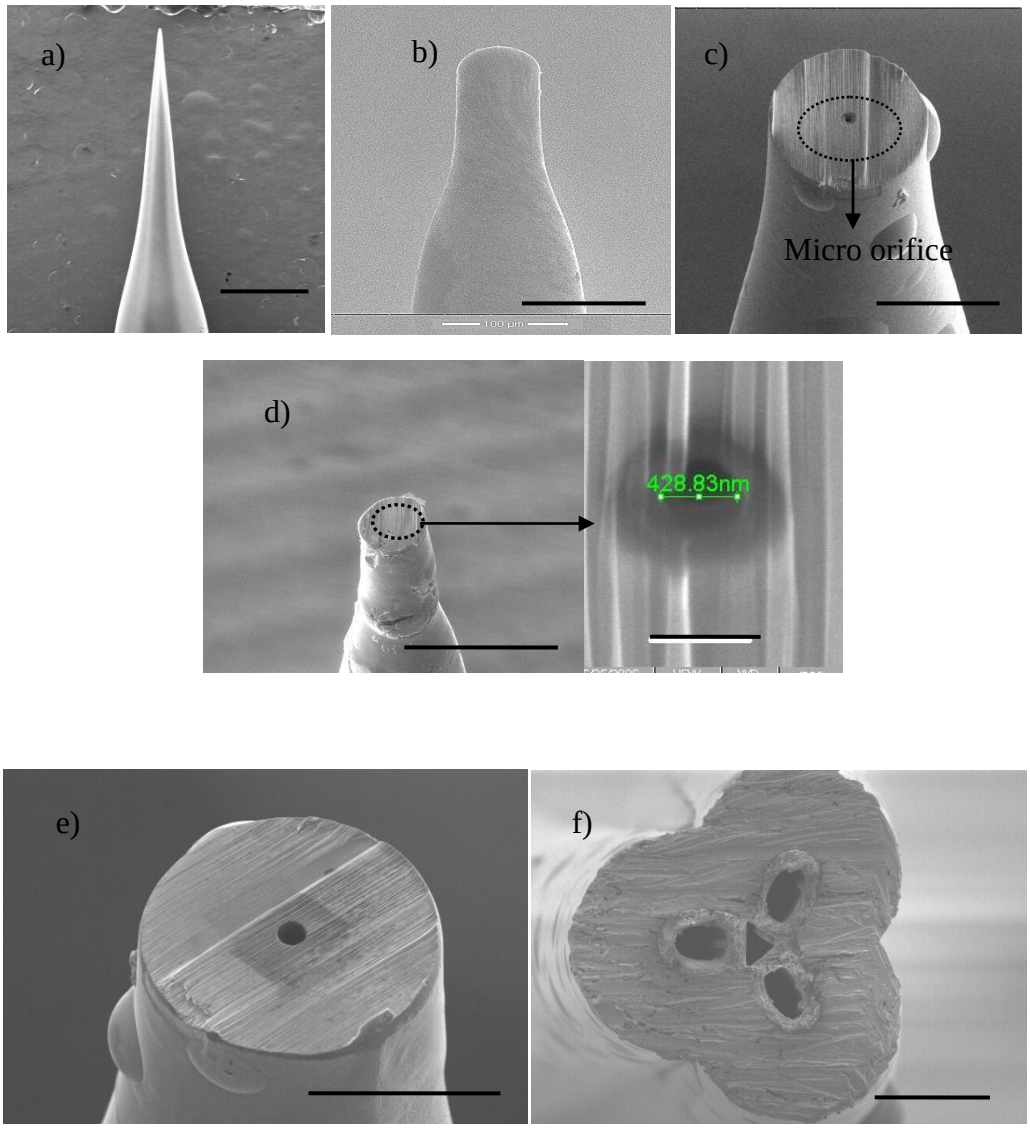

Figure 2.22. a) A glass micropipette pulled using a micropipette puller (scale bar = 50 µm), b) a micronozzle after electroplating with nickel (scale bar = 100 µm), c) a micronozzle after FIB milling to reveal the micro orifice tip (scale bar = 50 µm), d) a 430 nm glass-metal orifice (scale bars = 200 µm and 500 nm), e) an 8 µm diameter nickel micronozzle with glass layer etched away (scale bar = 50 µm), and f) a 3-barrel glass-nickel micronozzle (scale bar = 50 µm).

2.2.2.2 Testing and characterization

Burst pressures

The burst pressure for pulled glass capillaries (inner diameter (I.D.) = 1 μm) sans the nickel reinforcement was estimated to be 10000 psi using the Barlow formula (Equation 2.4). Upon empirical investigation, it was discovered that the glass capillaries fractured at pressures much below the predicted values. This premature failure could be attributed to the microcracks and local stress concentrations contained in the pulled glass micropipette tips resulting from the pulling process. Furthermore, the glass tips were very delicate and presented handling issues during the packaging steps without the metal layer. Nickel reinforcement of the glass pipettes helped overcome the pressure-withstanding and handling issues very effectively. With the metal reinforcement, the glass nozzles were observed to withstand pressures up to 1500 psi (10.5 MPa) (the maximum pressure generation capacity of the fluidic apparatus at the time of testing).

Liquid micro/nano jet generation

The glass-metal composite micro/nanonozzles were interfaced with the high-pressure generation apparatus, as discussed for the silicon micro/nanonozzles (Figure 2.23). Pressures ranging from 50 to 1500 psi were applied to generate butane and propane jets from nozzles with inner dimensions spanning from 450 nm to 10 μm.

Micro/nanojet characteristics, similar to the jets issued from silicon micro/nanonozzles were observed. Measurements for the breakup distances and velocities were made in the same fashion. Figure 2.24 illustrates a shadowgraph image of a stable 1.5 μm propane jet obtained by applying a driving pressure of 1000 psi (6.9 MPa). The

breakup distance of the jet was 150 μm and the velocity was estimated to be approximately 66 m/s.

Testing with evaporative fluids resulted in cooling of the jets due to Joule-Thomson and evaporative cooling effects. The condensation of moisture and dust in the atmosphere resulted in ice formation at the tip of the nozzles and led to jet obstruction. The glass-metal nozzles allowed for the incorporation of an induction-based wireless heating system that enabled heating of the nozzles (50 °C) during jet flow experiments. This feature successfully avoided the ice formation (Figure 2.25).

Nanojet formation

A 900 nm propane jet with a velocity of 22 m/s was generated at 1200 psi (Figure 2.26). To our knowledge, this is the first evidence of the generation and visualization of a pressure-driven nanofluidic jet.

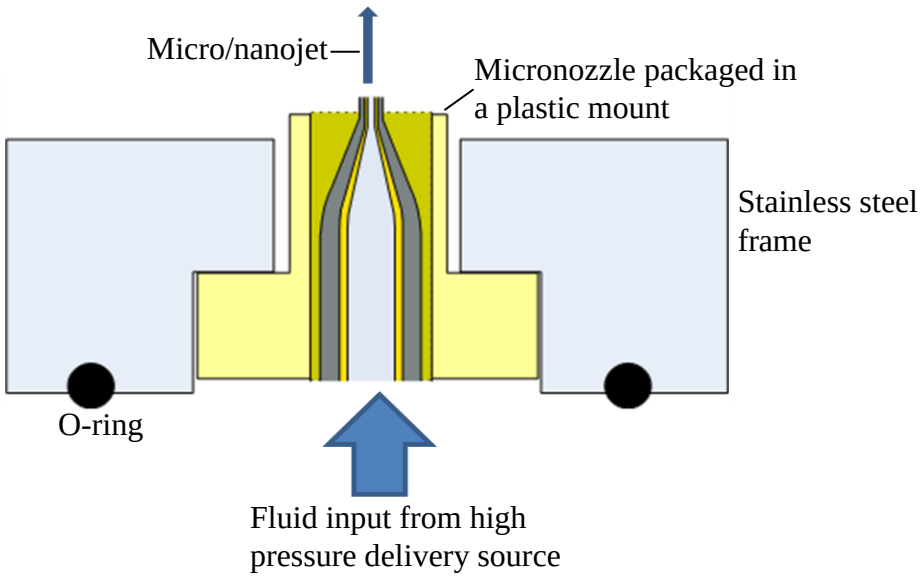

Figure 2.23. A stainless steel frame as a macro-to-micro interface for glass-metal composite micro/nanonozzles.

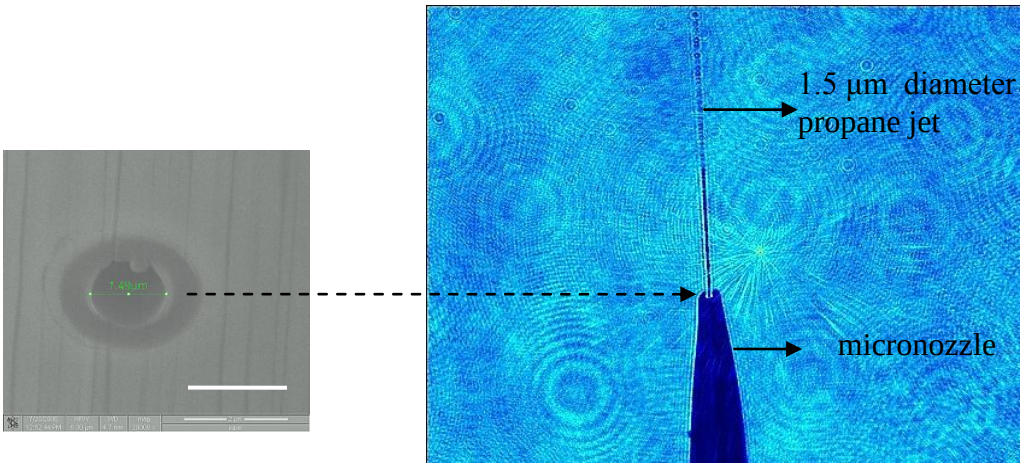

Figure 2.24. A shadowgraph image of a 1.5 µm diameter propane microjet (scale bar = 2 µm).

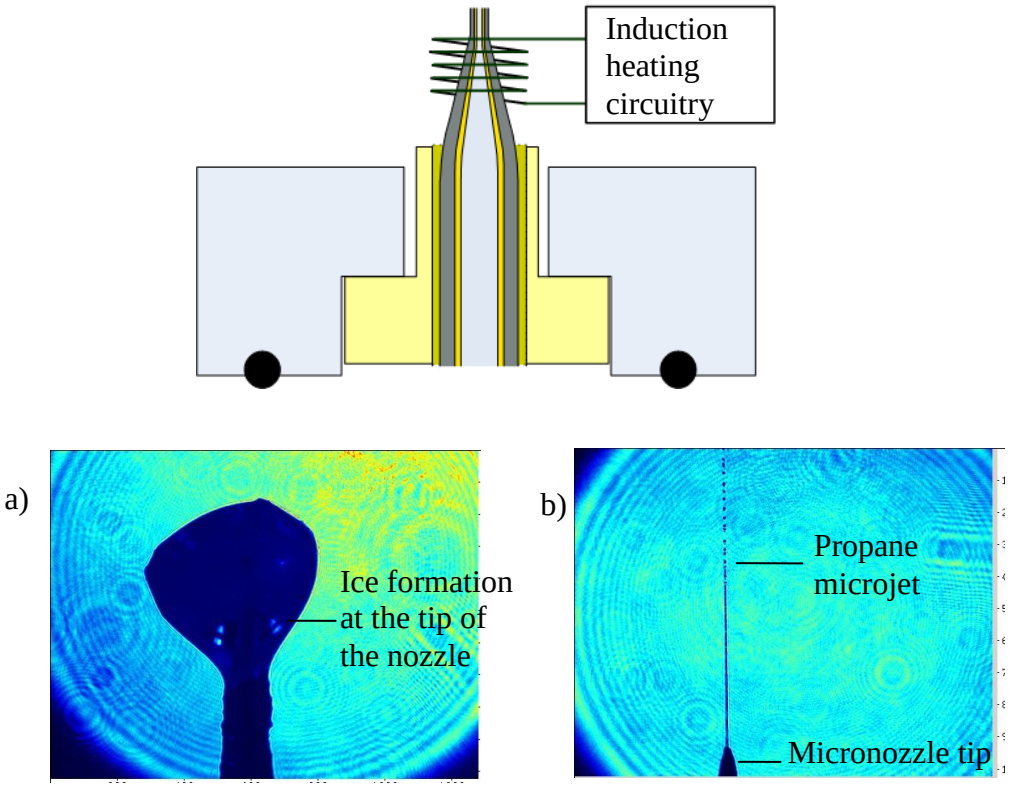

Figure 2.25. Shadowgraph images of, a) ice formation at the tip of the micronozzle, b) a 10 µm diameter propane microjet formed after removal of ice by induction heating of the nozzle.

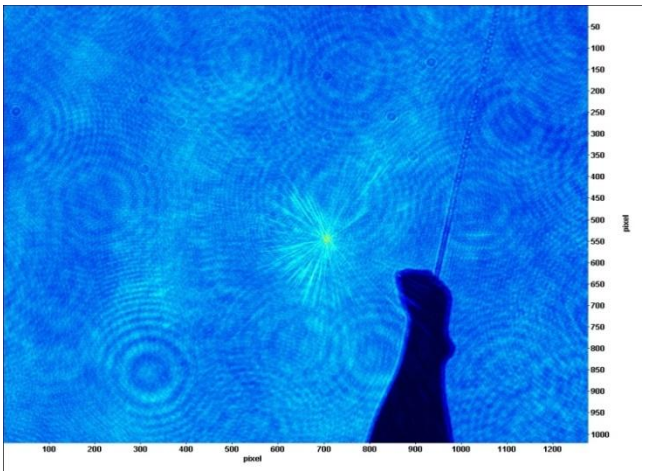

Figure 2.26. A shadowgraph image of a 900 nm propane jet driven at 1200 psi.

2.2.2.3 Discussion of the encountered problems

Even though the feasibility of pressure-driven nanojets was demonstrated, the inconsistency of jet parameters continued to exist. The glass-metal composite nozzles did not help resolve the clogging issue. It was surmised that the working fluids significantly contributed to the contamination. The use of evaporative fluids may have caused the heavier hydrocarbons to be left behind in the nozzle, impeding the jet flow. Conclusive data providing correlation between the different dimensions of the nozzles and their driving pressures, jet velocities, and jet breakup distances could not be obtained, and it was not possible to theorize the jet flow behavior.

2.2.3 Conclusion

The characterization of MEMS-based nozzles with test fluids, liquid butane and liquid propane, confirmed that nanojets could be issued from nanoscale nozzles under high-pressure conditions. But this method was significantly limited by nozzle clogging. On sub-10 μm scales it was challenging to identify or eliminate the source of

contamination. It was concluded that small openings are very sensitive to impurities, and the smallest variability in the system can cause a significant change in the flow property.

2.3 Wet-spinning-based collagen micro/nanofiber extrusion

The final objective of this study was to utilize the micromachined micro/nanonozzles for the development of a wet-spinning system for collagen micro/nanofibers with alterable dimensions. Having established the feasibility of pressure-driven nanofluidic jets, the first wet-spinning approach involved modulation of wet-spun collagen fiber dimensions by controlling the nozzle orifice diameters and using high pressure conditions to extrude collagen jets. But having discovered the nozzle clogging and contamination issues in small-dimension nozzles, an alternate wet-spinning approach using hydrodynamic focusing for controlling the fiber dimensions and geometries was developed.

2.3.1 Modulation of nozzle diameters for control over collagen fiber dimensions

In this approach, the inner diameters of the nozzles were varied to control the dimensions of the fibers extruded from it.

2.3.1.1 Apparatus design

The collagen fiber wet-spinning apparatus consisted of a micromachined glass-metal composite micro/nanonozzle (I.D.: 5, 10, and 20 um) interfaced with a stainless steel pressurized reservoir, as shown in Figure 2.27. The nozzles were packaged in plastic frames fabricated using stereolithography prior to assembly with the fluidic apparatus, as described in the previous section. The reservoir (volume = 100 μl) was connected to a nitrogen tank and a pressure gauge for controlled application of pressure. The nozzle exit

orifice was immersed in a coagulant wet-spinning buffer (WSB) medium (10 wt% poly (ethylene glycol) Mw = 35000, 4.14 mg/mL monobasic sodium phosphate, 12.1 mg/mL dibasic sodium phosphate, 6.86 mg/mL TES (N-tris (hydroxymethyl) methyl-2-aminoethane sulfonic acid sodium salt), 7.89 mg/mL sodium chloride, pH =8.0) [42].

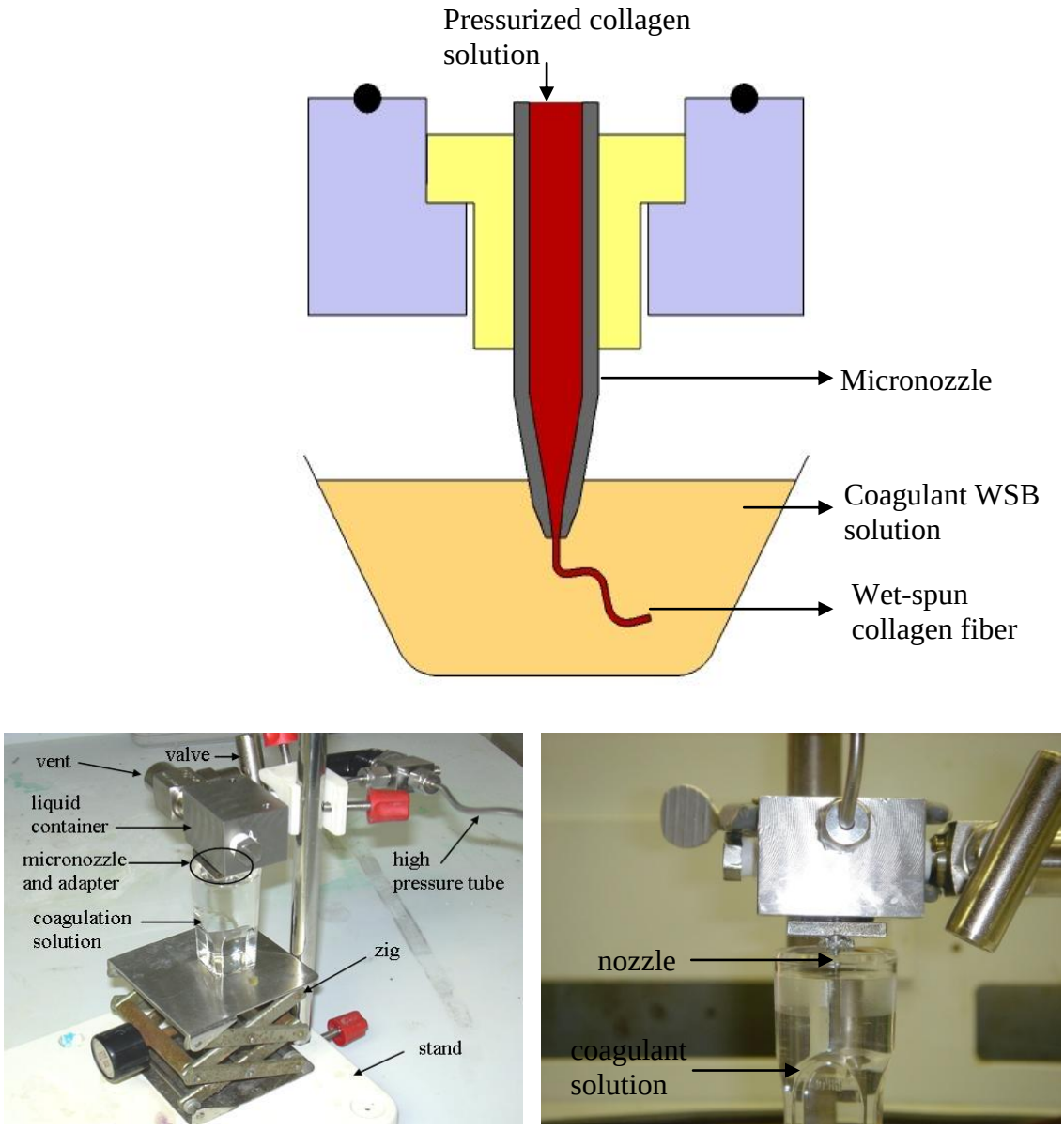

Figure 2.27. Micromachined-nozzle-based collagen micro/naofiber wet-spinning apparatus.

2.3.1.2 Wet-spinning tests and results

Collagen type I, obtained from rat tail tendons and solubilized in 10 mM HCl was utilized for the fiber production. The collagen solution (concentration= 2 mg/ml) was loaded into the high-pressure reservoir. The reservoir was pressurized to the desired level to extrude collagen jets into the WSB media. The diffusion of alkaline WSB solution into the generated acidic collagen jet created a neutral pH causing the viscosity of the neutralized collagen to increase nearly 300-fold and the collagen filaments to precipitate as fibers. For fiber collection, the WSB solution containing the fibers was passed through a filter paper with a nominal pore diameter of 800 nm and cleaned in deionized (DI) water before drying. The filtered collagen fibers were then observed under the SEM (Hitachi).

Nozzles with I.D. 5, 10, and 20 μm were used for these experiments. The produced dry fibers were observed to be ribbon-shaped. For 20 μm diameter nozzles, fibers with a width of 8.5 μm and a thickness of 2 μm were produced for driving pressures of 600-1000 psi (4-6.9 MPa). The smallest fibers fabricated by this method were yielded by a 10 μm orifice nozzle at 1000 psi (6.9 MPa) and were 2 μm in width and 400 nm in thickness (Figure 2.28). Sub-10 μm nozzles failed to produce any discernible fibers.

2.3.1.3 Limitations of the approach

After fiber-spinning, clusters of fibers of lengths varying from a few millimeters to approximately 2 centimeters were observed. Frequent fiber breakages and nozzle clogging resulting from gel formation at the interface of the nozzle tip and the coagulant solution were observed. The clogging issue was observed to intensify with decreasing

orifice diameter, being the most pronounced on sub-10 μm scales. To overcome this, an alternate approach involving hydrodynamic focusing was adopted to control the fiber dimensions.

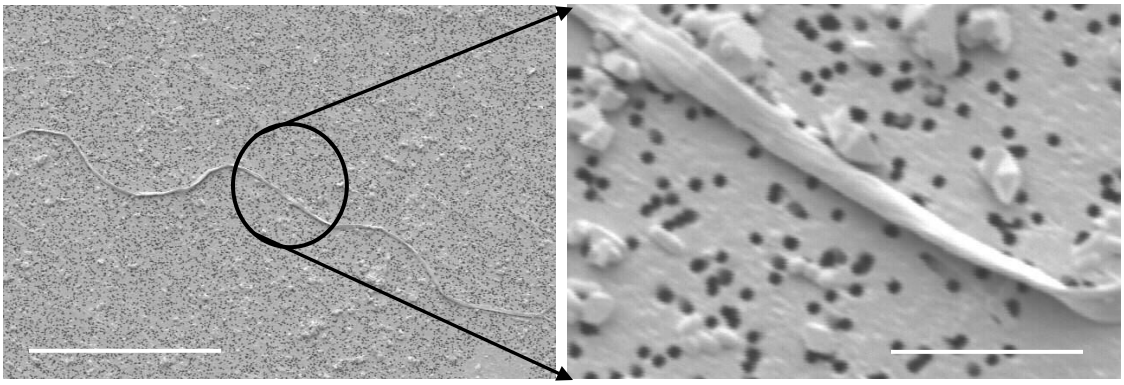

Figure 2.28. A 2-μm wide wet-spun collagen microfiber fabricated using a pressurized 10 μm nozzle (scale bars = 100 μm and 10 μm).

2.3.2 Hydrodynamic focusing for control over collagen fiber dimensions and geometries

The principle of hydrodynamic focusing was utilized to address the nozzle-clogging concern. Hydrodynamic focusing is characterized by coaxial laminar flows of a core and a sheath fluid. The sheath fluid flow constricts and compresses the flow of the core fluid using fluid dynamic forces, and its flow rate can be used to control the diameter of the core fluid jet. The sheath flow essentially acts as a virtual nozzle with fluidic walls for the core fluid jet. This approach has been used in applications such as cell cytometry [43] and fluid mixing [44]. This approach has also been demonstrated for the modulation of dimensions of chitosan and alginate microfibers [45-48]. Hydrodynamic focusing has been applied for creating localized pH gradients and studying their influence on the self-assembly of collagen fibrils [49].

This strategy was adopted for the fabrication of collagen fibers. Solubilized collagen in 10 mM HCl (concentration = 5 mg/ml) constituted the core stream, and the coagulant WSB solution was used as the sheath stream to compress the collagen jets and initiate the self-assembly of the collagen molecules into fibrils simultaneously. With this approach, it was feasible to use nozzles with larger diameters (>75 um) alleviating the clogging issues.

Generally, the mechanical properties and the dimensions of wet-spun fibers are influenced by two phenomena, hydrodynamic focusing and jet stretch. Hydrodynamic forces during the spinning process cause the fibrils to align in the direction of the flow and also reduce the diameter of the fiber. The generated fibers are usually collected using a motorized rotating setup and optionally subjected to a mechanical annealing process involving application of a longitudinal tensile load on the fibers. The tension applied to the fibers in these fashions causes a jet-stretch phenomenon resulting in the directional alignment of the fibrillar network to be further enhanced as compared to that obtained purely by hydrodynamic forces. It also results in smaller fiber dimensions. Since the goal of this research was to study the influence of the hydrodynamic focusing effect in isolation, a fiber collection setup was omitted from the wet-spinning system. The fibers exiting from the tube flowing the sheath fluid were directly immersed in a dish tin containing the WSB solution.

2.3.2.1 Apparatus design

The hydrodynamic focusing apparatus consisted of a micromachined glass-metal composite micronozzle for flowing the core collagen stream. The micronozzle was integrated with a T-fitting for the incorporation of a coaxial sheath flow of WSB solution around the collagen jet (Figure 2.29). Both the collagen and WSB inlets were interfaced with syringe pumps to control the flow rates of the solutions. The core micronozzle diameters used were 75, 150, and 250 µm. The diameter and length of the outer tube flowing WSB solution were 1.5 mm and 6 cm respectively.

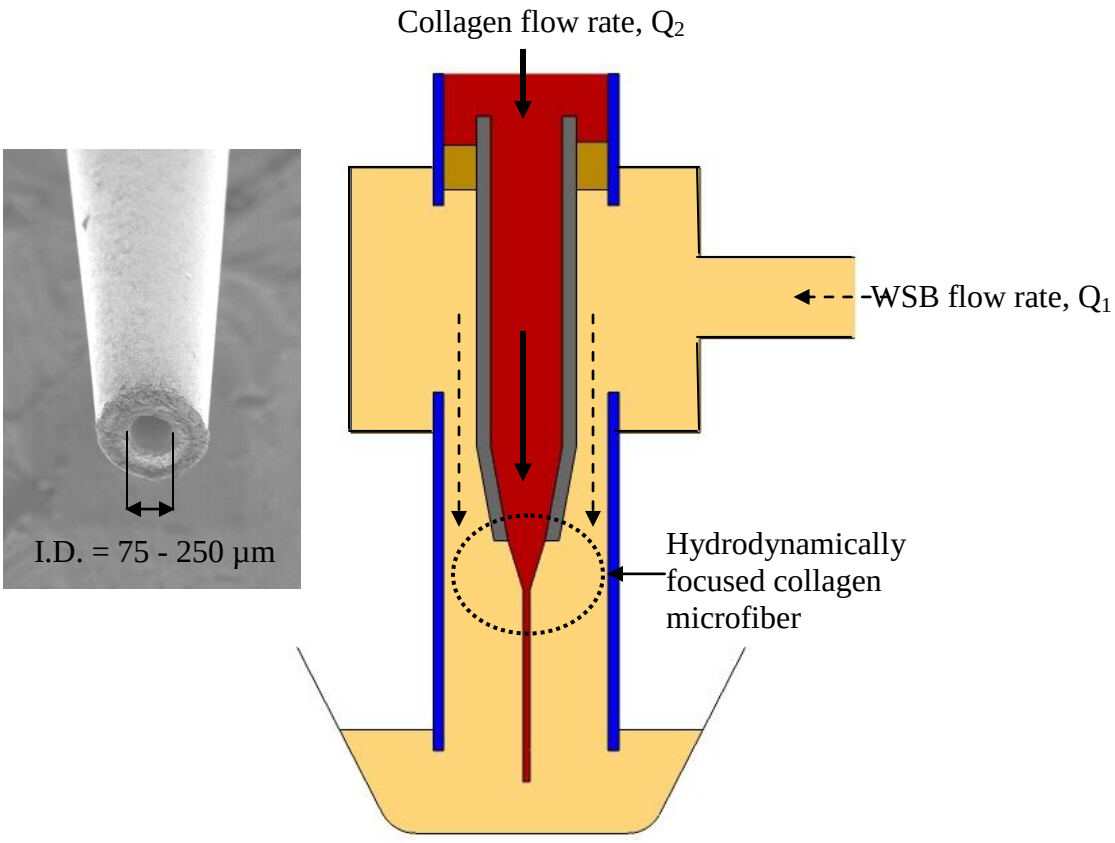

Figure 2.29. A collagen microfiber wet-spinning apparatus with hydrodynamic focusing.

2.3.2.2 Hydrodynamic focusing theory

A 2D model for hydrodynamic focusing was developed by Lee et al employing potential flow theory [50]. A schematic for the geometry utilized for this model is illustrated in Figure 2.30. The theory assumed the core and sheath flows to be laminar and the diffusion between the two flows to be negligible. By applying conservation of mass theory to the given flow configuration, Equations 2.5 and 2.6 were obtained.

$$v_2 . D_2 = v_c . d \tag{2.5}$$

$$\rho_a . v_a . D_a = \rho_1 . v_1 . D_1 + \rho_2 . v_2 . D_2 + \rho_3 . v_3 . D_3 \tag{2.6}$$

Where, ρ_a, ρ_1, ρ_2, and ρ_3 are densities of the fluids, v_a, v_1, v_2, and v_3 are flow velocities, and D_a, D_1, D_2, and D_3 are diameters of the respective areas.

Also, if $d << D_a$, the focused jet velocity, v_c could be assumed to be the maximum velocity of the jet through D_a.

$$v_c = 1.5 v_a \tag{2.7}$$

From Equations, 2.5, 2.6, and 2.7, the width of the focused jet can be derived as expressed in Equation 2.8.

$$d = \frac{\rho_a . D_a}{1.5 \left(\frac{\rho_1 . v_1 . D_1}{v_2 . D_2} + \frac{\rho_3 . v_3 . D_3}{v_2 . D_2} + \rho_2 \right)} \tag{2.8}$$

The assumptions of this theory differ from the process of wet-spinning of collagen fibers in several ways. While the theory assumes the fluids to be immiscible, wet-spinning is actually a dynamic process where the two fluids counter-diffuse such that the formation of the fiber gel and the focusing phenomenon occur simultaneously. The theory does not take into account the effects of the viscosities of the two fluids. In wet-spinning, the viscosity of the core fluid increases as the jet evolves in the sheath fluid forming fibers

and influences the geometry and the dimensions of the fibers. Therefore, the presented theory only acts as a guideline for predicting the general trend in a hydrodynamic focusing scenario.

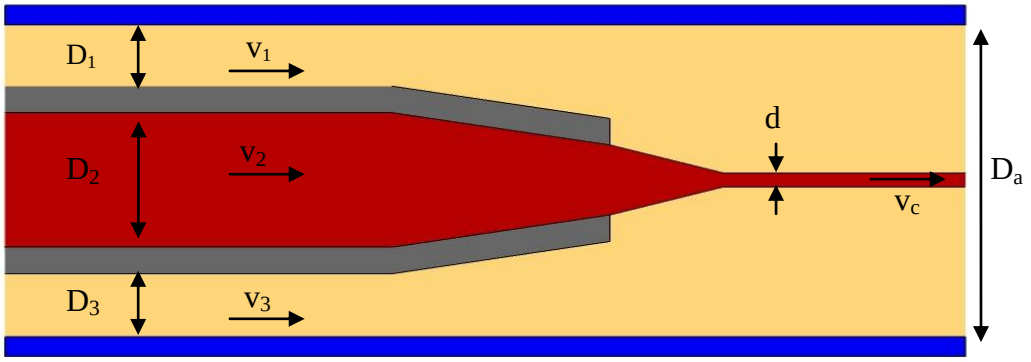

Figure 2.30. A 2D model for hydrodynamic focusing.

2.3.2.3 Wet-spinning tests and results

For wet-spinning with hydrodynamic focusing, flow rates of coaxial laminar flows of collagen and coagulant WSB solutions were varied to control the dimensions of the ensuing fibers. The fibers were collected in an aluminum dish-tin containing 2 ml of WSB solution. The WSB solution was replaced with DI water, and the hydrated fiber dimensions were measured with the fibers immersed in water using a Keyence VHX-600 digital microscope (Figure 2.32). The fibers were observed to be ribbon-shaped. The precise cause for the shape of the fibers was not identified. The flattening may have resulted from chemical or physical aspects of the wet-spinning process. It has been reported that native collagen fibrils self-assemble to form fibers of various sizes and shapes. Depending on the origin of the tissue, these fibers are either cord-shaped (circular cross-section) or tape-shaped (rectangular cross-section) [41]. This demonstrates that

under certain conditions, the collagen fibrils may have a tendency to self-assemble into ribbon-like fibers. The fiber flattening may also have been a product of an anisotropic stress experienced by the fibers in the flow.

The influence of the flow rates and nozzle dimensions on the wet-spun fibers is shown in Table 2.3 and Figure 2.33. It was observed that increasing the sheath flow rate or decreasing the core flow rate resulted in reduced fiber dimensions. In other words, increasing the sheath-to-core relative flow velocity resulted in finer fiber dimensions. At WSB flow rates greater than 8 ml/min, continuous fiber formation was not observed. Although reducing the nozzle diameters resulted in finer fibers, this effect was not as significant as compared to the influence of the flow rates. For example, fibers issued by a 250 μm nozzle at a collagen flow rate of 0.03 ml/min were smaller than those issued by a 75 μm nozzle at a collagen flow rate of 0.08 ml/min. The finest fiber was delivered by a 75 μm nozzle for a relative flow velocity of 33.3 and had a cross sectional dimension of 28 μm × 5 μm (effective diameter = 13.8 μm). Figure 2.34 compares the measured effective diameters with estimated focused diameters (Equation 2.8). The theoretical model overestimated the fiber dimensions and also displayed a more drastic reduction of fiber diameters with increasing flow velocity ratios as compared to the measured dimensions. Along with the various factors discussed in the previous section, the influence of the nozzle dimensions on the obtained fibers is not considered in the model resulting in larger fiber dimension estimates. Also, the model assumes non-mixing fluids of the same viscosities. The viscosity of the wet-spun collagen jet increases manifold as it evolves through the WSB sheath flow. This factor may contribute to the drastic reduction

in the estimated fiber dimensions with increasing sheath flow rates as compared to a gradual response exhibited by the wet-spun fibers.

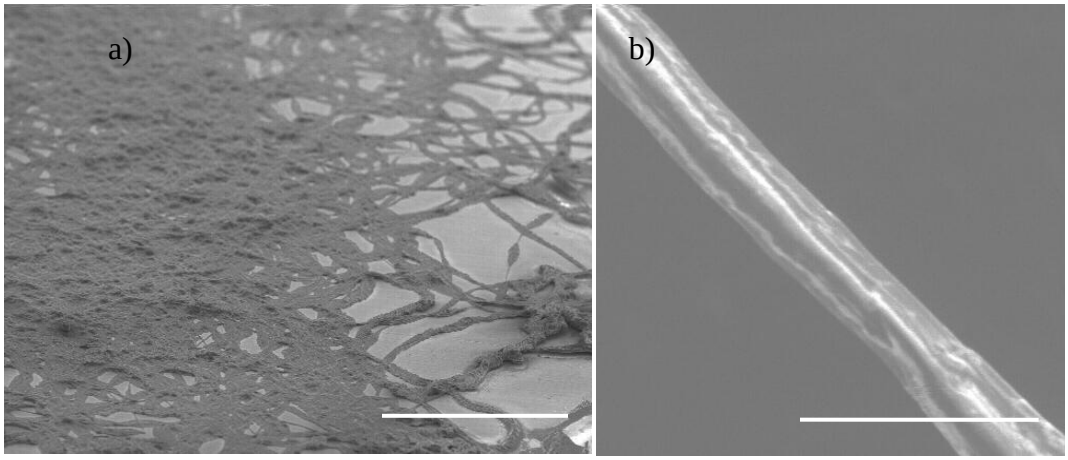

Figure 2.31. SEM images of hydrodynamically focused wet-spun collagen microfibers: a) a fibrous mesh (scale bar = 1 mm), b) an individual fiber (scale bar = 25 µm).

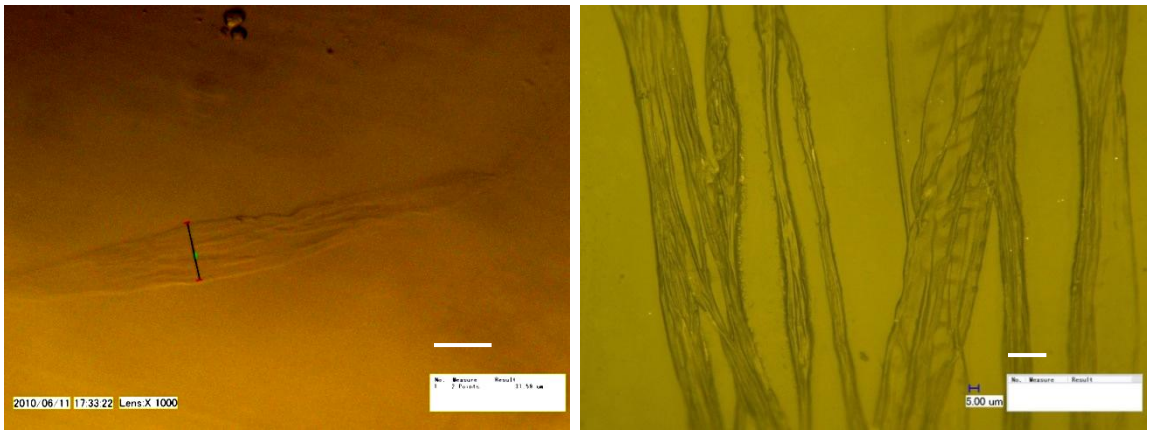

Figure 2.32. Microscope images of hydrodynamically focused wet-spun collagen fibers: a) a hydrated fiber immersed in water (scale bar = 30 µm), b) fibers collected on a rod for partial alignment (scale bar = 15 µm).

Table 2.3. The effect of flow rates and nozzle dimensions on the wet-spun collagen microfibers.

I.D.= 250 µm

Collagen flow rate, ml/min	WSB flow rate, ml/min	v_1/v_2	Wet dimensions, µm		Effective measured diameter, µm	Estimated diameter, µm
			Width	Thickness		
0.08	1	2.5	274±10 (n=5)	5	59.1	285.7
0.08	3	7.5	133±16 (n=5)	5	29.1	117.6
0.08	5	12.5	118±13 (n=5)	5	27.4	74.0
0.08	8	20	79±4 (n=5)	5	22.5	47.6
0.03	1	6.6	143±8 (n=5)	5	30.2	130.4
0.03	3	20	68±6 (n=5)	5	20.8	47.6
0.03	5	33.3	46±5 (n=5)	5	17.1	29.1
0.03	8	53.3	34±4 (n=5)	5	14.8	18.4

Table 2.3 continued

I.D.= 150 µm

Collagen flow rate, ml/min	WSB flow rate, ml/min	v_1/v_2	Wet dimensions, µm		Effective measured diameter, µm	Estimated diameter, µm
			Width	Thickness		
0.08	1	2.5	158±16 (n=5)	5	31.7	285.7
0.08	3	7.5	122±18 (n=5)	5	27.9	117.6
0.08	5	12.5	96±7 (n=5)	5	24.8	74.0
0.08	8	20	73±10 (n=5)	5	21.6	47.6
0.03	1	6.6	113±13 (n=5)	5	26.8	130.4
0.03	3	20	61±6 (n=5)	5	19.8	47.6
0.03	5	33.3	42±6 (n=5)	5	16.5	29.1

Table 2.3 continued

I.D.= 75 µm

Collagen flow rate, ml/min	WSB flow rate, ml/min	v_1/v_2	Wet dimensions, µm		Effective measured diameter, µm	Estimated diameter, µm
			Thickness	Width		
0.08	1	2.5	138±10 (n=5)	5	29.6	285.7
0.08	3	7.5	97±6 (n=5)	5	24.8	117.6
0.08	5	12.5	59±11 (n=5)	5	19.4	74.0
0.03	1	6.6	65±6 (n=5)	5	20.3	130.4
0.03	3	20	41±5 (n=5)	5	16.2	47.6
0.03	5	33.3	30±2 (n=5)	5	13.8	29.1

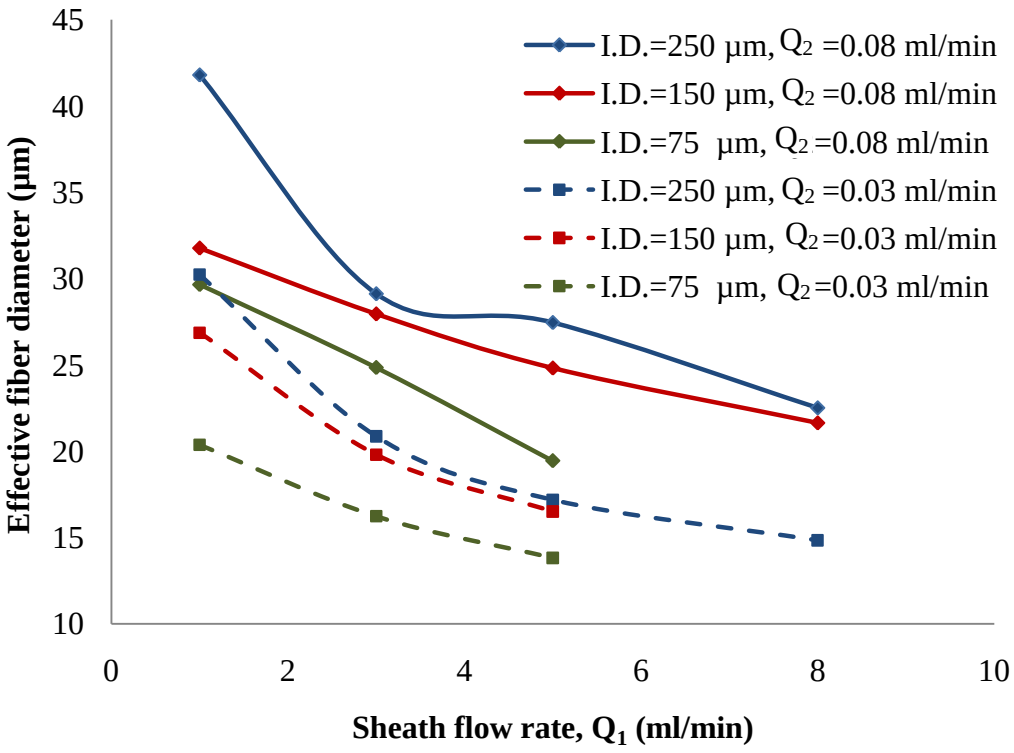

Figure 2.33. Variation of the effective diameter of the hydrodynamically focused collagen fibers with sheath (WSB) flow rates, collagen flow rates, and nozzle dimensions.

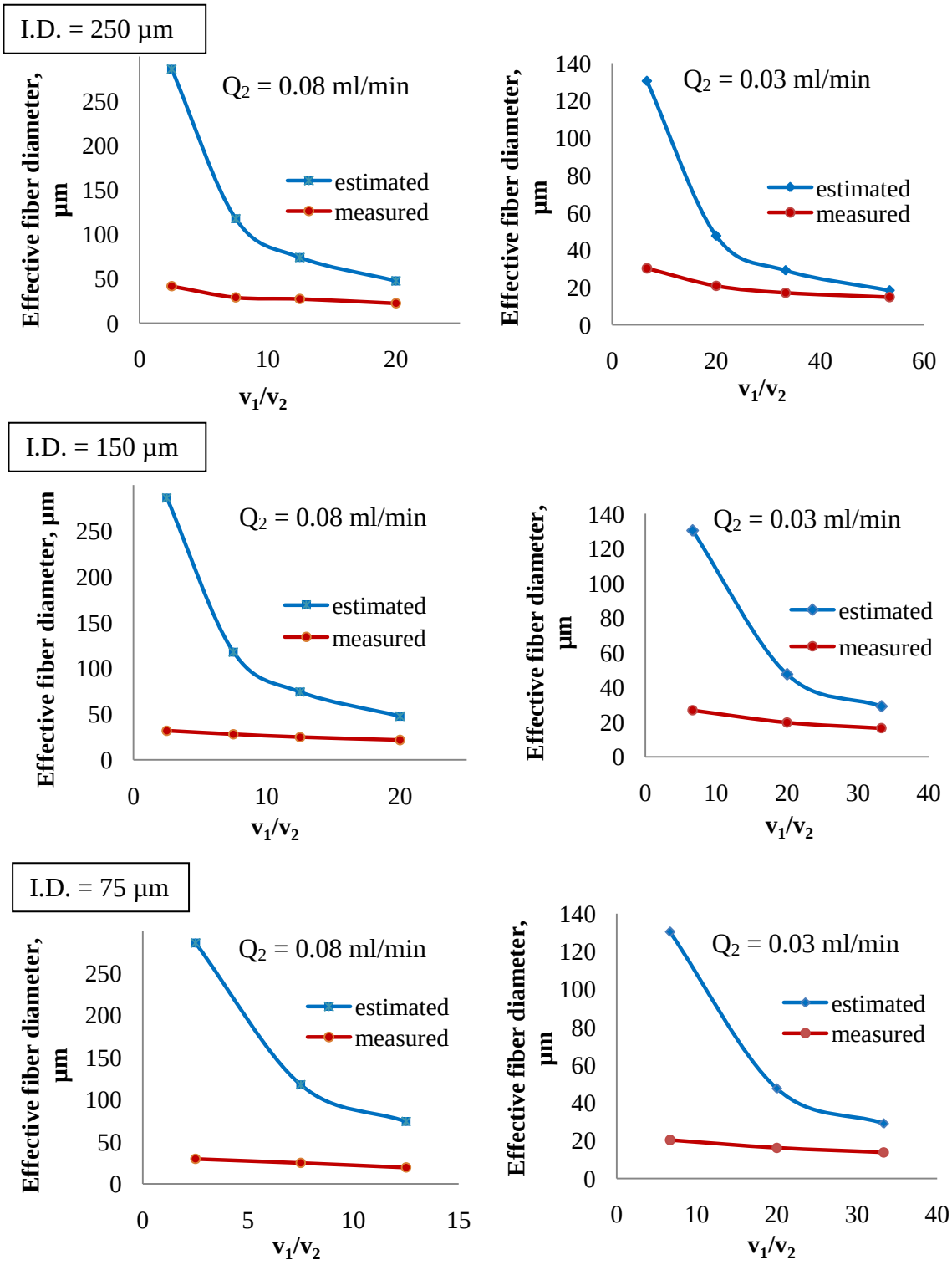

Figure 2.34. Estimated and measured effective diameters of hydrodynamically focused wet-spun collagen fibers for different flow velocity ratios and nozzle diameters.

2.3.2.4 Hydrodynamic focusing for crimped collagen fibers

Various soft tissues in the human body, such as tendons, ligaments, and blood vessels are made up of crimped collagen fiber bundles, as shown in Figure 3.15a. When the tissue comprising such fibers is loaded in tension, the fibers do not contribute significantly to the load bearing at low strains, resulting in a low modulus of elasticity. As the tissue progresses to higher strains, the fiber undulations start to straighten, and the material transitions to a higher modulus of elasticity regime. This results in a characteristic nonlinear elastic behavior and the stress-strain curves for these tissues display toe, heel, and linear regions, as shown in Figure 2.35 [51].

Caves et al. have demonstrated the use of an elastomeric deformable template as a crimping tool for wet-spun collagen fibers [52]. They established the feasibility of embedding such crimped fibers in an elastin matrix to obtain composite materials exhibiting non-linear elastic behavior as observed in native tissues.

When two liquids of significantly different viscosities are flowed together in a hydrodynamic focusing configuration, such that the higher viscosity fluid forms the core, the viscous thread encounters folding when faced with a sudden deceleration. This was demonstrated by Cubaud et al. using silicone oils (relative viscosity between core and sheath fluids > 15) flowing in a microfluidic chip (Figure 2.36) [53]. The source of deceleration of the core fluid was a sudden divergence in the flow channel. In this configuration, the core viscous threads underwent oscillatory instabilities instead of dilating for minimization of viscous dissipation. This phenomenon was also observed by Shin et al. during the wet-spinning of alginate fibers [54]. The core fluid folding was

attributed to its deceleration resulting from the high friction between the sheath fluid and forming solid fibers in the flow.

Crimped collagen fibers could be manufactured directly as a part of the wet-spinning process by using the above cited hydrodynamic effects. Undulations could be introduced in the collagen fibers collected in a dish tin containing WSB solution at certain sheath flow rates (Figure 2.37, Figure 2.38). To achieve these crimped structures, the coaxial flows of collagen and WSB solutions were immersed in the dish tin containing a static WSB solution. During the course of the fiber gel formation, the viscosity of collagen is amplified by approximately 200 times. The formation of viscous collagen fibers and subjecting them to a static fluid and a sudden divergence resulted in a folding instability due to the sudden velocity drop. This phenomenon was typically observed at low WSB flow rates (<3 ml/min) and was most repeatable at a WSB flow rate of 1 ml/min.

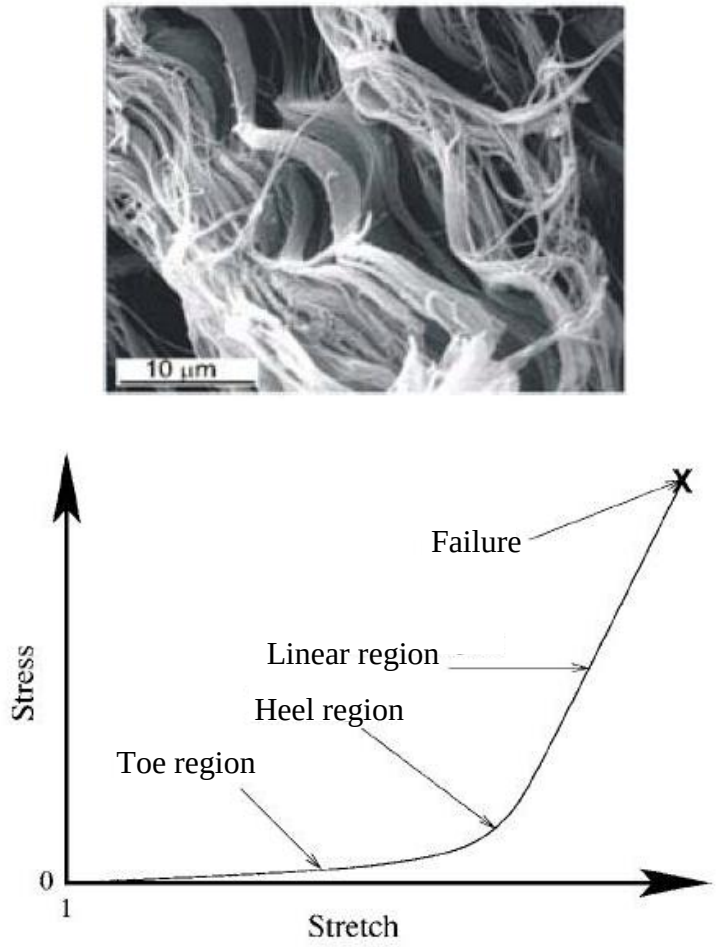

Figure 2.35. a) Crimped structure of collagen fibers in porcine tendons, and b) a representative stress-strain curve for soft tissues with crimped fibers illustrating a transition from a low stiffness to a high stiffness with increasing strains [51].

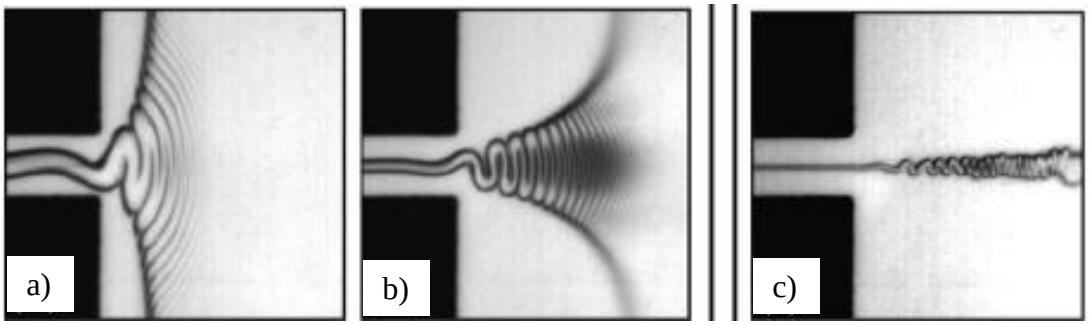

Figure 2.36. Folding instabilities in hydrodynamic focusing of silicone oils with different viscosities and flow rates. This phenomenon is observed when the core fluid viscosity is 15-fold or more greater than the sheath fluid. The ratio of sheath flow rate to core flow rate increases from a) to c) [53].

Although in principle, the relative flow rates of collagen and WSB solutions influence the amplitude and wavelength of these undulations, this effect was not predominantly observed in this study. Since the measurements for hydrated fibers were performed while immersed in water, a precise determination of the undulation geometrical properties was not feasible. The amplitude (a) of the crimps was observed to range from 5-10 μm and the wavelength (λ) ranged from 10-28 μm.

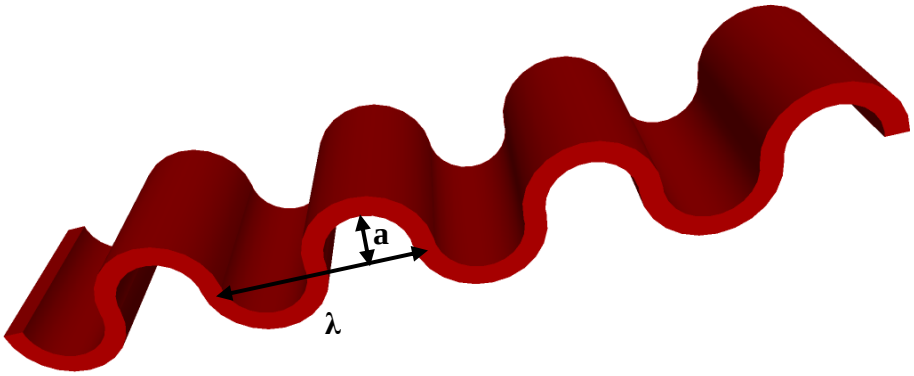

Figure 2.37. Crimped collagen fibers obtained using hydrodynamic focusing. The image shows a folded ribbon-like hydrated fiber in a tilted view.

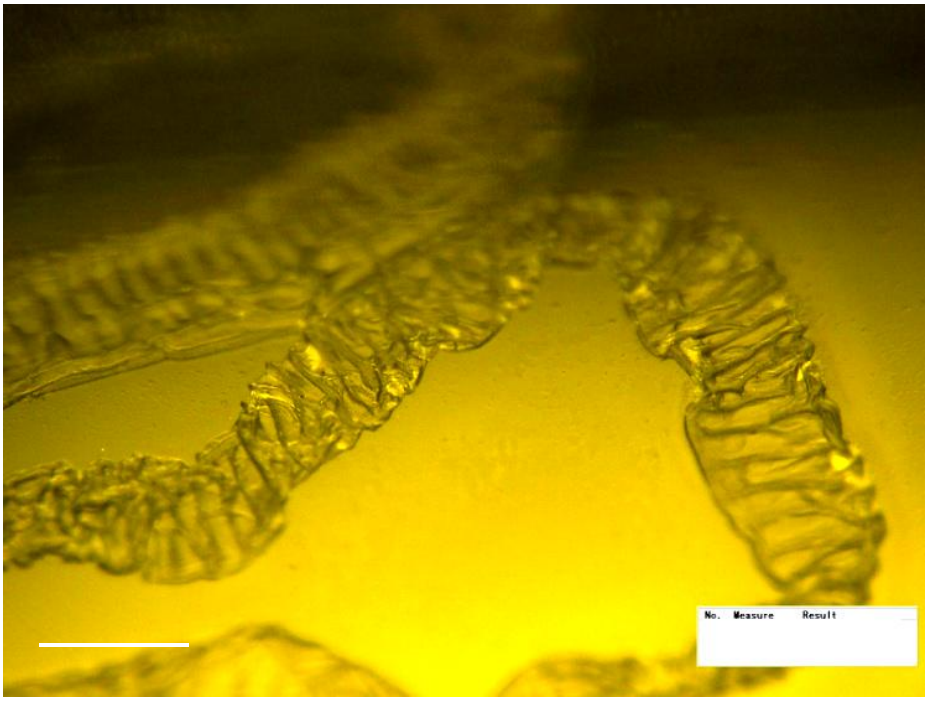

Figure 2.38. Crimped collagen fibers after air drying. The fibers lost distinct undulations but maintained periodic folds (scale bar = 100 µm).

2.3.3 Mechanical characterization of the wet-spun fibers

The mechanical properties of the wet-spun collagen microfibers were evaluated using a dynamic mechanical analysis (DMA) tool (Rheometrics Inc.).

2.3.3.1 Sample preparation

For the ease of handling, fibers with dimensions 50 µm × 20 µm were utilized for the mechanical characterization experiments. Prior to the DMA analysis, the fibers were incubated in a fiber incubation buffer (FIB, 7.89 mg/mL sodium chloride, 4.26 mg/mL dibasic sodium phosphate, 10 mM Tris, pH = 7.4) for 48 hours at 37 °C to facilitate the collagen fibril self assembly and crosslinked in vapor phase glutaraldehyde (0.5 wt% glutaric acid dialdehyde in 1× PBS) for 14 hours. They were then cut into 14 mm long specimens. Each fiber specimen was mounted on a C-shaped plastic frame for

mechanical support and handling, as shown in Figure 2.39a. The ends of the fibers were glued to the top and the bottom horizontal sections of the frame, such that the length of the suspended fiber was 8 mm. The horizontal portions of the plastic frame were clamped to the grips of the sample mount on the DMA equipment. The vertical portion of the frame was then cut to transfer the entire applied tensile load to the fiber. For obtaining properties of hydrated fibers, the sample mount was immersed into a PBS solution bath maintained at 37 ºC for the duration of the applied load. The dimensions of the fibers in the hydrated state were measured microscopically, and input to the DMA tool for the derivation of the stress-strain curves. A loading strain rate of 0.64 % per second was applied longitudinally to each fiber until failure. The stress-strain curves were produced by the DMA tool by measuring the force experienced by the fiber for each unit strain and calculating the engineering stresses utilizing the hydrated cross-sectional area of the fiber.

2.3.3.2 Observations

Three parameters were analyzed from the derived engineering stress-strain curves, as described below:

1. Young's modulus of the material determined by the slope of the stress-strain curve in the elastic regime
2. Ultimate tensile strength or the maximum stress experienced by the material in tension, and
3. Failure strain of the material

For all the parameters, the average and standard deviation were calculated from 4 measurements. The wet-spun collagen fibers exhibited a Young's modulus of 490 ± 50 MPa. The fibers fractured while still in the elastic regime (Figure 2.39b). The fibers

displayed a low failure strain of 8.3 ± 1 %. The ultimate tensile strength of the fibers was observed to be 40 ± 4.6 MPa.

Native collagen fibers display very high stiffness and strength, a property often attributed to the arrangement of the peptide strands in their molecules and the covalent bonds between them. Several studies have been conducted to assess the mechanical properties of collagen fibers extracted from tissues such as tendons. These fibers exhibit an approimate stiffness of 1000 MPa and a strength ranging from 50-100 MPa [55].

The properties of synthetic collagen fibers obtained from extrusion-based methods, such as electrospinning and wet-spinning, vary depending on the processing conditions such as, the collection approach, mechanical annealing of the fibers, and the crosslinking approach. Table 2.4 lists the range of the mechanical properties of engineered fibers as studied by other groups.

The hydrodynamically focused fibers exhibit properties in the range of the engineered fiber properties reported in the literature. The fibers fabricated in this research have favorable hydrodynamic forces that aid in the directional alignment of the collagen fibrils in the longitudinal direction of the fibers, enhancing the mechanical properties. But due to the absence of a fiber collection setup, the fibers do not undergo a further strain-based annealing process. As mentioned earlier, applying a tensile load at the collection stage of the fibers or at a later incubation stage can further enhance the mechanical properties of the fibers and also reduce their dimensions.

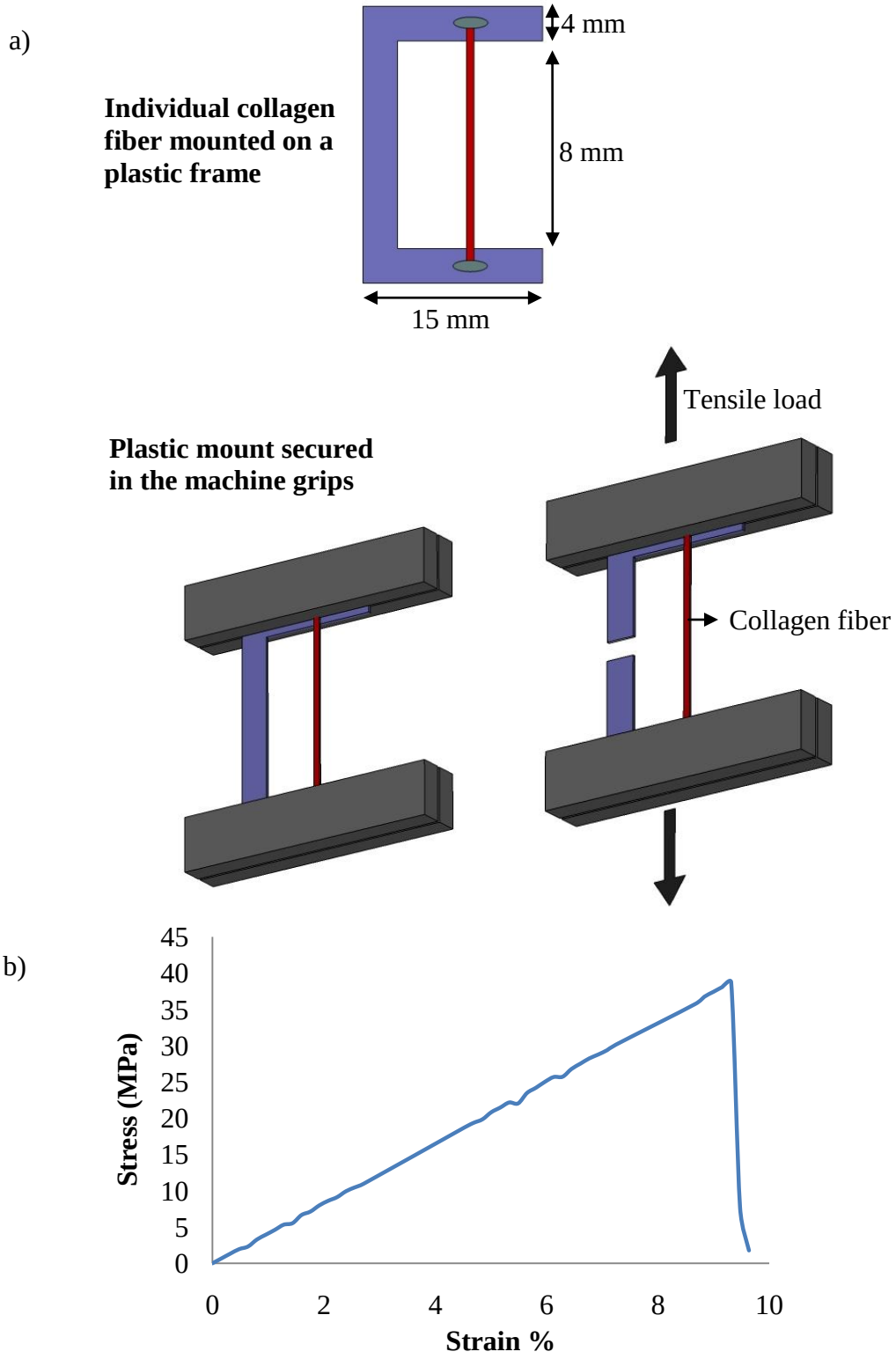

Figure 2.39. Mechanical characterization of wet-spun collagen fibers: a) sample preparation and loading, b) a representative stress-strain curve for 50-µm wide fibers.

Table 2.4. Mechanical properties of hydrodynamically focused fibers, native collagen fibers, and engineered collagen fibers.

Sample	Modulus of elasticity (MPa)	Ultimate tensile strength (MPa)	Failure strain (%)	Reference
Hydrodynamically focused fibers (current study)	490 ± 50 (n=4)	40 ± 4.6 (n=4)	8.3 ± 1 (n=4)	
Native collagen fibers	1000	50-100	10	[55]
Electrospun collagen type I fibers	2820 [low strain modulus (<5 %)]	25	33	[56]
Wet-spun collagen type I fibers (processing methods vary for different reports)	58-895	24-91	7-18	[57-60]

2.4 Conclusion

In this work, a microfluidic system for the generation, visualization, and characterization of pressure-driven micro/nanofluidic jets was developed. As a part of this system, microfabrication strategies for micro/nanonozzles capable of withstanding high pressures were designed. These included a lithographic approach for in-plane silicon micro/nanonozzles and a non-lithographic approach for glass-metal composite micro/nanonozzles. The smallest jet observed was a 900 nm propane jet issued from a glass-metal composite nanonozzle. Although, the feasibility of generating liquid nanojets emanating from nanonozzles under pressure was established using the developed system, contamination in the fluid and the microfluidic apparatus resulted in the obstruction of jet formation. It was concluded that it is very challenging to keep openings smaller than 10

μm free of contamination, and that such small pores respond adversely to the smallest variability in the system.

The pressure-driven microfluidic system was adopted for wet-spinning of collagen fibers for tissue engineering. The dimensions of the fibers could be modulated either by varying the nozzle dimensions or by creating a virtual nozzle using hydrodynamic forces in co-flowing collagen and coagulant WSB solutions. The smallest fiber was achieved using a 10 μm nozzle and had a cross-section of 2 μm × 400 nm. At sheath (WSB) flow rates smaller than 3 ml/min, the hydrodynamic focusing approach could generate crimped collagen fibers believed to be formed by folding instabilities observed in such a configuration.

Although following a standard extrusion-based approach for fiber production offered control over the fiber dimensions and geometries to a certain extent, it appeared challenging to precisely control the spatial layouts of the fiber networks in this fashion. This led to the development of a template-based approach for collagen micro/nanofiber fabrication described in chapter 3.

2.5 References

1. Poole K, Khairy K, Friedrichs J, et al., "Molecular-scale topographic cues induce the orientation and directional movement of fibroblasts on two-dimensional collagen surfaces," Journal of molecular biology, June 2005, 349(2), p 380-386

2. Matthews JA, Wnek GE, Simpson DG, et al., "Electrospinning of collagen nanofibers," Biomacromolecules, Mar 2002, 3(2), p 232-238

3. Rho KS, Jeong L, Lee G, et al., "Electrospinning of collagen nanofibers: Effects on the behavior of normal human keratinocytes and early-stage wound healing," Biomaterials, Mar 2006, 27(8), p 1452-1461

4. Carlisle CR, Coulais C, Guthold M, "The mechanical stress-strain properties of single electrospun collagen type I nanofibers," Acta Biomaterialia, Aug 2010, 6(8), p 2997-3003

5. Buttafoco L, Kolkman NG, Engbers-Buijtenhuijs P, et al., "Electrospinning of collagen and elastin for tissue engineering applications," Biomaterials, Feb 2006, 27(5), p 724-734

6. Matthews JA, Boland ED, Wnek GE, et al., "Electrospinning of collagen type II: A feasibility study," Journal of bioactive and compatible polymers, Mar 2003, 18(2), p 125-134

7. Zeugolis DI, Khew ST, Yew ESY, et al., "Electro-spinning of pure collagen nano-fibres - Just an expensive way to make gelatin?," Biomaterials, May 2008, 29(15), p 2293-2305

8. Schimpf WC, Rodriguez F, "Fibers from regenerated collagen," Industrial & engineering chemistry product research and development, 1977, 16(1), p 90-92

9. Dunn MG, Avasarala PN, Zawadsky JP, "Optimization of extruded collagen-fibers for ACL reconstruction," Journal of biomedical materials research, Dec 1993, 27(12) p 1545-1552

10. Zeugolis DI, Paul GR, Attenburrow G, "Cross-linking of extruded collagen fibers-A biomimetic three-dimensional scaffold for tissue engineering applications," Journal of biomedical materials research part A, Jun 2009, 89A(4), p 895-908

11. Pins GD, Huang EK, Christiansen DL, et al., "Effects of static axial strain on the tensile properties and failure mechanisms of self-assembled collagen fibers," Journal of applied polymer science, Mar 1997, 63(11), p 1429-1440

12. Wang, Ming-Che; Pins, George D.; Silver, Frederick H., "Collagen fibres with improved strength for the repair of soft tissue injuries," Biomaterials, Jun 1994,

15(7), p 507-512

13. Zeugolis, D.I. (Tissue Modulation Laboratory, National University of Singapore, 117510 Singapore, Singapore); Paul, R.G.; Attenburrow, G., "Factors influencing the properties of reconstituted collagen fibers prior to self-assembly: Animal species and collagen extraction method," Journal of Biomedical Materials Research - Part A, Sept 2008, 86(4), p 892-904

14. Caves JM, Kumar VA, Wen J, et al., "Fibrillogenesis in Continuously Spun Synthetic Collagen Fiber," Journal of biomedical materials research part b-applied biomaterials, Apr 2010, 93B(1), p 24-38

15. Z. U. A. Warsi, "Fluid dynamics: theoretical and computational approaches," CRC Press, 2006

16. E. N. Wang; L. Zhang; L. Jiang; J. -M Koo and J. G. Maveety; E. A. Sanchez, K. E. Goodson and T. W. Kenny; "Micromachined Jets for Liquid Impingement Cooling of VLSI Chips"; Journal of Microelectromechanical systems, 2005, 13(5), p 833-842

17. G. H. Wang, Z. Y. Zhou, Y. Y. Feng and X. Y. Ye, "A single-nozzle microjet for drug delivery," Proceedings of the International Symposium on Test and Measurement, 2003, p 145-148

18. L. Palm, L. Wallman, T. Laurell and J. Nilsson, "Development and characterization of silicon micromachined nozzle units for continuous ink jet printers," Journal of Imaging Science and Technology, 2000, 44(6), p 544-551

19. Fletcher, D.A.; Palanker, D.V. "Pulsed liquid microjet for microsurgery,"Applied Physics Letters, March 2001, 78(13), p 1933-5

20. Moseler, M.; Landman, U.; "Formation, stability, and breakup of nanojets"; Science, Aug. 2000, 289(18), p 1165-9

21. Eggers, Jens ; "Dynamics of liquid nanojets"; Physical Review Letters, Aug 2002m 89(8), p 084502/1-084502/4

22. Voigt, J.; Shi, F.; Edinger, K.; Guthner, P.; Rangelow, I.W.; "Nanofabrication with scanning nanonozzle 'Nanojet'"; Microelectronic Engineering, September 2001, 57-58, p 1035-1042

23. Ling Wang; Stevens, R.; Malik, A.; Rockett, P.; Paine, M.; Adkin, P.; Martyn, S.; Smith, K.; Stark, J.; Dobson, P.; "High-aspect ratio silica nozzle fabrication for nano-emitter electrospray applications"; Microelectronic Engineering, May-Aug. 2007, 84(5-8), , p 1190-3

24. Farooqui, M.M.; Evans, A.G.R.; "Microfabrication of submicron nozzles in silicon nitride"; Journal of Microelectromechanical Systems, , June 1992, 1(2), p 86-8

25. Shikida, M.; Hasada, T.; Sato, K.; "Fabrication of a hollow needle structure by dicing, wet etching and metal deposition"; Journal of Micromechanics and Microengineering, Oct. 2006, 16(10), p 2230-9

26. Brazzle, J.D.; Papautsky, I.; Frazier, A.B., "Fluid-coupled hollow metallic micromachined needle arrays," Proceedings of the SPIE - The International Society for Optical Engineering, 3515, p 116-24

27. Wang, Shengnian; Zeng, Changchun; Lai, Siyi; Juang, Yi-Je; Yang, Yong; Lee, L. James; "Polymeric nanonozzle array fabricated by sacrificial template imprinting"; Advanced Materials, May 2005, 17(9), p 1182-1186

28. Choi, Y.; McClain, M.A.; LaPlaca, M.C.; Frazier, A.B.; Allen, M.G., "Three dimensional MEMS microfluidic perfusion system for thick brain slice cultures," Biomedical Microdevices, Feb 2007, 9(1), p 7-13

29. Marc, Madou, "Fundamentals of microfabrication: the science of miniaturization," 2nd edition, CRC Press, 2002

30. Christopher L. Muhlstein, Stuart B. Brown, "Mechanical properties of structural films,", American Society for Testing and Materials, 2001

31. Joseph R. Davis, "Handbook of thermal spray technology," ASM International. Thermal Spray Society Training Committee

32. http://www.maropolymeronline.com, accessed in July 2010

33. Robert Osiander, M. Ann Garrison Darrin,John Champion, "MEMS and Microstructures in aerospace applications," CRC press 2006

34. Mair Zamir, "The physics of pulsatile flow," Springer, 2000

35. R. K. Shah, Dušan P. Sekulić, "Fundamentals of heat exchanger design," John Wiley and Sons, 2003

36. Deal, B.E.; Grove, A.S., "General relationship for the thermal oxidation of silicon," Journal of Applied Physics, Dec. 1965, 36(12), p 3770-3778

37. Eggers, J., Villermaux, E., "Physics of liquid jets," Reports on Progress in Physics, Mar 2008, 71(3), p 1-79

38. Wilson, K.R.; Rude, B.S.; Smith, J.; Cappa, C.; Co, D.T.; Schaller, R.D.; Larsson, M.; Catalano, T.; Saykally, R.J., "Investigation of volatile liquid surfaces by

synchrotron x-ray spectroscopy of liquid microjets," Review of Scientific Instruments, Mar 2004, 75(3), p 725-36

39. "Machinery's handbook for machine shop and drafting-room: a reference book on machine design and shop practice for the mechanical engineer, draftsman, toolmaker and machinist," The Industrial press, 1915

40. S. P. Lin, Sung-Piau Lin, "Breakup of liquid sheets and jets," Cambridge University Press, 2003

41. Ushiki T, "Collagen fibers, reticular fibers and elastic fibers. A comprehensive understanding from a morphological viewpoint," Archives of histology and cytology, Jun 2002, 65(2), p 109-126

42. Caves, J., "Architecturally defined scaffolds from synthetic collagen and elastin analogues for the fabrication of bioengineered tissues," Wallace H. Coulter Department of Biomedical Engineering. 2008, Georgia Institute of Technology: Atlanta

43. Gawad S, Schild L, Renaud P, "Micromachined impedance spectroscopy flow cytometer for cell analysis and particle sizing," Lab on a chip, 2001, 1(1), p 76-82

44. Park, Hye Yoon; Qiu, Xiangyun; Rhoades, Elizabeth; Korlach, Jonas; Kwok, Lisa W.; Zipfel, Warren R.; Webb, Watt W.; Pollack, Lois, "Achieving uniform mixing in a microfluidic device: Hydrodynamic focusing prior to mixing," Analytical Chemistry, July 2006, 78(13), p 4465-4473

45. Yeh, Chia-Hsien; Lin, Po-Wen; Zhao, Qiaole; Chou, Tsung-Che; Lin, Yu-Cheng, "Application of microfluidic system to construct cross-linked chitosan microfibers by PDMS chip," 4th IEEE International Conference on Nano/Micro Engineered and Molecular Systems, NEMS 2009, p 904-906

46. Yeh, Chia-Hsien; Lin, Po-Wen; Lin, Yu-Cheng, "Chitosan microfiber fabrication using a microfluidic chip and its application to cell cultures," Microfluidics and Nanofluidics, Jan 2010, 8(1), p 115-121

47. Kim, Byung; Kim, Intae; Choi, Wooseok; Kim, Sung Won; Kim, Joosung; Lim, Geunbae, "Fabrication of cell-encapsulated alginate microfiber scaffold using microfluidic channel," Journal of Manufacturing Science and Engineering, Transactions of the ASME, Apr 2008, 130(2), p 0210161-0210166

48. Shin S, Park JY, Lee JY, et al., "On the fly continuous generation of alginate fibers using a microfluidic device," Langmuir, Aug 2007, 23(17), p 9104-9108,

49. Köster, Sarah; Leach, Jennie B.; Wong, Joyce Y.; Pfohl, Thomas, "Microaligned collagen matrices by hydrodynamic focusing: Controlling the pH-induced self-assembly," Materials Research Society Symposium Proceedings, 2005, 898, p 86-91

50. Gwo-Bin Lee; Chen-I Hung; Bin-Jo Ke; Guan-Ruey Huang; Bao-Herng Hwei; Hui-Fang Lai, "Hydrodynamic focusing for a micromachined flow cytometer," Transactions of the ASME. Journal of Fluids Engineering, Sept 2001, 123(3), p 672-9

51. Freed, Alan D.; Doehring, Todd C., "Elastic model for crimped collagen fibrils," Source: Journal of Biomechanical Engineering, Aug 2005, 127(4), p 587-593

52. Caves, Jeffrey M.; Kumar, Vivek A.; Xu, Wenjun; Naik, Nisarga; Allen, Mark G.; Chaikof, Elliot L.; Allen, "Microcrimped collagen fiber-elastin composites," Advanced Materials, May 2010, 22(18), p 2041-2044

53. Cubaud, T.; Mason, T.G., "Folding of viscous threads in diverging microchannels," Physical Review Letters, Mar 2006, 96(11), p 114501/1-4

54. Shin, Su-Jung; Park, Ji-Young; Lee, Jin-Young; Park, Ho; Park, Yong-Doo; Lee, Kyu-Back; Whang, Chang-Mo; Lee, Sang-Hoon, ""On the fly" continuous generation of alginate fibers using a microfluidic device," Langmuir, Aug 2007 23(17), p 9104-9108

55. Joon Bu Park, Roderic S. Lakes, "Biomaterials: an introduction," Springer, 2007

56. C.R. Carlisle, C. Coulais 1, M. Guthold, "The mechanical stress–strain properties of single electrospun collagen type I nanofibers," Acta Biomater. Aug 2010, 6(8), p 2997-3003

57. Caves, Jeffrey M.; Kumar, Vivek A.; Wen, Jing; Cui, Wanxing; Martinez, Adam; Apkarian, Robert; Coats, Julie E.; Berland, Keith; Chaikof, Elliot L., "Fibrillogenesis in continuously spun synthetic collagen fiber," Journal of Biomedical Materials Research - Part B Applied Biomaterials, Apr 2010, 93(1), p 24-38

58. Gentleman, E., et al., "Mechanical characterization of collagen fibers and scaffolds for tissue engineering," Biomaterials, 2003, 24(21): p. 3805-13

59. Wang, Ming-Che; Pins, George D.; Silver, Frederick H. "Collagen fibres with improved strength for the repair of soft tissue injuries," Biomaterials, Jun 1994, 15(7), p 507-512

60. Pins, George D.; Huang, Eric K.; Christiansen, David L.; Silver, Frederick H., "Effects of static axial strain on the tensile properties and failure mechanisms of self-assembled collagen fibers," Journal of Applied Polymer Science, Mar 1997, 63(11), p 1429-1440

CHAPTER 3

A TEMPLATE-BASED APPROACH FOR SPATIALLY-DESIGNED COLLAGEN MICRO/NANOFIBER REINFORCED ELASTIN COMPOSITES

3.1 Introduction

Cardiovascular diseases such as coronary artery disease and peripheral vascular disease are a major cause of death in the United States. The treatment for these diseases often involves surgically implanting a vascular bypass graft to restore blood flow to the tissues insufficiently supplied by the affected artery. Currently, autologous vessels such as the saphenous vein, and synthetic grafts from materials such as expanded polytetrafluoroethylene (e-PTFE), and polyethylene terephthalate (PET) (also known as Dacron) are the most commonly utilized vascular bypass grafts [1]. The synthetic e-PTFE and Dacron grafts have shown significant results for medium (6-10 mm) to large (>10 mm) diameter grafts, but have not proven successful in small diameter (<6 mm) applications on account of limited patency caused by thrombosis (blood clot formation). Most small diameter graft bypass surgeries utilize autologous tissues from the patients. While the native grafts function very well as substitutes, the availability of suitable vessels is severely limited. The search for an ideal small diameter graft has thus motivated significant research efforts towards engineered vascular tissues.

Blood vessels in the human body are composed of three layers, namely, tunica adventitia, tunica media, and tunica intima [2]. The innermost layer, tunica intima, consists of a thin layer of connective tissue lined by a layer of endothelial cells. This

multifunctional layer of cells, also known as the endothelium, forms a non-thrombogenic surface between the vessel wall and the blood flow. Tunica media is composed of connective tissue, elastic fibers, and smooth muscle cells. Tunica adventitia is mainly composed of collagen and some elastin. Collagen and elastin function together and are responsible for the strength and the elasticity of the blood vessels respectively.

Prosthetic vascular grafts are often unsuccessful in mimicking the native structural properties and suffer mechanical mismatch with the native tissues. Lack of conformance of the engineered tissue to the mechanical properties of the host tissue near the implant site creates differences in the strain at the anastomosis (connection between the vessel and the artificial graft), and can incite graft failure by a condition known as hyperplasia. This is caused by proliferation of smooth muscle cells towards the lumen resulting in blockage [3].

Collagen-elastin fibrous composite materials make excellent candidates for the construction of tissue grafts with mechanical properties similar to that of the native tissues, as they integrate tensile strength with elasticity. They also most accurately represent the *in vivo* tissue structure. Mechanical properties of such composite tissues can be controlled by alterations in the relative proportions of the two structural components. Electrospun aqueous mixtures of collagen and elastin, or blends of collagen and elastin with other polymers such as polydioxanone and PLGA have been investigated previously [4-7]. However, the collagen structures obtained in this fashion were often observed to lack D-periodic banding and displayed collagen degradation into gelatin. Also, only a certain degree of fiber orientation could be achieved with this approach.

Recently, Caves et al. demonstrated the production of fiber reinforced composites (FRCs) using wet-spun collagen fibers with native morphology, embedded in an elastin-mimetic protein polymer [8]. FRCs are materials composed of a distributed phase in the form of fibers and a continuous phase in the form of a matrix material, as shown in Figure 3.1. The fibers are responsible for bearing the loads experienced by the materials, and the matrix is responsible for securing the fibers together and transferring the loads between them. The constituents of the FRCs function in a synergistic fashion such that the mechanical performance of the FRCs is superior to the constituents acting independently. The composite mechanical behavior is governed by various factors. In addition to the properties and dimensions of the constituent materials, these include the distribution, layout, and volume fraction of the fibers. Caves et al. demonstrated that the mechanical properties of the collagen-elastin FRC materials could be modulated by varying fiber orientations and volume fractions.

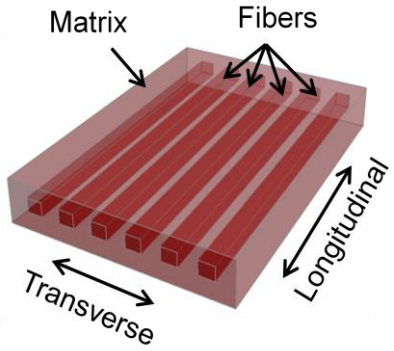

Figure 3.1. Schematic of a unidirectional FRC material.

Furthering the efforts of Caves et al., we aimed to apply MEMS processing technology for the fabrication of collagen micro/nanofibers and collagen FRCs in an elastin matrix. Applying MEMS processing technology allowed for precise construction of the engineered scaffold enabling mimicry of the laminated 3D architecture of the

native tissues. Micromolding could be used to define the spatial organization of the fiber networks offering control over the fiber alignment and a high packing density. The use of MEMS fabrication processes to sculpt and demold the fibers could produce fibers on dimensional scales relevant to the native tissue physiology and with controllable in-plane and out-of-plane geometries.

3.2 Fabrication development

The collagen-elastin FRCs were fabricated using the principle of microtransfer molding, a process used to fabricate 3D free-standing polymer negative replicas of a template [9].

3.2.1 Materials

The fabricated MEMS-based FRC tissue scaffolds consisted of collagen type I fibers and elastin-mimetic protein matrix, as described in Chapter 1. Collagen type I was extracted from rat tail tendons and processed in its acid-solubilized form in 10 mM HCl. The elastin-mimetic protein polymer was synthesized using principles of genetic engineering applied to a bacterial culture of E. coli. This material displayed a distinctive temperature dependent solubility in water. It solubilized in water at 4 ºC, and underwent gelation at room temperature.

3.2.2 Fabrication considerations

Two important considerations for the fabrication development for protein scaffolds were biocompatibility and preservation of the chemical structure of the proteins.

It was necessary to ensure that the fabrication process was gentle and biofriendly and did not introduce any toxic or contaminant residue in the scaffold. For example,

photolithography can leave behind residues of photoresists, known to induce toxic effects to internal organs, making it an unsuitable patterning approach for collagen.

Proteins undergo degradation when subjected to an external physical or chemical stress such as high temperature, an unfavorable pH or an organic solvent (such as alcohol and chloroform). Proteins degrade by either hydrolysis or denaturation. Hydrolysis breaks the peptide bonds in proteins by addition of a water molecule by resulting in a carboxylic acid and an amine. Denaturation causes the unfolding of the protein's secondary, tertiary or quaternary structure.

Reconstituted collagen is a particularly suitable biomaterial for tissue engineering primarily because of the recovery of its native chemical structure in *in vitro* preparations. As discussed earlier, collagen molecules are composed of three polypeptide strands, arranged into a triple helical structure stabilized by hydrogen bonds. The molecules connect in a periodic fashion to compose fibrils. This native structure can be lost when collagen is subjected to certain conditions such as heat and chemicals leading to its degradation. A typical product of degradation of collagen is gelatin and is marked by loss of conformation and disruption of the crystalline triple helical structure of collagen. Electrospinning of collagen is typically performed with collagen solubilized in organic solvents such as 1,1,1,3,3,3-hexafluoro-2-propanol (HFP). It has been reported that using such fluoroalcohols causes an irreversible gelatinization of collagen [10]. Thermal denaturation of collagen has been studied extensively and evaluated using methods such as second harmonic generation (SHG) [11] and differential scanning calorimetry (DSC) [12]. Denatuartion temperatures for collagen depend on various factors, such as the preparation methods, the pH, and the incubation temperatures [11-14]. Mammalian

collagens begin to denature at 40 °C and the denaturation temperatures can be as high as 100 °C when crosslinked [14]. Concentrated mineral acids such as HCl and sulfuric acid (H_2SO_4) also cause a chemical degradation of collagen resulting in a loss of chemical structure as seen in thermal degradation. These considerations precluded the use of high temperatures, organic solvents, and concentrated acids during the processing steps.

Another mechanism that leads to collagen degradation is called proteolysis. It results from contamination of collagen by bacteria, yeast or mold [15]. These microbes secrete collagenase enzymes that break down the collagen. This could be avoided by keeping collagen in a contamination free and sterile environment during processing and also storing it in cold temperatures (4-8 °C).

Ultraviolet (UV) irradiation can lead to a slow, progressive breakdown of the collagen molecule to eventually lose the helical organization when processed in the dry state [14, 16]. This process is very slow as compared to thermal and enzymatic denaturation of collagen.

All the described degradation characteristics change when the collagen is crosslinked with gluteraldehyde. The denaturation temperature is increased to almost 100 °C and reduces the susceptibility of collagen to enzymatic denaturation.

3.2.3 Fabrication of collagen fiber networks

The collagen fiber networks were fabricated in three phases as described below:

3.2.3.1 Template preparation

The process flow for template preparation is illustrated in Figure 3.2.

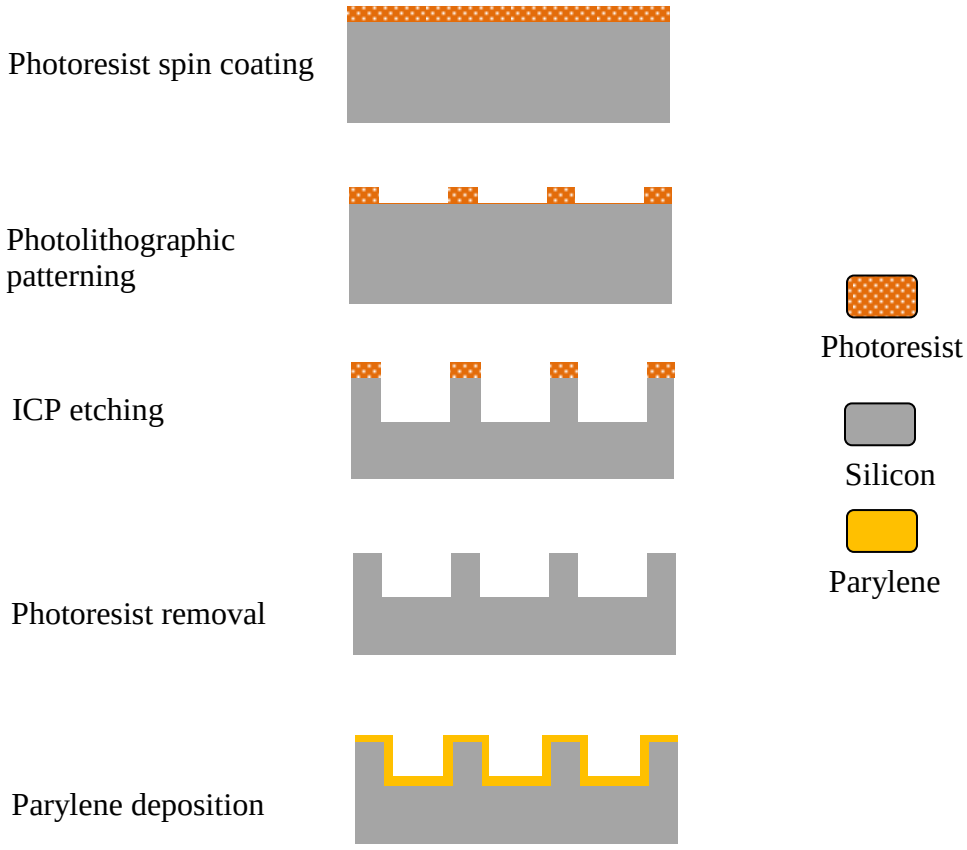

Figure 3.2. Fabrication process flow for the silicon templates.

Silicon template fabrication

Templates with the designed fiber network layouts were fabricated on (100) silicon wafers. Trenches with the required layout were defined photolithographically using positive photoresist SC 1827 (Shipley, Marlborough, MA), and etched into the silicon wafer using ICP etching. Finally, the photoresist was removed using acetone and oxygen plasma RIE leaving behind bare silicon templates (Figure 3.3).

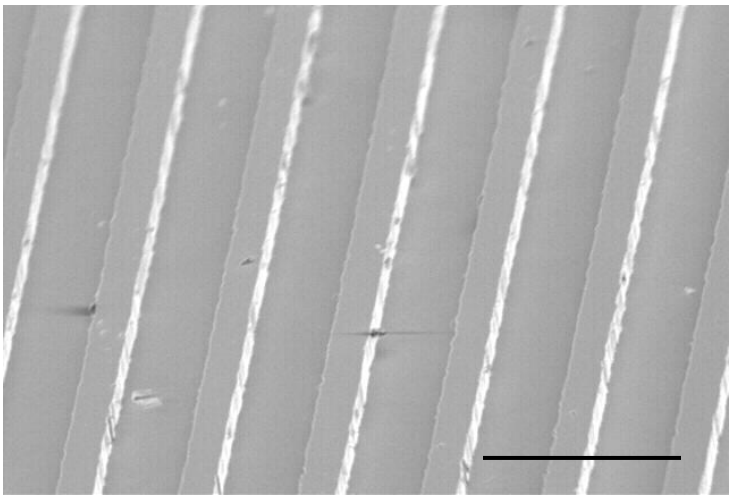

Figure 3.3. A silicon template for the fabrication of straight fibers (scale bar = 50 µm).

Adhesion promoter application and parylene coating

Molding of collagen on a bare silicon template revealed that the collagen film adhered to the silicon very strongly, posing a challenge during its separation from the mold. To facilitate subsequent fiber release, parylene was investigated as a potential release layer between the silicon template and the collagen film. Collagen solution contact angle measurements were performed to assess the wettability of parylene and silicon substrates, as shown in Figure 3.4. The contact angles were observed to be 95° and 53° for parylene and silicon respectively, rendering parylene a more suitable material as a collagen molding release layer. The silicon templates were coated with a thin (600-800 nm) layer of parylene film using a parylene deposition system (Specialty Coating Systems Inc., Indianapolis, IN). Prior to the parylene deposition, the silicon templates were treated with an adhesion promotion agent (A-174 Silane, 3-(Trimethoxysilyl) propyl methacrylate, Aldrich) to prevent delamination of the parylene film during fiber

demolding steps. This was achieved by dip-coating a 0.5% solution of A-174 Silane in isopropyl alcohol (IPA) and water on the silicon templates.

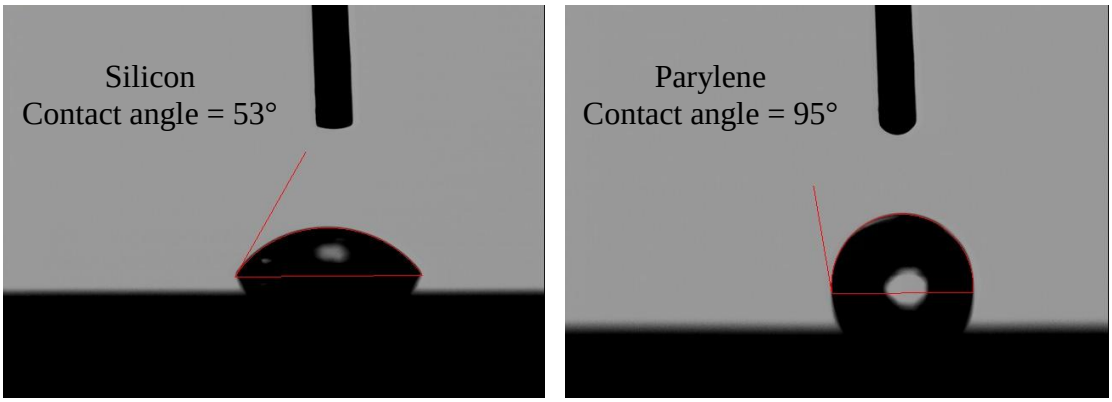

Figure 3.4. Contact angle measurement for studying wettabilty of silicon and parylene with acid-soluble collagen.

3.2.3.2 Collagen micromolding and self-assembly

The process flow for collagen micromolding is illustrated in Figure 3.5.

Solvent casting of collagen

Solvent casting of collagen films required certain template design and processing considerations to ensure conformal coating of the collagen layer on the silicon template. As a result of surface tension effects, a polymer webbing effect was often observed for certain silicon template geometries and conditions of solvent casting (Figure 3.6). This effect was most commonly observed in templates with a spacing width (s) greater than the trench width (w), or with a high depth-to-width (d/w) aspect ratio (>1). It was also observed when the solvent casting process was performed under atmospheric conditions. Given these factors, all the silicon templates were designed to have a spacing width smaller than the trench width (s < w), and a depth-to-width aspect ratio of unity or less

(d/w ≤ 1). Also, the solvent casting process was performed under vacuum conditions (27.5 inHg below atmospheric pressure).

The fabricated silicon templates were cleaved into 3 cm × 4 cm chips. Each chip was positioned in a polypropylene container (6 cm × 3.8 cm × 2.5 cm). The desired volume and concentration of solubilized collagen (in 10 mM HCl) was released on the template and degassed in vacuum. This was followed by solvent casting (in vacuum) to form a conformal collagen film on the template (Figure 3.7).

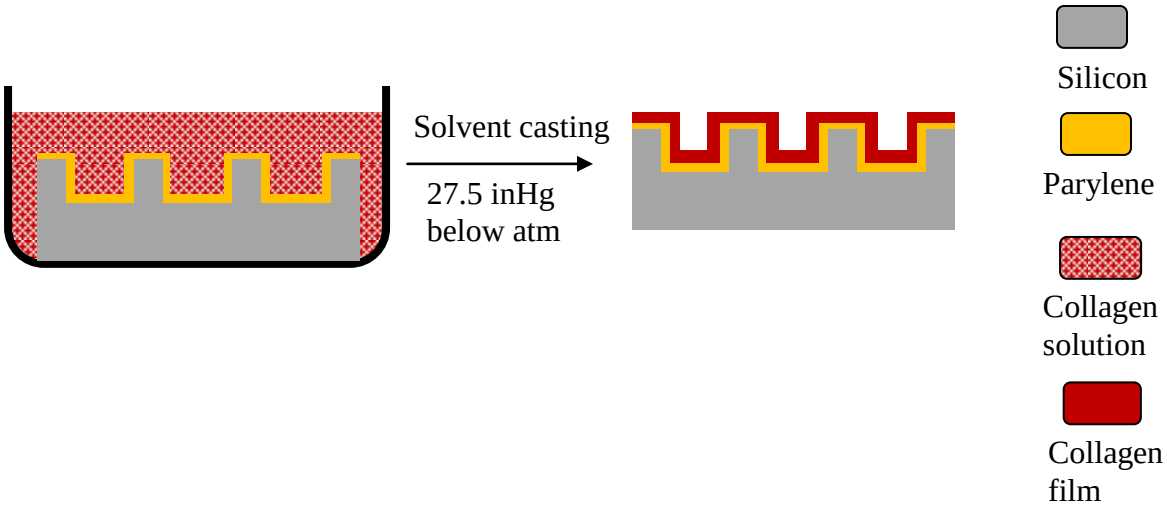

Figure 3.5. Fabrication process flow for collagen solvent casting.

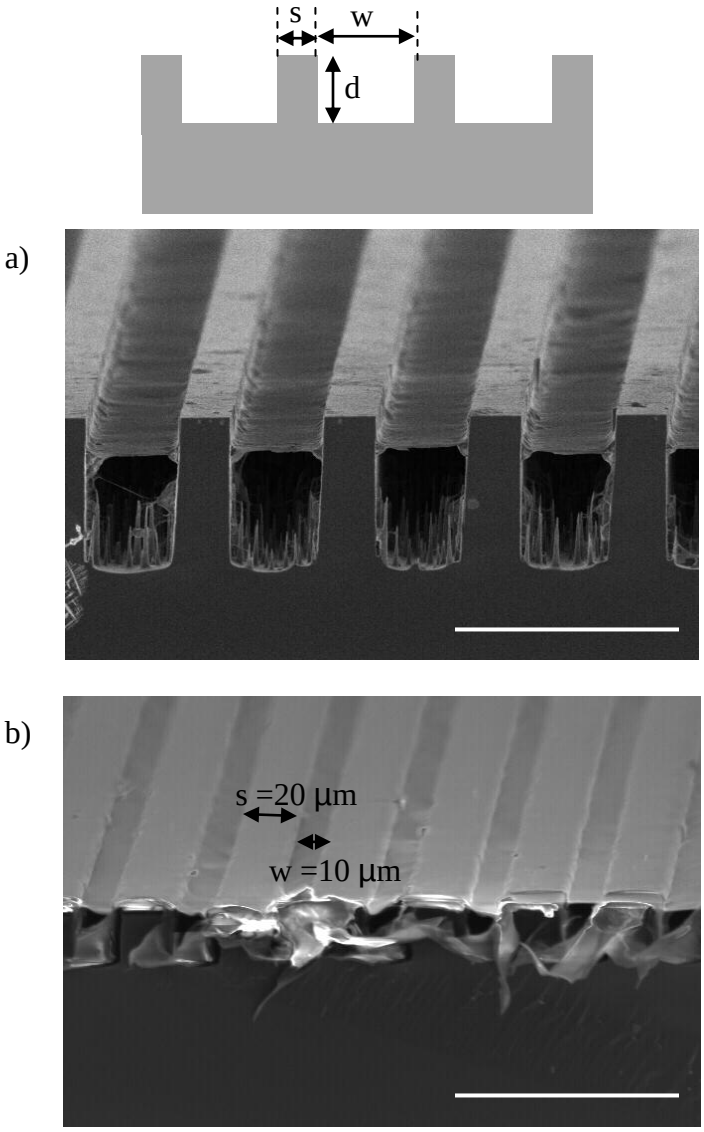

Figure 3.6. Polymer webbing caused by surface tension effects, a) in atmospheric pressure conditions, and b) for silicon templates with width of the spacing greater than width of the trench (scale bars = 50 µm).

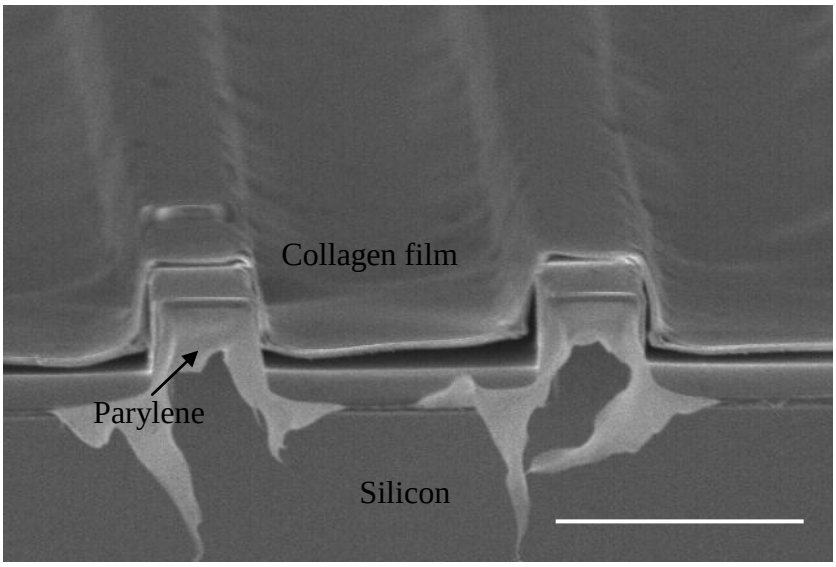

Figure 3.7. A solvent cast conformal collagen film on a silicon template (scale bar = 25 μm).

Collagen fibril self-assembly

The collagen film was coated with a monomeric acid-solubilized solution. The self-assembly of collagen molecules into fibrils could be initiated under physiological conditions of neutral pH and 37 ºC temperature. This was realized by treating the solvent cast collagen film with an alkaline mixture of WSB solution and 0.1 mM sodium hydroxide (NaOH) (WSB + NaOH, pH=11) for 10 hours at 37 ºC for neutralizing the monomeric collagen.

Crosslinking

The self-assembled collagen film was crosslinked in vapor phase glutaraldehyde (0.5 wt% glutaric acid dialdehyde in 1× PBS). A dessicator jar was saturated with glutaraldehyde. The templates to be treated were placed in the jar for 12 hours. The cross-linked samples were vented for 4 hours under the fumehood prior to futher processing.

3.2.3.3 Collagen fiber individualization and extrication

The process flow for collagen fiber individualization and extrication is illustrated in Figure 3.8.

Casting the first layer of Polyvinylpyrrolidone (PVP)

A thin layer of a water soluble polymer, PVP (1,300,000 MW, 10 mg/ml in water, 10 μm thickness), was solvent cast on the template, as shown in Figure 3.9a. This step served a two-fold purpose. The polymer filled up the trenches, selectively masking the collagen film inside the trenches and acting as a protectant for the area of interest of the collagen film during the fiber individualization steps. Also, this layer provided rigidity to the material being etched, preventing the delamination of the collagen film. High molecular weight PVP was deemed a suitable material for this process on account of its biocompatibility [17-18] and uniformity of the formed film.

Fiber individualization

A combination of dry mechanical polishing and oxygen plasma RIE was utilized to etch PVP and collagen from the upper portion of the template, consequently forming individualized collagen micro/nanofibers in the trenches, as shown in Figure 3.9b.

Fiber network extrication

For extrication of the fiber network from the trenches, a second layer of PVP (1,300,000 MW, 22 mg/ml, 50 μm thickness) was cast on the templates holding the individualized fibers. This layer of PVP fused with the first layer of PVP (now individualized into fibers). A water soluble tape (1stmaskingtape inc., Torrance, CA) was adhered to the second layer of PVP and peeled off, extricating the collagen fiber network from the trenches. The water soluble tape was biodegradable and comprised of a water

soluble adhesive with a PVA backing. The final structure obtained from this step was a fiber network arranged on a water soluble film (PVP + water soluble tape), as shown in Figure 3.9c.

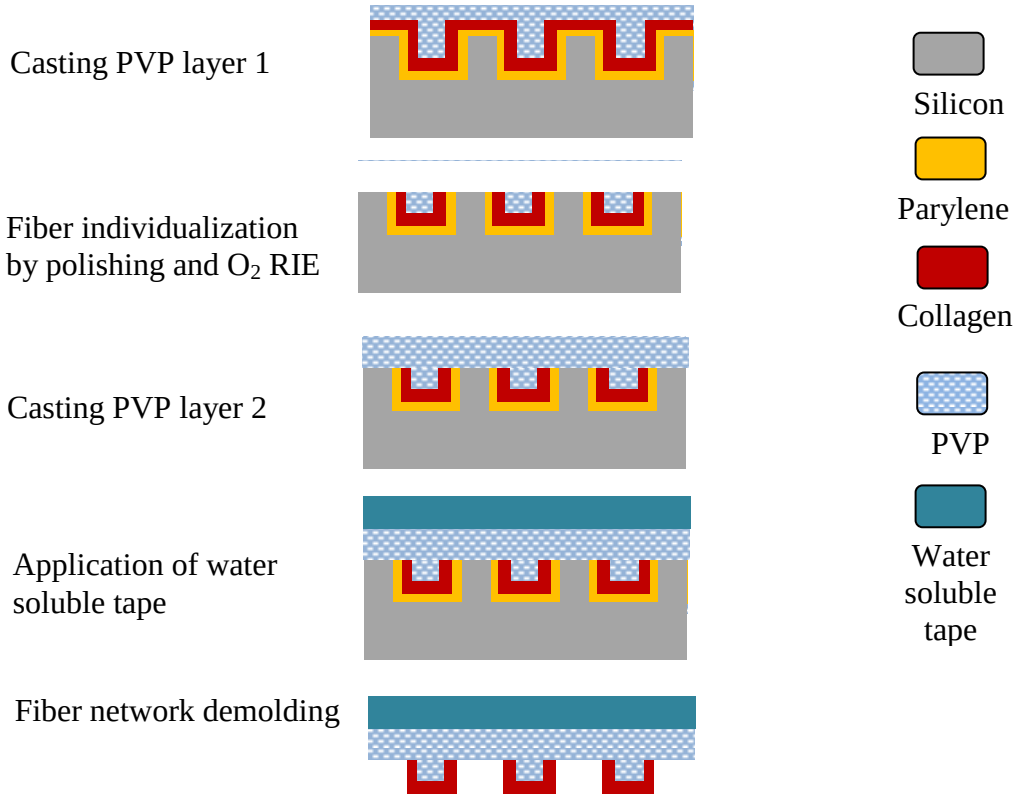

Figure 3.8. Fabrication process flow for collagen fiber individualization and extrication.

Previous attempts for fiber extrication included casting an elastin film on the template for direct encapsulation of the fibers and demolding of the fibers using the water soluble tape. Both of these approaches failed to produce adequate repeatability and uniformity of transfer. The reason for this may have been uneven adhesion of the fibers to elastin and the tape. Using a second layer of PVP, prior to applying the water soluble tape, yielded almost a 100 % fiber release from the template.

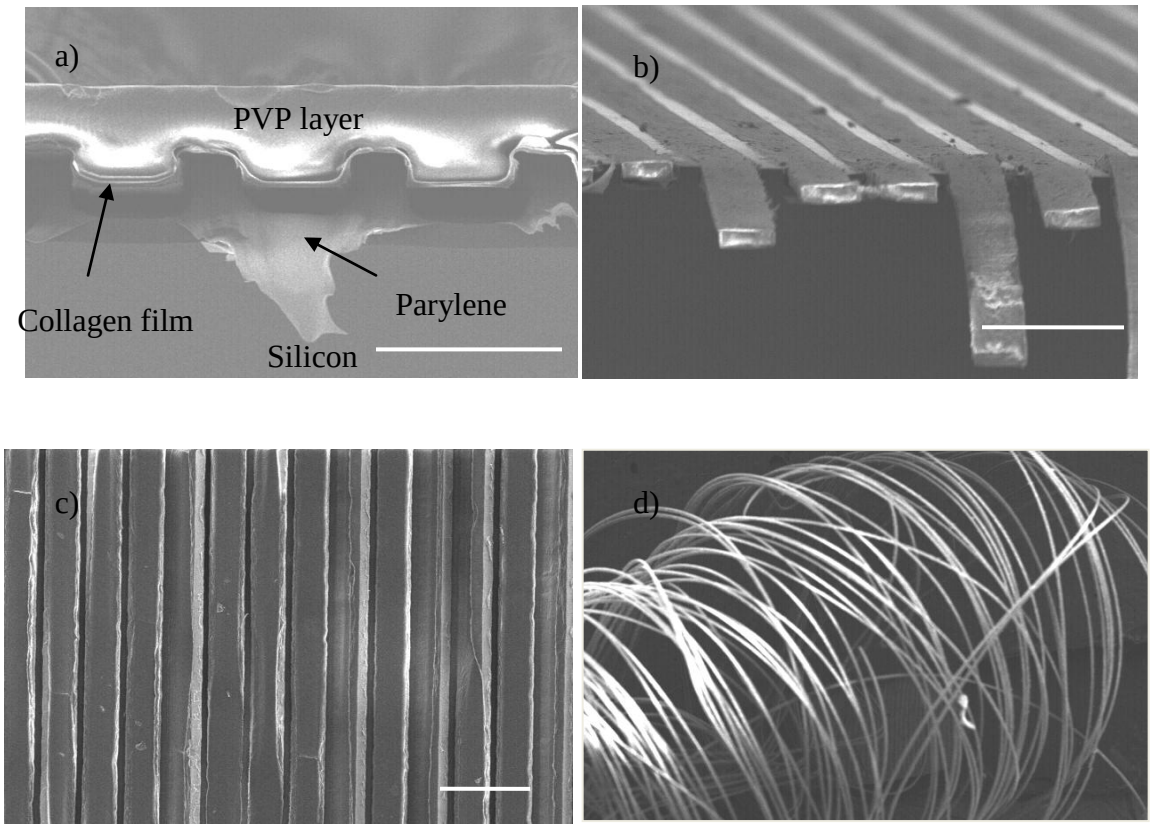

Figure 3.9. SEM images illustrating, a) different polymer layers after casting the first layer of PVP, b) Individualized collagen-PVP fibers after mechanical polishing and RIE, c) an aligned fiber network arranged on a water soluble film, and d) free suspended fibers (scale bars = 50 μm).

3.2.4 Fiber dimensions and shapes

The fiber dimensions and shapes could be controlled by the template design and the collagen solution properties. The width and length of the fibers were determined by the template design. The wall thickness of the fibers was a function of the concentration and volume of the collagen solution used for a given surface area.

The solvent cast film thickness could be roughly estimated by Equation 3.1.

$$T_d = T_w \times M = \frac{V}{S} \times \frac{C}{\rho} \tag{3.1}$$

Where,

T_d = Thickness of dry cast film

T_w = Thickness of wet film

M = % of solid collagen in the solution

V = Volume of collagen solution used

S = Effective surface area of the template used for solvent casting

C = Concentration of collagen solution used

ρ = Density of collagen

The expected film thickness was estimated by assuming the density of collagen to be 1 gm/cc and estimating an effective surface area used for solvent casting (taking into account the template ridges). Figure 3.10 illustrates the predicted and measured fiber thicknesses varying with the concentration and volume of the collagen solution, respectively. The measured values follow the same trend as the estimated values. The noted difference between them may have resulted from losses caused by the seepage of polymer solution to the bottom of the die, hence increasing the effective surface area. This method was used to fabricate fibers with widths spanning from 2 μm (length = 2 cm) (Figure 3.11) to 50 μm (length = 4 cm), and wall thicknesses varying from 300 nm to 3 μm. The minimum fiber width attained was constrained by the limits of the photolithography process.

By regulating the depth of the template and the collagen solution properties used, hollow or solid fibers could be obtained. Solid ribbon-like fibers were fabricated by using a greater amount of collagen material with either a higher concentration or a larger volume of the collagen solution, cast on a template with shallow trenches (<6 μm). A thin

conformal collagen film coating the templates with deeper trenches yielded hollow fibers. Figure 3.12 illustrates a rectangular cross-section hollow fiber fabricated using a 20 μm deep template with 3 ml of 1.5 mg/ml concentration collagen, and a ribbon-like solid fiber fabricated using a 4 μm deep template with 5 ml of 2 mg/ml concentration collagen, respectively.

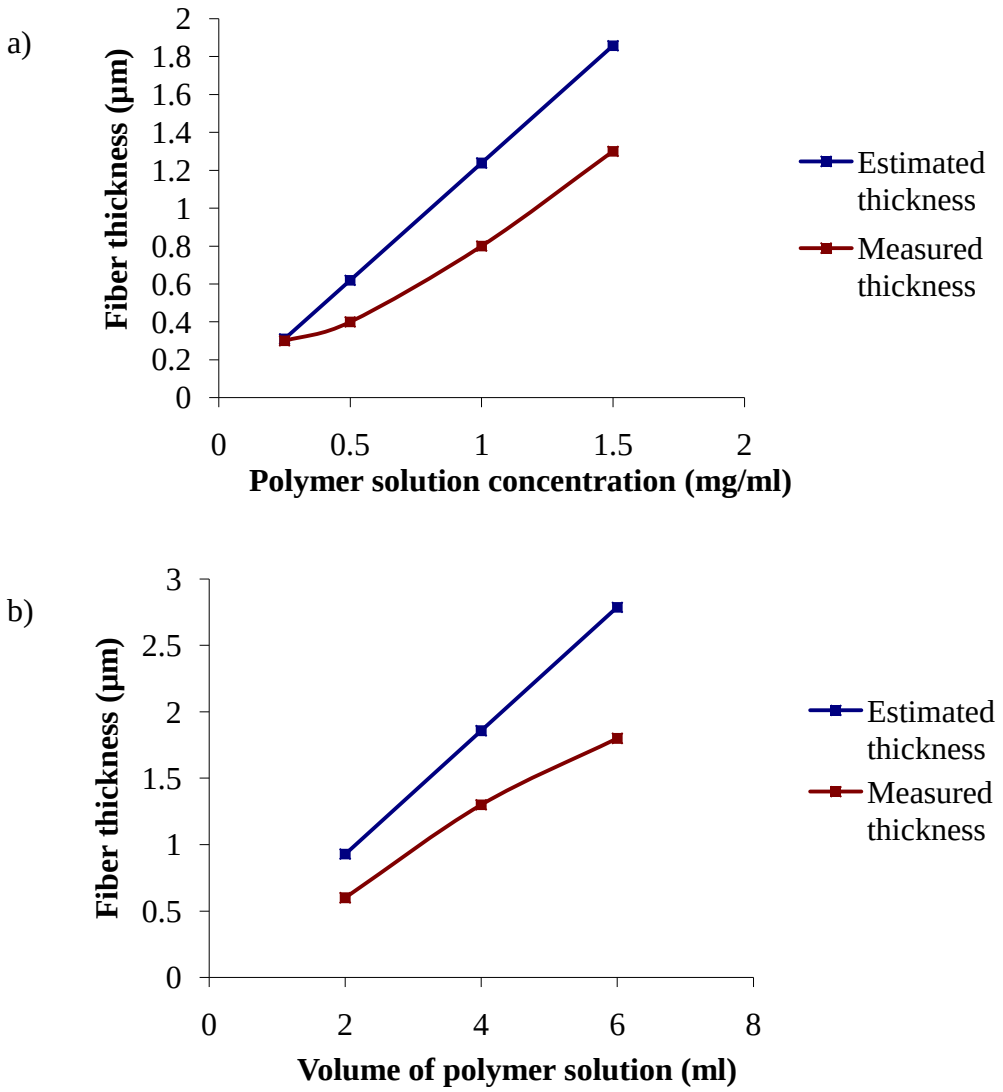

Figure 3.10. Variation of the fiber wall thickness as a function of: a) collagen solution concentration for a fixed volume of 4 ml, and b) volume of the collagen solution for a concentration of 1.5 mg/ml.

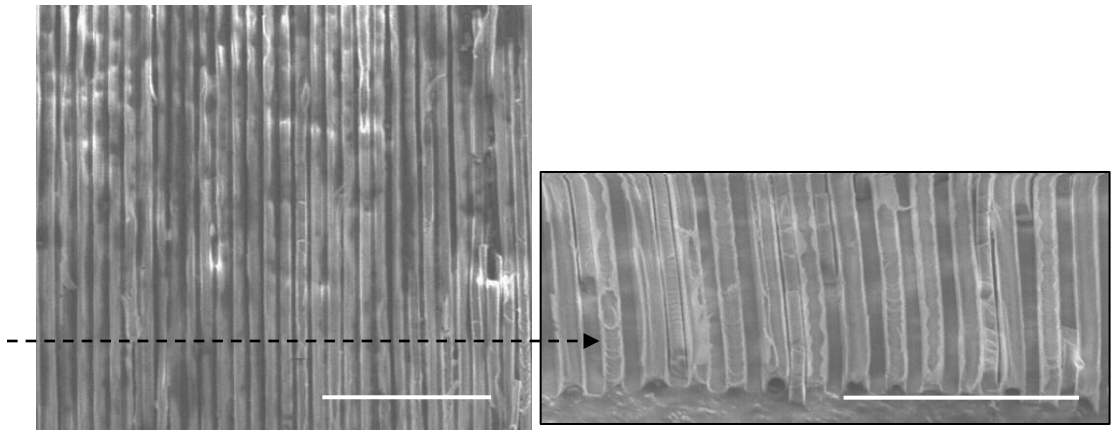

Figure 3.11. 2-µm wide and 300-nm thick hollow collagen fibers on tape (scale bars = 25 µm).

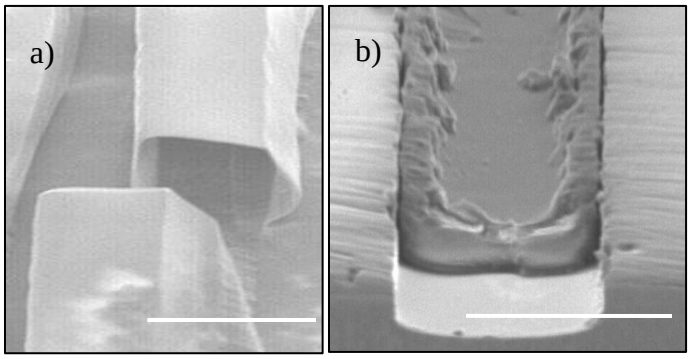

Figure 3.12. SEM images of, a) a hollow collagen fiber, and b) a ribbon-like solid collagen fiber (scale bars = 20 µm).

3.2.5 Spatial layouts of the fiber networks

Various spatial layouts of fiber networks were explored using appropriate silicon template designs with the desired geometries in the horizontal and vertical planes.

Unidirectional straight fiber networks

Straight fiber networks were fabricated using straight trenches built into the silicon substrates. These fibers were used for manufacturing unidirectional FRCs (Figure 3.13). The template illustrated in Figure 3.13 was fabricated using successive ICP etching

and KOH etching to sharpen the teeth of the trenches. This step helped reduce polymer webbing resulting from surface tension effects for higher aspect ratio (>1) trenches.

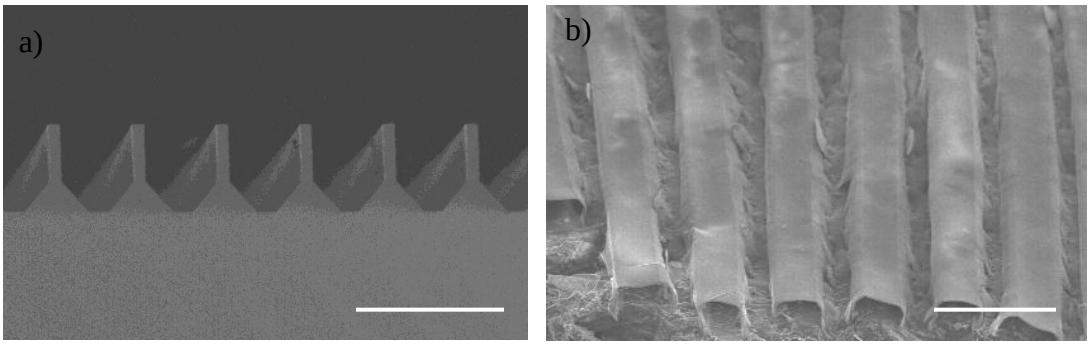

Figure 3.13. SEM images of, a) a straight trench silicon template, and b) unidirectional straight fibers (scale bars = 50 μm).

In-plane and out-of-plane crimped fibers

A certain amount of slack in the load bearing fibers held in a matrix material increases the deflection range of the resultant composite material. As described in chapter 2, several soft tissues are composed of such crimped collagen fibers and display a strain dependent elasticity. Caves et al. reported an elastomeric deformable crimping tool for introducing undulations in wet-spun collagen fibers [19]. They demonstrated a non-linear elastic behavior displayed by collagen-elastin composites with such crimped collagen fibers, such that the material transitioned from a low elastic modulus to a high elastic modulus as the fibers uncrimped with the application of strain. In the current study, a hydrodynamic focusing approach for *in situ* crimping of wet-spun fibers was developed, as described in chapter 2. While the crimping strategies for wet-spun fibers provided means for altering the geometry of each fiber, precise control over the fiber dimensions, alignment and packing density could not be achieved.

The current template-based approach was utilized to develop similar crimped geometries and characteristics, but with miniaturized fibers. A finer control over the fiber dimensions, densities, and layouts could be obtained, and the structure of the crimps could be easily adjusted to a designed transition strain. The designed transition strain was calculated as a ratio of a differential of the arc length and wavelength of the fiber crimp to the wavelength of the fiber crimp (Equation 3.2, Figure 3.14).

$$\varepsilon_d = \frac{L - \lambda}{\lambda} \tag{3.2}$$

Where,

ε_d = Designed transition strain of the crimp

L = Arc length of the crimp

λ = Wavelength of the crimp

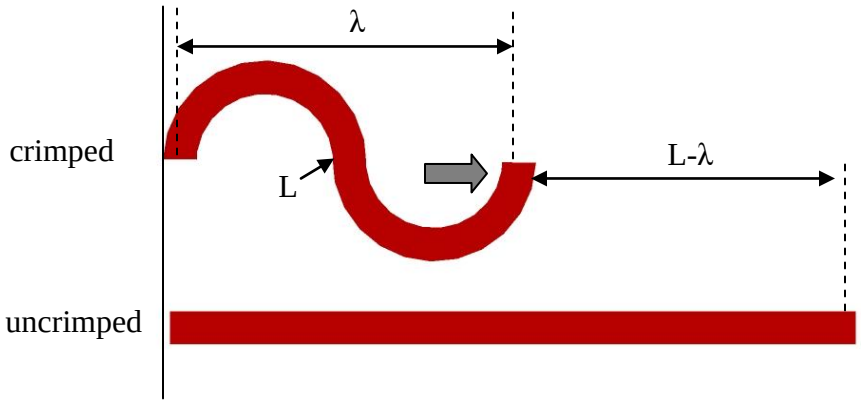

Figure 3.14. Designed transition strain.

For in-plane undulated fibers, templates with serpentine trenches were used. The wavelength and amplitude of the serpentine patterns could be modified to control the

mechanical property imparted by the fibers to the FRC, as will be discussed later. Figure 3.15 illustrates SEM images of a silicon template with serpentine trenches, and the corresponding individualized in-plane crimped collagen-PVP fibers on the template and on a tape.

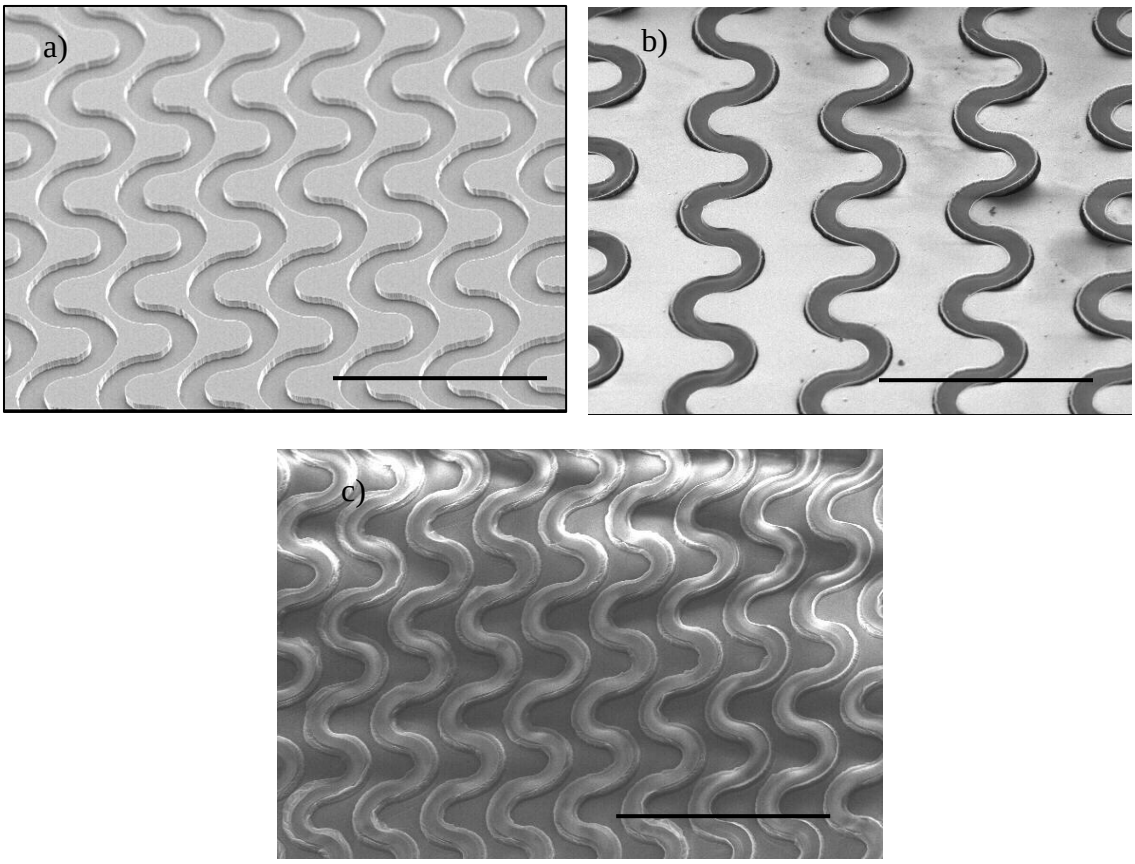

Figure 3.15. a) A serpentine trench silicon template, and in-plane serpentine collagen-PVP fibers with a designed strain of 27%, b) in the silicon template, c) on tape (scale bars = 200 μm).

The silicon templates for the fabrication of out-of-plane crimped fibers were constructed to have a multi-depth structure necessary for delineating the out-of-plane geometries of the resultant fibers. Sequential ICP and KOH etching steps were used to

fabricate these templates. The process flow for the fabrication of silicon templates for out-of-plane crimped fibers is illustrated in Figure 3.16. The template was built on a (100) silicon wafer. A 1-μm thick SiO_2 layer was thermally grown on the silicon wafer using wet-oxidation (2.5 hours, 1100 ºC). Photolithography and ICP etching of SiO_2 were used to define straight patterns in the SiO_2 layer. The spacing between the patterns equaled half the desired wavelength of the crimps. Another layer of photoresist SC1827 was spin-coated on the patterned SiO_2. Using photolithography, straight patterns reflecting the width of the subsequent fibers were aligned and defined perpendicular to the existing straight patterns in the SiO_2 layer. ICP etching was utilized to etch silicon to obtain a depth equal to the differential of the total depth and the amplitude of undulations. The photoresist layer was then etched using acetone and RIE. ICP etching was carried out with the SiO_2 pattern masks to obtain a depth defining the crimp amplitude. The SiO_2 layer was etched in HF acid. The silicon template was immersed in a KOH bath to etch the bridges between the structures for fiber fabrication and also to give a slanting profile to the sidewall of the silicon structure for the fibers.

Having fabricated the silicon template, a collagen film was cast on the template by sequential spray coating rather than solvent casting. Spray coating prevented any collagen from depositing on the slant sidewalls, forming undulated fibers, pre-separated from one another (Figure 3.17). The fibers could then be transferred directly to a water soluble tape.

Porous fibers

Using templates with pillars in the trenches, porous fibers were fabricated (Figure 3.18). The pore size and density could be controlled by the template design

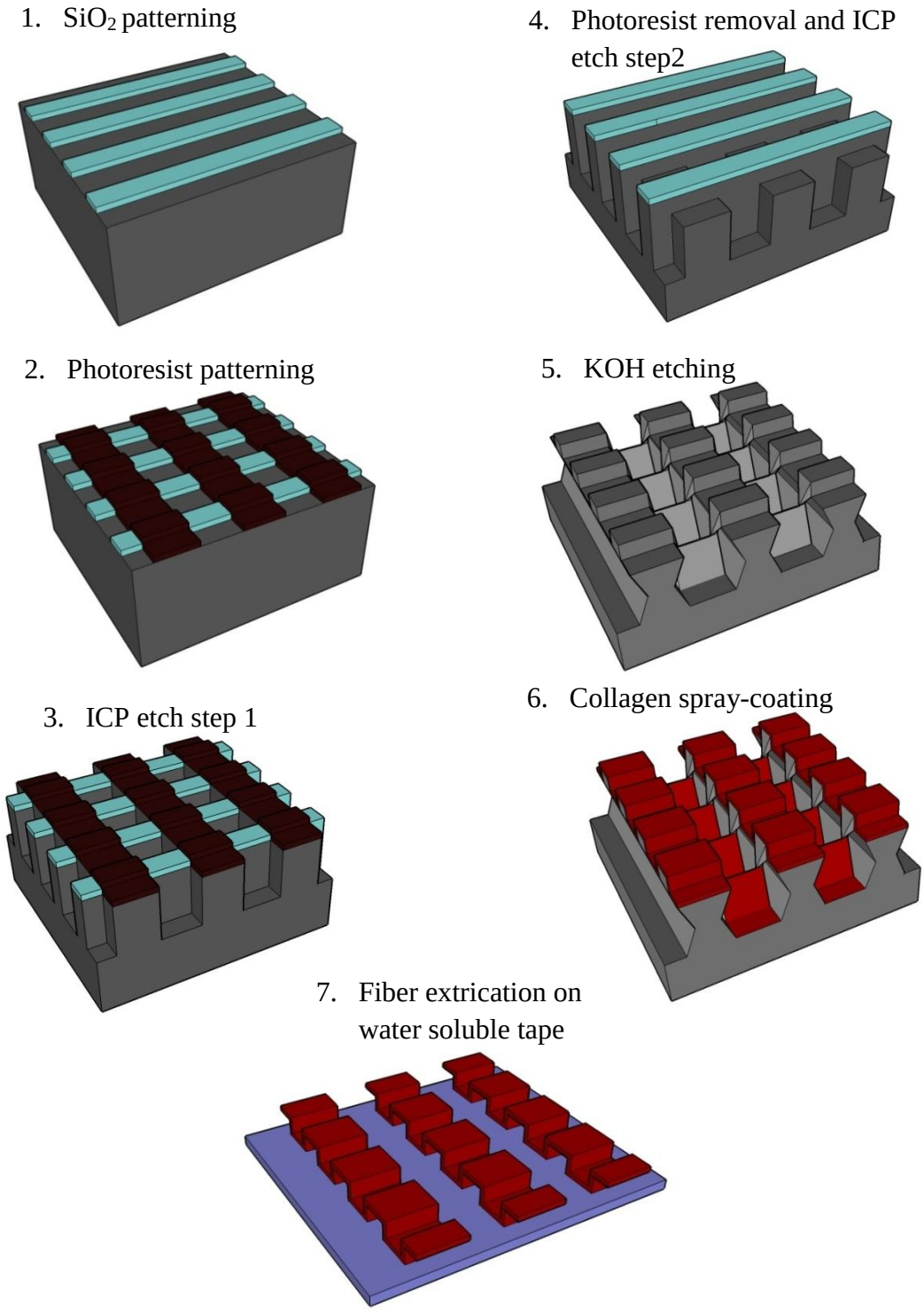

Figure 3.16. Fabrication process flow for multi-depth silicon templates for out-of-plane crimped fibers.

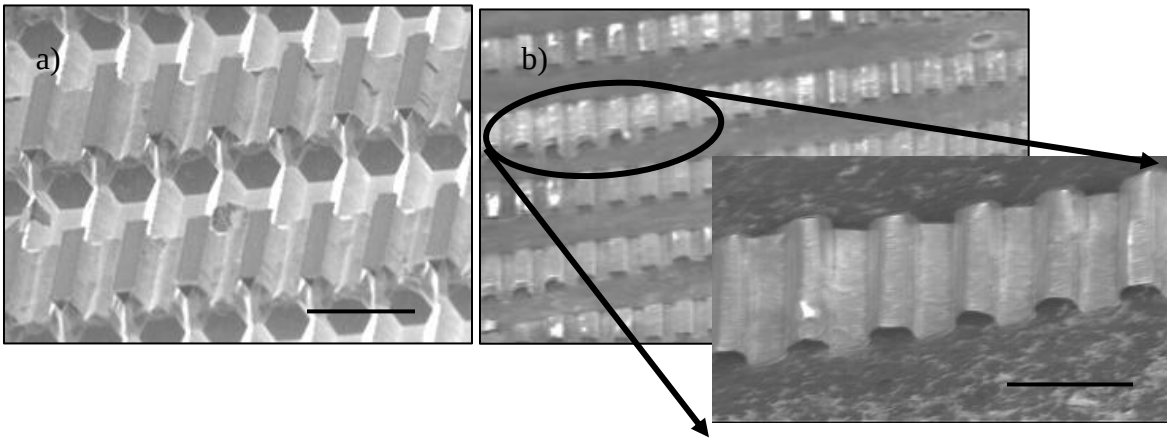

Figure 3.17. a) A multi-depth silicon template for the fabrication of out-of-plane crimped fibers, and b) out-of-plane crimped collagen fibers (scale bars = 50 μm).

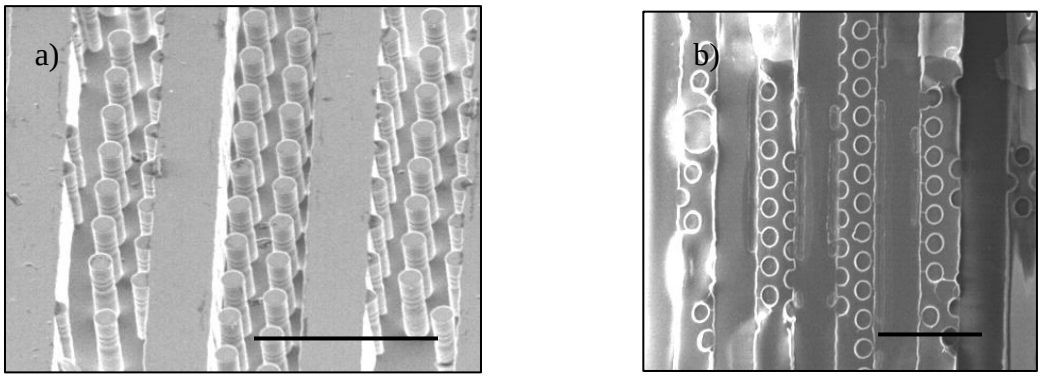

Figure 3.18. a) A silicon template with pillars in the trenches, and b) porous collagen fibers on tape (scale bars = 50 μm).

3.2.6 Collagen fibril self-assembly

As discussed earlier, native collagen fibers display a fibrillar structure. Collagen molecules self-assemble to form collagen fibrils. The molecules are staggered from each other by 67 nm resulting in a signature striated appearance known as D-periodic banding. The length of each D unit depends on the hydration state of the collagen but is typically

reported to be 67 nm. To initiate the formation of this native collagen structure in the acid-solubilized collagen *in vitro*, it is required to subject the collagen to physiological conditions of neutral pH environment at 37 ºC temperature. Under these conditions the collagen molecules spontaneously self assemble to recreate the native collagen structure.

The collagen film obtained from the template-based approach was coated from a monomeric acidic solution of collagen (in 10 mM HCl, 2 pH). It was required to optimize the conditions for the initiation of self-assembly of the monomeric precursors into fibrils for this process. The solvent-cast collagen film on the silicon template was treated with a neutralization solution (NS), an alkaline mixture of WSB and 0.1 mM sodium hydroxide (NaOH) (WSB + NaOH in a 2:1 ratio, pH=11) to trigger fibrilogenesis. These experiments were carried out at 37 ºC for 10 hours.

The volumetric ratio of collagen solution and NS was varied to find the optimum conditions for collagen self-assembly and the results were examined using an atomic force microscope (AFM) imaging technique (Table 3.1). The ratio of collagen solution and NS required to obtain a pH of 7 was estimated to be 6:1 using a pH meter. The collagen fibril self-assembly experiments were initiated using this estimated ratio. The AFM images for this ratio indicated the formation of globular protrusions and the absence of collagen fibrils. Such formations have been reported in the literature for acidic pH (<5) collagen [20]. It was believed that there were losses resulting from the seepage of the alkaline mixture to the bottom of the template leading to a lower effective pH than estimated. To account for this, 0.4 ml excess alkaline solution was introduced. Fibril formation and D-periodic banding were observed for this volumetric ratio. Using 0.4 ml excess alkaline solution overcame the losses and provides a ‘neutral to basic’

environment necessary for the solubilized collagen molecules to self assemble. Finally, excess alkaline mixture was introduced to examine the effect of a highly alkaline environment on the fibril formation. It was observed that the width of the fibrils was reduced as compared to the previous case. Based on these experimental results, 0.4 ml of neutralizing alkaline solution was added in addition to the estimated volume to neutralize collagen in 10 mM HCl. The fibril formation was achieved in a neutral to basic pH and that the fibril width could be modified with the pH of the environment. The observed length of each D subunit was 65-72 nm and seemed to match well with native collagen [21]. These observations are illustrated in Figure 3.19 and Figure 3.20.

Table 3.1. Volumetric ratios of collagen solution and NS employed for collagen fibril self-assembly

	Collagen solution (in 10 mM HCl) used for solvent casting, ml	**NS, ml**	**Ratio of the volumes of the collagen solution NS**
Case 1	3.5	0.58	6:1
Case 2	3.5	1	6:1 + 0.4ml NS
Case 3	3.5	2.5	1.4:1 (excess NS)

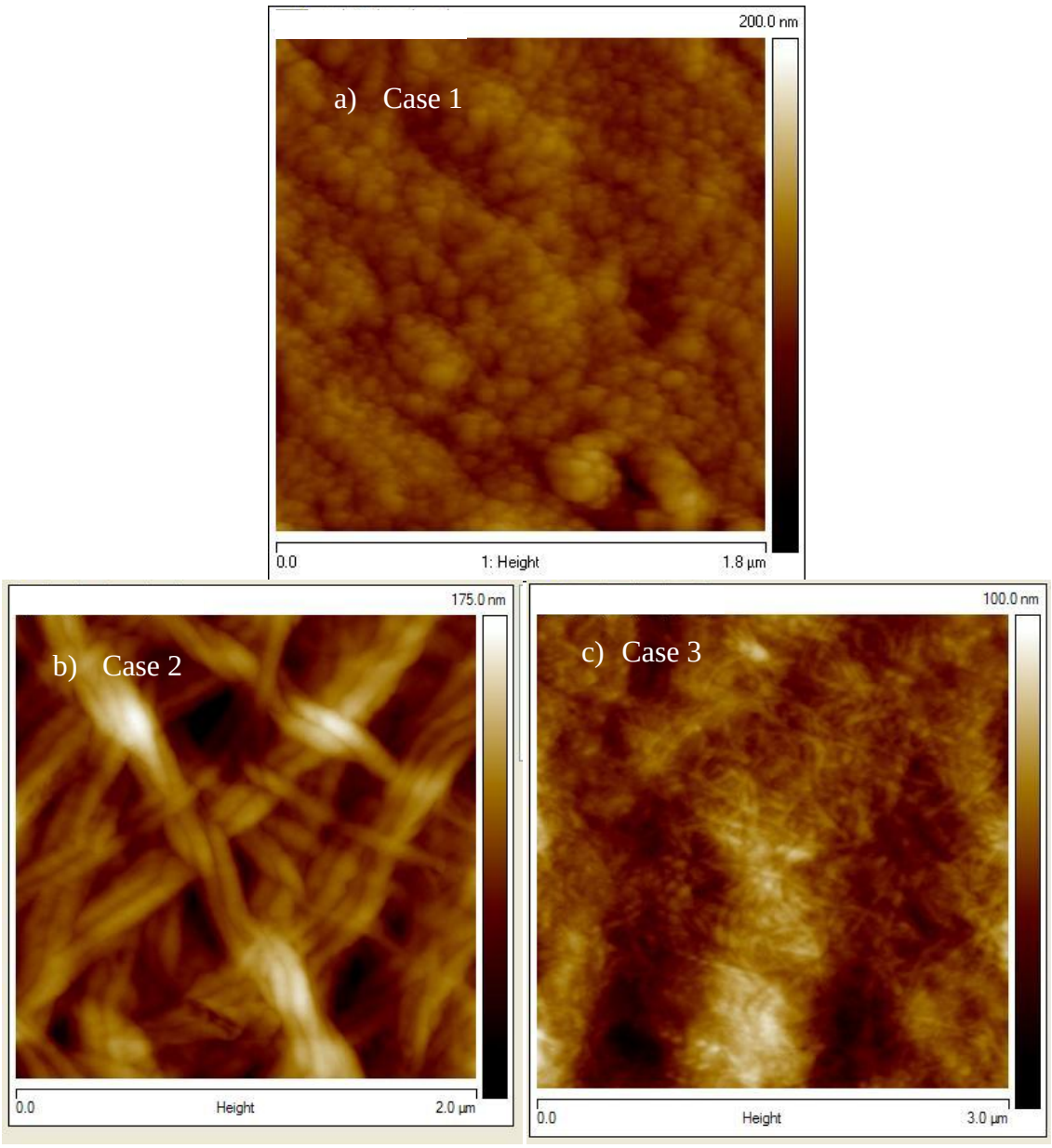

Figure 3.19. AFM images of self-assembled collagen, observed for different volumetric ratios of collagen and NS, a) 6:1 (pH< 7), b) 6:1 + 0.4ml NS (pH~=7), and c) 1.4:1 (excess NS) (pH>>7).

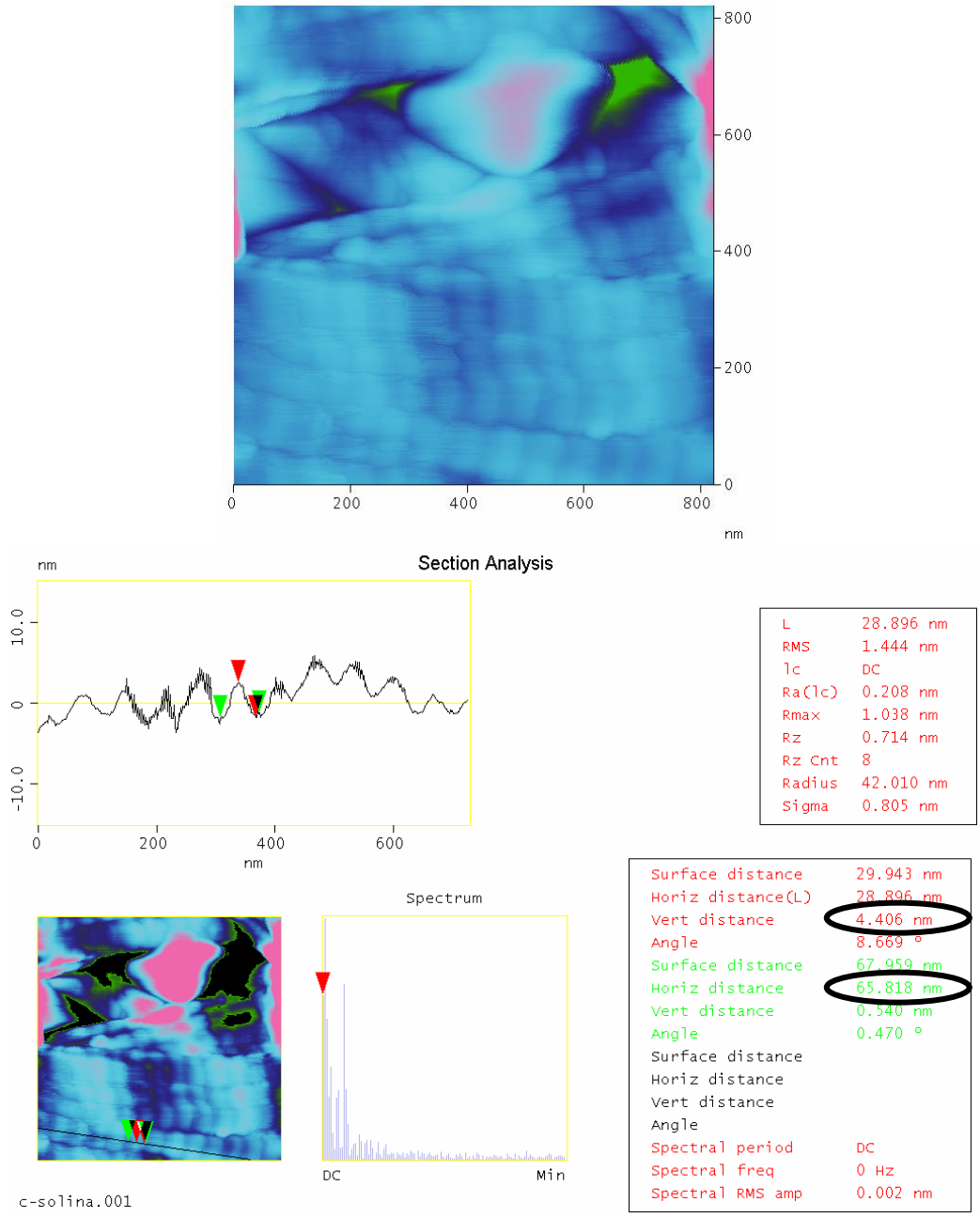

Figure 3.20. An AFM image of a collagen fiber illustrating D-periodic banding. A sectional analysis of the image displays the subunit dimensions.

3.2.7 Fabrication of laminated collagen-elastin FRCs

The process flow for the fabrication of an FRC is illustrated in Figure 3.21.

Elastin casting

Elastin (50 mg/ml in water) was cast on the water soluble film holding the collagen fiber network. The processing was carried out at 4 °C using liqueous elastin. The elastin film was gelled at 37 °C for 1 hour followed by incubation in fiber incubation buffer (FIB) for 1 hour.

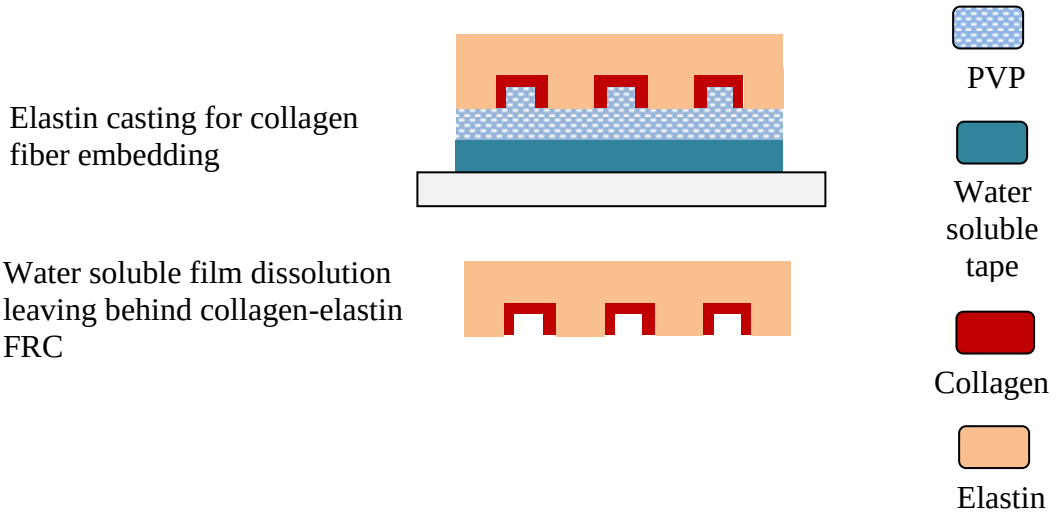

Figure 3.21. Fabrication process flow for elastin matrix casting on collagen fiber networks.

Water soluble film dissolution

The water soluble film was dissolved away in water at 37 °C, leaving behind fibers embedded in the elastin matrix. A single lamina of the fiber composite was designed to be approximately 100-µm thick in the hydrated state with the aid of plastic shims of the desired thickness. Each lamina contained approximately 1% fiber volume fraction.

Quality control: Fiber staining and inspection

The collagen fibers were stained using Van Gieson's, a stain used for differential staining of collagen. The composite materials were inspected using an optical microscope. This inspection indicated that during the elastin casting process, a number of fibers tended to lose their alignment with respect to each other causing entanglement, as shown in Figure 3.22. To prevent this, a second generation of fiber networks was designed to consist of bridges placed between the fibers at regular intervals (250-500 μm). This was observed to prevent fiber entanglement and loss of alignment. Figure 3.23 illustrates the collagen fiber network on a water soluble film, and stained collagen fibers in elastin fabricated with bridges for straight and serpentine fibers respectively. Occasional delamination of the fiber network from the elastin film was encountered (Figure 3.24). Such laminae with delaminated fiber networks were discarded and not used for further fabrication.

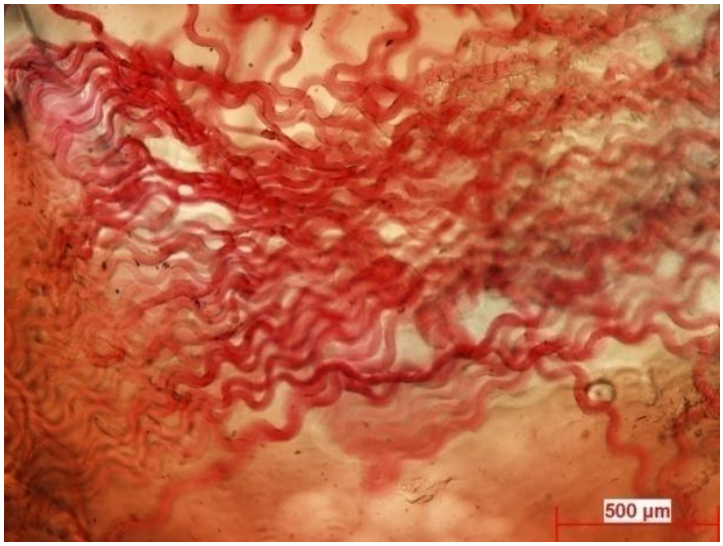

Figure 3.22. Collagen fibers entangled during elastin matrix casting.

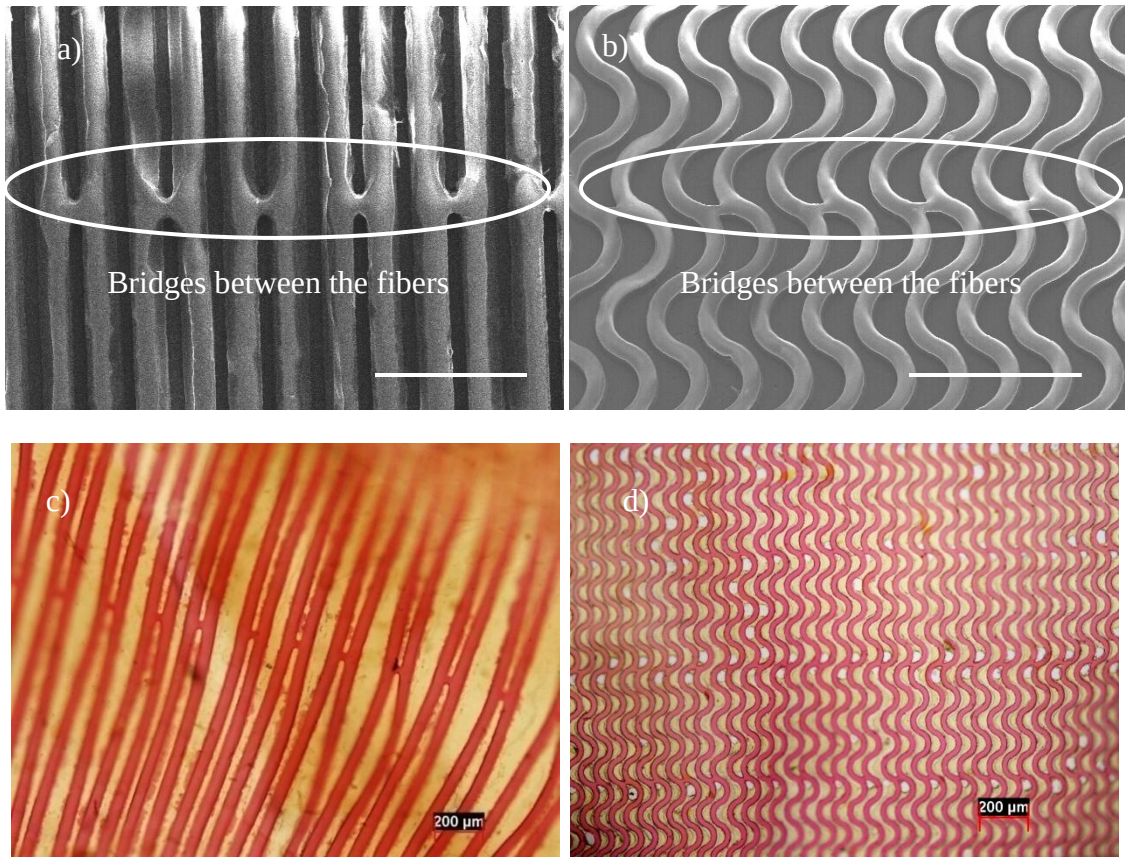

Figure 3.23. Collagen microfibers with bridges on a water soluble film: a) straight (scale bar = 100 µm), and b) serpentine (scale bar = 200 µm). Collagen-elastin FRC with bridges for: c) straight, and d) serpentine fibers. Collagen fibers were stained red using Van Gieson's.

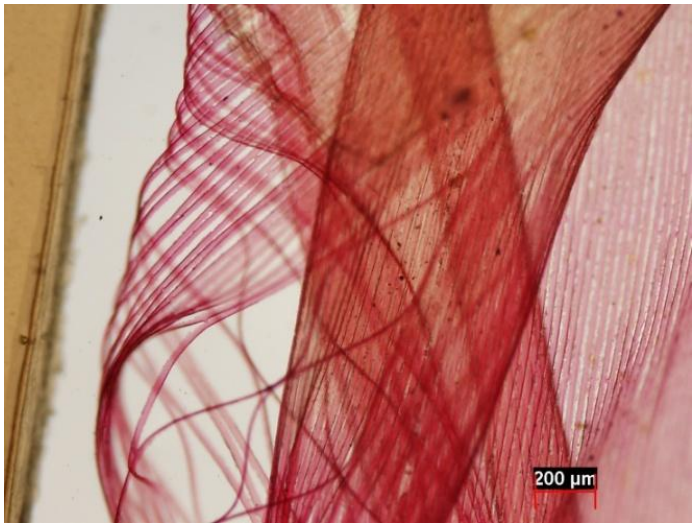

Figure 3.24. A collagen fiber network delaminated from the elastin matrix.

Lamination of composite material

To augment the influence of the fibers on the mechanical behavior of the FRC materials, it was required to increase the fiber volume fraction within the matrix. This was achieved by a 'stack, fuse and squeeze' approach, as shown in Figure 3.25. The required number of composite laminae were first aligned with each other under a microscope and layered. The layered materials were moved to a 4 °C atmosphere for 17 hours to liquefy the elastin matrix. The elastin layers liquefied and fused with one another. It was observed that some amount of water was introduced in the material while stacking layers of hydrated composite materials. This reduced the weight percent of elastin, significantly weakening the material. The weakening of the material was avoided by estimating the amount of water added by weighing samples before and after hydration, and evaporating the additional water in the cold room during the fusion process. This step approximately brought the material back to the original weight percent. The material was then gently pressed down using a glass slide to condense the film thickness to 100 μm, hence increasing the fiber volume fraction in the material (Figure 3.26).

Crosslinking

The composite materials were crosslinked in liquid-phase glutaraldehyde prior to mechanical testing.

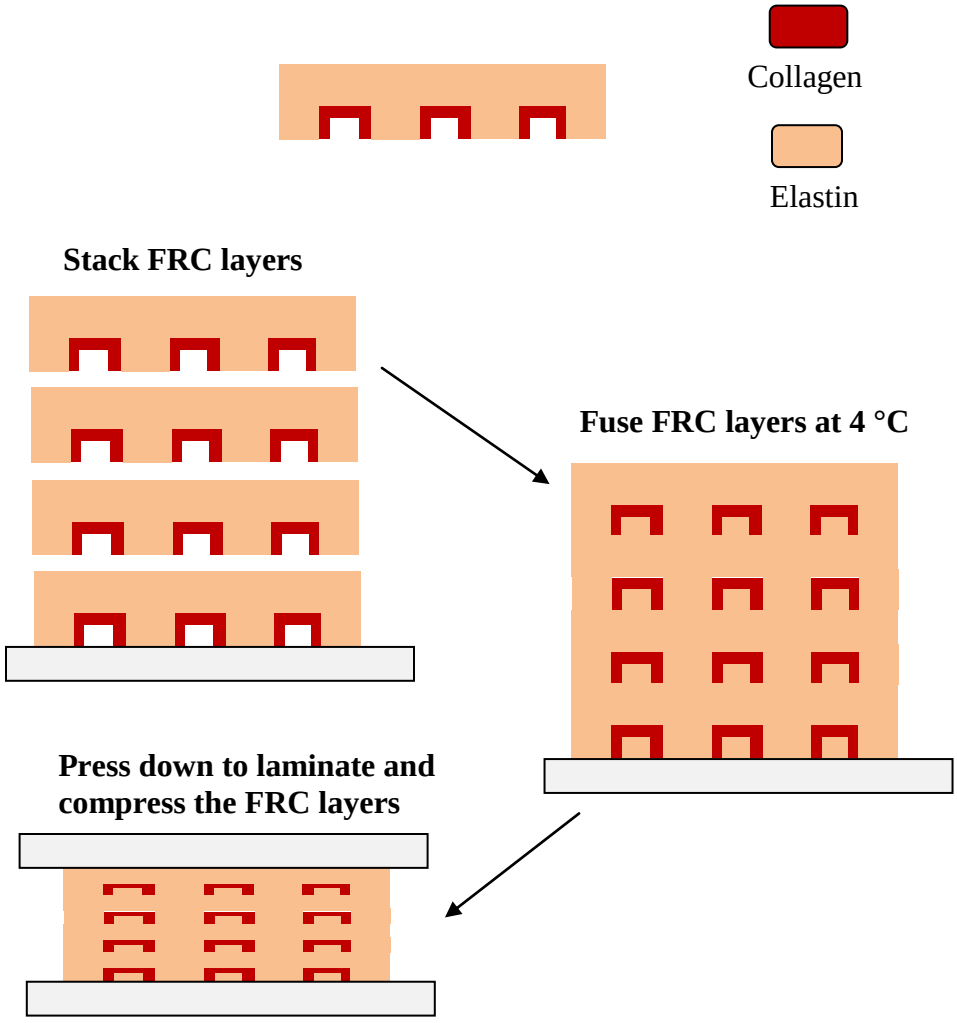

Figure 3.25. Fabrication process flow for laminated collagen-elastin FRCs.

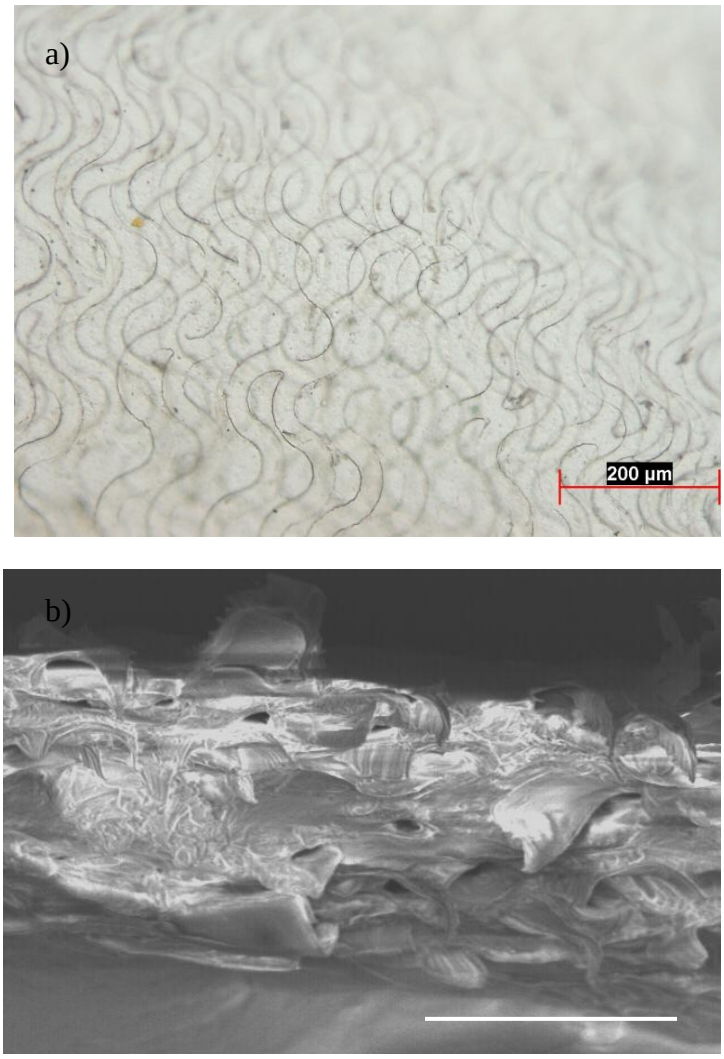

Figure 3.26. Laminated collagen-elastin FRCs: a) a microscope image illustrating overlapping fiber networks, and b) a cross-sectional SEM image displaying collagen fibers embedded in an elastin matrix (scale bar = 50 µm).

3.3 Mechanical characterization results

The FRC constituents, collagen fibers and elastin matrix, and the FRC tissue scaffolds were characterized for their mechanical properties in tension. The stress-strain relationship was derived by applying a tensile load (with a constant strain rate) to the material until failure. The hydrated material dimensions were considered for all these measurements.

Three parameters were analyzed from the derived engineering stress-strain curves:

1. Young's modulus of the material determined by the slope of the stress-strain curve in the elastic regime
2. Ultimate tensile strength or the maximum stress experienced by the material in tension
3. Failure strain of the material

3.3.1 Single fiber

3.3.1.1 Sample preparation

Straight fibers without bridges connecting them were employed for the mechanical characterization of individual collagen fibers. Fibers with a cross sectional dimension of 100 μm × 2 μm were utilized for these experiments, for ease of handling. Since fibers of all dimensions were carved out of the bulk material, it was expected that they would have similar mechanical properties. Single collagen fibers were isolated by dissolving the water soluble film holding them. These fibers were soaked in water for 12 hours to ensure complete dissolution of the water soluble film. The fibers were then manually separated under the microscope, and each fiber specimen was mounted on a C-

shaped plastic frame for mechanical support and handling, as shown in Figure 3.27. The ends of the fibers were glued to the top and the bottom horizontal sections of the frame, such that the length of the suspended fiber was 8 mm. The horizontal portions of the plastic frame were clamped to the grips of the sample mount on the DMA equipment (Rheometeric Inc.). Prior to application of the load, the vertical portion of the frame was cut to transfer the entire applied tensile load to the fiber. For obtaining properties of hydrated fibers, the sample mount was immersed into a PBS solution bath maintained at 37 ºC for the duration of the applied load. The dimensions of the fibers in the hydrated state were measured microscopically, and input to the DMA tool for the derivation of the stress-strain curves. A longitudinal loading strain rate of 0.64 % per second was applied to each fiber until failure. The stress-strain curves were derived by the DMA tool by measuring the force experienced by the fiber for each unit strain, and calculating the engineering stresses utilizing the input hydrated cross-sectional area of the fiber.

3.3.1.2 Observations

For all the parameters, the average and standard deviation were calculated from 10 measurements. The wet-spun collagen fibers exhibited a Young's modulus of 126 ± 61 MPa. The fibers fractured while still in the elastic regime and displayed a low failure strain of 5.4 ± 2.2 %. The ultimate tensile strength of the fibers was observed to be 7 ± 3.2 MPa (Figure 3.28, Table 3.2).

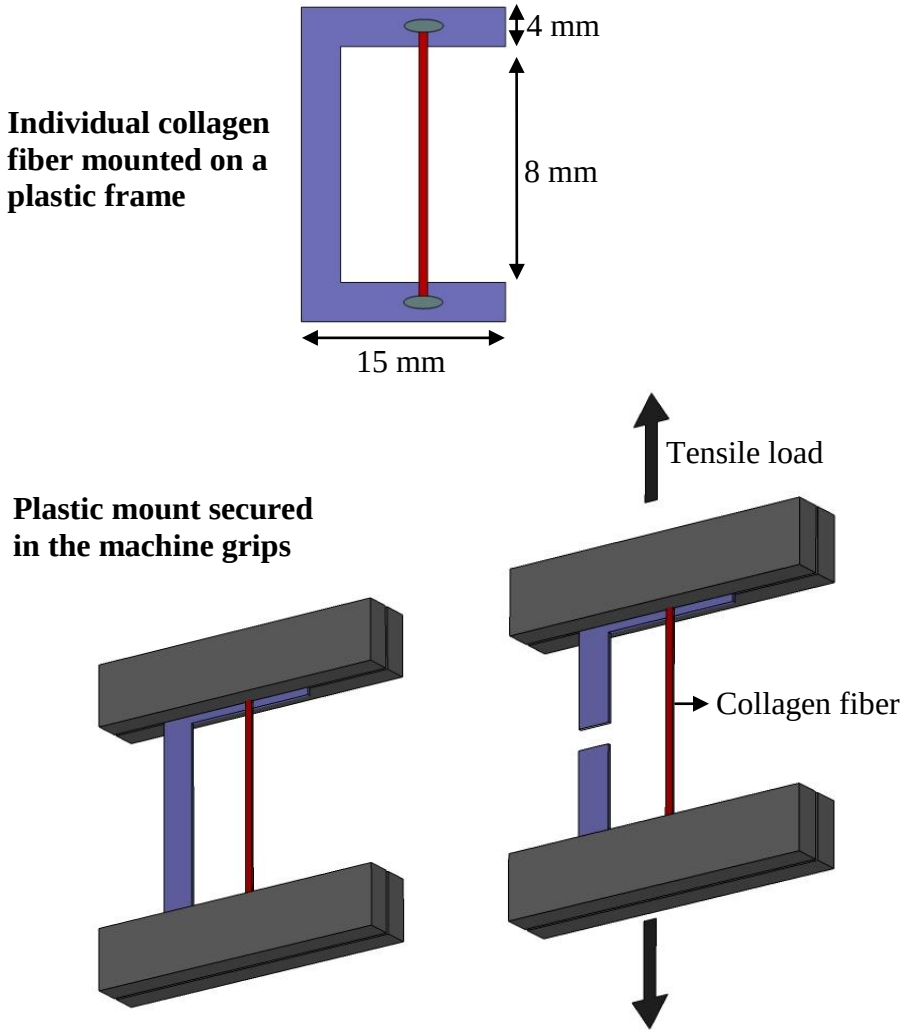

Figure 3.27. Sample preparation for mechanical characterization of a single collagen microfiber.

Table 3.3 lists the the mechanical properties of fibers obtained by the wet-spinning method in the current research, native collagen fibers, and engineered fibers as studied by other groups. As compared with the fibers fabricated by the wet-spinning method, the Young's modulus and strength of the template-based fibers were observed to be approximately 4-fold and 6-fold smaller respectively. There could be two possible

explanations for this. The flow-based approaches result in the alignment of collagen fibrils in the longitudinal direction of the fibers resulting from the hydrodynamic forces of the sheath fluid [22]. While the template-based method yields excellent alignment of the fibers, the fibrils within them primarily display a random orientation, as observed by AFM imaging. The alignment of the fibrils in the direction of the applied loads results in a higher load-bearing capacity in the resultant extruded fibers. Also, fibers obtained by spinning-based methods exhibit a higher strength as compared to their bulk material counterpart owing to the smaller imperfections observed in a smaller cross-section materials [23]. Since the template-based material provides fibers that are carved out of a bulk material, they have properties comparable to the bulk material.

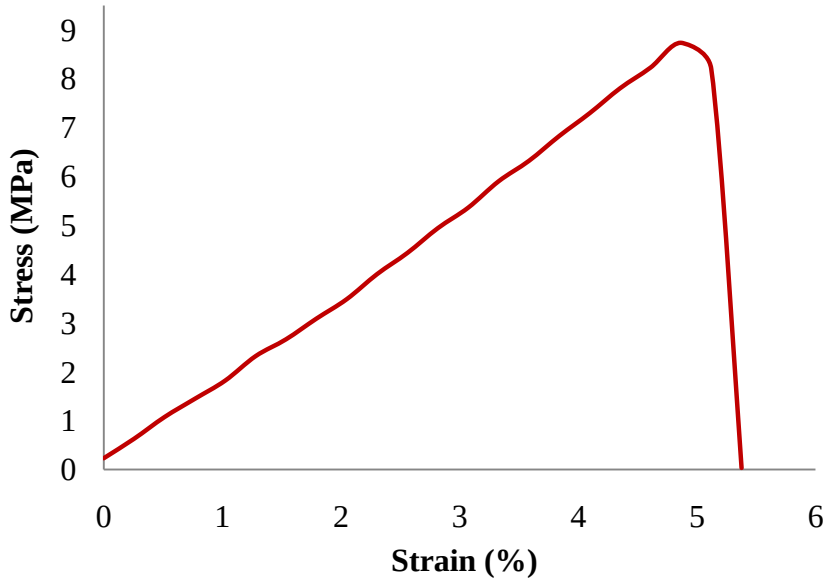

Figure 3.28. A representative stress-strain curve for single collagen fibers fabricated by the template-based method.

Table 3.2. Mechanical characterization of single collagen fibers fabricated by the template-based method.

Sample	Modulus of elasticity (MPa)	Ultimate tensile strength (MPa)	Failure strain (%)
Single fiber fabricated by the template-based method	126 ± 61 (n=10)	7 ± 3.2 (n =10)	5.4 ± 2.2 (n =10)

Table 3.3. Mechanical properties of hydrodynamically focused wet-spun fibers, native collagen fibers and engineered collagen fibers.

Sample	Modulus of elasticity (MPa)	Ultimate tensile strength (MPa)	Failure strain (%)	Reference
Hydrodynamically focused fiber (current study)	490 ± 50 (n=4)	40 ± 4.6 (n=4)	8.3 ± 1 (n=4)	
Native collagen fibers	1000	50-100	10	[24]
Electrospun collagen type I fibers	2820	25	33	[25]
Wet-spun collagen type I fibers (processing methods vary for different reports)	58-895	24-91	7-18	[26-29]

3.3.2 Elastin film

3.3.2.1 *Sample preparation*

Elastin solubilized in water (50 mg/ml) was cast into 100-μm thick elastin films on a glass substrate. The films were cut into 14 mm × 3 mm specimens in preparation for the mechanical characterization tests. The specimen to be tested was directly clamped to

the grips of the sample mount on the DMA equipment (Rheometeric Inc.) such that the suspended length of the specimen was 8 mm. For obtaining properties of hydrated fibers, the sample mount was immersed into a PBS solution bath maintained at 37 ºC for the duration of the applied load. The dimensions of the elastin specimens in the hydrated state were measured microscopically, and input to the DMA tool for the derivation of the stress-strain curves. A longitudinal loading strain rate of 0.64 % per second was applied to each specimen until failure. The stress-strain curves were derived by the DMA tool by measuring the force experienced by the specimen for each unit strain, and calculating the engineering stresses utilizing the input hydrated cross-sectional area of the fiber. The non-uniformities in the elastin film were not considered in these measurements.

3.3.2.2 Observations

For all the parameters, the average and standard deviation were calculated from 4 measurements. Elastin exhibited low stiffness and strength. The collagen fibers were observed to be 50-100 times stiffer than the elastin films. Elastin films were highly extensible and went through a considerable amount of deformation (strain 190 ± 65 %) before failure (Figure 3.29, Table 3.4).

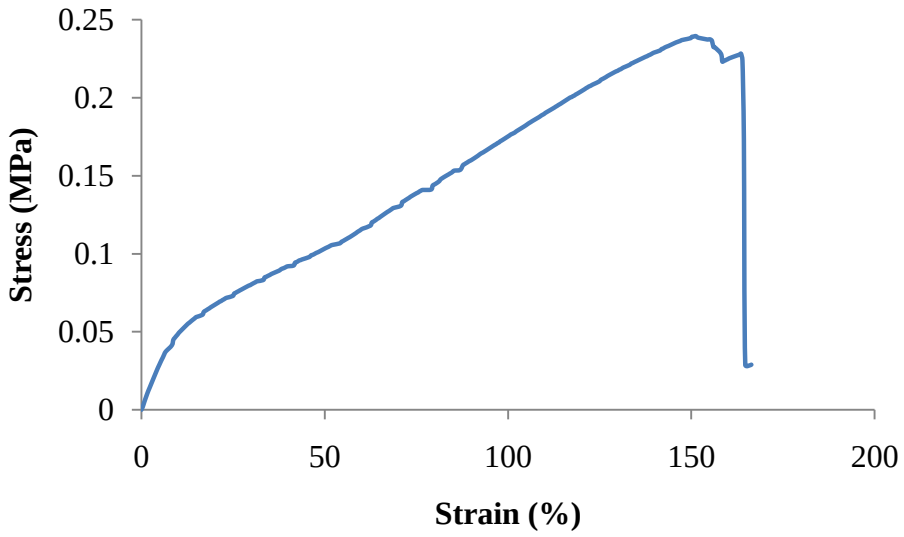

Figure 3.29. A representative stress-strain curve for an elastin film.

Table 3.4. Mechanical characterization of the elastin matrix.

Sample	Young's modulus (MPa)	Ultimate tensile strength (MPa)	Failure strain (%)
Elastin matrix (5 wt %)	0.25 ± 0.21 (n=4)	0.19 ± 0.05 (n=4)	190 ± 65 (n=4)

3.3.3 Straight fiber reinforced composites

3.3.3.1 FRC theory

The unidirectional FRC laminates with collagen fibers embedded in elastin matrix were tested in tension to study their property changes as a result of the combination of the constituents. In theory, the fibers and matrix in a fiber reinforced composite work synergistically to exhibit a property superior to the constituent properties, and the contribution of the fibers to a composite material attribute is determined by a parameter

known as the ‘fiber volume fraction’(FVF). It is defined as the volume percentage of the fibers over the total volume of the material (Equation 3.3).

$$V_f = \frac{v_f}{v_f + v_m} \tag{3.3}$$

Where,

V_f = FVF

v_f = volume of the fibers

v_m = volume of the matrix

Increasing the FVF enhances the strength and stiffness of the material owing to an increase in the load bearing components. In fact, the stiffness of the material in the direction of the fiber alignment can be estimated by a sum of fractions of the individual component properties. This theory is known as the ‘rule of mixtures’ and is expressed by Equation 3.4 [30].

$$E_c = E_f \times V_f + E_m \times V_m \tag{3.4}$$

Where,

E_c = Young’s modulus of the FRC

E_f = Young’s modulus of the fibers

V_f = FVF

E_m = Young’s modulus of the matrix

V_m = matrix volume fraction

3.3.3.2 <u>Sample preparation</u>

For the ease of fabrication and handling, 20-μm wide fiber networks with bridges were used for preparing composite laminates for the mechanical characterization experiments. The composite material was imaged using a microscope for the inspection

of the fiber alignment. Each laminate was cut into specimens of dimension 14 mm × 3 mm for DMA measurements. The length of the specimen under test was oriented in the direction of the fiber alignment for the measurement of the longitudinal properties, and the length of the specimen under test was oriented in the direction perpendicular to the fiber alignment for the measurement of the transverse properties. The thickness of each specimen was approximately 100 μm in the hydrated state. Composites with a FVF of 1, 4, 8, and 10 % were tested in tension. The specimen to be tested was directly clamped to the grips of the sample mount on the DMA equipment (Rheometeric Inc.) such that the suspended length of the specimen was 8 mm (Figure 3.30). For obtaining properties of hydrated fibers, the sample mount was immersed into a PBS solution bath maintained at 37 ºC for the duration of the applied load. A longitudinal loading strain rate of 0.64 % per second was applied to each specimen until failure. The loads applied to the longitudinal direction (aligned with the fiber direction) and the transverse direction (aligned perpendicular to the fiber direction) for prescribed strains were recorded to examine the orthotropic nature of the materials. The stress-strain curves were derived by the DMA tool by measuring the force experienced by the specimen for each unit strain, and calculating the engineering stresses utilizing the input hydrated cross-sectional area of the material. The non-uniformities in the composite films were not considered in these measurements.

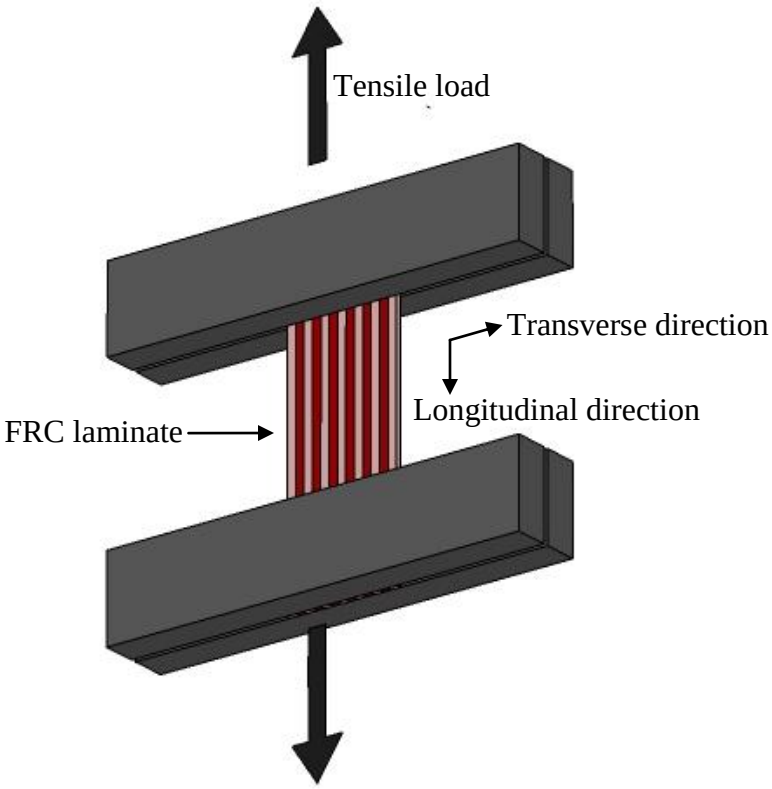

Figure 3.30. Sample preparation for mechanical characterization of an FRC.

3.3.3.3 Observations

The characterization revealed that the material exhibited the expected trend of stiffening in the longitudinal direction as compared to the transverse direction, demonstrating the orthotropic nature of the unidirectional FRCs. Figure 3.31 and Table 3.5 compare stress-strain relationships for FRCs with FVFs of 1, 4, 8, 10 % and an elastin film. In the longitudinal direction, the stiffness and the strength of the material were observed to increase with the FVF. Figure 3.32 illustrates the comparison of the measured moduli of stiffness for the FRCs and moduli of stiffness estimated using the rule of mixtures (Equation 3.4). The observed discrepancy between the measured and the

estimated curves may have resulted from an error in the FVF estimation. The failure strains were typically observed to decrease with the increasing concentrations of the fibers. But this was variable depending on the non-uniformities and imperfections present in the film. In the transverse direction, the FRC mechanical properties resembled that of the matrix material, elastin.

Table 3.5. Summary of mechanical characterization of the constituents and unidirectional straight fiber FRC laminates.

Sample	**Young's modulus (MPa)**	**Ultimate tensile strength (MPa)**	**Failure strain (%)**	
Single fiber	126 ± 61	7 ± 3.2	5.4 ± 2.2	n=10
Elastin matrix	0.25 ± 0.21	0.19 ± 0.05	190 ± 65	n=4
FRC 1% longitudinal	0.95 ± 0.35	0.22 ± 0.08	56.5 ± 12	n=3
FRC 1% transverse	0.31±0.04	0.17±0.03	81±12	n=2
FRC 4% longitudinal	3.1 ± 0.42	0.51 ± 0.08	42 ± 4.2	n=4
FRC 4% transverse	0.43±0.1	0.23±0.07	94±13	n=3
FRC 8% longitudinal	7.7 ± 1.9	0.87 ± 0.2	23 ± 4.7	n=4
FRC 8% transverse	1.4 ± 0.14	0.27 ± 0.04	103 ± 8.4	n=3
FRC 10% longitudinal	10.4 ± 0.5	0.87 ± 0.5	22 ± 2.8	n=2
FRC 10% Transverse	0.5	0.3	112	n=1

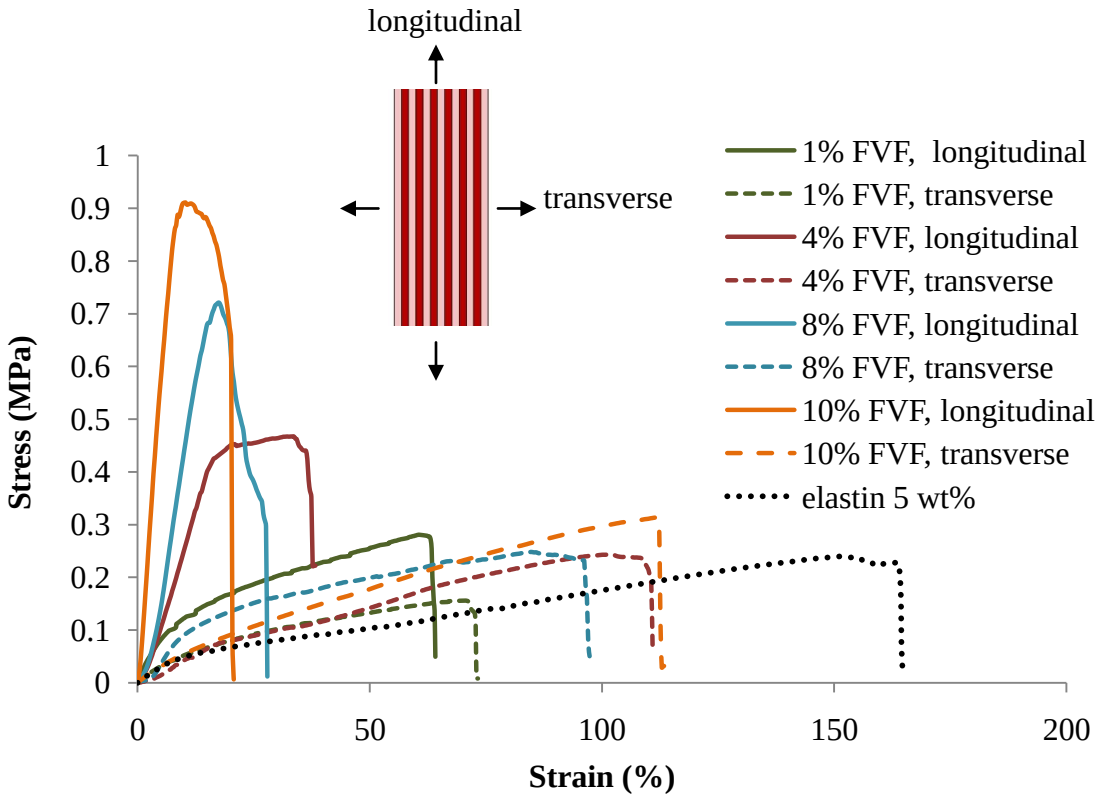

Figure 3.31. Mechanical characterization results for unidirectional straight fiber FRCs with volume fractions 1, 4, 8, and 10 %.

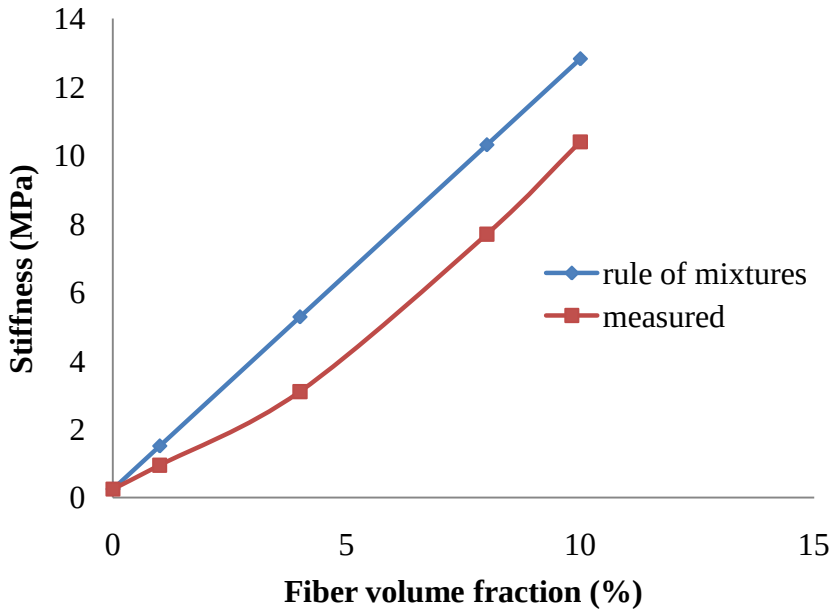

Figure 3.32. Influence of the FVF on the modulus of elasticity.

3.3.4 Crimped fiber composite

3.3.4.1 Sample preparation

For the ease of fabrication and handling, 25-μm wide in-plane crimped fiber networks with bridges were employed for constructing composite laminates for mechanical testing. These in-plane crimped fibers were fabricated to have a designed transition strain (Equation 3.2) of 27.4 %. The FVF for the tested FRCs was 4 %. The FRC material was imaged using a microscope for the inspection of fiber alignment. Each laminate was cut into specimens of dimension 14 mm × 3 mm for DMA measurements, with the length of the sample spanning in the direction of the fiber alignment. The thickness of each specimen was approximately 100 μm.

The specimen to be tested was directly clamped to the grips of the sample mount on the DMA equipment (Rheometeric Inc.) such that the suspended length of the specimen was 8 mm. For obtaining properties of hydrated fibers, the sample mount was immersed into a PBS solution bath maintained at 37 ºC for the duration of the applied load. A longitudinal loading strain rate of 0.64 % per second was applied to each specimen until failure. The load was applied to the longitudinal direction (aligned with the fiber direction) to examine the strain-dependent stiffness property of the materials. The non-uniformities in the composite films were not considered in these measurements.

3.3.4.2 Observations

A strain dependent stress-strain curve was predicted for the crimped FRCs. It was expected that at low strains, with the fibers still in a crimped state, the material would display a low modulus of elasticity dominated by the elastin material, slightly augmented by bending of the collagen fibers. At higher strains, as the fibers start to straighten, the

material would switch to a high modulus of elasticity characteristic of the fiber stiffness. This transition from a low modulus regime to a high modulus regime was exhibited by the in-plane crimped FRC materials, as dictated by the designed transition strain (Figure 3.33). For a designed strain of 27.4 %, the measured transition appeared to occur between 15-20 %. For a FVF of 4%, the Young's modulus of the material was observed to transition from 0.7 ± 0.14 MPa to 3.15 ± 0.49 MPa forming a toe-region as seen in native soft tissues. It was observed that the modulus of the crimped fiber FRCs in the low strain region (<10%) was comparable to, but slightly higher than, the modulus of elastin matrix (0.25 ± 0.21 MPa), as expected. At higher strains (>20 %), the modulus of this material matched well with the modulus of straight fiber FRCs with a FVF of 4% (3.1 ± 0.42 MPa).

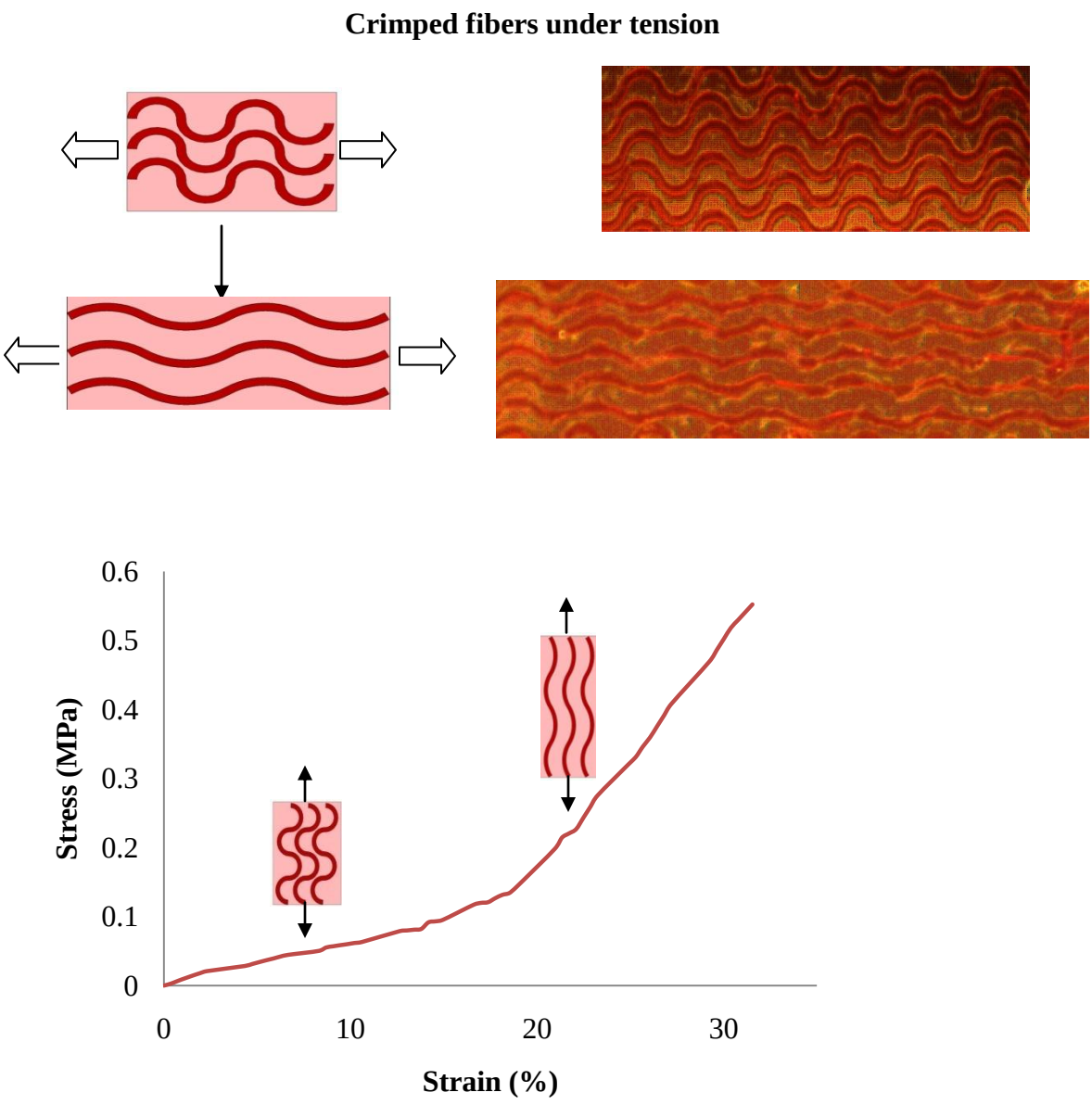

Figure 3.33. Mechanical characterization results for in-plane crimped fiber unidirectional FRC displaying a transition from a low modulus to a high modulus.

3.4 Conclusion

A microtransfer-molding-based methodology was established for the fabrication of spatially-designed collagen micro/nanofiber networks and collagen-elastin FRCs. The fabrication approach could produce fibers with a defined distribution and adjustable dimensions. Collagen micro/nanofibers with native morphology could be reproduced from acid-solubilized collagen making these scaffolds suitable for *in vivo* studies. The collagen fiber networks were encapsulated in elastin matrices to form FRC tissue scaffolds. The spatial layout of the fibers could be designed to create FRCs with anisotropic mechanical characteristics. Unidirectional straight fiber composites were tested in tension in the longitudinal and transverse directions with respect to the fiber network alignment to demonstrate their orthotropic nature. Increasing the FVF in these FRCs enhanced the contribution of the fibers to the elastic behavior resulting in stiffer materials. Finally, dual-elasticity materials with a strain-dependent stiffness were developed using in-plane crimped collagen fibers embedded in an elastin matrix resulting in non-linear mechanical characteristics as observed in native soft tissues. It was successfully demonstrated that controlling the microstructure of the tissue influences its macromechanical behavior.

3.5 References

1. Joseph D. Bronzino, "The biomedical engineering handbook: Tissue engineering and artificial organs," 3rd edition, CRC Press, 2006

2. Richard C. Becker, "Textbook of coronary thrombosis and thrombolysis," Springer, 1997

3. Chlupac, J; Filova, E; Bacakova, L, "Blood Vessel Replacement: 50 years of Development and Tissue Engineering Paradigms in Vascular Surgery," Physiological research, 2009, 58, p S119-S139

4. Buttafoco, L; Kolkman, NG; Engbers-Buijtenhuijs, P, et al., "Electrospinning of collagen and elastin for tissue engineering applications," Biomaterials, Feb 2006, 27(5), p 724-734

5. McClure, MJ; Sell, SA; Simpson, DG, et al., "Electrospun Polydioxanone, Elastin, and Collagen Vascular Scaffolds: Uniaxial Cyclic Distension," Journal of engineered fibers and fabrics, 2009, 4(2), p 18-25

6. Stitzel, J; Liu, L; Lee, SJ, et al., "Controlled fabrication of a biological vascular substitute," Biomaterials, 2006, 27, p 1088-1094

7. Boland, ED; Matthews, JA; Pawlowski, KJ, et al., "Electrospinning collagen and elastin: Preliminary vascular tissue engineering," Frontiers in bioscience, May 2004, 9, p 1422-1432

8. Caves, Jeffrey M.; Kumar, Vivek A.; Martinez, Adam W.; Kim, Jeong; Ripberger, Carrie M.; Haller, Carolyn A.; Chaikof, Elliot L., "The use of microfiber composites of elastin-like protein matrix reinforced with synthetic collagen in the design of vascular grafts,"Biomaterials, Sept 2010, 31(27), p 7175-7182

9. Brehmer, Martin; Conrad, Lars; Funk, Lutz; "New developments in soft lithography," Journal of Dispersion Science and Technology, May/July, 2003, 24(3-4), p 291-304

10. Zeugolis DI, Khew ST, Yew ESY, et al., "Electro-spinning of pure collagen nano-fibres - Just an expensive way to make gelatin?," Biomaterials, May 2008, 29(15), p 2293-2305

11. Yen Sun (Dept. of Phys., Nat. Taiwan Univ., Taipei, Taiwan); Wei-Liang Chen; Sung-Jan Lin; Shiou-Hwa Jee; Yang-Fang Chen; Ling-Chih Lin; So, P.T.C.; Chen-Yuan Dong ,"Investigating mechanisms of collagen thermal denaturation by high resolution second-harmonic generation imaging," Biophysical Journal, Oct 2006, 91(7), p 2620-5

12. Bigi A, Cojazzi G, Roveri N, et al., "Differential scanning calorimetry and x-ray-diffraction study of tendon collagen thermal-denaturation," International journal of biological macromolecules, Dec 1987, 9(6), p 363-367

13. Gross J, "Thermal denaturation of collagen in dispersed solid state," Science, 143(360), p 960

14. Peter Fratzl, "Collagen: Structure and Mechanics," 1st edition, Springer, 2008

15. Yost MY, Terracio L, Price RL., "Collagen processing," Encyclopedia of biomaterials and biomedical engineering 2004, p 348–354

16. Davidson RJ, Cooper DR, "Effect of ultraviolet irradiation on acid-soluble collagen," Biochemical journal, 1967, 105(3), p 965

17. Xuebin Tan; Zhuyuan Wang; Jing Yang; Chunyuan Song; Ruohu Zhang; Yiping Cui "Polyvinylpyrrolidone- (PVP-) coated silver aggregates for high performance surface-enhanced Raman scattering in living cells," Nanotechnology, Nov 2009, 20(44), p 445102

18. Risbud H, Hardikar A, Bhonde R, "Chitosan-polyvinyl pyrrolidone hydrogels as candidate for islet immunoisolation: *In vitro* biocompatibility evaluation," Cell transplantation, Jan 2000, 9(1), p 25-31

19. Caves, Jeffrey M.; Kumar, Vivek A.; Xu, Wenjun; Naik, Nisarga; Allen, Mark G.; Chaikof, Elliot L.; "Microcrimped collagen fiber-elastin composites," Advanced Materials, May 2010, 22(18), p 2041-2044

20. Jiang FZ, Horber H, Howard J, et al., "Assembly of collagen into microribbons: effects of pH and electrolytes," Journal of structural biology, 148(3), p 268-278

21. Venturoni M, Gutsmann T, Fantner GE, et al., "Investigations into the polymorphism of rat tail tendon fibrils using atomic force microscopy," Biochemical and biophysical research communications, Apr 2003, 303(2), p 508-513

22. Köster, Sarah; Leach, Jennie B.; Struth, Bernd; Pfohl, Thomas; Wong, Joyce Y., "Visualization of flow-aligned type I collagen self-assembly in tunable pH gradients," Langmuir, Jan 2007, 23(2), p 357-359

23. A. R. Bunsell, Jacques Renard, “Fundamentals of fibre reinforced composite materials,” CRC Press, 2005

24. Joon Bu Park, Roderic S. Lakes, “Biomaterials: an introduction,”

25. C.R. Carlisle, C. Coulais 1, M. Guthold ,“The mechanical stress–strain properties of single electrospun collagen type I nanofibers,”

26. Caves, Jeffrey M.; Kumar, Vivek A.; Wen, Jing; Cui, Wanxing; Martinez, Adam; Apkarian, Robert; Coats, Julie E.; Berland, Keith; Chaikof, Elliot L. “Fibrillogenesis in continuously spun synthetic collagen fiber,”Journal of Biomedical Materials Research - Part B Applied Biomaterials, Apr 2010, 93(1), p 24-38

27. Gentleman, E., et al., “Mechanical characterization of collagen fibers and scaffolds for tissue engineering.,” Biomaterials, 2003, 24(21): p. 3805-13

28. Wang, Ming-Che; Pins, George D.; Silver, Frederick H. “Collagen fibres with improved strength for the repair of soft tissue injuries,” Biomaterials, Jun 1994, 15(7), p 507-512

29. Pins, George D.; Huang, Eric K.; Christiansen, David L.; Silver, Frederick H., “ Effects of static axial strain on the tensile properties and failure mechanisms of self-assembled collagen fibers,” Journal of Applied Polymer Science, Mar 1997, 63(11), p 1429-1440

30. Donald R. Askeland, Pradeep Prabhakar Phulé, “The science and engineering of materials,” Cengage Learning, 2006

CHAPTER 4

CELL-BASED THERAPEUTICS IN MICROVASCULAR SCAFFOLDS

4.1 Introduction

The circulatory system in the human body consists of three kinds of interconnected blood vessels: arteries, veins, and capillaries, as shown in Figure 4.1. This vascular system is responsible for the transportation of blood within the body and the exchange of oxygen, carbon dioxide, nutrients, and waste materials between blood and various tissues. Blood vessels in the human body display a wide range of dimensional scales. The largest artery (aorta) measures 2.5-3 cm in diameter; whereas the capillaries are only 8-10 μm in diameter [1].

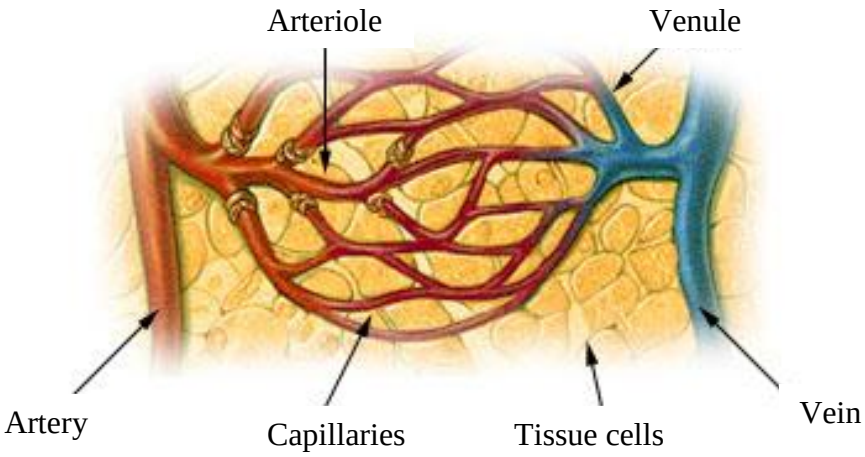

Figure 4.1. Blood vessels and their interconnections [2].

A substantial effort has been dedicated towards the development of vascularized tissues *in vitro* to ensure the nourishment and viability of engineered living tissues.

Although various approaches have been investigated for individual vascular grafts with diameters 1 mm and above, the development of *in vitro* models for microcapillary networks has advanced substantially since the advent of MEMS technology. Micromachining strategies have allowed for the construction of microchannel fluidic devices with complex shapes necessary for developing a functional cell-seeded 'living' microvasculature network. Micromolding is the most commonly used fabrication approach for microvascular networks and has been applied for the fabrication of both 2D and 3D structures. A wide range of materials have been utilized for this application. On account of its high permeability, biocompatibility, and elastomeric nature, PDMS has been used for fabricating microvasculature by various groups, including Borenstein et al., who reported the first microfabricated capillary network in 2002 [3-6]. PDMS microvascular networks incorporating bifurcations, different size scales, and optimized fluidic transport conditions have been reported. The micromolding fabrication approach for microcapillary networks has been extended to biodegradable polymers such as PLGA [7], PCL [8], and polyglycerol sebacate (PGS) [9]. Molded microcapillaries with circular cross-sections have been developed to mimic the geometry of blood vessels and prevent the problems associated with cell seeding of sharp corners of rectangular channels. Master molds for this purpose have been fabricated using electroplating [10] and isotropic xenon difluoride etching of silicon [11].

The current research adopted the aforementioned micromolding methodology for the fabrication of two different microvascular structures and focused on the incorporation of cells in these networks using a fluidic self-assembly process. Two types of cells, islet

cells and endothelial cells, were explored for the emulation of specific tissue and organ functionalities, as described below:

Islet cells

The islets of Langerhans are cell clusters constituting the endocrine part of the pancreas. These cells secrete insulin, a hormone responsible for the regulation of the blood glucose level. A body's inability to produce sufficient insulin results in the condition known as Type 1 diabetes. Normally, when blood glucose rises above the basal level, the islet cells respond by secreting insulin. This causes the blood glucose to be taken up by various cells and stored as glycogen in the liver and muscles. In the diabetic case, the insulin-producing cells undergo autoimmune destruction resulting in hyperglycemia or high blood glucose. The typical treatment for diabetes involves the administration of hypoglycemic drugs or daily insulin injections, depending on the severity of the disease in the patient. These remedies imply a lifetime dependence on medication and do not provide realtime blood-glucose regulation as is performed by the pancreas. This has motivated extensive research in an alternative therapy involving extravascular or intravascular islet-cell-based bioartificial pancreas constructs. The first cell-based construct in this dissertation comprised a collagen microvascular bioreactor with localized immobilization of islet cells for potential bioartificial pancreatic device applications.

Endothelial cells

The innermost layer of the lumen of a native blood vessel is composed of a monolayer of multifunctional endothelial cells. This endothelium layer provides a smooth surface for the blood to flow over. The blood contains cell fragments known as platelets,

which play a fundamental role in blood clot formation or thrombosis. Any damage to the endothelium lining exposes the sub-endothelial membrane with proteins and other factors that trigger platelet activation and thrombosis. Owing to the lack of such an endothelium layer, intravascular small-bore constructs often exhibit poor long term patency as a result of thrombosis. The necessity for a nonthrombogenic surface in these vascular grafts has resulted in the examination of *in vitro* seeding of endothelial cells on the luminal surface of the grafts. Reports have demonstrated that endothelialized vascular grafts display a higher patency rate and a smaller thrombotic response as compared to non-seeded grafts [12]. The second construct in this dissertation comprised a deformable, reentrant PDMS microvascular scaffold allowing for a more uniform endothelial cell seeding of high length-to-depth aspect ratio microvasculature.

The microvascular constructs with incorporated islet cells and endothelial cells are discussed in the following sections.

4.2 Localized immobilization of islet cells in microvascular scaffolds

As discussed in chapter 1, a large number of extravascular and intravascular devices have been investigated for bioartificial organ applications. Although both classes of devices have shown success, they face some implementation challenges. Extravascular constructs typically suffer from limited cell viability resulting from a lack of contact with the blood stream. Most intravascular devices tend to be larger than their microscale bioreactor counterparts. Such devices also face potential cell aggregation resulting in issues with the mass transport of oxygen and nutrients to the cells.

The current research focused on the development of a MEMS-based microvascular tissue network hosting and nourishing islet cells for potential application as a bioartificial pancreas. It was hypothesized that the microvascular networks housing islet cells would provide better cell viability as compared to extravascular devices. A circuit of compartments for localized immobilization of organ-specific cells built into the microvascular network would offer a dispersed immobilized cell system and avoid cell aggregation. Additionally, a microvasculature carrying a dense array of cells would allow for miniaturization of the overall device.

4.2.1 Fabrication development for particle immobilization in microvascular scaffolds

A prototypical fabrication approach for localized particle immobilization in microvascular scaffolds was first demonstrated using glass beads (diameter: 10-30 µm, 150-210 µm, Polysciences Inc.) as proxy particles. The fabrication process applied two MEMS processing techniques, namely, micromolding and template-guided fluidic self-assembly.

The process flow employed for the development of a microvascular tissue scaffold with localized particle encapsulation is illustrated in Figure 4.2. The fabrication was initiated by designing a suitable silicon template. The template was tailored to bear microcompartments placed periodically in fluidic microchannels to capture the particles. The compartment diameter was designed to be larger, and the channel width was designed to be smaller than the target particle size to ensure that all the particles were restricted inside the compartments. A (100) silicon wafer was used as the substrate for the

fabrication of the templates. Photoresist AZ 4620 (Hoechst Celanese Corp., Somerville, NJ) was spin-coated and patterned using photolithography. The microchannels and compartments were etched into the silicon wafer using ICP etching (Bosch process). The photoresist was etched using acetone and oxygen plasma RIE, leaving behind a silicon template for localized particle encapsulation, as shown in Figure 4.3a. The silicon wafer was cut into 2 cm × 2 cm chips. Each silicon chip was utilized for micromolding of the tissue matrix collagen. The molding was performed by solvent casting of collagen solution (concentration = 1.5 mg/ml in 10 mM HCl) to form a 500-700-nm thick conformal collagen film.

The glass beads were then planted and immobilized in the compartments by template-guided fluidic self-assembly, a technique involving the assembly of microscale objects into a template with complementary patterns etched into them [13]. The glass beads were suspended in water (0.5 gm/ml). 2 ml of the glass bead suspension was released over the template using a pipette. The template was provided with agitation allowing the glass beads to be directed into the microcompartments under gravitational and fluid dynamic forces, as shown in Figure 4.3b. The beads that failed to occupy an empty site were washed away. A fill factor of 96 - 98 % was achieved for this process (Figure 4.4).

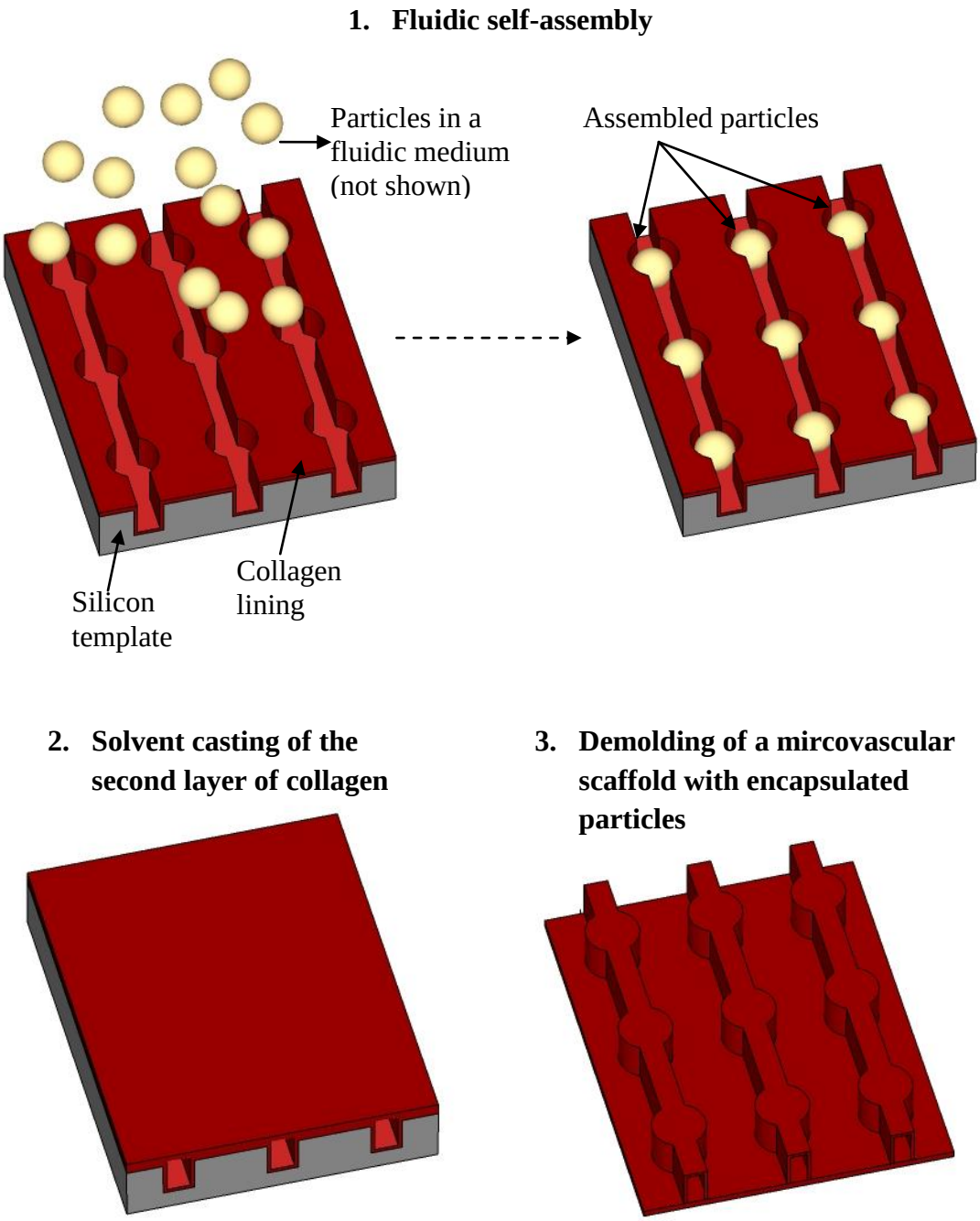

Figure 4.2. Fabrication process flow for localized particle encapsulation in microvascular scaffolds.

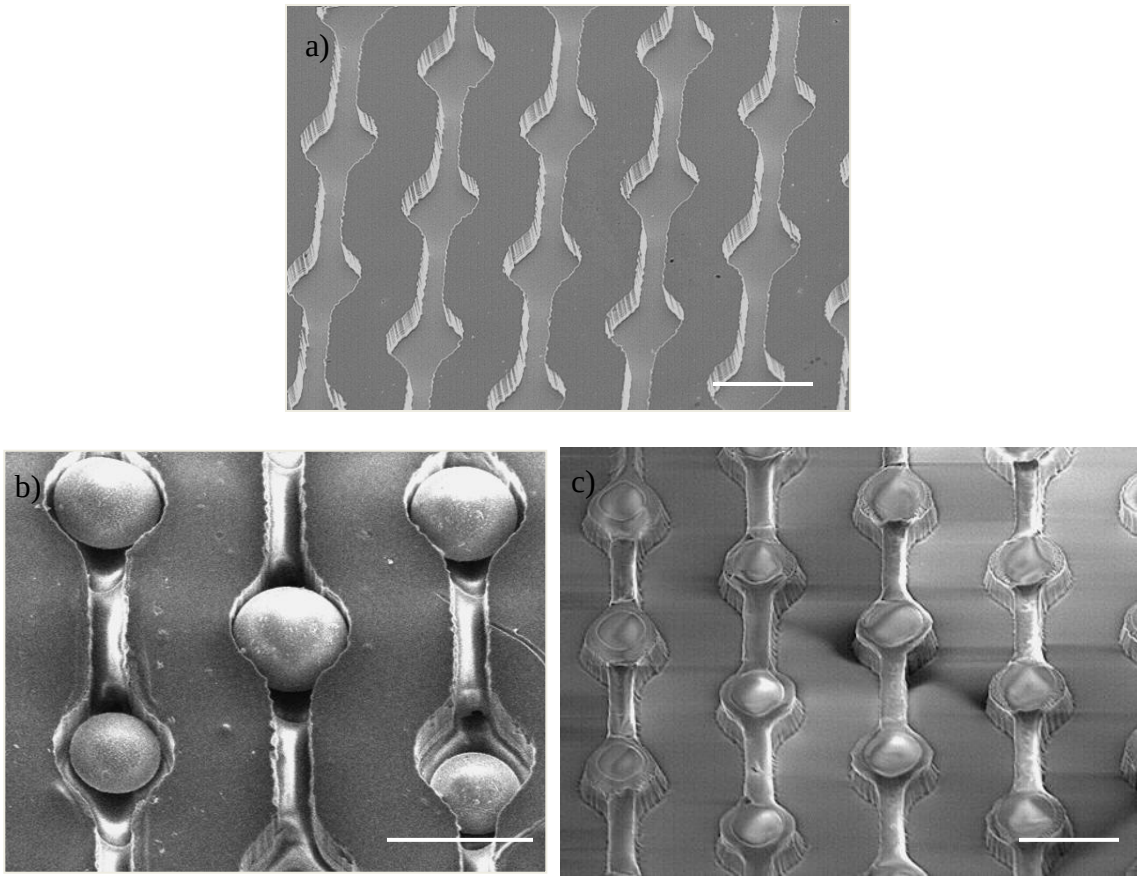

Figure 4.3. SEM images of a) a silicon template for the fabrication of microvascular scaffolds with localized particle encapsulation, b) glass beads assembled in the microcompartments in the scaffold, and c) a standalone collagen microvascular tissue scaffold with locally immobilized glass beads extricated using a water soluble tape. (scale bars = 50 μm)

To form enclosed microvascular scaffolds, a viscous solution of collagen (concentration = 5 mg/ml) was solvent cast on the existing layer of molded collagen with the embedded particles. Surface tension effects resulted in a planar, non-conformal film above the first layer of collagen. The two layers were fused, creating a hollow collagen tissue scaffold with encapsulated glass beads. The 3-D tissue structure was extracted from the silicon template using a water soluble tape. A standalone microvascular tissue scaffold with locally immobilized particles was obtained, as shown in Figure 4.3c.

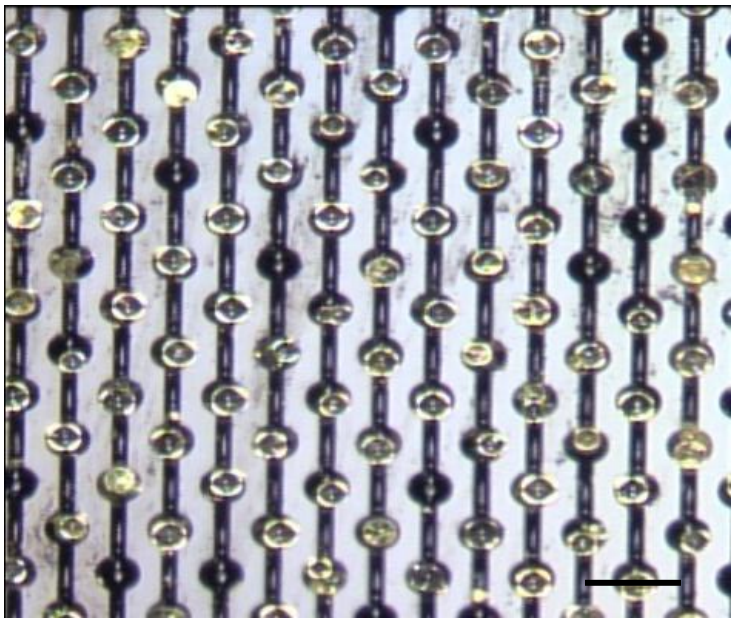

Figure 4.4. Fluidic self-assembly with glass beads illustrating a fill efficiency > 96 % (scale bar = 500 µm).

4.2.2 Microvascular insulin bioreactor

A functional tissue or organ construct requires successful integration and interaction of scaffold structures with various cells. Therefore, the next step was to adopt the devised fabrication technology for the incorporation of pancreatic islet cells in microvascular tissues for imparting therapeutic characteristics. To acknowledge and investigate the additional complexities involved in confining cells in such a configuration, this research was initiated with the development of a microfluidic bioreactor device. A MEMS-based microvascular insulin bioreactor housing locally immobilized islet cells was constructed towards the development of a bioartificial pancreas with an inbuilt microcirculatory system, as a first step to addressing some of the discussed problems encountered in bioartificial organs. As described in the fabrication

development, micromolding of collagen and fluidic self-assembly of islet cells were employed for constructing this device.

Template guided fluidic self-assembly of cells, such as hepatocytes, lymphocytes, and islet cells has previously been applied for microwell and microchamber bioreactor arrays for cell-based studies and the fabrication of cell-encapsulated hydrogel tissues [14-17]. Additionally, fluidically assembled islet cells on microfluidic platforms have been investigated for the evaluation of insulin secretion, calcium influx, and mitochondrial potential changes of islet cells [15, 18]. In the current study, this approach was employed for the demonstration of the immobilization of islet cells in a microvascular tissue bioreactor and the examination of its potential for bioartificial pancreas applications. The cellular functionality in such an environment was studied by adopting principles from perfusion-based microchannel bioreactors.

4.2.2.1 Device development

Bioreactor device fabrication

A silicon microfluidic chip (area = 2.4 cm × 2.4 cm, volume = 40 µl) formed the foundation of the bioreactor. The chip comprised a reservoir connected to an array of microchannels with microcompartments located periodically in the channels. The islet cell clusters used for the experiments ranged from 70-250 µm in diameter. The compartment diameter (250 µm) and the channel width (70 µm) were designed to ensure that all the cells were confined to the compartments. The fabrication process was modified from the prototype development to construct a multi-depth structure. This modification was significant for two reasons. High-aspect-ratio constructs were not suitable for casting collagen films and led to polymer webbing and nonuniformities. The

multi-depth design allowed the channels and compartments to have a near-unity depth-to-width aspect ratio facilitating the formation of a conformal collagen film. Also, in this geometry, the compartments for organ-specific cell encapsulation were deeper than the microchannels allowing the cells to settle in deeper regions. The fluid flow profile in such an arrangement was believed to reduce the shear stress experienced by the cells. This hypothesis was based on reports presenting grooved microchannel bioreactors with cells cultured inside grooves in the flow channels [19]. In these reports, it was experimentally and numerically proved that this design minimized the shear stress exerted on the cells. The process flow for the multi-depth templates is illustrated in Figure 4.5.

The multi-depth microfluidic templates were fabricated using photolithography and two-step ICP etching. A 1-μm thick SiO_2 layer was deposited on a (100) silicon substrate using plasma enhanced chemical vapor deposition (PECVD). Positive photoresist SC 1827 (Shipley Co., Marlborough, MA) was spin-coated and patterned to define the microchannels and compartments. The pattern was transferred to the SiO_2 layer using ICP etching. A second layer of photoresist AZ 4620 (Hoechst Celanese Corp, Somerville, NJ) was then spin-coated and patterned to mask the SiO_2 channel patterns, while leaving the microcompartment patterns exposed. ICP etching was carried out to etch the compartments into the silicon substrate to achieve a depth equal to the differential of the final depths of the compartments and the channels.

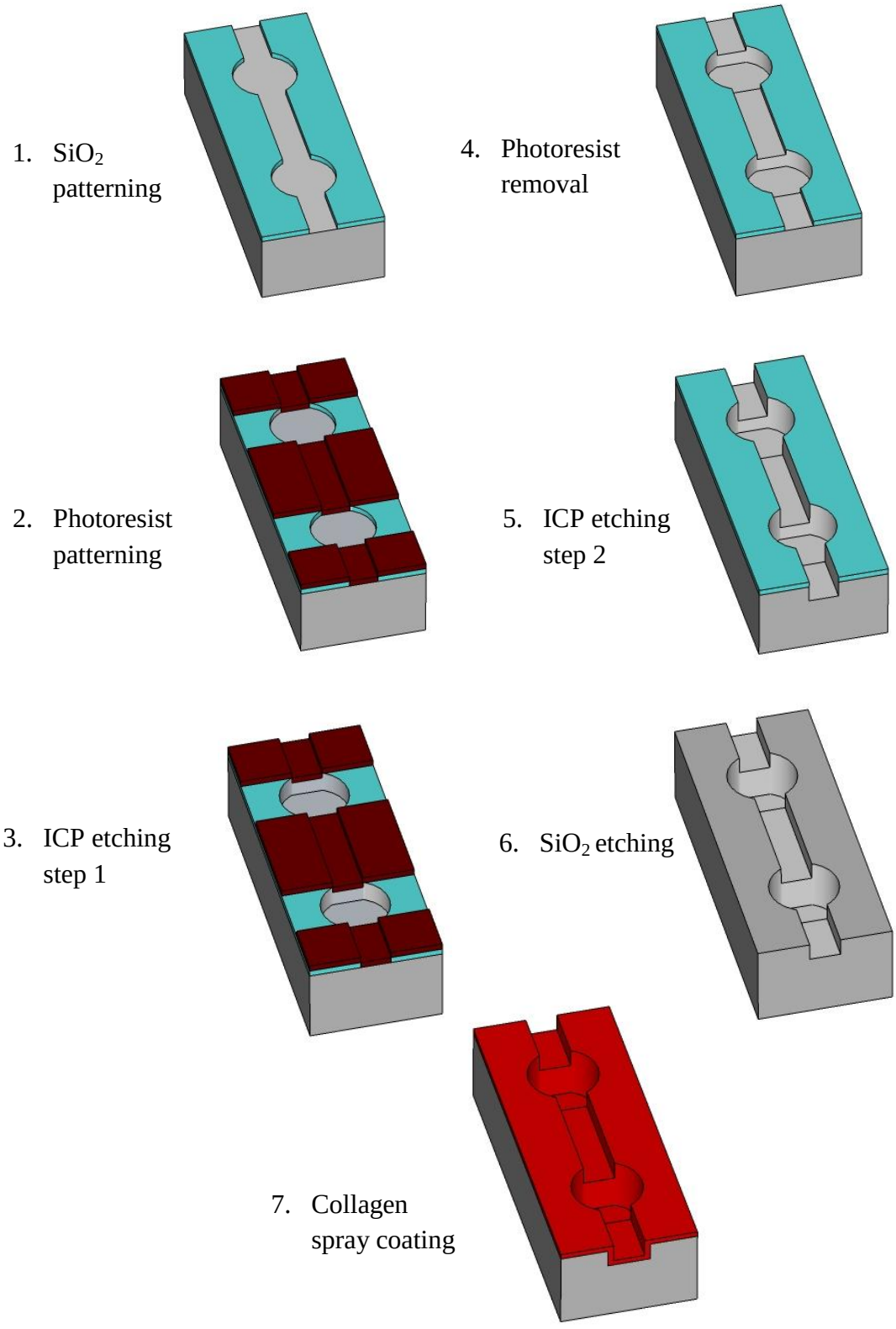

Figure 4.5. Fabrication process flow for a multi-depth template for an insulin bioreactor.

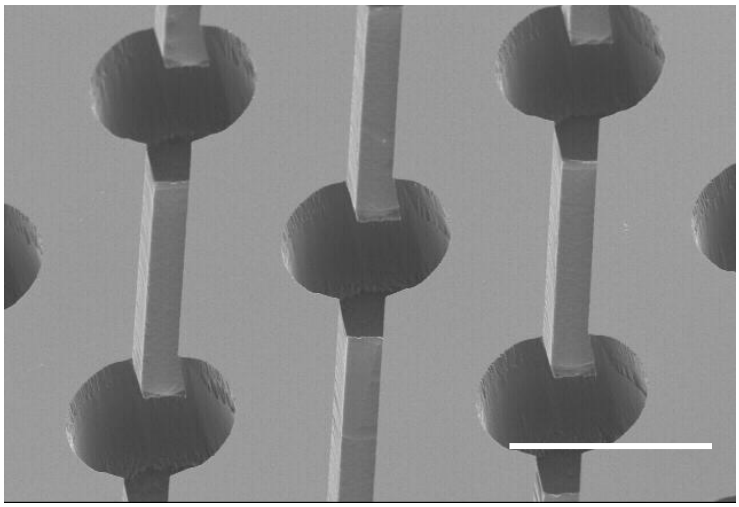

Figure 4.6. A multi-depth silicon template used for the insulin bioreactor (scale bar = 250 μm).

The photoresist layer was etched away using acetone and oxygen plasma RIE, unmasking the microchannels in the SiO_2 film. The ICP etching was then continued to etch the channels and compartments to attain the respective target depths. The resultant template consisted of shallow channels and deep compartments, as shown in Figure 4.6. Finally, tissue matrix collagen was spray-coated over the template to form a 700 nm - 1 μm thick conformal film.

Isolation of islet cells

Pancreatic islet cells were isolated from a murine model. For obtaining the cells, a solution of collagenase enzyme was intraductally delivered to the pancreas to cause its distension and subsequent digestion releasing the islet cells. The collected islet cells were then purified to separate them from the exocrine tissue. Prior to glucose stimulation fluidic experiments, the islet cells were cultured in RPMI1640 media for 2 days. The obtained islet cell clusters ranged from 50-300 μm in diameter, as shown in Figure 4.7.

65-80% of each cell cluster was composed of beta cells responsible for the production of insulin in response to glucose stimulation.

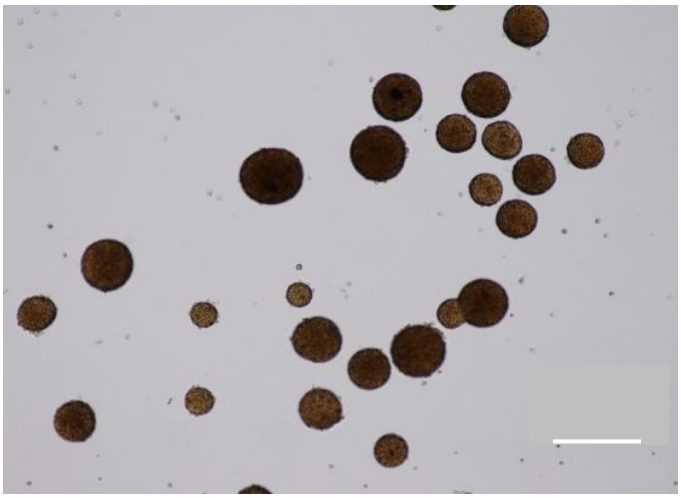

Figure 4.7. Islet cell clusters in a cell culture media. The diameters of the islet cells vary from 50- 300 μm. (scale bar = 300 μm)

Immobilization of islet cells

Prior to the delivery of the islet cells to the template, a PDMS (Sylgard 184, Dow Corning Co., Midland, MI) frame was clamped onto the microfluidic chip to contain the islet cells to a specific area (Figure 4.8a). The desired number of islet cells (in RPMI1640 media) were pipetted into the PDMS container. The template was placed on a micropipette shaker to provide fluidic convection facilitating the fluidic self-assembly of the islet cells into the molded tissue scaffolds. 97-99 % of the cells used were observed to take position in the wells. The cells failing to occupy an empty site were washed away with the excess cell culture media upon the release of the PDMS frame, as shown in Figure 4.8b.

a)

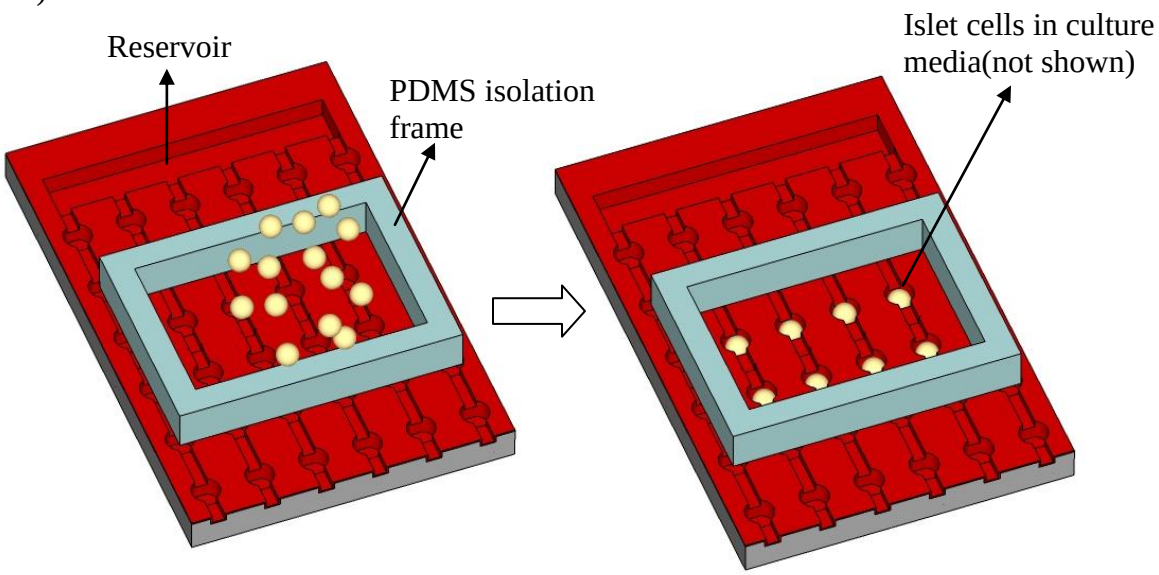

b)

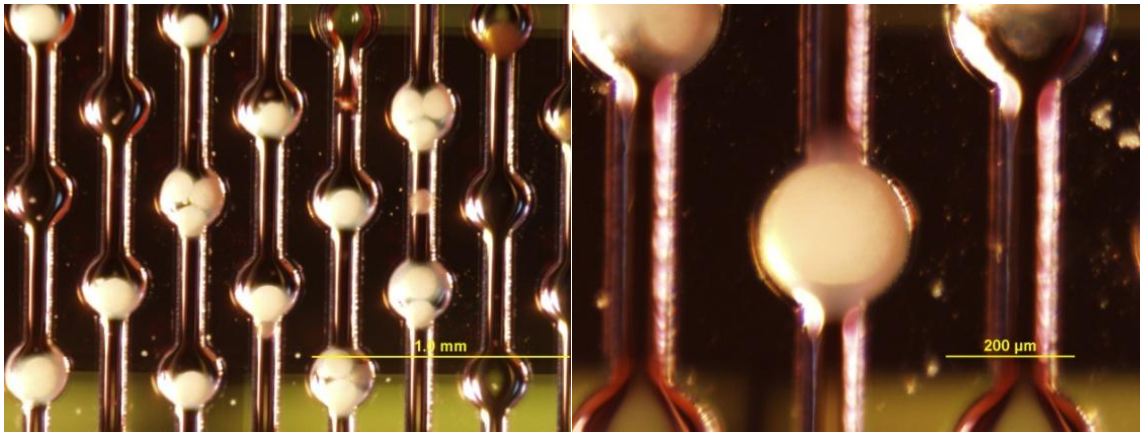

Figure 4.8. a) A PDMS isolation frame for fluidic self-assembly of islet cells, and b) murine islet cells self-assembled into compartments in a collagen-coated silicon template.

4.2.2.2 Experimental apparatus

The microvascular fluidic chip with entrapped islet cells was enclosed by bonding it with a glass plate (thickness = 2 mm) coated with a PDMS layer and clamping the two substrates together using an aluminum frame. The glass plate offered rigidity to the bioreactor lid, and the PDMS layer helped form a leak proof interface. Prior to the bonding step, an input port was drilled into the glass plate and aligned with the reservoir supplying the microchannels. The assembly was integrated with a syringe pump to regulate the flow rate of glucose solution through the microchannels. The experimental apparatus for the bioreactor device is illustrated in Figure 4.9. The flow experiments were performed in an incubator at 37 °C with 1.5% CO_2. Glucose solutions (in Dulbecko's phosphate buffer saline (DPBS) and 1% bovine serum albumin (BSA) stock solution) with basal concentration (60 mg/dl) and high concentration (300 mg/dl) were flowed alternately through the bioreactor device. A flowrate of 5 ml/hr was used to study the behavior of the cells in response to changing glucose concentrations. The insulin secretion was quantified by assaying the output.

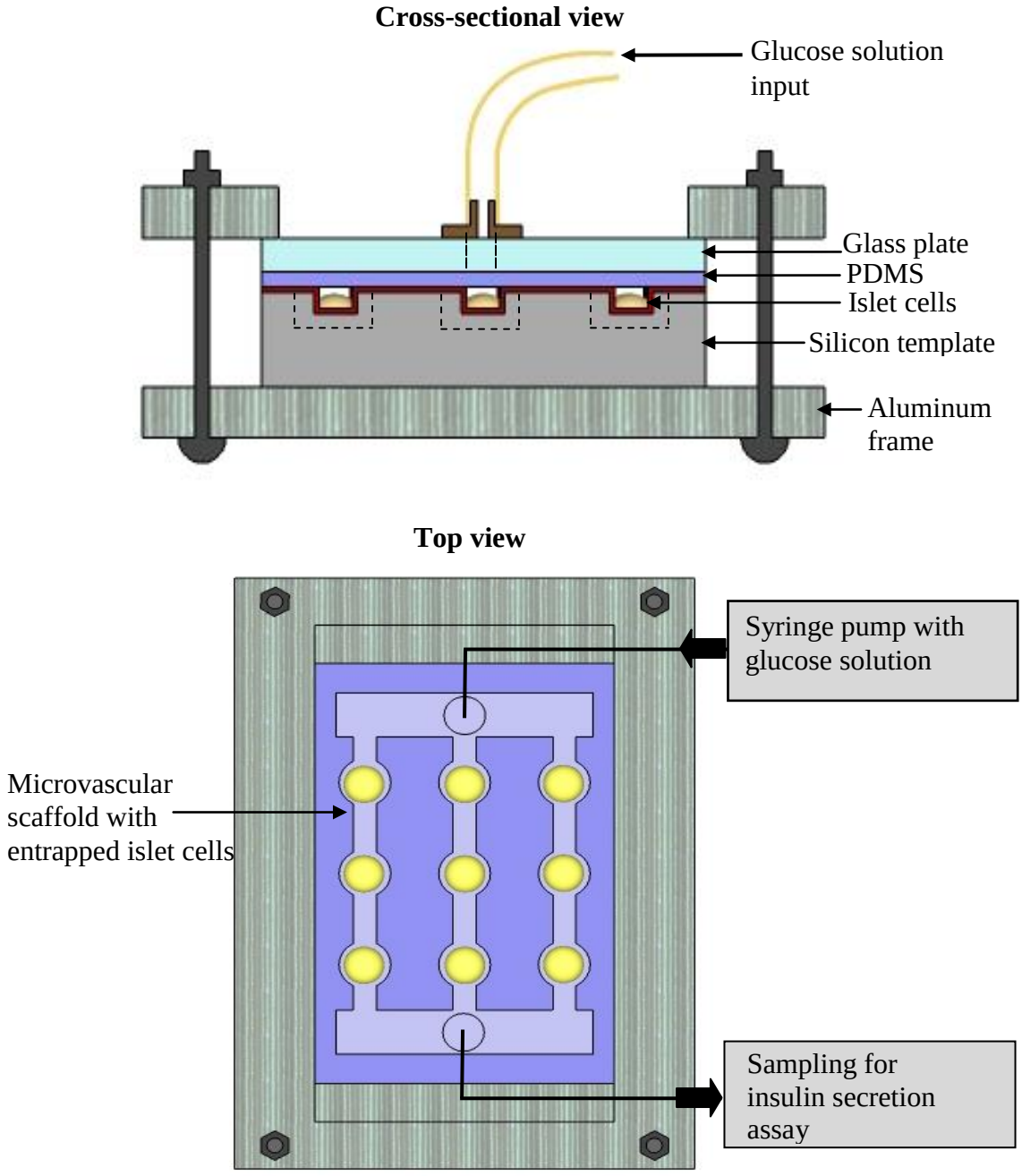

Figure 4.9. Experimental apparatus for a microvascular bioreactor device.

4.2.2.3 Insulin secretion assay

The glucose stimulation output solution from the bioreactor was assayed for insulin secretion using a rat insulin enzyme linked immunosorbent assay (ELISA, Mercodia Inc.) using the manufacturer's protocol (Figure 4.10) [20]. The process exploited two different antigenic properties of insulin for binding with two monoclonal anti-insulin antibodies. Antibodies are proteins produced by the immune system of the body to identify and remove foreign bodies, and antigens are molecules targeted by the antibodies. Monoclonal antibodies are formed from the same immune cell and can be used to target two different antigens of a subject. The ELISA kit consisted of a 96 well plate coated with a monoclonal anti-insulin antibody, calibrator solutions with known concentrations of insulin, and an enzyme-conjugated anti-insulin antibody. The sample solution with an unknown insulin concentration was introduced into the microtitration wells followed by the introduction of enzyme-conjugated antibody. The plate was then incubated for 2 hours allowing the insulin in the sample to bind with the antibody coating the well as well as the enzyme-conjugated antibody. Any unbound enzyme-conjugated antibody was washed away using a buffer solution. The enzyme conjugate was finally reacted with 3,3',5,5'-tetramethylbenzidine with a timed colorimetric stop. The absorbance of each resulting well, indirectly determined by the concentration of the insulin, was measured at 450 nm using an ELISA reader (Multiskan spectrum microplate spectrophotometer, Thermo Fisher Scientific Inc., MA).

Figure 4.11 illustrates the results from a glucose stimulation test of the bioreactor with approximately 40 entrapped cells. Basal and high concentration glucose solutions were flowed alternately for 30 minutes each. The insulin-secretion/cell/hour was

observed to be 1.6µg/l and 13.5µg/l for basal and high concentration glucose respectively. The insulin secretion assay demonstrated that the bioreactor responded to high concentration glucose (300mg/dl) by secreting 8-fold more insulin as compared to basal concentration glucose (60mg/dl). Previous reports on islet cell glucose stimulation have documented insulin secretion peaks observed for stimulatory levels of glucose to be approximately 1.5 to 10 times the secretion for basal levels of glucose, varying based on factors such as the number and size of the cells, the concentration of glucose, the experimental conditions, and the temporal resolution [21-23].

The glucose stimulation tests successfully demonstrated the feasibility of the developed microvascular insulin bioreactor in bioartificial pancreas applications.

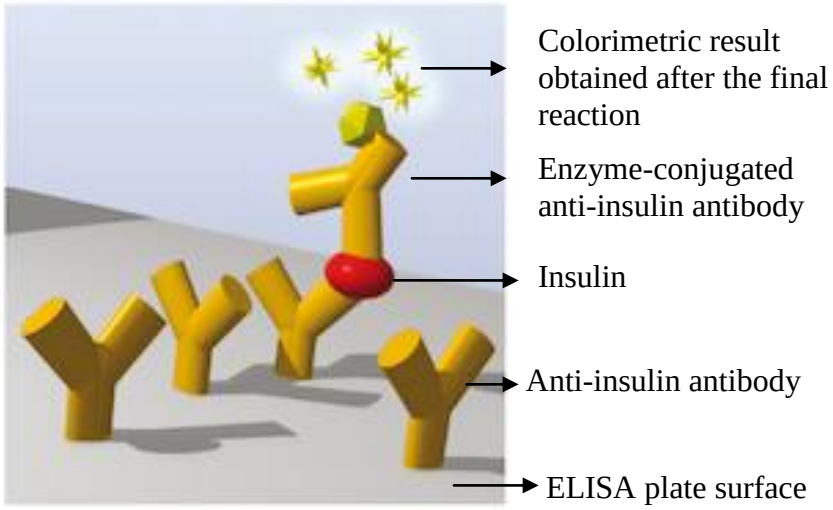

Figure 4.10. Schematic illustration of the principle of ELISA [20].

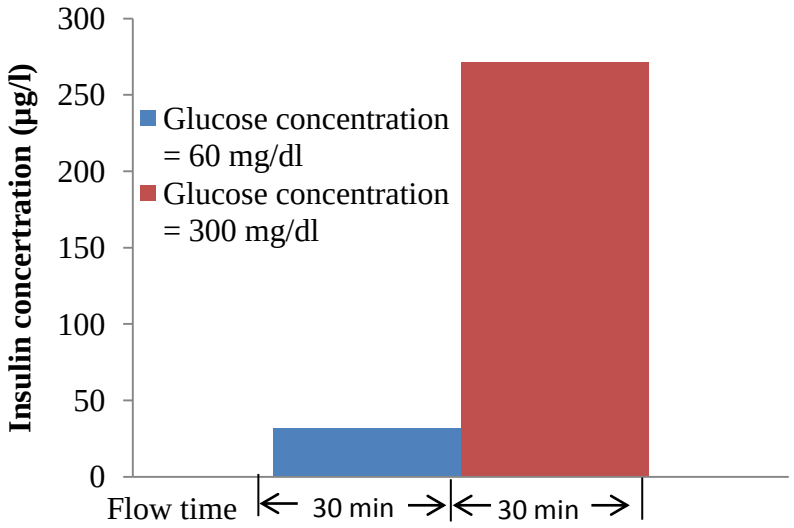

Figure 4.11. Insulin secretion exhibited by the bioreactor device in response to changing levels of glucose concentration.

4.3 Endothelialization of high length-to-width aspect ratio microvascular scaffolds

The second microvascular device in this research focused on the development of an approach for a uniform incorporation of endothelial cells on the luminal surface of the construct. Several static and dynamic endothelial cell seeding strategies have been reported for the construction of a confluent layer of endothelium on the interior surface of synthetic vascular grafts [24-26]. Static cell seeding approaches involve delivering a cell suspension to the graft and culturing the cells under static conditions. To enhance the cell attachment and obtain a more uniform cell distribution, the cell culture is often performed under dynamic conditions. This entails agitation of the graft containing the cells (typically under flow conditions), such that the additional forces involved in this process facilitate the cell distribution (Figure 4.12). Cell seeding of microvascular networks is typically performed under a dynamic perfusion-based system [9].

Endothelial cell seeding of a tubular geometry construct is influenced by mass transport of the cells in the culture media through the lumen of the tube. As the diameter of the tube shrinks (as in the case of microvascular devices), and the length of the tube increases, efficient delivery of the cells to the interiors of the tubes becomes challenging. This can limit the spatial homogeneity of the cells and their exposure to sufficient cell media during cell culture. An approach to overcome this was suggested by Perea et al. [27]. They investigated labeling the endothelial cells with magnetic particles and seeding them on a 3.5 mm diameter scaffold under the influence of a radial magnetic field. Although this strategy was observed to improve the cell seeding efficiency and provide rapid attachment of the cells to the interiors of the vascular graft, the diameter of the magnetic particles used was 4.4 μm, rendering this approach unsuitable for progressing towards microvascular conduits.

The current research presents an endothelial cell seeding approach for high length-to-depth aspect ratio microvascular scaffolds using MEMS technology.

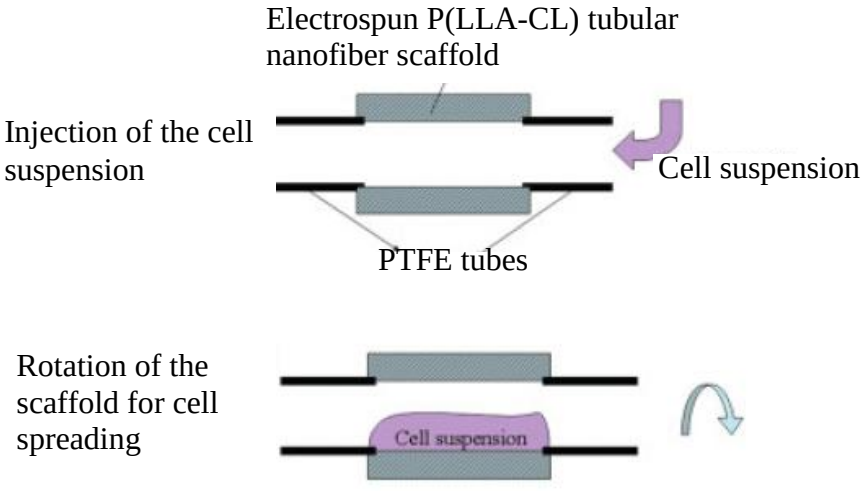

Figure 4.12. A dynamic approach for endothelial cell seeding of a tubular construct [28].

4.3.1 Device concept

As described earlier, endothelial cell seeding of tubular constructs is a function of the conduit diameter and length, and an efficient delivery of the cells and culture media through high length-to-width aspect ratio microvascular networks is challenging. We endeavored to address the above cited concerns by developing a MEMS-based approach for the fabrication of an elastomeric, deformable microfluidic chip with reentrant trenches. This device allowed for a 'stretch open - seed endothelial cells - seal' operation, as shown in Figure 4.13 and Figure 4.14. The width of the cleft on the sealing wall of the reentrant channels was designed to be 2-3 times the diameter of the endothelial cells. For endothelial cell seeding of these constructs, the device could be stretched or bent outwards to widen the opening of the microchannels, seeded with cells, and released or bent inwards to seal up the opening. It was believed that the reentrant geometry of the proposed deformable microvascular network and a 'stretch open - seed cells - seal' approach would allow the passage of the cells without being limited by mass transport through long channels, and provide access to sufficient cell media to the cells during the cell culture. This would potentially result in a more spatially homogeneous cellularization of the conduit, efficient cell seeding, and therefore, higher patency of the microvascular conduit.

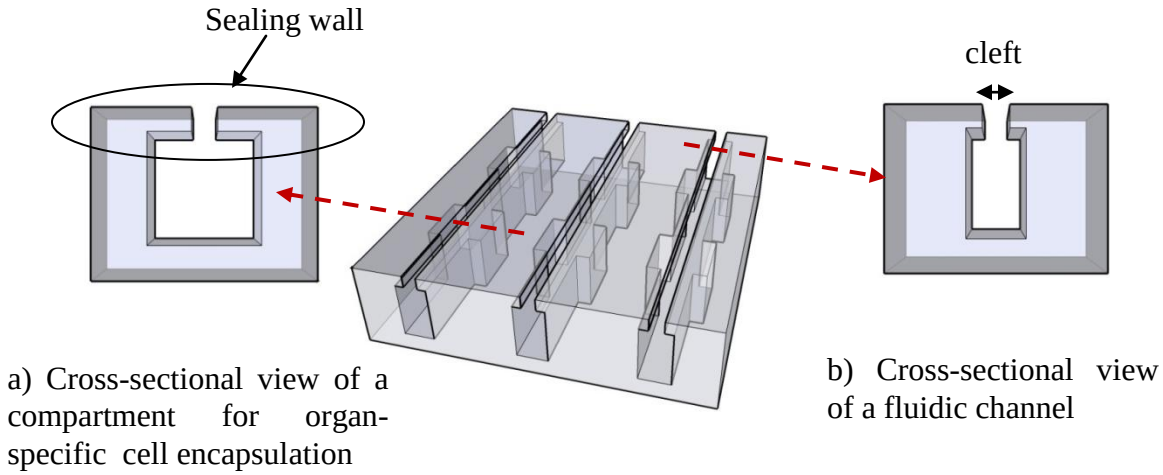

Figure 4.13. Schematic representation of an elastomeric, deformable microvascular network with a) compartments for localized organ-specific cell encapsulation, and b) fluidic channels forming the microvascular network.

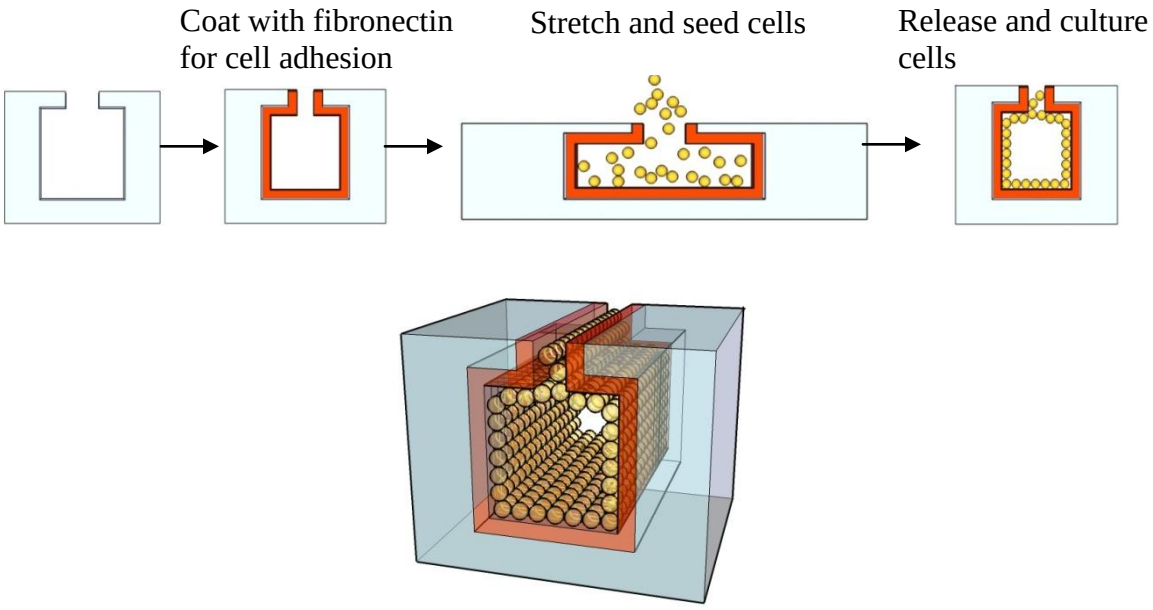

Figure 4.14. A schematic illustration of the 'stretch open - seed cells - seal' operation for endothelialization of elastomeric, deformable reentrant microvascular networks.

4.3.2 Fabrication development

The fabrication process sequence for a PDMS reentrant microvascular scaffold is illustrated in Figure 4.15. A titanium-copper-titanium metal seed layer was sputter-coated on a (100) silicon wafer. A 10-µm thick positive photoresist AZ 4620 (Hoechst Celanese Corp., Somerville, NJ) was first spin-coated and patterned on the seed layer. This layer defined the thickness of the sealing wall of the microvascular scaffold. A second layer of negative photoresist NR21 (Futurrex Inc., Franklin, NJ) was spin-coated and patterned on the existing layer of photoresist to form an 80-100-µm thick film. The negative mold for the PDMS scaffold was constructed using nickel electroplating of the fabricated photoresist mold. The photoresist was etched away using acetone and RIE, leaving behind the nickel negative mold (Figure 4.16a). PDMS (Sylgard 184, Dow Corning Co., Midland, MI) was released on the nickel mold, degassed in vacuum and cured at 60 °C for 10 hours. PDMS conformed to the shape of the metal mold to form a reentrant microvascular construct. Finally, the PDMS construct with reentrant trenches was gently separated from the metal mold (Figure 4.16b).

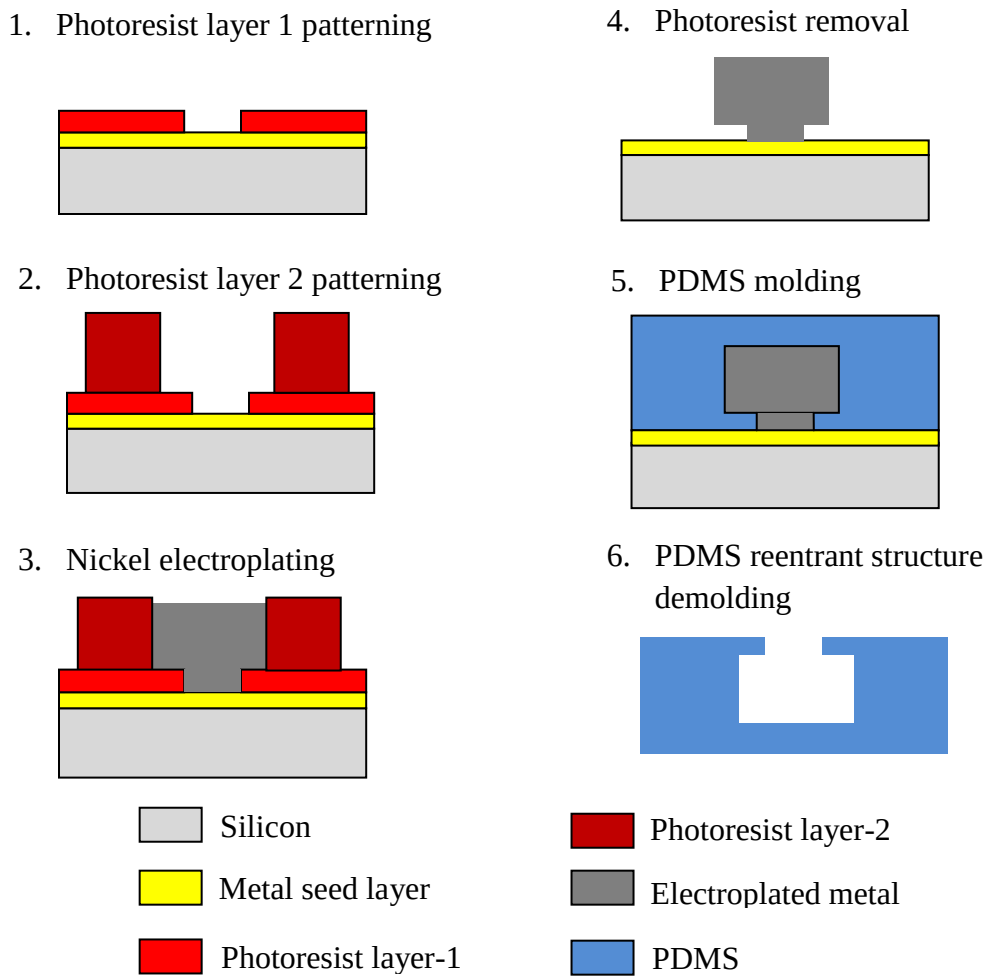

Figure 4.15. Fabrication process flow for PDMS reentrant microvascular networks.

The reentrant microvascular scaffold was designed to have microcompartments and microchannels for potential incorporation of organ-specific cells (Figure 4.17). The width of the microcompartments was 80-100 µm and the width of the microchannels was 40 µm. The depth of the trenches was 50-120 µm. The diameter of the endothelial cells was approximately 12-15 µm. The clefts (20-30 µm) were designed to be approximately 2-3 times the cell diameter.

The openings of the resultant reentrant trenches could be widened and sealed by applying tensile and compressive loads respectively. The deformability of the PDMS scaffold for opening and sealing the microchannel clefts by bending actions is illustrated in Figure 4.18.

4.3.3 Endothelialization of reentrant microvascular scaffolds

4.3.3.1 Endothelial cell culture

Cultured human umbilical vein endothelial cells (HUVEC) were utilized for endothelialization of the PDMS reentrant microvascular scaffolds. HUVECs are endothelial cells isolated from a human umbilical vein. The HUVECs used in the current work were cultured using a standard protocol [29]. Cytopreserved HUVECs (Lonza Inc.) were thawed and cultured in a cell culture flask with endothelial cell growth medium. Cultured HUVECs were spun down to a pellet and resuspended in serum free media at 10^6 cells/mL.

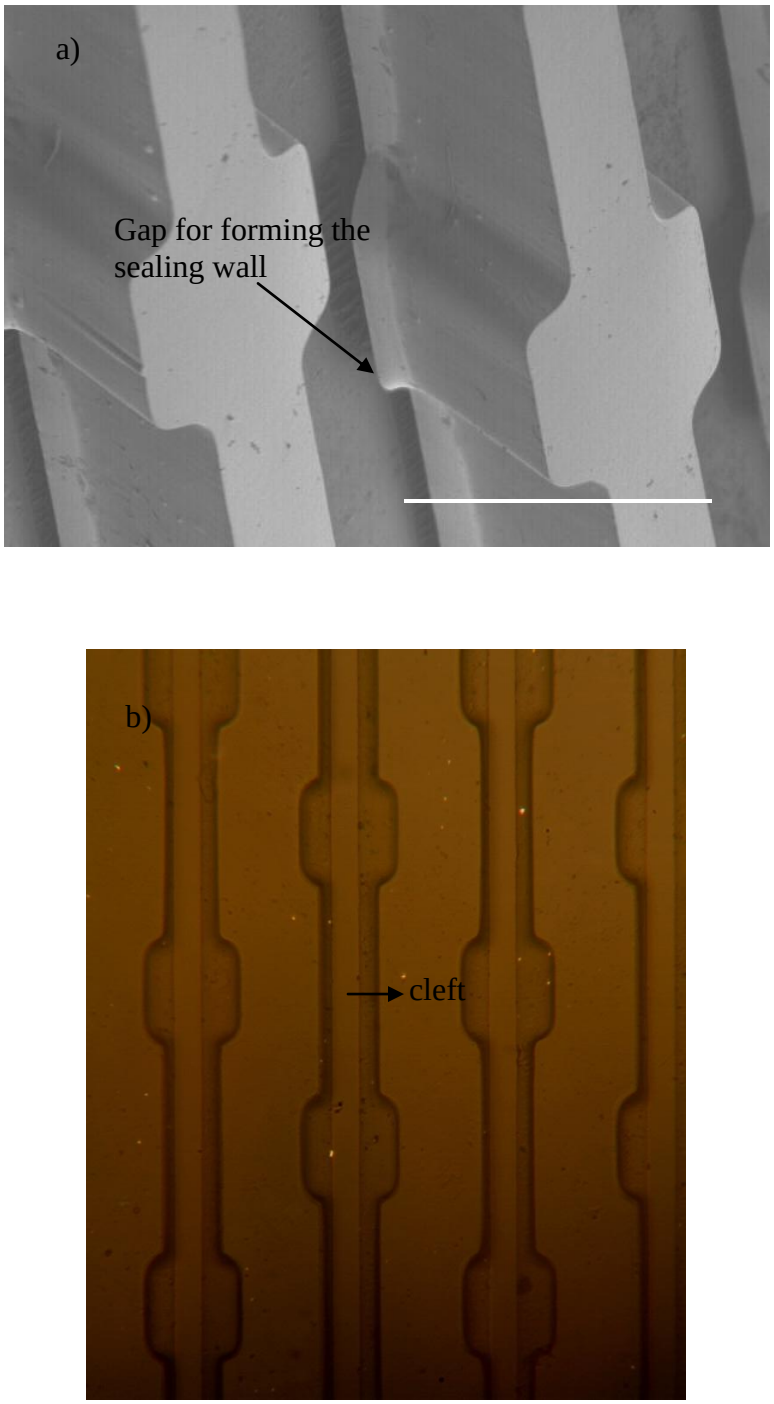

Figure 4.16. a) A nickel mold for a reentrant microvascular scaffold (scale bar = 100 μm), and b) top view of a micromolded PDMS reentrant microvascular scaffold.

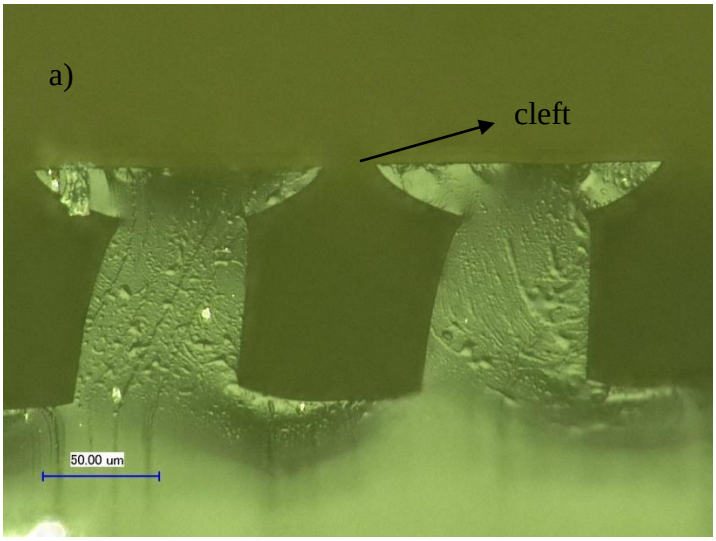

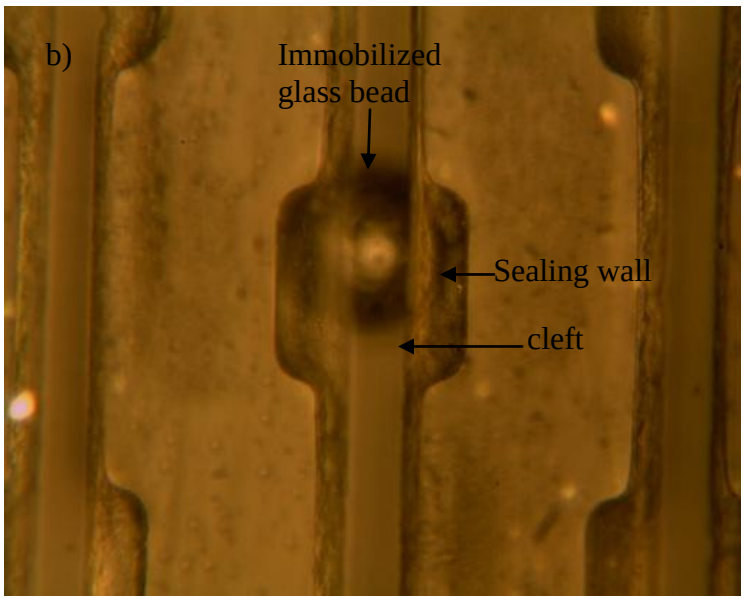

Figure 4.17. a) Cross-sectional view of a reentrant microvascular scaffold illustrating the cleft on the sealing wall (scale bar = 50 µm), and b) a locally immobilized glass bead entrapped in a reentrant microvascular scaffold.

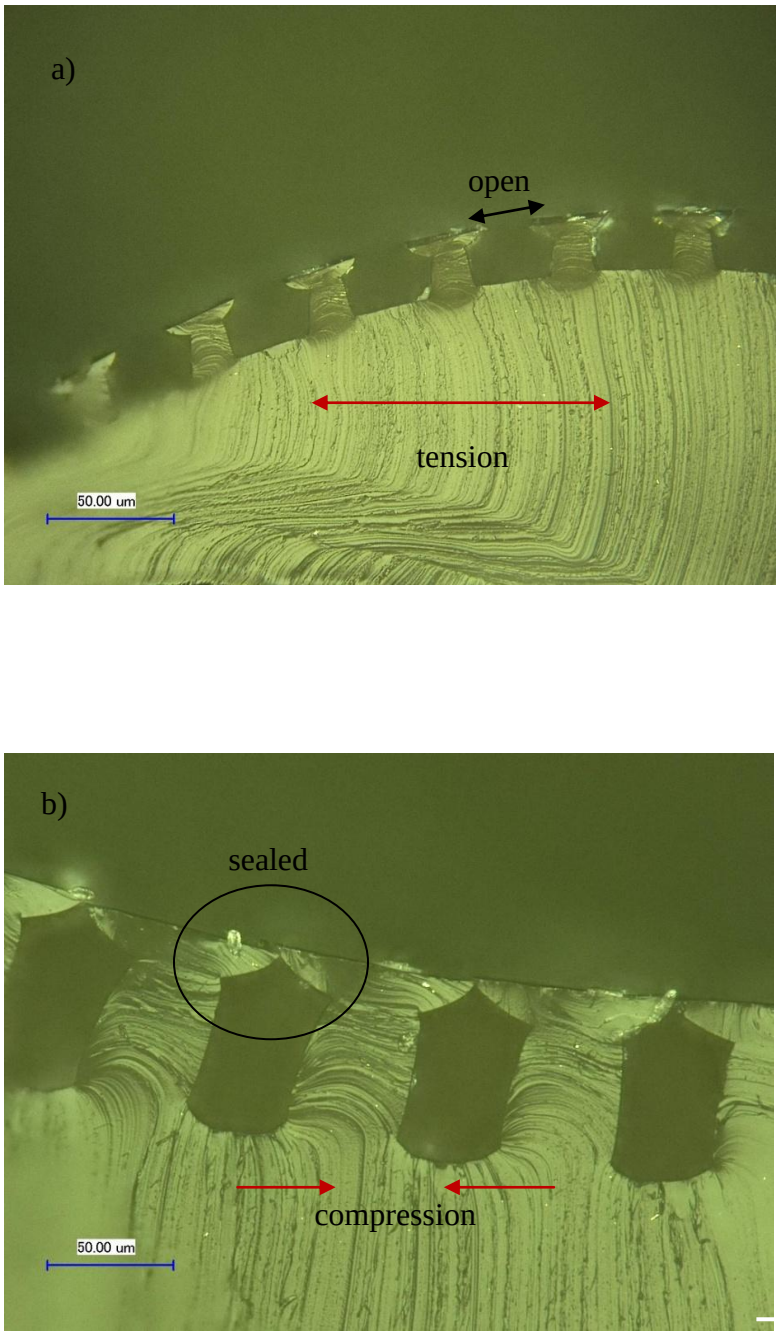

Figure 4.18. Deformability of the reentrant microvascular networks illustrating opening and sealing of the microchannel cleft. a) A reentrant microvascular scaffold in the open state under tension and b) a reentrant microvascular scaffold in the sealed state under compression. (scale bars = 50 µm)

4.3.3.2 Endothelial cell seeding experiments

Endothelialization of the microvascular network was performed using the described ‘stretch open - seed cells - seal’ approach. In preparation for cell seeding, the PDMS reentrant microvascular scaffold was first treated with oxygen plasma to render it hydrophilic. It was then sterilized in ethanol for 2 hours. After vacuum drying, it was incubated in 8 ml of 50 µg/ml fibronectin (Sigma-Aldrich Inc.) for 24 hours at 4 °C to ascertain the adhesion of the cells to the microchannels. Fibronectin is an extracellular matrix protein that plays an important role in cell adhesion in the native tissues [30]. The reentrant microvascular scaffold was washed with 5 mL of 1xPBS to wash away excess fibronectin. It was placed in full serum media at 37 °C for 2 hours prior to the cell seeding.

An acrylic stretching apparatus was machined for securing the reentrant microvascular scaffolds and stretching the clefts open during the cell seeding process. The reentrant microvascular scaffold was clamped down using the stretching contraption, and stretched open to widen the cleft of the templates (Figure 4.19). 150 µl of HUVECs in the cell media was used to seed a single device using static and dynamic approaches. 5 mL of full serum media was then added to each well and the apparatus was placed in a 37 °C incubator for 5-10 days to culture the cells.

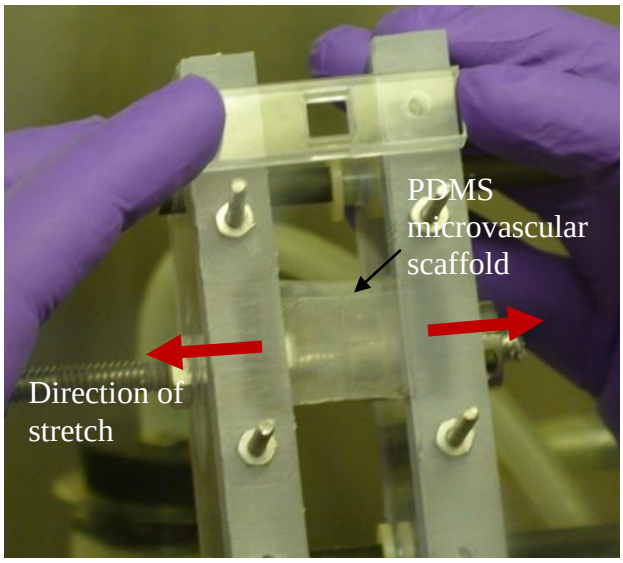

Figure 4.19. A stretching apparatus for widening the microchannel clefts of the microvascular reentrant scaffolds prior to cell seeding.

4.3.3.3 Observations

After the prescribed time, the microchannel scaffold was washed in DPBS to remove the non adherent cells. The cells in the trenches were labeled with dilute (2 uM) calcein AM (Invitrogen corp.) in DPBS and incubated at 37 °C for 1 hour. Calcein AM is a fluorescent dye that produces a green fluorescence in live cells at 495 nm wavelenth. The cells in the microvascular scaffolds were imaged using confocal microscopy (CM) (wavelength: 488 nm) for a qualitative analysis of the cell seeding approach.

Static endothelialization experiments involved stretching the scaffold open using the stretching apparatus and releasing the cell suspension on it. The scaffold was held in the open position for 5 minutes to allow the cells to settle inside the channels prior to releasing. The cells were cultured for 5 days. CM imaging indicated that this approach resulted in a significant number of HUVECs adhered to the top surface. Figure 4.20a

illustrates a CM image of a microchannel scaffold with HUVECs growing on the top surface of a scaffold. It was concluded that static culture does not provide sufficient stimulus to the cells to assemble into the channels.

Following this, a dynamic seeding approach was developed. After the stretching and cell suspension release steps, the stretching apparatus was agitated on a microplate shaker for 5 minutes with the reentrant microvascular scaffold in the open state. This step allowed for the HUVECs to be assembled into the trenches and adhere to the interior surface of the scaffold. A qualitative CM investigation revealed that a significant number of HUVECs were successfully seeded onto the walls of the reentrant microvascular scaffold. This demonstrated the feasibility of this approach for a uniform endothelialization of high length-to-depth aspect ratio microvascular networks. (Figure 4.20b).

a)

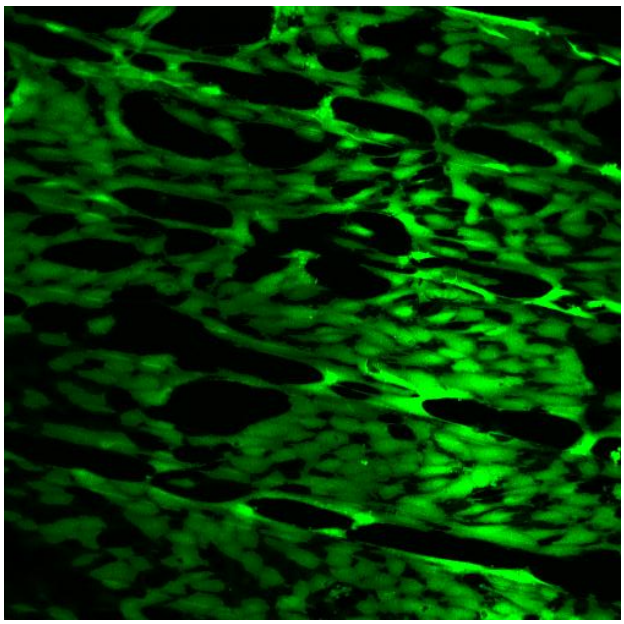

b)

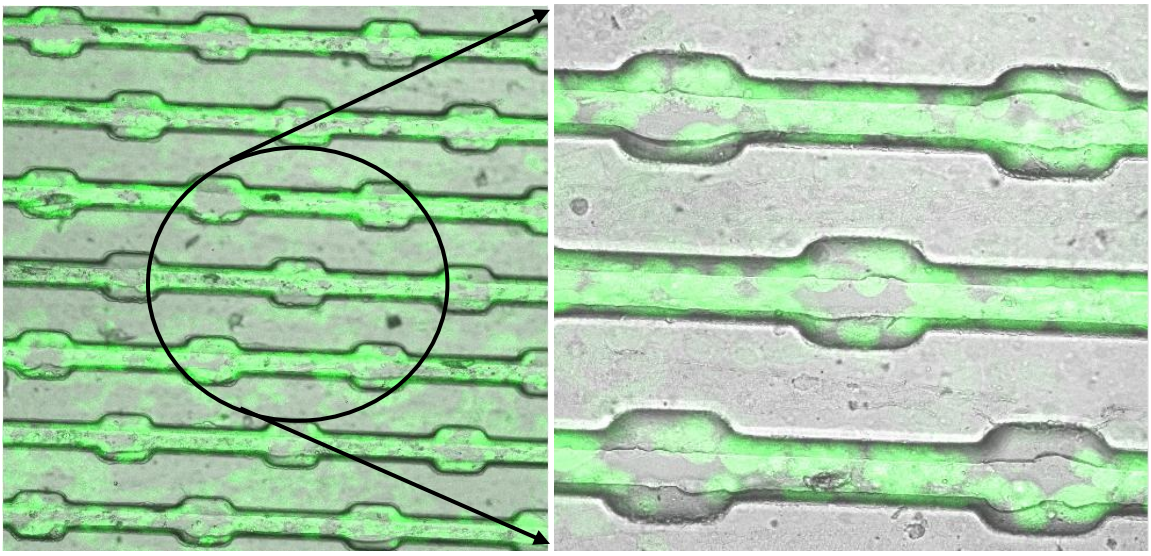

Figure 4.20. a) A CM image of a static seeding endothelial cell culture (5-day) on a reentrant microvascular scaffold. A significant number of cells (seen as fluorescent green) remained adhered to the top surface. b) CM images of a dynamic seeding endothelial cell culture (10-day) on a reentrant microvascular scaffold. The cells were successfully seeded inside the reentrant channels.

4.4 Conclusion

MEMS-based approaches were explored for cellular incorporation in microvascular networks. First, micromolding and template-guided fluidic self-assembly were employed to develop a fabrication approach for collagen microvascular scaffolds with localized encapsulation of therapeutic particles. A prototypical strategy was demonstrated with glass beads as proxy particles. This method was adopted for the construction of a microvascular insulin bioreactor device with locally immobilized pancreatic islet cells. The bioreactor was tested under a glucose solution perfusion configuration. The bioreactor device responded to a stimulatory glucose concentration with 8-fold more insulin secretion as compared to basal glucose concentration. This research displayed the ability of the fabricated bioreactor device to regulate insulin secretion in response to glucose level modulations, demonstrating its potential towards a vascularized bioartificial pancreas.

Next, a micromolding-based fabrication approach was developed for deformable, reentrant microvascular scaffolds. A ‘stretch open – seed cells – seal’ operation was implemented for a spatially homogeneous endothelial cell seeding of high length-to-width aspect ratio microvascular constructs. CM was utilized to establish the feasibility of this cell seeding approach.

4.5 References

1. James Larimer Dubuque, Iowa, W. C., "Introduction to animal physiology," Brown Co., 1968

2. SEER Training Modules, Anatomy and Physiology. U. S. National Institutes of Health, National Cancer Institute. Accessed on 29 August 2010, <http://training.seer.cancer.gov/anatomy/cardiovascular/blood/classification.html>

3. Borenstein, J.T.; Terai, H.; King, K.R.; Weinberg, E.J.; Kaazempur-Mofrad, M.R.; Vacanti, J.P,."Microfabrication technology for vascularized tissue engineering,"Biomedical Microdevices, July 2002, 4(3), p 167-75

4. Shin, Michael; Matsuda, Kant; Ishii, Osamu; Terai, Hidetomi; Kaazempur-Mofrad, Mohammed; Borenstein, Jeffrey; Detmar, Michael; Vacanti, Joseph P., "Endothelialized networks with a vascular geometry in microfabricated poly(dimethyl siloxane),"Biomedical Microdevices, December 2004 6(4), p 269-278,

5. Shevkoplyas SS, Yoshida T, Gifford SC, et al., "Direct measurement of the impact of impaired erythrocyte deformability on microvascular network perfusion in a microfluidic device ," Lab on a chip, 2006, 6(7), p 914-920

6. Rosano, Jenna M.; Tousi, Nazanin; Scott, Robert C.; Krynska, Barbara; Rizzo, Victor; Prabhakarpandian, Balabhaskar; Pant, Kapil; Sundaram, Shivshankar; Kiani, Mohammad F. "A physiologically realistic *in vitro* model of microvascular networks," Biomedical Microdevices, 11(5), p 1051-1057

7. King KR, Wang CCJ, Kaazempur-Mofrad MR, et al., "Biodegradable microfluidics," Advanced materials, Nov 2004, 16(22),p 2007+

8. Armani, Deniz K.; Liu, Chang, "Microfabrication technology for polycaprolactone, a biodegradable polymer,"Journal of Micromechanics and Microengineering, , March 2000, 10(1), p 80-84

9. Fidkowski, Christina; Kaazempur-Mofrad, Mohammad R.; Borenstein, Jeffrey; Vacanti, Joseph P.; Langer, Robert; Wang, Yadong "Endothelialized microvasculature based on a biodegradable elastomer," Tissue Engineering, Jan 2005, 11(1-2), p 302-309

10. Borenstein, Jeffrey T.; Tupper, Malinda M.; MacK, Peter J.; Weinberg, Eli J.; Khalil, Ahmad S.; Hsiao, James; García-Cardeña, Guillermo, "Functional endothelialized microvascular networks with circular cross-sections in a tissue culture substrate," Biomedical Microdevices, Feb 2010, 12(1), p 71-79\

11. Camp, J.P.; Stokol, T.; Shuler, M.L., "Fabrication of a multiple-diameter branched network of microvascular channels with semi-circular cross-sections using xenon

difluoride etching," Biomedical Microdevices, Apr 2008, 10(2), p 179-86

12. Pasic M, MullerGlauser W, vonSegesser L, et al., "Endothelial cell seeding improves patency of synthetic vascular grafts: Manual versus automatized method," European journal of cardio-thoracic surgery, May 1996, 10(5), p 372-379

13. Srinivasan, U. (Berkeley Sensor and Actuator Center, University of California, Berkeley, CA 94720-1174, United States); Liepmann, D.; Howe, R.T., "Microstructure to substrate self-assembly using capillary forces," Journal of Microelectromechanical Systems, March 2001, 10(1), p 17-24

14. Tokilmitsu Y, Kishi H, Kondo S, et al., "Single lymphocyte analysis with a microwell array chip," Cytometry part A., De 2007, 71A(12), p 1003-1010

15. Adewola, Adeola F.; Lee, Dongyoung; Harvat, Tricia; Mohammed, Javeed; Eddington, David T.; Oberholzer, Jose; Wang, Yong, "Microfluidic perifusion and imaging device for multi-parametric islet function assessment," Biomedical Microdevices, June 2010, 12(3), p 409-417

16. Korin N, Bransky A, Khoury M, et al., "Design of Well and Groove Microchannel Bioreactors for Cell Culture," Biotechnology and bioengineering, Mar 2009, 102(4) p 1222-1230

17. Rago AP, Chai PR, Morgan JR.,"Encapsulated arrays of self-assembled microtissues: an alternative to spherical microcapsules," , Feb 2009, 15(2), p 387-95

18. Jonathan V. Rocheleau, Owen P. McGuinness, David W. Piston, W. Steven Head, Glenn M. Walker, "Microfluidic glucose stimulation reveals limited coordination of intracellular Ca2+ activity oscillations in pancreatic islets," Proceedings of the National Academy of Sciences of the United States of America, 2004, 35,p 12899-12903

19. Park J, Berthiaume F, Toner M, et al., "Microfabricated grooved substrates as platforms for bioartificial liver reactors," Biotechnology and bioengineering, Jun 2005, 90(5), p 632-644

20. http://www.mercodia.se/learning-center/mercodia-elisa-technology/principle-of-technology.html, accessed on August 31, 2010

21. Yao, Nan-Kuang; Tang, Sheng-Huei; Chang, Liang-Wey "A cell perifusion system of isolated rat islets for studies on rapid insulin-glucose dynamics," Medical Engineering and Physics, Oct 1997, 19(8), p 759-764

22. Shackman, J.G.; Dahlgren, G.M.; Peters, J.L.; Kennedy, R.T., "Perfusion and chemical monitoring of living cells on a microfluidic chip," Lab on a Chip, Jan 2005,

5(1), p 56-63

23. Mertz RJ, Worley JF, Spencer B, et al., "Activation of stimulus-secretion coupling in pancreatic beta-cells by specific products of glucose metabolism - Evidence for privileged signaling by glycolysis," Journal of biological chemistry,Mar 1996, 271(9), p 4838-4845

24. Burg KJL, Holder WD, Culberson CR, et al., "Comparative study of seeding methods for three-dimensional polymeric scaffolds," Journal of biomedical materials research, Sep 2000, 51(4), p 642-649

25. Fernandez, P. (Univ. Bordeaux, France); Deguette, A.; Pothuaud, L.; Belleannee, G.; Coste, P.; Bordenave, L., "Quality control assessment of ePTFE precoating procedure for *in vitro* endothelial cell seeding," Biomaterials, Aug. 2005, 26(24), p 5042-7

26. Shan-hui Hsu; I-jine Tsai; Da-jun Lin; Chen, D.C., "The effect of dynamic culture conditions on endothelial cell seeding and retention on small diameter polyurethane vascular grafts," Medical Engineering & Physics, April 2005, 27(3), p 267-72

27. Perea H, Aigner J, Hopfner U, et al., "Direct magnetic tubular cell seeding: A novel approach for vascular tissue engineering," Cells tissues organs , 2006, 183(3), p 156-165

28. He W, Ma ZW, Teo WE, et al., "Tubular nanofiber scaffolds for tissue engineered small-diameter vascular grafts," Journal of biomedical materials research part A, Jul 2009, 90A(1), p 205-216

CHAPTER 5

CONCLUSIONS

5.1 Summary

This dissertation focused on applying MEMS technology to the fabrication of acellular and cellularized engineered tissue constructs. There are three specific contributions made by this research.

The first part of this research involved wet-spinning of collagenous fibers for synthetic tissue scaffolds using MEMS-based micro/nanonozzles (as detailed in Chapter 2). In this effort, two distinct strategies were developed for the fabrication of high-pressure-withstanding micro/nanonozzles. Silicon fusion bonding and oxidative sealing were utilized for the construction of in-plane silicon micro/nanonozzles with inner dimensions ranging from 500 nm to 12 μm. A non-lithographic approach involving glass micropipette pulling and electroplating was adopted for the fabrication of glass-metal composite micro/nanonozzles with inner diameters ranging from 450 nm to 100 μm. As a first step, the micromachined nozzles were integrated with a high-pressure (up to 2200 psi) delivery source and a shadowgraph imaging system for establishing the feasibility of generation, imaging, and characterization of liquid sub-10 μm jets. This microfluidic system was utilized for imaging and investigating liquid butane and propane micro/nanojets. Although the micromachined nozzles were able to successfully withstand the differential pressures necessary for driving nanofluidic jets and demonstrate the generation of pressure driven liquid nanojets, the effects of nozzle clogging impeding the flow could not be completely eliminated. This resulted in a significant variability in the

jet dynamics. It was concluded that small pores are extremely sensitive to contamination and present a significant challenge in the analysis of pressure driven sub-10 μm fluidics. In the next stage, a collagen fiber wet-spinning apparatus was developed using the high-pressure fluidic apparatus and the micromachined nozzles. Control over the fiber dimensions was exercised in two ways. In the first approach, the nozzle dimensions were adjusted to accordingly modify the extruded fiber dimensions. A 10 μm glass-metal composite nozzle yielded a 2-μm wide × 0.3-μm thick collagen fiber at 1000 psi for a 1.5 mg/ml collagen solution. This approach experienced fiber breakages and nozzle clogging, and this effect was particularly pronounced for sub-10 μm nozzles. In the second approach, hydrodynamic focusing was employed to control and modulate the width of collagen fibers by creating a virtual nozzle with fluidic walls. A collagen solution and a coagulant WSB solution were flowed coaxially, and their relative flow rates were modulated to obtain fibers of different dimensions. Also, collagen microfibers with crimped geometries could be produced using this strategy.

The second part of this research focused on the development of a microtransfer-molding-based approach for the fabrication of spatially designed collagen fiber networks and collagen-elastin FRCs based on these networks. Using conventional MEMS processing strategies allowed for an excellent control over the fiber dimensions, alignment, and distribution. These parameters could be modified by the template design and the collagen solution properties. Hollow and solid collagen fibers with widths ranging from 2 μm to 50 μm and thicknesses ranging from 300 nm to 3 μm were fabricated. Fiber network spatial layouts explored included unidirectional straight fibers, in-plane crimped fibers, out-of-plane crimped fibers, and porous fibers. The collagen

fibers exhibited native collagen morphology with D-periodic banding. These fiber networks were embedded in an elastin matrix to construct collagen-elastin FRC tissue scaffolds. These collagen-elastin composites enabled a combination of high strength and extensibility. The orthotropic elastic nature of unidirectional straight fiber composite laminates was demonstrated, and the concentration, orientation, and layout of the fibers were identified as the determinants of the FRC mechanical properties. Also, in-plane crimped fibers were used to develop FRCs with a strain-dependent stiffness as observed in many native soft tissues. The crimped FRCs displayed a non-linear elastic behavior whereby the tissue material transitioned from a low stiffness regime to a high stiffness regime at a transition strain determined by the designed crimp geometry of the fibers.

The third and final part of this research involved developing strategies for the incorporation of cells into hollow microvascular scaffolds. Two types of cells were explored: murine pancreatic islet cells and HUVECs. A stand-alone collagen microvascular scaffold with local encapsulation of glass beads as proxy particles was developed using micromolding and a template guided fluidic self-assembly process. A fill efficiency of 96-98% was observed for the glass beads. This fabrication approach was used towards the construction of a microvascular insulin bioreactor with localized immobilization of islet cells. Glucose solution perfusion was performed to investigate the insulin secretion capability of the device. The bioreactor with 40 encapsulated islet cells was observed to respond to a stimulatory concentration of glucose (300 mg/dL) with 8-fold insulin as compared to basal concentration glucose (60 mg/dL) as determined by a mouse insulin ELISA. Finally, a MEMS-based approach was developed for a more uniform endothelial cell seeding of high length-to-depth aspect ratio microvascular

scaffolds. A micromolding strategy was devised for the fabrication of a deformable reentrant PDMS microvascular scaffold. A 'stretch - seed cells - seal' operation was demonstrated for endothelilization of the constructed microvascular network, allowing for a more uniformly distributed and spatially homogenous cell seeding.

5.2 Discussion and future directions

In this dissertation, the potential of MEMS technology for the fabrication and engineering of acellular and cellularized tissue constructs was explored. The various developed tissue constructs can be further improved with additional characterization and optimization, and enhancement of their performance characteristics. The immediate goals for the different constructs are outlined in Figure 5.1, and some specific suggestions are made in the following sections.

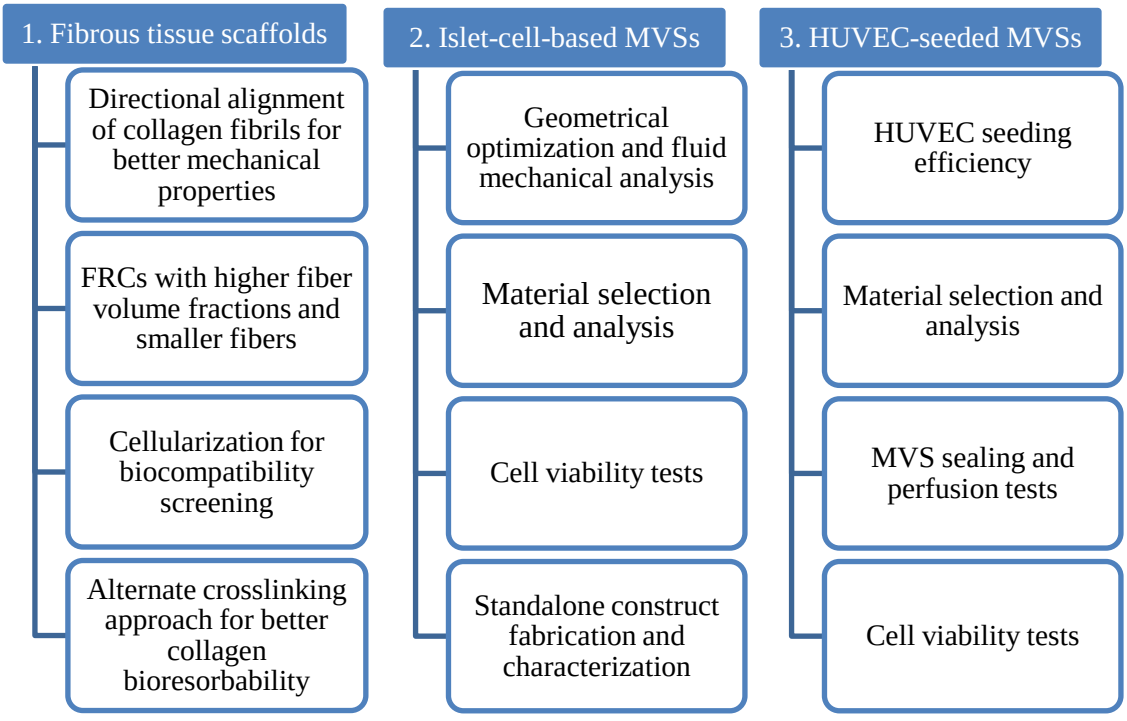

Figure 5.1. Characterization and performance improvement goals for the developed tissue constructs.

5.2.1 Fibrous tissue scaffolds

The next steps for the synthetic fibrous scaffolds fabricated by the template-based approach would involve the enhancement of the material characteristics and investigation of the properties of the scaffolds indicative of their quality and performance in actual blood vessel or artificial organ applications.

Although the collagen fibers fabricated using the template-based approach allowed for an excellent control over the layout and alignment of the fibers, the collagen fibrils composing the fibers were randomly oriented. This caused the mechanical strength and stiffness of the fibers produced in this fashion to be lower than the wet-spun fibers which undergo a mechanical annealing process under hydrodynamic forces. Directional alignment of self-assembled collagen fibrils has been demonstrated using microfluidics, electric fields, magnetic fields, and application of strain [1-4]. To enhance the performance of the fabricated collagen fibers, one of the reported methods may be adopted for generating fibrils oriented in the longitudinal direction of the fibers.

Although the fabrication of submicron collagen fibers was demonstrated using the template-based approach, 20-μm wide fibers were used for the development and characterization of the FRCs for the ease of handling and characterization. The conditions needed for the fabrication of FRCs reinforced by submicron collagen fibers need further optimization. Such materials with fibers in the submicron range would make very attractive biomimetic tissue materials.

The rarity of the protein polymers utilized in the demonstrated fabrication approach, especially elastin, constrained the maximum FVF investigated for these materials. As has been discussed earlier, the FVF in an FRC dictates its strength and

stiffness. It is essential to test the maximum FVF achievable using this approach. One potential approach for conserving elastin prior to FRC lamination would be to fabricate thinner elastin films for individual FRC layers.

Cell seeding is one of the approaches traditionally followed to screen biomaterials for their biocompatibility [5-6]. The biocompatibility of the developed FRCs and their functionality in vascular graft applications can be examined by their endothelialization. This experiment can additionally determine the influence of the alignment of the fibers on the cell proliferation and phenotype development.

Although glutaraldehyde is a commonly used crosslinking agent for collagen and elastin, it is limited by its cytotoxicity [7]. A possible alternative for glutaraldehyde crosslinking could be genipin, which has been reported to show better results in implanted constructs with respect to cytotoxicity and bioresorbability [8].

5.2.2 Islet-cell-based MVSs

In this dissertation, a prototypical islet cell bioreactor construct was fabricated and its short term insulin secretion capability was demonstrated. Several features of the bioreactor device need further optimization and characterization. The most significant metric that requires to be examined is the long term cell viability in these constructs. Improvements over the current geometry and materials are recommended to facilitate the long term survival of the cells. The topology of the microvascular network would have a significant influence on the survival and performance of the islet cells in the microenvironments they are contained in. Taking this into consideration, the geometrical layout of the microchannels should be optimized both numerically and empirically such

that the mass transport to and from the cells is maximized while the shear stress experienced by the cells is minimized. Figure 5.2 illustrates a potential geometry with microchannels with sidepockets that can be employed to achieve this. In addition to the geometry, the construct should be fabricated on a permeable substrate assisting easier oxygen transport to the cells. PDMS can be a possible candidate material for this. The influence of these modifications may be examined using dynamic insulin secretion tests to display the real time behavior of the cells.

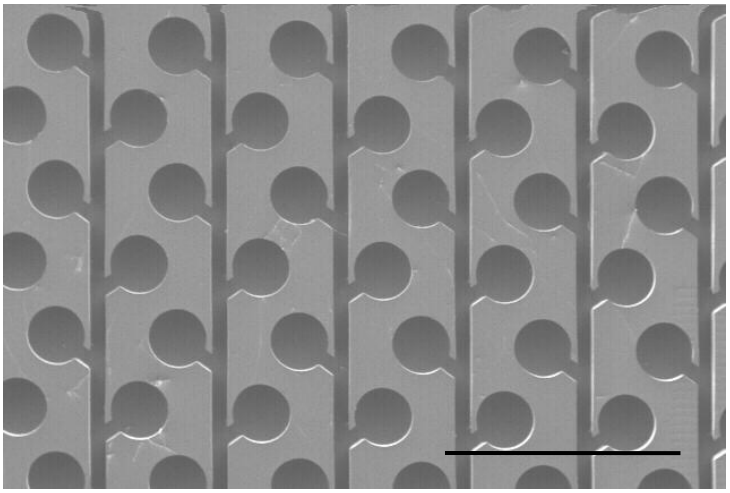

Figure 5.2. A silicon template for insulin bioreactor with sidepockets for islet cell immobilization (scale bar = 1mm).

5.2.3 HUVEC-seeded MVSs

The current study established a new approach for a uniform endothelial cell seeding of microvascular networks. In the subsequent experiments, material suitability, cell seeding efficiency, confluency, and spatial homogeneity offered by the strategy need to be examined. Also, after endothelialization, the construct cleft may be sealed for

carrying out fluidic tests. The long term viability of the endothelial cells in such microvascular scaffolds may be examined

5.2.4 The vision

As discussed earlier, mammalian native tissues are a combination of acellular elements and cells, each responsible for carrying out different functionalities. The vascular system, necessary for nourishing all the tissues and organs in the body, is a good representation of this. It is composed of three significant layers, tunica intima, tunica media, and tunica adventetia, as illustrated in Figure 5.3 [9]. While tunica intima is composed of a monolayer of endothelial cells, tunicas media and adventitia are significantly composed of acellular fibrous proteins.

In an effort to mimic the native tissue structures and funtionalities, tissue engineering focuses on three important factors (Figure 5.4).

1. In-vitro preparations of structures mimicking native extracellular fibrous tissues or tissue scaffolds for providing mechanical strength and structural integrity to the tissues
2. Isolation and utilization of cells for emulation of organ functions or carrying out tissue regeneration
3. Introduction of vasculature for supplying nutrients and oxygen to the tissues

Each one of these components is either developed independently as an implantable construct or integrated with the other components for the development of a fully functional tissue or organ in vitro.

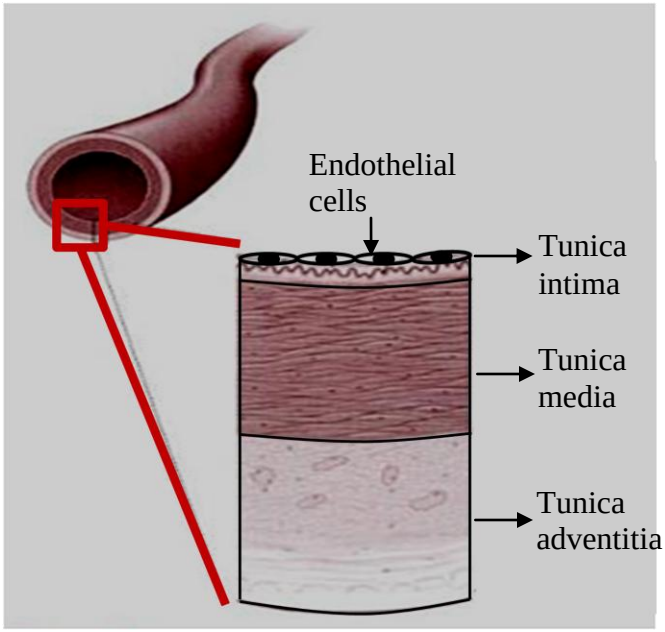

Figure 5.3. Cross-sectional view of a blood vessel lumen [9].

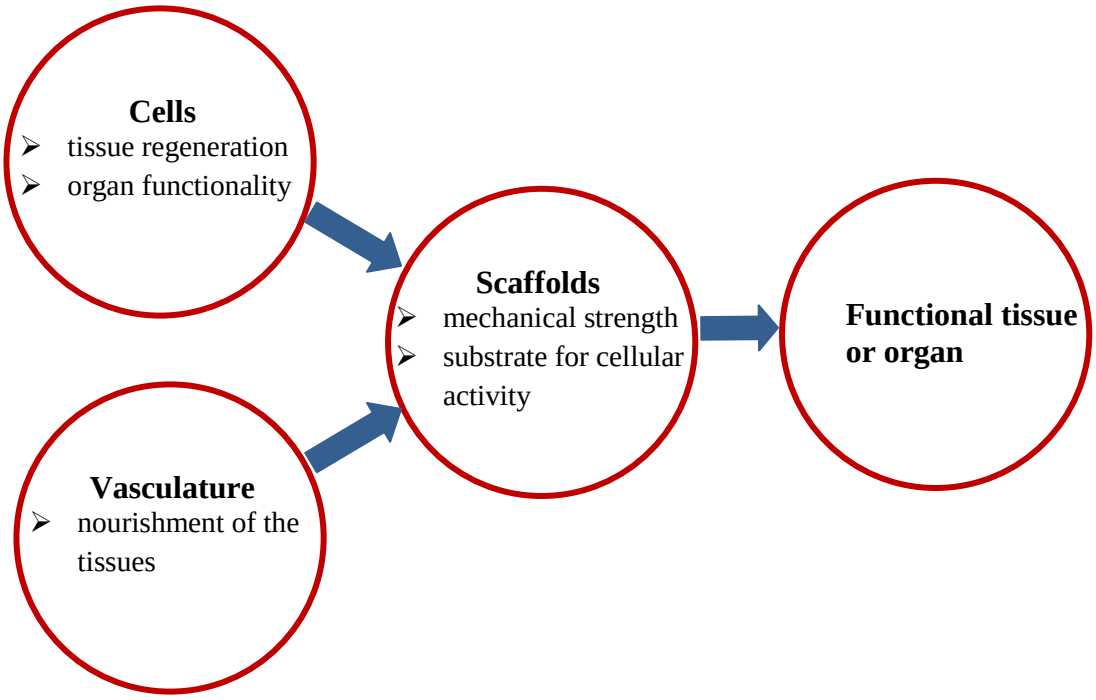

Figure 5.4. The development of a fully functional tissue or organ in-vitro.

This dissertation primarily focused on the fabrication and characterization of distinct tissue constructs focusing on the three aforementioned tissue engineering components. The long term vision of this research would be to move towards the unification of the cellular and acellular concepts developed in this work. This convergence along with the incorporation of vasculature would potentially result in a fully functional implantable tissue or organ exhibiting long term viability (Figure 5.4).

The envisioned multifunctional tissue construct could comprise a microvascular framework composed of a collagen-elastin composite material for mechanical strength and integrity of the tissue, endothelial cells uniformly lining the microvascular networks to ensure their long term patency, and locally immobilized islet cells for emulating pancreatic functionalities.

5.3 References

1. Guo, Cheng, Kaufman, Laura J., "Flow and magnetic field induced collagen alignment," Biomaterials, February 2007, 28(6), p 1105-1114

2. Rosner, Benjamin I. (Univ of Minnesota, Minneapolis, United States); Dubey, Naren; Letourneau, Paul C.; Tranquillo, Robert T., "Simulated peripheral nerve regeneration in magnetically aligned collagen gels derivatized with laminin peptides and seeded with Schwann cells,"Annual International Conference of the IEEE Engineering in Medicine and Biology - Proceedings, 1999, 1, p 117

3. Köster, Sarah; Leach, Jennie B.; Struth, Bernd; Pfohl, Thomas; Wong, Joyce Y. "Visualization of flow-aligned type I collagen self-assembly in tunable pH gradients," Langmuir, January 2007, 23(2), p 357-359

4. Caves, Jeffrey M.; Kumar, Vivek A.; Wen, Jing; Cui, Wanxing; Martinez, Adam; Apkarian, Robert; Coats, Julie E.; Berland, Keith; Chaikof, Elliot L., "Fibrillogenesis in continuously spun synthetic collagen fiber," Journal of Biomedical Materials Research - Part B Applied Biomaterials, April 2010, 93(1), p 24-38

5. Correa-Duarte MA, Wagner N, Rojas-Chapana J, et al., " Fabrication and biocompatibility of carbon nanotube-based 3D networks as scaffolds for cell seeding and growth," Nano letters, Nov 2004, 4(11),p 2233-2236

6. Beumer GJ, Vanblitterswijk CA, Bakker D, et al., "Cell-seeding and in-vitro biocompatibility evaluation of polymeric matrices of peo pbt copolymers and plla," Biomaterials, Jul 1993, 14(8), p 598-604

7. Gough JE, Scotchford CA, Downes S ," Cytotoxicity of glutaraldehyde crosslinked collagen/poly(vinyl alcohol) films is by the mechanism of apoptosis," Journal of biomedical materials research, Jul 2002, 61(1), p 121-130

8. Sung HW, Huang RN, Huang LLH, et al., "*In vitro* evaluation of cytotoxicity of a naturally occurring cross-linking reagent for biological tissue fixation,", Journal of biomaterials science-polymer edition, 1999, 10(1), p 63-78

9. Seifter et al., "Concepts in medical physiology", Lippincott Williams and Wilkins, 2005